David Kristiansen

Wave Induced Effects on Floaters of Aquaculture plants

Doctoral thesis
for the degree of philosophiae doctor

Trondheim, March 2010

Norwegian University of Science and Technology
Faculty of Engineering Science and Technology
Department of Marine Technology

NTNU
Innovation and Creativity

NTNU

Norwegian University of Science and Technology

Doctoral thesis
for the degree of philosophiae doctor

Faculty of Engineering Science and Technology
Department of Marine Technology

ISBN 978-82-471-1995-2 (printed version)
ISBN 978-82-471-1997-6 (electronic version)
ISSN 1503-8181

Doctoral theses at NTNU, 2010:20

Printed by NTNU-trykk

Abstract

The main objective of this work is to study wave loads on floaters of fish farms. Several incidents of major fish escapes due to structural collapse of fish farms in harsh weather have motivated this study, as a step towards obtaining better load models for the wave loads on the floaters. Floaters of fish farms are typically small compared to dimensioning waves. The local two-dimensional problem of a floater subject to beam sea regular waves is considered. The problem is addressed by means of numerical simulations, model tests and simplified numerical models. A CFD numerical wave tank (NWT) for fully nonlinear wave body interaction problems is developed. The numerical model applies a one-fluid model, where a fractional step approach is used to solve the incompressible Navier-Stokes equations in time on a Cartesian staggered grid. Further, a combined Constrained Interpolation Profile (CIP-) and finite difference procedure is used. An immersed boundary technique is applied to impose boundary conditions on the floater.

Two sets of model tests have been conducted. In the first set, wave loads on fixed horizontal cylinders in beam sea waves were studied. The purpose was to obtain validation data for the numerical wave tank. Two models were tested. One with a circular cross-section and one with a rectangular cross-section. Model draft was varied. Other test parameters were wave period and wave steepness. The primary variables measured were the clamping forces of the model and the wave elevation at eight positions in the flume. Numerical simulations similar to the physical experiments were performed and results compared, showing good agreement. Wave over-topping on the models was observed, both in the experiments and in the simulations.

In the second set of experiments, a floating circular cylinder in beam sea regular waves was tested. The cylinder was moored using pre-tensioned mooring lines, yielding a natural frequency of the sway motion which is representative for fish farms. Primary variables measured here were the model accelerations used to obtain the body motion, surface elevation and mooring line forces. Results were compared with linear potential flow theory, semi-empirical theories and simulations with the CIP-based numerical wave tank. An instability phenomenon was observed in the experiments when the wave frequency was two times the natural frequency in sway, causing large amplitude sway motion which is not predicted by linear potential flow theory. The same instability behaviour was also observed in simulations with the CIP-based numerical wave tank and is believed to be due to nonlinear hydrodynamic effects. Experiments and numerical simulations also shows that linear potential flow theory largely over-predicts the sway motion near resonance. This is explained by effects of viscous flow separation. It is also shown that higher order harmonics of the wave loads can be significant and should be considered when fatigue analyses of fish farms are performed.

Acknowledgements

This work has been carried out under the supervision of Professor Odd M. Faltinsen at the Center for Ships and Ocean Structures (CeSOS) and Department of Marine Technology, Norwegian University of Science and Technology (NTNU). I would like to thank him for his excellent supervision during this PhD study. This work would not have been possible without his continuous guidance, suggestions and motivation, which are most appreciated.

The major part of this work has been financed by the Research Council of Norway through the IntelliSTRUCT program at SINTEF Fisheries and Aquaculture. Also the Center for Ships and Ocean Structures and the Department of Marine Technology at the Norwegian University of Science and Technology have contributed.

My fellow students and the staff at CeSOS and the department deserve gratitude for encouragement and for making an enjoyable working environment. In particular I would like to thank my room-mate and friend Trygve Kristiansen for the many fruitful discussions and suggestions. He contributed a lot to the model tests and to the subsequent analysis of the results, for which I am grateful.

I would also like to thank Tone M. G. Vestbøstad for the many discussions on the CIP-method, Petter Andreas Berthelsen for introducing me to CFD in general, Eivind Ruth, Marilena Greco, Bjørn Christian Abrahamsen, Ken-Robert Gjelstad Jakobsen and Jørgen Hals for discussions and suggestions and Renato Skejic for providing numerical verification data. Karl Gunnar Aarsæther and Csaba Pakozdi should be thanked for setting up the computers which have been used for the numerical simulations in this work.

Thanks to Vegar Johansen for giving me time off from my work at SINTEF Fisheries and Aquaculture to finish my thesis.

Trygve Kristiansen, Marilena Greco, Arne Fredheim, Asle Natskår and Bjørn Christian Abrahamsen are acknowledged for proof-reading parts of the thesis.

My gratitude goes to my family for all their encouragement and support.

Contents

Nomenclature

General rules

- Only the most used symbols are listed in the following sections
- Meaning of symbols are given when introduced in the thesis
- Sometimes the same symbol is used to indicate different quantities
- Vectors and matrices are represented by bold-face letters

Superscript

$*$	Tentative value after advection step
$**$	Tentative value after diffusion step
k	Line-segment number of body boundary
n	Time-step number

Subscripts

a	Material properties for air, sometimes amplitude
n	Natural period, natural frequency
i	Horizontal node index
j	Vertical node index
w	Material properties for water
0	Deep water limit

Roman letters

A	Area of floater cross-section
a	Beam of rectangular model cross-section
a_{kk}	Added mass coefficient
B	Mean wetted beam of floating body
b	Height of rectangular model cross-section
b_{kk}	Damping coefficient
C	Wave phase-speed
CFL	Courant-Friedrichs-Lewy number (defined when used)
C_d	Drag coefficient
C_g	Group velocity of wave train
c_{kk}	Restoring coefficient
D	Diameter of circular cylinder
d	Draft of floater
E_k	Kinetic energy
E_p	Potential energy
F_x	Horizontal force component
F_y	Vertical force component
F^D	Drag force
F^{FK}	Froude-Kriloff force
F^{HD}	Hydrodynamic force
F^{HS}	Hydrostatic force
$F_i^n(\xi)$	Interpolation polynomial for the 1D CIP-method
$F_{i,j}^n(\xi,\eta)$	Interpolation polynomial for the 2D CIP-method
Fn	Froude number (defined when used)
F_v	Skin friction force
f	Advected variable
f_{high}	High filter cut-frequency
f_{low}	Lower filter cut-frequency
f_x	Horizontal volume force
f_y	Vertical volume force
$G_i^n(\xi)$	Interpolation polynomial for spatial derivative in the 1D CIP-method
$G_{i,j}^n(\xi,\eta)$	Interpolation polynomial for spatial derivative in the 2D CIP-method
g	Acceleration of gravity, also spatial derivative of advected variable
H	Wave height
H_{input}	Input wave height to the wavemaker
h	Water depth
I	Roll moment of inertia
K	Interpolation polynomial for the vertical spatial derivative
KC	Keulegan-Carpenter number (defined when used)
k	Wave number, sometimes counter variable
L_{dz}	Length of numerical damping zone
L_{wm}	Distance between the wavemaker paddle and the model
l	Length of model
m	Structural mass
m_k	Spectral moments

N	Number of time steps
N_x	Number of grid cells in the horizontal direction
N_y	Number of grid cells in the vertical direction
p	Fluid pressure
p_0	Atmospheric pressure
RHS	Right hand side of equation
Rn	Reynolds number (defined when used)
r	Order of convergence
S	Domain boundary
S_b	Body boundary
S_t	Strouhal number (defined when used)
S_0	Wavemaker stroke
T	Wave period
T^s	Seiching period
T^t	Transverse sloshing period
t	Time
U	Fluid velocity
u	Horizontal component of fluid velocity vector
u^*, u^{**}	Horizontal velocity component of tentative velocity field
v	Vertical component of fluid velocity vector
u^*, u^{**}	Vertical velocity component of tentative velocity field
x	Horizontal spatial coordinate
x_c	Horizontal coordinate for center of gravity of floater
y	Vertical spatial coordinate
y_c	Vertical coordinate for center of gravity of floater
z	Transverse horizontal coordinate

Bold roman letters

$\boldsymbol{A}$	Coefficient matrix for linear set of equations
$\boldsymbol{b}$	Forcing vector for linear set of equations
$\boldsymbol{E}$	Local-error array
$\boldsymbol{F_p}$	Body-force vector due to pressure forces
$\boldsymbol{F_v}$	Body-force vector due to viscous stresses
$\boldsymbol{f}$	Fluid volume-force vector
$\boldsymbol{g}$	Spatial derivatives in the horizontal direction
$\boldsymbol{k}$	Spatial derivatives in the vertical direction
$\boldsymbol{M}$	Moment vector, sometimes preconditioning matrix
$\boldsymbol{n}$	Normal vector
$\boldsymbol{r}$	Distance vector
$\boldsymbol{u}$	Fluid velocity vector
$\boldsymbol{u_b}$	Body velocity vector
$\boldsymbol{x}$	Vector of unknowns

Greek letters

β	Grid stretching coefficient
γ	Grid parameter
δ	Phase angle
$\delta_{0.99}$	Boundary layer thickness
ζ_a	Wave amplitude
η_{ka}	Body motion amplitude for mode k
θ	Roll angle
ε	Wave steepness, also numerical error
κ	Draft-to-height ratio of model cross-section
λ	Wave length
μ	Dynamic viscosity
ν	Kinematic viscosity
σ	Standard deviation
$\boldsymbol{\tau}$	Viscous stress tensor
τ_w	Wall shear stress
Φ	Color function transform
φ	Color function
ρ	Mass density
(ξ, η)	Local coordinates in upwind cell
Ω	Computational domain
ω	Frequency
ω_w	Wave frequency

Abbreviations

2D	Two-dimensional
3D	Three-dimensional
BEM	Boundary element method
CFD	Computational fluid dynamics
CIP	Constrained interpolation profile
CPU	Central processing unit
Exp	Experimental values
FFT	Fast Fourier transform
GMM	Generalized Morison model
NWT	Numerical wave tank
SPH	Smoothed particle hydrodynamics
VOF	Volume of fluid

Mathematical operators and other symbols

∇	Gradient operator
$\nabla\cdot$	Divergence operator
∇^2	Laplace operator
$\sum$	Summation
$\lVert\cdot\rVert$	Eucledian norm

Chapter 1

Introduction

The focus of this work is wave loads and wave induced motions of the floaters of open cage fish farms. Better understanding of the hydrodynamic loads on floating fish farms is necessary in order to develop more reliable structures for fish farming at exposed locations. Structural collapse of floating fish farms in harsh weather conditions, causing large fish escapes, is still a problem. We have investigated the hydrodynamic loads by means of dedicated model tests, numerical simulations using a presently developed computational fluid dynamics (CFD) code, in addition to theoretical methods.

1.1 Background and motivation

In 2006, the state of world aquaculture was presented in a comprehensive report by the Food and Agriculture Organization of the United Nations (FAO 2006). According to FAO, fishing and harvesting of the oceans can not supply additional landings of most wild-caught species in order to meet the increasing demand for sea-food products in the world, without endangering the resources. In fact, many species are already over-exploited. This has in recent years motivated a rapid growth of aquaculture around the world. Aquaculture is today probably the fastest growing form of food production in the world. We define aquaculture as the propagation and rearing of freshwater and saltwater organisms in controlled or selected environments. In 2004, about half of the global total aquaculture production was from aquaculture in marine environments, while the other half was from fresh-water aquaculture. The scope of fish farming is increasing year by year. In 2006, about 50% of the worlds food fish was produced by fish farms. Based on the projected growth in the world population over the next two decades, it is estimated that at least an additional 40 million tonnes of aquatic food (67% of the total production in the world in 2004) will be required by 2030 to maintain the current per capita consumption (FAO 2006). We will in the following focus on fish farming in marine environments, in particular at exposed coastal or offshore locations.

Fish farm installations and technologies which are capable of operating profitably at truly offshore locations are a clear focus for development in many regions that lack indented coastlines. For example, the U.S. Government plans to increase the value of marine and freshwater aquaculture production from $ U.S. 900 million in 1999 to $ U.S. 5 billion by 2025 (NOAA 2007a). In this plan, marine aquaculture in U.S. federal waters plays a central role and development of technologies for sustainable aquaculture operations

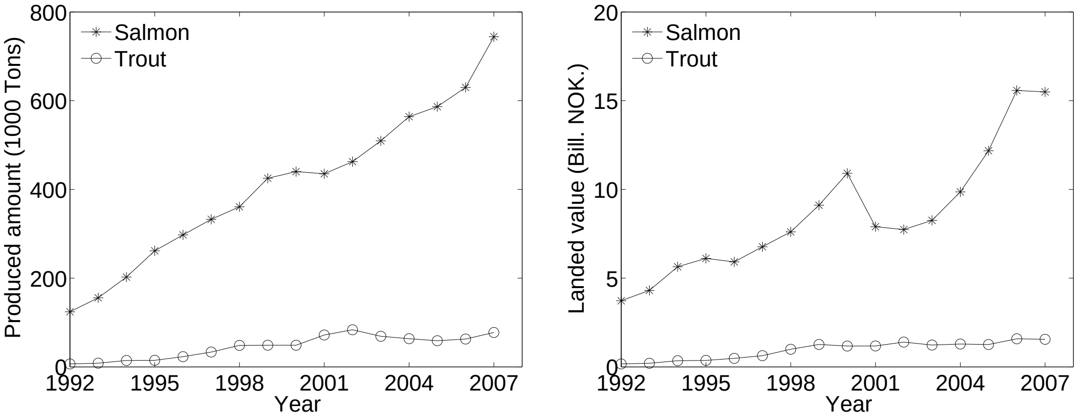

Figure 1.1: Produced amount and corresponding landed value of salmon and trout in Norway from 1992 to 2007 (www.ssb.no).

for fish and shellfish are emphasized (NOAA 2007b). As U.S. federal waters are 3 to 200 miles off the coast, the scope of offshore aquaculture in the U.S. is believed to increase significantly in the near future. In Korea, China and Taiwan, marine fish-farms are often installed at offshore locations due to lack of available sheltered sites with adequate water conditions. These regions experience several typhoons each year, and the fish farms here must be designed to cope with these in addition to the seasonal monsoons and strong ocean currents.

Atlantic salmon (*Salmo salar*) is by far the dominating breed in Norwegian fish farming, which in 2007 counted for 89% of the total amount of sold farmed fish. Other important species in Norwegian aquaculture are rainbow trout (*Oncorhynchus mykiss*) and Atlantic cod (*Gadus morhua*). We will in the following refer to Atlantic salmon, Atlantic cod and rainbow trout as salmon, cod and trout, respectively. The produced amounts of salmon and trout by Norwegian fishfarms and corresponding landed values during the years from 1992 to 2007 are presented in Fig. 1.1. The produced amounts of especially salmon and cod have had an explosive growth during the last three decades. In 2007 the total production of farmed salmon and trout in Norway reached 821,000 tons (www.ssb.no). The increasing scope of fish farming has lead to a lack of new available locations in sheltered areas. Hence, there is a trend that fish farms are installed at more and more exposed locations. This puts stronger demands on the structure in order to withstand the environmental loads. Many Norwegian fish farmers have experienced that the North-Atlantic ocean has a rather harsh weather climate, especially in the winter season. This is exemplified in Fig. 1.2, which shows a fish farm in Flatanger, Norway, during the winter storm Narve in January, 2006. Expansion of the Norwegian fish farming industry has been accompanied by a recent increase in the incidence of escapes. Several occurrences of structural collapse of fish farms in harsh weather has been reported during the years, many which have resulted in large fish escapes. Escaped farmed fish is considered to be harmful to the wild Atlantic salmon. Mainly, this is because the farmed fish may bread with the wild salmon and lead to genetic pollution of the wild fish, which have developed through thousands of years to adept to the conditions in a particular river. It is also claimed that the increased scope of salmon fish-farming and the large concentration of salmon in the fish cages is the main cause to the growing problem

Figure 1.2: Open cage fish farm of the circular collar type in Flatanger, Norway. The photo is taken during the winter storm Narve in January 2006. Large elastic deformations of the structure are seen. (Photo: Marius Dahle Olsen)

of sea-lice in Norway the recent years. Research efforts have been put into developing more reliable structures for fish farming with the result of new regulations for the design and operation of floating fish farms, which were introduced in 2003 through NS 9415 (Standard Norway 2005). Although the fish farming industry in Norway has become more mature now since its beginning in the early 1980-ies, the problem of fish escape is still not resolved. In 2007, the total number of escaped fish reported from Norwegian fish farms was 450,000. The largest single escape in Norway occurred in 2005 and counted nearly 500,000 fish. Number of escaped salmon and trout from Norwegian fish farms reported to the Norwegian Fisheries Directorate in (Norwegian Fisheries Directorate 2009a) and (Norwegian Fisheries Directorate 2009b), for the years from 2001 to 2009 are presented in Fig. 1.3. However, it is believed that the true numbers of escaped salmon and trout from Norwegian fish farms are higher. Reports by Norwegian fish farming companies to the Norwegian Fisheries Directorate of escape events during the period 2001-2006 indicate that escapes of salmon can be categorized broadly into structural failure (52%), operational-related failure (31%) and other causes (17%). This can be escapes due damage on the net caused by predators (e.g. seal), damage due to ship colliding with the fish farm, or damage caused by driftwood. Significant escape events have also occured in other major salmonid producing countries, such as Scotland, Chile and Canada (Soto, Jara, and Moreno 2001). In particular, the introduction and rearing of Atlantic salmon as a non-native breed in Chile has been controversial, as the environmental effects of escapes are unknown. We believe that better knowledge on the hydrodynamics related to the wave loads on the floaters of fish farms is necessary to improve the structural reliability of fish farms. Improved reliability of the fish farm structures will in turn reduce the probability of escape. This is the main motivation for the present work.

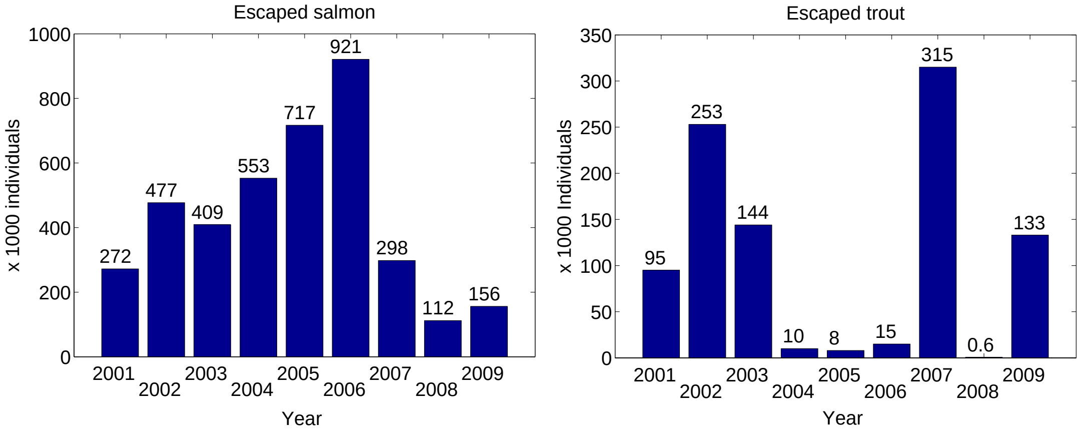

Figure 1.3: Number of escaped salmon and trout from Norwegian fish farms in the time period 2001 to 2009 reported to the Norwegian Fisheries Directorate. The numbers from 2009 are due October 5th.

1.1.1 Open cage fish farms

Open cage fish farms are the most common type of plants used for farming Atlantic salmon and Atlantic cod today. The open cage fish farm is characterized by a slender floating structure which forms circular or rectangular cages. Each cage is equipped with a net-pen, where sinkers are used to splay the net-cage. The buoyancy is obtained by distributed pontoons or by floating collars. A spread mooring system composed of a larger number of pre-tensioned mooring lines is used to keep the structure on its location. However, other concepts like single point mooring of plants have been tested. Then the fish farm is free to weather vane around the moored buoy. Usually open cage fish farms are equipped with a feeding system, often including a feed barge.

The structural design of the fish farms has during the years been modified and improved, often on a trial and error basis. About twenty years ago, the floating structure were typically made of wood, forming small cages as shown in Fig. 1.4. Today, fish farm structures are usually made of steel, aluminium or high density poly-ethylene (HDPE) plastic. Further, there exists many different concepts of fish farm structures as described by Fredheim and Langan (2009). The most common fish farm concepts used by the Norwegian fish farming industry today are described in the following.

Circular plastic collar fish farm

This type of structure has cages formed by pipes with an outer pipe diameter between 225mm to 500mm. The pipes made of high-density polyethylene (HDPE) are welded to obtain a preferred length and then wrapped to form a circle. The two free ends of the pipe are then welded together to form a ring. Usually, a floating collar is composed of two or three such rings which are connected using steel or HDPE clamps. Typical circumference of the collar is from 60m to 200m. It is from such collars that the fish farm obtain its buoyancy. Some manufacturers also deliver walkways which can be mounted between the pipes of the collar. The circular plastic collar fish farms are elastic and deforms when subjected to waves and current (see e.g. Fig. 1.2). An issue for such structures is the safety for personnel in relation to access to the cages.

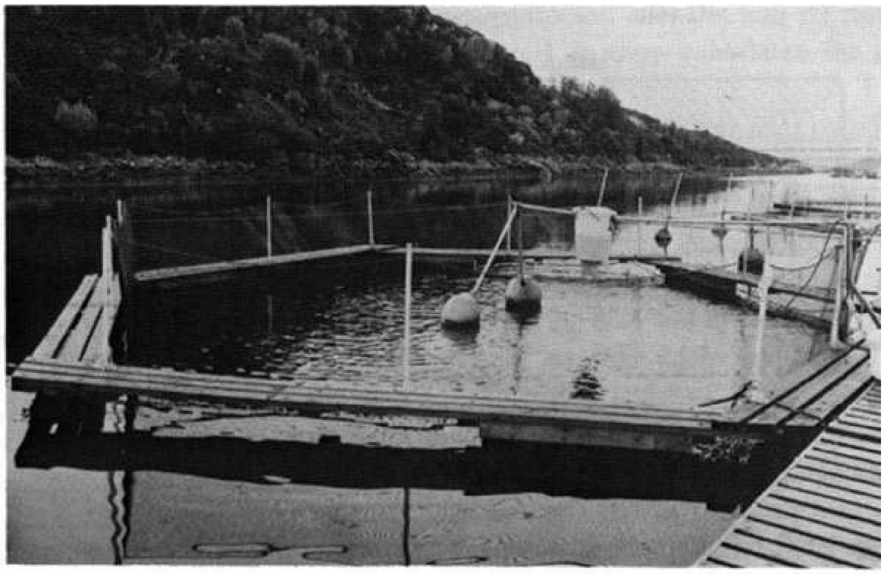

Figure 1.4: Typical old Norwegian fish farm in a sheltered location. The super structure is characterized by wooden frames supported by floaters or pontoons.

Interconnected hinged steel fish farm

Typically, this is a steel structure composed of more or less stiff bridges that are hinged or interconnected by flexible joints to form square or rectangular cages. The bridges are typically 12 meters of length, are made of steel and supported by distributed pontoons. Normally, the hinges only allow for rotation around one axis in the horizontal plane. Limited flexibility of the joints has shown to be a weak part of such fish farms, as large point loads may occur here for some of the flexible modes of the structure. This can result in fatigue related failures. Further, breaking of only one or a few mooring lines is critical for such structures due to the limited flexibility of the hinges. Breaking of mooring lines may cause unfavorable loads on the plant due to redistribution of mooring line forces which may lead to structural collapse. An illustration of the underwater structure of a hinged steel cage is shown in Fig. 1.5, which also indicates how salmon usually tend to be schooling inside the pen. Schooling is when a group of fish swim together in a coordinated manner and in the same direction.

Catamaran steel fish farm

Catamaran fish farm structures are composed of parallel slender steel hulls which are connected with bridges and hinges into different configurations. The buoyancy of such fish farms are provided by the hulls. Catamaran fish farms are often large and with integrated feeding barges as shown in Fig. 1.6(a). A better overview of the structure is obtained from Fig. 1.6(b), which shows an instantaneous situation of the visualization output from a commercial computer software tool for structural analysis of fish farms when the structure is subjected to a uniform steady current and regular waves. Limited flexibility of the hinges, which may lead to fatigue problems for the bridges, is an issue also for this type of structure.

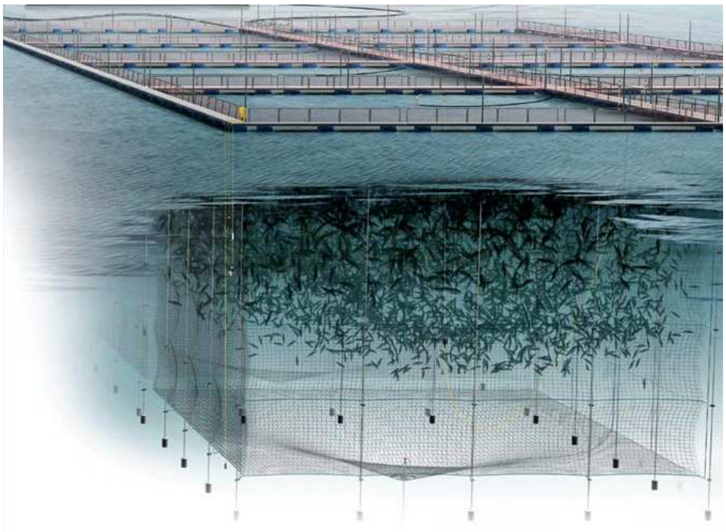

Figure 1.5: Illustration of the underwater structure of a hinged steel type fish farm. Sinkers are attached to the pen in order to stretch the net.

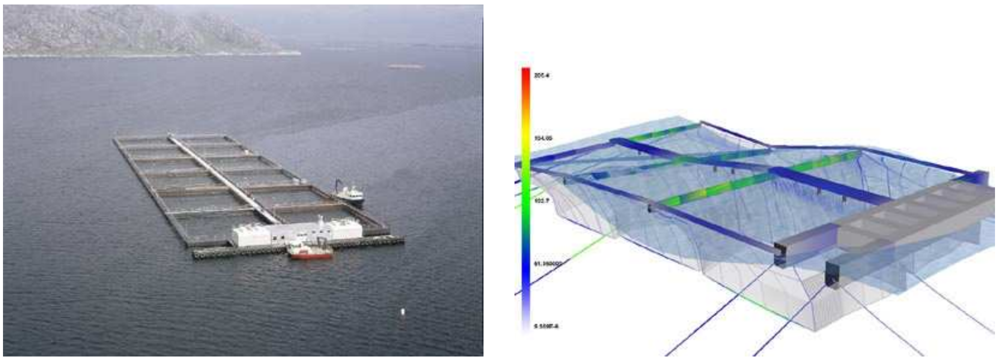

(a) (b)

Figure 1.6: A modern fish farm in Norway is shown to the left. To the right is the visualization from a commercial computer software tool for structural analysis of fish farms (www.procean.no/fishfarms.html).

Rigid steel fish farm

This is a large category with several different fish farm designs intended for operation at exposed locations. The most common type of the rigid steel fish farm is composed of robust steel pipes with diameter of order 1m that are welded together to form rectangular or square cages. The floating collar then appears as semi-submerged circular cylinders oriented with the cylinder axis horizontally in the free surface. Also fish farms made of truss work exists. This type of structure is characterized by a small water-plane area, which implies low natural frequencies in heave, pitch and roll of the structure. Buoyancy are mainly obtained from submerged pontoons. The submerged pontoons also makes the structure less exposed to wave excitation loads. Knowledge and experience from offshore engineering and the oil-industry have been utilized in the development of this structure type.

Submersible fish farm

By adding a “roof” on the net-pens, the fish cage can be submerged for some period of time, e.g. during a storm. Benefits of a submerged fish cage are reduced wave loads on the structure and that problems related to icing on the super-structure are avoided. However, there are biological issues related to submerging the fish cages. One is that salmon needs access to the free surface for “breathing” in order to supply its swim bladder with air. Submerging the fish cages for a longer period of time will cause the fish to be more stressed. This has a negative effect on the fish growth and welfare. The operation of submerging a plant is performed by a controlled filling of water into the pontoons or plastic collars. Elevation of the plant is done by pumping compressed air back into the pontoons while evacuating the water through valves. Such submerge-able fish farms are still on the development stage. More novel fish farm systems are presented in Fredheim and Langan (2009).

1.1.2 Norwegian fish farms at present

Common for all the previously mentioned types of fish farms is that the floating structure forms square or circular cages to where net pens are mounted. A modern fish farm can have as much as 16 cages. The size of the cages has increased significantly through the years, and so has the number of fish in each cage. An aspect of the increasing size of the fish farms is that the consequences of structural collapse become more severe, both environmentally and economically, as more fish is likely to escape. Today, a typical length of the sides of a large square cage is 40m, while a large circular cage can have a diameter of 64m. Net cage volumes are most typically 10,000 m^3 to 20,000 m^3 and a single cage may contain up to 1,000 tons of fish. This means that if the mean weight of the fish is five kilograms, which is a representative value for Atlantic salmon when the fish is ready to be slaughtered, a single cage may contain as much as 200,000 fish. Salmon have a swim bladder which is filled with air such that the fish become neutrally buoyant. Hence, the volume of the fish is approximately equal to the total mass of the fish divided by the mass density of the water. The upper limit for the average fish density inside a pen is 25kg/m^3, which is kilograms of fish per cubic meter of water. This means that about 2.5% of the total volume of a fish cage can be occupied by the fish. However, the fish is usually not evenly distributed within the cage. For instance, salmon often tend to be schooling inside

Figure 1.7: Salmon forming a school inside a fish cage. This shows that the local fish density inside a fish cage can be relatively high due to the schooling behaviour.

the pen, making the fish density locally higher than the average value. An example of salmon forming a school inside a fish cage is shown in Fig. 1.7. Another factor causing higher fish density is current forces on the net which lead to deformations of the net cage, yielding a reduced enclosed volume of the pen. The vertical position of the fish inside the pen is a function of feeding time, daylight, water temperature, dissolved oxygen in the water in addition to current and waves. A modern Norwegian plant typically has 5,000 to 6,000 tons of fish, totally. However, there exist plants with up to 10,000 tons (Fredheim 2009).

1.1.3 Challenges

In order to design reliable structures for fish farming at exposed locations, it is crucial to know what are the loads the structure will be subject to. Figure 1.8 shows an example of a damaged fish farm after a storm, where parts of the floating collar is below the free surface. Such damages are often caused by breaking of mooring lines due to wave and current loads on the structure. This may lead to buckling of the floating structure due to large point loads caused by redistribution of mooring line forces. Due to the change of the mooring forces associated with line breakage, transient motions of the plant will occur until a new equilibrium position is reached, or if several mooring lines are broken, the structure might simply drift to the shore. Damage can also be caused by fatigue from continuous wave loading. An example of fatigue damage is shown in Fig. 1.9. Fatigue is mostly a problem for the joints of hinged or rigidly connected steel types of fish farms, with members being more or less elastic. Elasticity of the structure also implies that the structure will theoretically have an infinite number of natural frequencies in case of no damping. Although oscillations at higher natural frequencies are effectively damped by structural damping, the lower natural frequencies are important from a fatigue point of view. If the structure is regularly excited at a natural frequency with small damping, this will have a negative effect on the fatigue life of the structure. Resonant elastic motions imply cyclical loads in the structure at a relatively high stress-level. Such cyclical stresses

Figure 1.8: Example of a collapsed fish farm after a storm, with large fish escape as a result.

may over time lead to fatigue damage of the structure. The fatigue life of a given structure can be estimated from the S-N curve, showing the magnitude of a cyclical stress (S) and the corresponding number of cycles to failure (N) in logarithmic scale. At present, linear three-dimensional (3D) panel methods based on potential flow theory like e.g. WAMIT are not common to use for response-analysis of fish farms in waves. Engineering tools developed for structural analysis of open cage fish farms usually apply linear potential flow theory (long wave theory) and strip theory, where drag forces as in Morison's equation are added to the potential flow solution, for simulating the global response of such plants when subjected to waves and current. Only regular waves are considered, such that the frequency-dependent hydrodynamic coefficients of the floaters corresponding to the wave frequency can be used. For the hinged steel type fish farm, global hydroelasticity of the structure is usually accounted for by solving the coupled equations of motions for hinged rigid bridges.

The approach using linear potential-flow theory for structural analyses of fish farms may yield good results for smaller sea-states. However, for larger sea-states linear theory may largely over-predict the true response near resonance, or perhaps more crucial, miss to capture important features associated with nonlinear fluid-structure interaction. In addition, higher order harmonics of the wave loads may be important when it comes to excitation of flexible modes of the structure, which eventually may lead to fatigue.

A practical challenge is related to that salmon requires a high level of dissolved oxygen in the water and are also intolerant of pollution (Monahan 1993). Hence, the flow of water through densely stocked pens must be good to maintain adequate oxygen supplies and to remove polluted water. The exchange of water in the pens is important for the fish health and growth, which means that desired locations for fish farming should have a sufficient level of current. One factor that is important to consider relative to water exchange is bio-fouling or marine growth on the nets. Bio-fouling on the nets is hard to prevent and will reduce the flow through the net, implying a reduction of the water exchange in the

Figure 1.9: Example of fatigue on a steel type fish farm. The crack has propagated through the whole section.

pens. Bio-fouling also leads to larger wave and current forces on the net as the effective area of the net cage increases, and increased inertial loads due to additional weight on the pen.

1.2 Previous and on-going related work

The purpose of the present work, which addresses the wave loads on floaters of fish farms, is to contribute to the higher goal of obtaining more reliable structures for fish farming. This goal is also shared with other studies, where other components of fish farms or more or less complete fish farm structures are considered. In order to get an overview of the bigger picture, we will in the present section also give reference to work which is not directly relevant for wave loads on the floaters but for modelling of fish farms in general.

Design of complete floating fish farms and modelling of their response in waves and current is challenging and involves several disciplines such as hydrodynamics, structural mechanics and ethology. When it comes to hydrodynamic modelling of large complex fish farms, the literature is limited. Further, existing studies of more or less complete floating fish farm structures mostly rely on wave-load models which in general are not validated for floaters of fish farms. Previous and on-going work relevant for modelling floating fish farm structures in waves and current are given in the following.

The net structure

One of the first detailed theoretical analysis on the hydrodynamic force acting on a net panel suspended in a current was presented by Tauti (1934). He considered a stretched net panel as a continuous membrane and proposed differential equations for mechanical equilibrium of the membrane, based on the assumption that the drag force on the net was proportional to the square of the current velocity. Similarity laws for scaling of net structures were also proposed. A comprehensive review of theoretical and experimental work on hydrodynamics related to fishing gear, with focus on the mathematical modelling of net structures, was presented by Kawakami (1959). A semi-empirical formula expressing the drag force F_D on a plane net panel subject to a uniform current in the normal direction of the panel was proposed by Kawakami (1964) as $F_D = 0.5\rho C_D A U^2$. Here, ρ is the density of water, C_D is an experimentally determined drag coefficient, A is the spanned area of the net panel and U is the fluid velocity. A thorough study on the current forces on net cages and the resulting net deflections was presented by Aarsnes et al. (1990). Based on a series of model tests where net panels were towed with different orientation angles relative to the towing direction, a mathematical model for the current induced loads on net panels was proposed. The new mathematical model included a lift term in addition to the drag force proposed by Kawakami (1964). Løland (1991) modelled the flow through fish farms using the wake flow equations, which for steady flow can be found in Schlichting and Gersten (2000). By utilizing the linearity of the wake flow equations, he was able to model the flow through a screen by adding together the wake flow caused by the individual cylinders forming the screen. Both steady and unsteady ambient flow were considered. This method has shown to be appropriate for screens with low solidity ratio. The solidity ratio Sn is defined as the projected area of the screen divided by the total spanned area of the screen. Hence, for a square mesh of cylinders with diameter d and separation l we get $Sn = 2d/l - (d/l)^2$. The possibility of hydrodynamic interaction between twines of a net can be assessed by the CFD studies by Herfjord (1996). He studied the 2D problem of two circular cylinders in a side-by-side arrangement subject to uniform cross flow. The cylinders were separated a distance l in the transverse direction relative to the incident flow. He found that wake interaction occurs when $l < 2d$, with d being the cylinder diameter. This means that when $Sn > 0.75$ the linearity assumption of the wake flows is no longer applicable, and for increasing solidity ratio wake interaction becomes increasingly important. Typical values of the solidity ratio for clean unfouled nets of fish cages for Atlantic salmon is in the range $Sn = 0.15 - 0.25$. Fridman (1998) pointed out that for small values of the Reynolds number $Rn = Ud/\nu$, where U is the current velocity, d is the diameter of the twines of the net and ν is the kinematic viscosity coefficient, the drag coefficient C_D of a net panel is highly dependent on the Reynolds number (see also Faltinsen and Timokha 2009). When $Rn < 600$ the drag coefficient C_D shows a strong increase with decreasing Reynolds number, while for $Rn > 600$ the drag coefficient is nearly independent of the Reynolds number. A typical twine diameter of a fish cage for salmon is $d = 3$mm. With a design current speed of $U = 1$m/s and with $\nu \approx 10^{-6}\,\mathrm{m}^2/\mathrm{s}$, this yields $Rn \approx 3000$. This means that the drag coefficient for a full scale net cage for a typical design value of the current speed is nearly independent of the Reynolds number. However, for model testing of fish farms where geometric scaling of the net is used to obtain a model scale fish cage, the Reynolds number dependence of the drag coefficient of the net is important. Scaling laws for net structures were discussed by Hu et al. (2001), and drag coefficients obtained from experiments with trawl nets in model scale and full scale were compared. Good comparison was shown when the Reynolds dependence of the drag coefficient was accounted for. Bessonneau and Marichal (1998) presented an iterative method for computing the deformation of net structures in current, where a flexible net was modelled by a set of rigid bars connected through flexible joints. A Morison type of model was used to compute the drag force and added mass force of the individual bar elements in the transverse direction, while in the tangential direction, a friction force was applied.

The individual bar elements were assumed to be hydrodynamically independent. Presented numerical simulations of a towed trawl structure were reported to be qualitatively in agreement with flume tank observations. Tsukrov et al. (2003) presented a structural finite element model to compute the response of net panels due to current loads based on an empirical drag formulation. Results from numerical simulations were compared with experiments and analytical results and good agreement was observed. An approximate model for analysis of current forces and corresponding response of three-dimensional (3D) net structures with solidity ratios $Sn \lesssim 0.5$ was established by Fredheim (2005), where the twines of the net structure was modelled as linear elastic due to axial stretching. He found that elasticity of the net structure has a direct influence on the geometry of the deformed net when exposed to external forces.

Due to bio-fouling, the porosity of the net cages will change. The influence of porosity and fish-induced internal circulation on the flow around fish cages are studied in an ongoing PhD-project by Gansel (2009). This study includes both experiments and CFD-simulations.

Modelling of a net cage is challenging also from a structural point of view, as the net cages vary in raw material, size, structure and surface treatment. Strength analysis of net structures typical for aquaculture cages was performed by Moe (2009). The strength analysis included experiments with tensile testing of various netting materials and numerical simulations of a net cage subject to uniform current. A quasi-static approach was used in the numerical simulations, where a Finite Element Method was applied for the structure to compute the net deformations due to the current loads. Netting materials can be divided into knotted- and knot-less structures, where the latter is the one most used for Norwegian fish cages. The structure of the netting material is also relevant for hydrodynamic modelling of the net. We do not consider net loads in the present work.

The floaters

Wave induced loads and motions of floating bodies is a classical branch of problems in marine hydrodynamics dealing with ships and offshore structures. General aspects and theoretical methods for solving such problems are discussed in many text books, e.g. by Newman (1977), Faltinsen (1990), Dean and Dalrymple (1991) and Molin (2002). The floaters of fish farms are often characterized as horizontal cylinders floating in the free surface. Relevant work for the wave loads and wave induced motions of the floaters are given in the following.

The pioneering frequency domain theoretical work related to wave induced effects on cylinders in the free surface was made by Ursell. He studied the two-dimensional (2D) heave added mass and damping of a semi-submerged circular cylinder, and gave a general expression of the potential flow in terms of flow singularities satisfying the free surface and radiation condition (Ursell 1949). For the 2D problem of an infinitely long cylinder oriented horizontally below the free surface, Ursell (1950) derived the frequency-domain analytical expressions for the wave forces due to beam sea waves using potential flow theory. Theoretical work on the waves generated by a 2D body oscillating in the free surface was presented by Ursell (1954), where he studied how the wave amplitude at infinity is dependent on the body geometry and the frequency of oscillation. This dependence is relevant for the wave damping force of floating bodies. Based on Ursell's work, theoretical methods for computing linear wave induced loads on fixed and moving bodies in the free surface were presented by Newman in (Newman 1962) and (Newman 1965), respectively. Further, based on Ursell (1950), Ogilvie (1963) presented first- and second-order forces on a horizontal cylinder submerged below a free surface. Tasai presented two-dimensional values of the hydrodynamic force and moment due to forced sway and roll motion of cylinders with Lewis-form sections, which was obtained using linear potential flow theory (Tasai 1959; Tasai 1961). A Lewis form section assumes the cross-sectional shape can be adequately described by the cross-sectional area, beam and draft (see e.g. Faltinsen (2005) for the geometric limitations of such a technique). The obtained hydrodynamic coefficients were used with a strip theory to give the total sway force and roll moment on two actual ship hulls due to forced sway and roll. Results were compared with experiments. The frequency-domain linear potential flow associated with the wave excitation loads on a cylinder of arbitrary cross-section in oblique sea that is not close to head or following sea can be described by the Helmholtz equation (see e.g. Bolton and Ursell (1973)). The head sea case is more complicated and was studied by Faltinsen (1971) in his Ph.D. thesis for a ship by using the near-field solution by Ursell (1968) as part of his analysis. The above-mentioned work are all in the frequency domain. Solutions to transient potential flow problems in time-domain for a floating body in waves are described by Cummins (1962) and Ogilvie (1964).

A thorough experimental study on the two-dimensional hydrodynamic coefficients for horizontal cylinders in the free surface due to forced sway-, heave- and roll motion was presented by Vugts (1968). Measurements of wave excitation loads on the cylinders when being clamped and subject to regular waves were also presented. Wave forces on partially submerged cylinders were studied by Dixon et al. (1979) by means of model test experiments and numerically using modified versions of Morison's equation (Morison, O'Brien, Johnson, and Schaaf 1950). An experimental study of nonlinear wave loads on a horizontal circular cylinder beneath linear deep-water waves for Keulegan-Carpenter numbers $2 \lesssim KC \lesssim 3$, was presented by Chaplin (1984). The cylinder was submerged below the free surface such that interaction with the free surface was assumed to be unimportant. For the waves tested, the ratio between the wave lengths λ and the diameter D of the cylinder was in the range $\lambda/D \approx 3.8 - 15$. The non-linearity of the measured forces was believed to be associated with viscous flow separation from the cylinder surface, and the measured wave forces on the cylinder was observed to be as much as 50% less than that predicted by linear potential flow theory. The potential flow problem of a horizontal cylinder submerged below a free surface has later been addressed using numerical methods by for instance Wu and Taylor (2003), who studied nonlinear wave-body interaction using a domain decomposition approach. A finite element method (FEM) was coupled with a boundary element method (BEM), where the former method was used away from the body while the latter was used in the near-field region of the body. BEM was also used by Kristiansen (2009) to construct a two-dimensional fully nonlinear numerical wave tank for wave-body interaction problems. A ship section by an offshore LNG-terminal was considered where effects of flow separation from the bilges of the ship section were studied. The free shear layers were modelled using an inviscid vortex tracking method. Simulations in 2D of a moving body on the surface of a viscous fluid, based on the incompressible Navier-Stokes equations, were presented by Gentaz et al. (1997). They computed the added mass and damping coefficients in heave, sway and roll, in addition to the coupling coefficients of roll in sway, for a rectangular body. Numerical results were compared with experiments (Vugts 1968) and with potential flow theory results. Good agreement with experiments and potential flow theory were observed the coefficients in heave and sway, while the agreement for the added mass and damping coefficients due to roll and the coupling coefficients were less good. A 2D numerical wave tank (NWT) based on the constrained interpolation profile (CIP) method was presented by Hu et al. (2003). Validation of the NWT was performed by means of simulations of forced heave of a wedge and an elliptic body. The 2D added mass and damping coefficient were obtained from the simulation and compared with potential flow theory, with resonable agreement. Further, numerical simulations of a floating body subject to nonlinear waves were presented. A numerical wave tank for three-dimensional (3D) simulations were presented by Hu et al. (2005). The 3D NWT was verified by means of computing the added mass and damping in heave of a hemisphere. Results from a simulation with a Wigley hull at forward speed in head sea waves were also presented.

The floaters of fish farms can generally be characterized as small volume structures, with cross-sectional dimensions being small relative to the wave lengths of dimensioning waves. However, the length of the floaters can be large compared to a characteristic wave length. The relative motion between the structure and the free surface may locally be large relative to the cross-sectional dimension of the floater. If the relative motion between the free surface and the floater becomes too large, the floater or parts of the floating collar might leave the water for then to re-enter into the water domain. If the relative velocity between the floater and the water surface is large and the floater is characterized by a blunt geometry, significant forces may occur as the floater impacts with the free surface. This is referred to as water impact or slamming, and is characterized by impulse loads with high pressure peaks (Faltinsen 1990). Slamming events may cause damage to the local structure, or cause global vibrations of the structure which in turn can lead to fatigue of steel structures. Water entry and exit of a circular cylinder was studied experimentally and theoretically by Greenhow and Lin (1983) and Greenhow (1988). Water entry of different two-dimensional sections has been investigated numerically by Zhu (2006) and Vestbøstad (2009) using a CIP-based computational fluid dynamics (CFD) method and by Sun (2007) using BEM. Another important scenario which is relevant for the hydrodynamic loads on the floaters of fish farms is waves over-topping on the floater geometry. This will be referred to simply as over-topping. Finding the wave excitation loads on the floater due to over-topping is numerically challenging and characterized by nonlinear effects. Little work has been done relative to over-topping on slender structures in the free surface. However, over-topping has similarities to the hydrodynamic problem of green-water on the deck of a ship studied by Greco (2001).

Dynamic analysis of fish farms

Engineering tools that have been developed for simulations of the response of fish farms subject to waves usually applies strip theory together with potential flow theory to compute wave forces on the floaters. The added mass and damping coefficients used in the strip theory formulation can be found from potential flow theory using a boundary element method (BEM) as the Frank close fit method (Frank 1967), which is a 2D source panel method using a Green function satisfying the free-surface condition and radiation condition in deep water. Another approach is to use conformal mapping, e.g. a Lewis form technique, to obtain these coefficients. However, Lewis form technique has limited applicability and is approximate for cross-sections with sharp corners (Faltinsen 1990).

Making a long wave assumption relative to the cross-sectional dimension of the floaters, the diffraction forces on the floaters can be expressed in terms of the added mass and damping coefficients. Viscous forces are then added to the potential flow solution, similarly as the drag term in Morison's equation (Morison et al. 1950). Such a hydrodynamic load model for the floaters was applied together with a finite element model for the structure by Ormberg (1991), allowing for flexible deformations of the structure due to waves and current loads. A simplified representation of the net cages was implemented, where the drag and lift forces on net panels were expressed in terms of a Morison formulation. Good comparison with model tests was reported. Higher order harmonic components of the sway response in regular waves was observed. A fatigue analysis of the fish farm in irregular long-crested waves was also presented. Later, Thomassen (2008) studied fatigue of a fish cage due to regular waves. Lader et al. (2003) modelled 3D net structures, with configuration as an open cage fish farm, subject to waves and current. Comparisons between cage deformations obtained from numerical simulations and model test results were presented, showing good agreement for the intermediate current speeds. However, for the lowest current speed tested, the agreement is less good. Huang, Tang, and Liu (2006) presented results from numerical simulations and model tests, where the numerical model was based on Lader et al. (2003). Dynamics of a moored spar type fish cage in waves and currents was studied numerically by Fredriksson et al. (2005), using post processed data for waves and currents obtained from field measurements as input to the numerical model.

1.3 Outline of the thesis

This thesis is organized as follows. The physical case of wave loads on floaters of fish farms is discussed in Chapter 2, where an idealized problem is formulated. In Chapter 3, the mathematical formulation of the physical problem is presented, followed by a description of the numerical representation of the mathematical problem and the development of a numerical wave tank (NWT) in Chapter 4. In chapter 5, a verification study of the numerical model is presented. Two sets of dedicated model tests are described in Chapter 6, where the first set deals with wave loads on fixed horizontal cylinders due to regular waves, while in the second set, wave-induced motions of a moored floating circular cylinder in regular waves are considered. The two main studies of this work are presented in Chapter 7 and Chapter 8. First, in Chapter 7, our study on non-linear wave loads on fixed horizontal cylinders due to regular waves are presented. Second, our study on the non-linear wave-induced motions of a moored floating circular cylinder is presented in Chapter 8. Both studies include comparisons between numerical results obtained from CFD-simulations using our NWT and the experiments presented in Chapter 5. Finally, a summary of the present work and suggestions for further research are given in the last chapter.

1.4 Main contributions

A 2D numerical wave tank (NWT) was developed as a tool for studying nonlinear wave loads and wave induced motions for floaters of fish farms. The NWT was based on the Navier-Stokes equations for incompressible flow, where a one-fluid formulation with varying fluid properties in the domain was used to simulate two-phase flows. The NWT was also capable of handling both forced and free motions of solid bodies.

Experiments were conducted in 2006 where wave loads on fixed horizontal cylinders in the free surface were considered. Two models were tested. One with a circular cross-section and one with a rectangular cross-section. The models were fixed and subjected to regular waves. Test parameters were wave period, wave steepness and model draft. The clamping forces on the models were measured. Over-topping on the cylinders were observed for some of the test conditions. Some results from the model tests in 2006 were presented by Kristiansen and Faltinsen (2008b). From Fourier analyses of the measured force time series, we found that over-topping introduce higher order harmonics in the vertical component of the wave excitation force. However, the horizontal force component was nearly linear when over-topping occurred. When it comes to wave excitation loads on cylinders with small draft, we found that the second harmonic component is important for the horizontal force component.

A generalized Morison model (GMM) was implemented and applied using the wave conditions from the model tests with the fixed cylinders. Computed forces were compared with measured forces from the experiments. We found that the GMM is not adequate for computation of wave forces on horizontal cylinders in the free surface when over-topping occur. However, good comparison was shown for the cases without over-topping. The GMM was presented by Kristiansen and Faltinsen (2008a).

Experiments were also conducted with a floating circular cylinder. The cylinder was moored with the cylinder axis oriented horizontally in the free surface and subject to regular waves. An instability-like phenomenon yielding sub-harmonic response of the sway motion was discovered for the test with the wave period being half the natural period in sway. This wave period was also close to the natural period in heave of the cylinder. Measured sway motion was about 250% that predicted by linear potential flow theory. It was also found that viscous flow separation matters at sway resonance, where linear potential flow theory overpredicts the measured sway motion by more than 500%. By Fourier analysis of the measured accelerations from the model tests, it was found that the second harmonic component of the vertical wave excitation force at sway resonance did excite the natural heave frequency. This caused the Fourier amplitude corresponding to the second harmonic component of the body acceleration in heave to exceed the linear harmonic component. Results from the study on the moored horizontal cylinder in waves were published by Kristiansen and Faltinsen (2009).

Based on the discussion above, we consider the main contributions of the present work to be the following

- Development including verification and validation of a CIP-based numerical wave tank for simulation of fully nonlinear wave-body interaction problems in those dimensions of a viscous laminar flow

- A generalized Morison model is not adequate for wave load computation when over-topping occurs. However, such a model can give good force predictions when over-topping is not present

- Nonlinear effects due to over-topping are dominant only for the vertical component of the wave excitation force

- Nonlinear effects for the wave excitation forces on floaters with small draft are most important for the horizontal force components
- An instability-like sub-harmonic parametric resonance phenomenon associated with nonlinear hydrodynamic effects was discovered for the moored horizontal circular cylinder. Numerical simulations with linear restoring forces in sway showed that this phenomenon was not associated with nonlinear effects from the mooring arrangement
- Viscous damping due to flow separation is important for limitation of the sway motion of floaters at resonance

Chapter 2

The physical problem

Wave loads on floaters of fish farms is from a hydrodynamic point of view an extensive topic which can be addressed in many ways. When concretising this topic into a relevant hydrodynamic problem, we should elaborate on what are the goals we are aiming for.

In previous studies of integrated fish farm systems in waves, strip theory and potential flow theory where viscous drag forces are added to the potential flow solution, have been used when computing the wave loads on the floating collars of fish farms (Ormberg 1991) (Thomassen 2008). However, this method has not been validated for slender structures in the free-surface zone as the floating collars of fish farms. According to Ormberg (1991), there is a lack of confidence for this wave load model when applied to slender structures in the free-surface zone. To obtain better confidence and possibly improve existing load models, he suggested that simple cross sections subjected to well defined waves should be considered. With this in mind, we believe that a first step towards obtaining better wave load models for floaters of fish farms is to investigate the wave loads and wave induced motions of floaters in a 2D situation by means of numerical simulations and experiments. Results can then be compared with existing wave load models for the floaters and eventually lacks or weaknesses of the existing models can be revealed.

2.1 A 2D-problem of floaters in beam sea waves

As explained in Chapter 1, there exist many different structural concepts of floating fish farms. In this work we decided to focus on the stiff surface steel structure, which is designed for use at exposed locations in the coastal zone. The floaters for this type of structure appear as horizontal cylinders with the cross-section partly submerged in the free surface, as can be seen in Fig. 2.1. The diameter of the floater is typically of order 1m. A 2D flow situation occur when the cylindrical floater is subjected to beam sea waves. Two floater geometries will be considered in the present study, one with a circular cross section and one with a rectangular cross section. A deterministic approach is used in the present study where wave loads due to regular waves are investigated. Possible flow effects that are believed to be relevant for the floaters in beam sea waves will now be discussed. Such a discussion is necessary early in a study like the present one in order to decide which tools to apply. By “tools” we here mean mathematical models, numerical methods or experiments.

Figure 2.1: Floater of a steel type fish farm. The floater appears as a semi-submerged horizontal cylinder. The floater has a circular cross-section with diameter 1m. A walkway is mounted to the floater.

2.1.1 Possible physical effects

The most relevant physical effects that may occur and which are not covered by linear potential flow theory are wave over-topping on the structure, viscous flow separation and water entry and exit with associated forces. Figure 2.2 illustrates a 2D situation where the rectangular floater is subject to beam sea waves. Viscous flow separation will always occur at the sharp corners of the cross-section, meaning that effects of viscosity must be considered. Wave over-topping is another scenario that might occur. The wave over-topping process can be dam-break like or it could be like a plunging breaker (Greco 2001). The latter may lead to impact loads when the breaking wave hits the top of the floater. Impact loads can also occur when a steep breaking wave hits the side of a floater. The plunging breaker may lead to entrapment of air (cf. Fig. 2.2), which can result in high pressures on the floater over the area covered by the cavity. When the relative

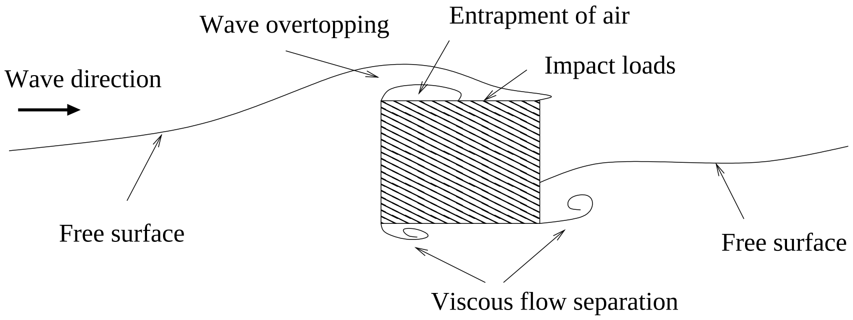

Figure 2.2: Rectangular floater in beam sea waves. Some possible physical effects. Viscous flow separation will always occur from the sharp corners of the cross-section, but the extent (and hence the importance) of the separated flow will depend on the KC-number.

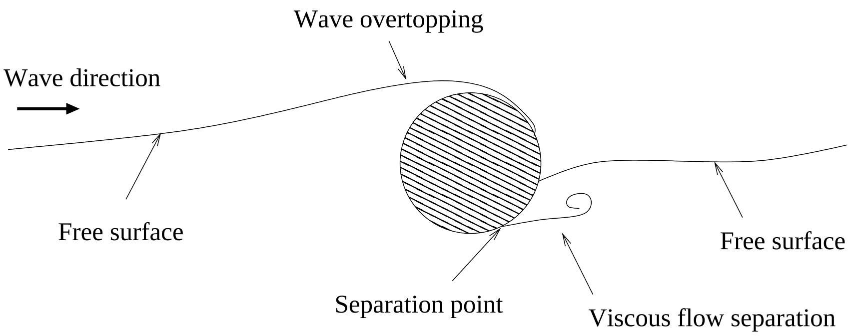

Figure 2.3: Circular floater in beam sea waves. Viscous flow separation may occur for large KC-number flow. The location of the separation point depends on whether the boundary layer flow is laminar or turbulent.

motion between the floater and the waves is large, the floater can leave the water domain completely (water exit) for then to dive back into the water (water entry). If the relative velocity between the floater and the sea surface during water entry is large, water impact or slamming may occur (Faltinsen 1990). Slamming is characterized by high pressures which can damage the local structure.

A possible flow scenario for the circular floater is illustrated in Fig. 2.3. Wave overtopping, water exit and water entry are relevant also for the circular floater. However, air-entrapment is believed not to be an issue, and probably not impact forces due to wave breaking over the cylinder top. However, over-topping will influence significantly on the vertical forces. If the relative motion between the floater and the surrounding water is sufficiently large, viscous flow separation can also occur for the circular floater. However, in contrast to the rectangular floater where the flow always separate from the sharp edged corners, the location of the separation point on the circular floater depends on the boundary layer flow and is not known a priory.

2.1.2 Relevant flow parameters

Based on the possible physical effects listed above, the following non-dimensional parameters are assumed to be relevant for the general hydrodynamic problem of wave loads on floaters of fish farms.

Reynolds number: Describes the relative importance of the viscous forces and inertia forces. The Reynolds number for a cylinder with diameter D in separated oscillatory flow is defined as $Rn = UD/\nu$, where U is the undisturbed relative fluid velocity at the location of the cylinder and ν is the kinematic viscosity coefficient. Consider a fixed cylinder. The fluid velocity amplitude due to waves with frequency ω and amplitude ζ_a, is given as $U = \omega\zeta_a \exp{(ky)}$, where $k = \omega^2/g$ is the wave number and y is the vertical coordinate axis with origin at the mean free surface and positive direction upwards. g is the acceleration of gravity. In attached flow, the Reynolds number is defined as $Rn = U_m^2/(\omega\nu)$, where U_m is the maximum velocity outside the boundary layer. The critical Reynolds number Rn_{crit} indicates the limit for which the boundary layer flow goes from being laminar to turbulent. For the circular cylinder in oscillatory flow $Rn_{crit} = 10^5$ is used.

Keulegan-Carpenter number: Expresses the convective fluid acceleration relative to the local fluid acceleration on the cylinder surface when subjected to oscillatory flow. The Keulegan-Carpenter number is defined as $KC = UT/D$, where $T = 2\pi/\omega$ is the period of oscillation and U is ambient velocity. For a semi-submerged cylinder subject to regular waves, $U = \omega\zeta_a$ and hence $KC = 2\pi\zeta_a/D$. For a circular cylinder in infinite fluid, flow separation may occur if $KC \gtrsim 2$ for laminar boundary layer flow.

Euler number: Expresses the relative importance between pressure loads and hydrodynamic pressures and is defined as $Eu = p_0/\left(0.5\rho U^2\right)$, where p_0 is atmospheric pressure and U is the incident fluid velocity. This is important if waves cause air to be entrapped in a cavity on the body surface.

Froude number: Expresses the relative importance between inertia forces and gravity forces in the fluid. The Froude number in oscillatory flow is defined as $Fn = \omega\sqrt{D/g}$.

2.2 The sea environment and design conditions

Fish farms must be designed to withstand environmental loads from waves and current. Typical wave conditions used for the design of fish farms are presented.

2.2.1 Design conditions for floating fish farms

In the Norwegian regulations for the design and operation of floating fish farms, NS 9415 (Standard Norway 2005), design wave climates or wave classes are presented. These wave classes are defined in terms of ranges of significant wave heights H_s and wave peak periods T_p. H_s is defined as the mean of the one third highest waves in a sea-state, while T_p is the wave period corresponding to the wave component that contains most energy in the sea-state. The design wave classes from NS 9415 are quoted in Tab. 2.1. It should be noted that state of the art computer programs for simulating floating fish farm systems in waves usually apply long-crested regular waves in the analyses, where the regular wave corresponds to the most probable largest wave for the given design sea-state.

Table 2.1: Definition of design wave classes from NS 9415 (Norwegian Standards 2003) for the design and operation of floating fish farms. H_s is significant wave height and T_p is wave peak period.

Wave classes	H_s [m]	T_p [s]	Level of exposure
A	0.0 - 0.5	0.0 - 2.0	Small
B	0.5 - 1.0	1.6 - 3.2	Moderate
C	1.0 - 2.0	2.5 - 5.1	Large
D	2.0 - 3.0	4.0 - 6.7	High
E	> 3.0	5.3 - 18.0	Huge

Extreme waves

Based on the PM-spectrum, an estimate of the most probable largest wave height for N number of waves is found as $H_{max} = H_{m0}\sqrt{0.5\ln(N)}$. $H_{m0} = 4\sqrt{m_0}$ is the significant wave height estimated from the wave spectrum $S(\omega)$, where m_0 is the spectral moment defined as

$$m_k = \int_0^\infty \omega^k S(\omega)\mathrm{d}\omega \tag{2.1}$$

with $k = 0$. The number of waves for a sea-state of duration t (seconds) can be approximated as $N = t/T_{m2}$, where $T_{m2} = 2\pi\sqrt{m_0/m_2}$ is the mean wave period obtained from the wave frequency spectrum with m_2 found from (2.1) with $k = 2$. It can be shown that the relation between the mean wave period and the wave peak period for PM-spectra is $T_{m2} = T_p/1.41$ (Faltinsen 1990). Thus, estimates of the most probable largest wave height based on H_s and T_p can be found as

$$H_{max} \approx H_s\sqrt{0.5\ln(1.41t/T_p)}. \tag{2.2}$$

Estimates of the most probable largest wave height in a sea-state of duration four hours, using data from Tab. 2.1, are presented in Tab. 2.2. A rule of thumb is that the most probable largest wave height for a sea-state described by a PM-spectrum and with duration four hours, is about two times the significant wave height.

Table 2.2: Estimates of the most probable largest wave height H_{max} in a sea-state with duration four hours represented by a PM-spectrum. The obtained values of H_{max} are based on the significant wave heights H_s and wave peak periods T_p presented in Tab. 2.1.

Wave classes	H_{max} [m]	Level of exposure
A	< 1.1	Small
B	1.1 - 2.1	Moderate
C	2.1 - 4.1	Large
D	4.1 - 6.0	High
E	> 6.0	Huge

Current

Current is an important design parameter. From a fish-health point of view, current is necessary for replacement of dirty water and for the supply of oxygen to the fish-cage. For the structure, current means additional loads that must be accounted for in the design of the fish farm. The current will cause drag forces on the net pens and the floaters. In addition to the design wave classes, also design classes for current are given in NS 9415 (Standard Norway 2005). Current loads are not addressed in the present work. However, some aspects of current loads on fish farms are presented in the following section.

2.3 Relative importance of hydrodynamic forces on the floater and the net

It is the total hydrodynamic horizontal force on the fish farm that matters for the mooring system of a fish farm. However, it is interesting to know the contribution from the floater and the net to the total hydrodynamic load on the structure. The relative importance of the horizontal component of the hydrodynamic force on the net cage and on the floater per unit length of the floater and the net will now be discussed.

Consider the two-dimensional flow problem where the floater and the net is subjected to a uniform current with speed $U_c = 1.0$m/s and regular beam sea waves with height $H = 2.0$m and period $T = 3.6$s. The wave frequency is then $\omega = 2\pi/T = 1.76$rad/s. This corresponds to the wave steepness $H/\lambda = 1/10$, where λ is the wave length. The waves are propagating in the same direction as the current. Consider a semi-submerged circular cylinder with diameter $D = 1.0$m, representing the floater. Further, consider a vertical strip of the net cage with depth $h = 25$m and unit width. We assume the netting material is characterized by a knot-less square mesh with solidity ratio $Sn = 0.20$. The floater and the net is restrained from moving. An Earth-fixed coordinate system Oxy is introduced with origin in the free surface, where x is the horizontal coordinate and y is the vertical coordinate positive upwards.

Wave and current loads on the net

The viscous drag force is the dominating force on the net. Due to the waves, the incident fluid velocity experienced by the net varies with depth. Under a wave crest, the fluid velocity can using linear wave theory be expressed as $u(y) = U_c + \omega\zeta_a \exp{(ky)}$. The drag force amplitude on the net is then computed as

$$F_d = 0.5\rho C_d \int_{-h}^{0} u(y)^2 \mathrm{d}y, \tag{2.3}$$

where h is the depth of the net-panel. The drag coefficient for a knot-less square mesh with solidity $Sn = 0.2$ is $C_d = 0.3$ (Løland 1991). This yields $F_d = 6.1$kN/m as the amplitude of the wave- and current-induced drag force on the net.

Wave and current loads on the floater

The wave excitation forces on a cylinder in the free surface can according to potential flow theory be found as

$$F_a = \zeta_a \sqrt{\rho g^2 b_{kk}/\omega}, \tag{2.4}$$

where b_{kk} with $k = 2, 3$ is the frequency-dependent 2D damping coefficient of the cylinder in sway and heave, respectively (Newman 1962). The damping coefficient in sway of a semi-submerged circular cylinder with diameter $D = 1.0$m for infinite water depth, is for $\omega = 1.75$rad/s found to be $b_{22} = 108.6$kg/s. With $\zeta_a = 1.0$m, this means the wave excitation force amplitude in the $x-$direction is $F_e = 2.5$kN. Now, assume that we can approximate the drag force on the floater due to current and waves as half the drag force on the cylinder in infinite fluid as $F_d = 0.25\rho C_d^{(2)} D U_0^2$, where $U_0 = U_c + \omega\zeta_a$. Strictly speaking this is not a good assumption as we cannot mirror the hydrodynamic problem about the free surface and consider the double body in infinite fluid for the general case, due to a frequency dependent free surface condition (Faltinsen 1990). The drag coefficient due to the steady current in combination with the wave induced oscillatory flow is not known. However, for pure oscillating flow, the drag coefficient for a circular cylinder in infinite fluid is $C_d^{(2)} = 0.2KC$ when $KC < 10$ (Graham 1980). Using $KC = 2\pi\zeta_a/D$ we get $KC = 6.3$, which yields $C_d^{(2)} = 1.25$. For the case of a smooth circular cylinder in infinite fluid subject to uniform steady flow, the drag coefficient is $C_d^{(2)} \approx 1.0$ when $Rn \approx 10^6$. To give a conservative approximation, we use $C_d^{(2)}$ as the drag coefficient for the floater. Hence, we obtain $F_d = 2.4$kN as the horizontal force amplitude caused by viscous flow separation on the floater. This is about the same as the wave excitation force on the floater. Due to the long wave length relative to the diameter of the floater ($\lambda \approx 20D$), we assume that the horizontal component F_e of the wave force on the floater due to potential flow is 90° out of phase relative to horizontal fluid velocity in the wave. Hence, the total wave and current induced force amplitude per unit length of the floater is found as $F_{floater} = \sqrt{F_d^2 + F_e^2} = 3.5$kN.

Discussion

Based on the simplified analysis above, we see that it is the drag force on the net cage that gives the largest contribution to the total horizontal force on the fish cage. However, for this case, we found that the hydrodynamic horizontal force on the floater is of the same order of magnitude as the drag force on the net panel. Here, the horizontal force due to wave excitation on the floater was found to be about 28% relative to the total horizontal force on the floater and net. This indicates that wave forces on the floater should be considered in the design and dimensioning of mooring systems for such fish farms. It should be noted that the analysis presented above is very approximate. It is questionable to consider the fixed structure as the floater and the net structure in reality will be set in motion due to the waves. However, the analysis is considered to be valuable in the sense of getting an impression of the relative importance of the hydrodynamic forces on the floater and on the net cage. Forces on the net cage are not further pursued in this work. The reason for this is that the aim of our study is a thorough understanding of the wave induced motions and loads on the floater.

2.4 Problem limitations and discussion

In the previous two sections we discussed relevant physical effects with their associated flow parameters, and quoted the design wave conditions for fish farms given in NS 9415 (Standard Norway 2005). We will now discuss the relevant physical effects for the floaters in waves in the context of these design wave parameters. The flow parameters due to regular waves corresponding to the most probable largest waves for the design sea-states are estimated.

Consider a horizontal circular cylinder with diameter $D = 1$m which is fixed in the free surface zone. Using the wave heights in Tab. 2.2, we obtain $KC > 3$ for all the design sea-states. For a circular cylinder in infinite fluid subject to oscillatory flow, viscous flow separation occur when $KC \gtrsim 2$. Considering the fixed cylinder might not be relevant for floaters of fish farms for the higher sea-states since then the structure will respond to the waves, and the relative motion between the water and the floater should be considered. However, since the KC-number is larger than two for all the design sea-states, effects of viscous flow separation cannot be neglected.

Viscous flow separation will introduce additional drag forces on the floater. For the circular cylinder, the location of the separation point is affected by whether the boundary layer flow on the cylinder surface is laminar or turbulent. Again, using the design wave parameters in Tab. 2.2 to compute the Reynolds number for the fixed cylinder, we obtain $Rn = 1.0 \times 10^6 - 2.1 \times 10^6$. This suggests that the boundary layer flow on the floater can be turbulent in reality. Turbulent boundary layers combined with free surface flow will introduce too much complexity to our numerical model relative to what we believe is the importance of turbulence. We circumvent this problem by applying a model scale where the boundary layer flow is laminar. Consequences of this approach when it comes to the wave induced motions of the floaters in full scale are discussed in Chapter 8.

Slamming is not considered in the present work, neither are the effects of air pocket formation considered. However, we focus on the fully nonlinear wave loading on 2D floater sections due to regular waves. The study is performed by means of model tests and numerical simulations. The numerical simulations are performed with the presently developed Computational Fluid Dynamics (CFD) code which is used to model the 2D problem of floaters subjected regular waves.

Chapter 3

Mathematical formulation

In order to study the 2D hydrodynamical problem represented by a cylindrical floater in beam sea waves, a numerical model of a physical wave-tank as illustrated in Fig. 3.1 is developed. This is called a numerical wave-tank (NWT). A floating body is introduced into the NWT to represent the floater. We define an Earth fixed coordinate system Oxy in our domain with origin at the initial position of the gravity center of the floater. In this chapter, the mathematical foundation for the NWT is presented. The mathematical model includes the governing equations with proper boundary conditions describing the motions of the water and the air, in addition to the equations of motion for the floating body. As in a physical wave flume, a wave maker and a beach is needed also in the NWT. The mathematical formulation of the numerical wave-tank is presented below.

3.1 General assumptions

It is not practical to include "all" physical effects in our mathematical model. Hence, the mathematical problem is simplified by neglecting physical effects that are believed not to be important for our hydrodynamic problem. With the physical reasoning from Chapter 2 in mind, the following assumptions have been made:

- Incompressible fluid
- Viscous fluid
- Laminar flow
- Surface tension is not important
- 2D-flow conditions
- Planar (2D) floater motion
- No air pockets
- Rigid floater, i.e. no hydroelastic effects

Based on these assumptions, the governing equations are established.

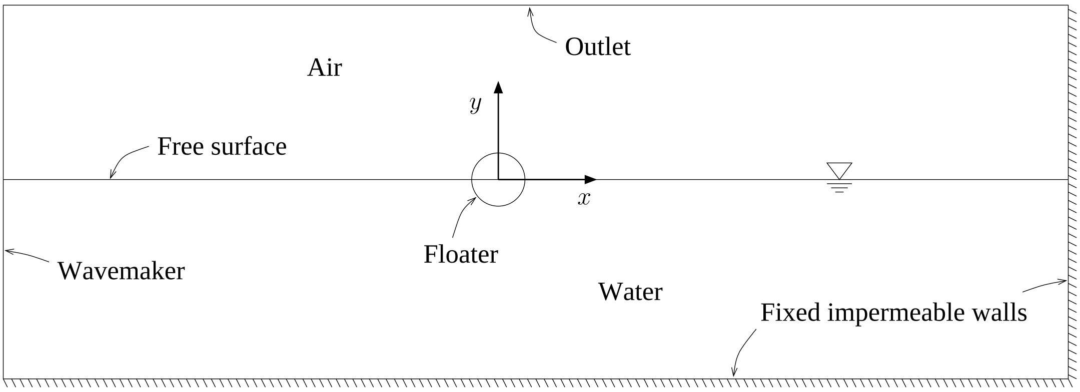

Figure 3.1: The domain of the numerical wave-tank. An Earth-fixed coordinate system Oxy is introduced with origin at the initial position of the body center. The bottom boundary and the right hand boundary are fixed and impermeable walls. The left boundary is the wavemaker, while the top boundary is open.

3.2 Governing equations

We will apply a one-fluid formulation for the water and for the air. This means the flow of both the air and the water is described by the same set of equations, with the coefficients of the mass density and the dynamic viscosity set according to which fluid is occupying the region considered. In reality, there is a discontinuity of the mass density and the viscosity of the fluid at the air-water interface which requires special attention in the derivation of the governing equations.

3.2.1 The continuity equation

Continuity of fluid mass is a basic concept in classical fluid mechanics, which states that fluid mass cannot just appear or disappear in the interior of a control volume. This implies that the amount of fluid mass inside the control volume can only change by means of mass transport through its boundaries. Mathematical formulation of continuity for the fluid mass is not trivial when solving two-phase flow using a one-fluid model. Conservation of the fluid mass for a fixed control volume Ω gives the relation between the rate of change of the fluid mass in Ω and the mass flux through its boundary $\partial\Omega$ as

$$\frac{\mathrm{d}}{\mathrm{d}t}\iint_{\Omega}\rho\,\mathrm{d}\Omega+\oint_{\partial\Omega}(\rho\boldsymbol{u})\cdot\boldsymbol{n}\,\mathrm{d}S=0, \tag{3.1}$$

where $\boldsymbol{u}=[u,v]^T$ is the fluid velocity vector and $\boldsymbol{n}$ is the unit outward normal vector of Ω. Now consider the case of two-phase fluid flow in Ω, where the two phases are separated by a sharp interface Γ. If the density of the two phases is different, the fluid momentum $\rho\boldsymbol{u}$ is discontinuous across Γ. This is the case for air-water interaction flows in reality. We want to obtain the differential form of the continuity equation, which requires the application of Gauss theorem on the second term of (3.1). However, the use of Gauss theorem requires that $\rho\boldsymbol{u}$ is continuous throughout the domain Ω. To circumvent this problem, we will assume that the interface has a finite but small thickness where the fluid density varies smoothly, meaning also that the fluid momentum will be continuous. Then we get

$$\frac{\partial \rho}{\partial t} + \nabla \cdot (\rho \boldsymbol{u}) = 0. \tag{3.2}$$

This is the conservative formulation of the continuity equation. By applying the chain rule for differentiation to (3.2) and introducing the material derivative operator $\frac{\mathrm{D}}{\mathrm{D}t}(\cdot) = \left(\frac{\partial}{\partial t} + \boldsymbol{u} \cdot \nabla\right)(\cdot)$, the non-conservative form of the continuity equation is obtained as

$$\frac{\mathrm{D}\rho}{\mathrm{D}t} + \rho \nabla \cdot \boldsymbol{u} = 0. \tag{3.3}$$

The first term of (3.3) expresses the rate of change of the fluid mass density as one follows a fluid particle. Since the mass density is a fluid property which moves with the fluid flow, the mass density represented by a fluid particle should be constant if we assume incompressible flow and that no diffusion of the mass density occur. This means $\frac{\mathrm{D}\rho}{\mathrm{D}t} = 0$. Thus, for two-phase incompressible flow where the fluid density is smeared at the interface, the continuity equation reduces to

$$\nabla \cdot \boldsymbol{u} = 0, \tag{3.4}$$

i.e. that the divergence of the velocity field is zero. This will be referred to as the divergence-free constraint.

3.2.2 The momentum equations

We have assumed the fluid to be viscous and incompressible. Hence, the governing equations describing the fluid flow are the incompressible Navier-Stokes equations. Applying the same assumptions of smoothness as in the derivation of the continuity equation, we can obtain the incompressible Navier-Stokes equations on differential non-conservative form. For the case of 2D-flow, we get

$$\frac{\partial u}{\partial t} + u\frac{\partial u}{\partial x} + v\frac{\partial u}{\partial y} = -\frac{1}{\rho}\frac{\partial p}{\partial x} + \frac{1}{\rho}\left[\frac{\partial}{\partial x}\left(2\mu\frac{\partial u}{\partial x}\right) + \frac{\partial}{\partial y}\left(\mu\left(\frac{\partial u}{\partial y} + \frac{\partial v}{\partial x}\right)\right)\right] + f_x \tag{3.5}$$

$$\frac{\partial v}{\partial t} + u\frac{\partial v}{\partial x} + v\frac{\partial v}{\partial y} = -\frac{1}{\rho}\frac{\partial p}{\partial y} + \frac{1}{\rho}\left[\frac{\partial}{\partial x}\left(\mu\left(\frac{\partial u}{\partial y} + \frac{\partial v}{\partial x}\right)\right) + \frac{\partial}{\partial y}\left(2\mu\frac{\partial v}{\partial y}\right)\right] + f_y \tag{3.6}$$

where u and v is the horizontal and vertical components of the fluid velocity, respectively. Further, p is pressure, ρ the mass density of the fluid and μ the dynamic viscosity coefficient. Finally, f_x and f_y are volume "forces" acting on the fluid in the horizontal and vertical direction, respectively. The quotes are added because strictly speaking, f_x and f_y do not have the unit of force, but the unit of acceleration. The only volume force in our model is gravity, acting in the negative $y-$direction.

3.3 The free surface

We define the free surface as the interface between the air and the water. When using a one-fluid model to describe two-phase flow, here represented by the air and the water, no explicit boundary condition is imposed on the free surface, simply because the air-water interface is not a boundary of the fluid domain. However, the instantaneous position of the free surface must be found in order to know the material properties of the fluid at a given point. As argued in the derivation of the continuity equation, the condition $\frac{\mathrm{D}\rho}{\mathrm{D}t} = 0$ must be satisfied for all points in the domain. Now, let the fluid mass density in the domain be described by $\rho(x, y, t) = \rho_w \varphi(x, y, t) + \rho_a (1 - \varphi(x, y, t))$, where $\varphi(x, y, t) \in [0, 1]$ is a continuous scalar function similar to a Heaviside function but where the discontinuity is replaced by a smooth transition. Further, ρ_w and ρ_a are constants representing the density of water and air, respectively. This means $\frac{\mathrm{D}\rho}{\mathrm{D}t} = (\rho_w - \rho_a) \frac{\mathrm{D}\varphi}{\mathrm{D}t} = 0$. Hence, the evolution of $\rho(x, y, t)$ in time is found by solving

$$\frac{\partial \varphi}{\partial t} + \boldsymbol{u} \cdot \nabla \varphi = 0, \tag{3.7}$$

where $\mathbf{u}$ is the fluid velocity vector. One can also simply say that φ is a fluid property which then must satisfy (3.7). The dynamic viscosity of the fluid can similarly be found as $\mu(x, y, t) = \mu_w \varphi(x, y, t) + \mu_a (1 - \varphi(x, y, t))$ where μ_w and μ_a are the dynamic viscosity coefficients of water and air in that order. Due to the smeared air-water interface in our mathematical model, we will have to define what to interpret as the physical free surface. Here, we define the free surface as the contour represented by $\varphi(x, y, t) = 0.5$.

3.4 Initial conditions

Unless otherwise specified, the initial conditions used are that the fluid and the body are at rest initially. This means the velocity field in the domain is zero. Hence, the pressure field below the free surface is hydrostatic and described by $p = -\rho_w g y$. Similarly, due to the mass density of the air, an aerostatic pressure distribution $p = -\rho_a g y$ is applied initially for the air-part of the domain. Continuity of the initial pressure field is ensured.

3.5 Boundary conditions

In order to solve the field equations in a prescribed domain, boundary conditions (BC) for the prime variables, i.e. fluid velocity and pressure, must be specified. We will consider a rectangular domain where the boundaries are fixed in space. In addition, the presence of a floater inside the domain yields an internal or immersed boundary for which boundary conditions must be imposed. Obtaining mathematical formulations of boundary conditions for the Navier-Stokes equations is not a simple task in general. Often, the quantities to be prescribed on the boundaries are not known. Some commonly used concepts are discussed below.

Fixed and moving impermeable walls

A no-slip boundary condition is applied on all impermeable walls in the domain, i.e. the bottom and the end wall at the beach side of the flume. The no-slip condition is also applied on the floating body boundary. No-slip means that the fluid particles that are initially located at points on the solid boundary, remain attached to the same points of the boundary. There are no relative motion between the boundary and the fluid particles located on the boundary. This is an assumption based on physical observations of viscous fluid flows near solid boundaries (Schlichting and Gersten 2000). Mathematically, the no-slip boundary condition on fixed impermeable walls S_w is expressed as

$$\mathbf{u} = \mathbf{0} \quad \text{on} \quad S_w. \tag{3.8}$$

When it comes to the floating body, the no-slip condition implies that fluid particles on the body surface will have to move with the body, i.e. the relative velocity between the fluid particles at the body surface and the body itself is zero. Mathematically speaking,

$$\mathbf{u} = \mathbf{u_b} \quad \text{on} \quad S_b \tag{3.9}$$

where $\mathbf{u_b} = [u_b, v_b]^T$ is the local velocity vector of a point on the surface of the floating body. The body velocity is either enforced or governed by the equations of motion for the body. Also the wave maker can be modelled as a body with forced motion, yielding (3.9) as boundary condition for the wave maker.

A boundary condition for the pressure on impermeable no-slip boundaries for the case of time-dependent incompressible flows is not easy to define since the pressure here in general is unknown. The pressure boundary condition must be seen in combination with the numerical method used to solve the governing equations for the fluid flow. However, the normal component of the momentum equations to the impermeable boundary suggests a Neumann BC for the pressure, meaning that $\frac{\partial p}{\partial n}$ should be prescribed on the boundary. This issue will be described more in detail in the next chapter.

Outlet

The ceiling of the tank is open and thus an outlet boundary condition should be applied. This means the fluid is allowed to flow out of the domain. The pressure outside the tank is assumed to be atmospheric, which means the Dirichlet condition $p = p_{atm}$ is imposed on the upper boundary of the domain. In reality, we know little about the flow at the outlet boundary. Therefore, a general concept is that outlet boundaries should be located far away from the region of interest (Ferziger and Peric' 2002). The outlet boundary condition which is applied in the ceiling of the tank will have influence on the air flow. However, for our case it is the water flow that is of interest. Since transfer of fluid momentum from the air to the water is negligible for most cases, the requirement of the outlet boundary to be located far away from the region of interest (the free surface) is less important. Further, commonly used criterions are that the convective and diffusive fluxes through the outlet boundary are zero, meaning the flow has no velocity gradients in the direction normal to the boundary.

3.6 Computation of forces and moments

The forces and moments acting on the floater from the surrounding fluids (water and air) are in general due to the pressure and due to skin friction and normal viscous stresses on the body surface. In the 2D problem, pressure forces $\mathbf{F_p}$ and moments $\mathbf{M_p}$ are found by integrating the total fluid pressure p over the boundary S_b of the body, i.e.

$$\mathbf{F_p} = -\int_{S_b} p\,\mathbf{n}\mathrm{d}S \tag{3.10}$$

$$\mathbf{M_p} = -\int_{S_b} p\,(\mathbf{r} \times \mathbf{n})\,\mathrm{d}S = \int_{S_b} \mathbf{n} \times (\mathbf{r}p)\,\mathrm{d}S, \tag{3.11}$$

where $\mathbf{n}$ is the unit normal vector of the body boundary S_b, pointing into the fluid domain. Further, $\mathbf{r}$ is the distance from the incremental element $\mathrm{d}S$ located at the point $(x,\, y)$ on the body boundary to the centre of gravity $(x_c,\, y_c)$ of the body, i.e. $\mathbf{r} = (x - x_c)\mathbf{i} + (y - y_c)\mathbf{j}$. Since it is the total pressure that is integrated, the pressure loads here are due to both hydrodynamic and hydrostatic pressures.

The fact that the fluid is viscous implies that there is a skin friction force acting on the body from the water (and vice verse). There is also a force component due to normal viscous stresses on the body surface. The viscous forces on the floater can be found by integrating the product of the viscous stress tensor and the unit normal vector of the body over the boundary S_b. Hence,

$$\mathbf{F_v} = \int_{S_b} \boldsymbol{\tau}\, \mathbf{n}\, \mathrm{d}S. \tag{3.12}$$

Similarly, viscous stresses also cause a roll moment on the body which can be expressed as

$$\mathbf{M_v} = \int_{S_b} \boldsymbol{\tau}\, (\mathbf{r} \times \mathbf{n})\, \mathrm{d}S. \tag{3.13}$$

The viscous stress tensor $\boldsymbol{\tau}$ for two dimensional flow is defined as

$$\boldsymbol{\tau} = \begin{pmatrix} 2\mu\frac{\partial u}{\partial x} & \mu\left(\frac{\partial u}{\partial y} + \frac{\partial v}{\partial x}\right) \\ \mu\left(\frac{\partial u}{\partial y} + \frac{\partial v}{\partial x}\right) & 2\mu\frac{\partial v}{\partial y} \end{pmatrix}. \tag{3.14}$$

By prolonging the outer pressure field to the inside of the body, an artificial flow problem can be solved in the interior of the body. If this artificial pressure field inside the body is continuous and differentiable, we can make use of Gauss theorem to transform the line integrals in the expressions for the pressure forces and moment, (3.10) and (3.11) respectively, to surface integrals over the area enclosed by the body boundary. Then the pressure forces can then be found as

$$\mathbf{F_p} = -\iint_{\Omega_b} \nabla p\, \mathrm{d}A. \tag{3.15}$$

Here, $\nabla = \boldsymbol{i}\frac{\partial}{\partial x} + \boldsymbol{j}\frac{\partial}{\partial y}$ is the gradient operator and Ω_b is the area enclosed by the body boundary. Further, the roll moment due to the fluid pressure can be written as

$$\begin{aligned} \mathbf{M_p} &= \iint_{\Omega_b} \nabla \times (\mathbf{r}p)\ \mathrm{d}A \\ &= \iint_{\Omega_b} p\,(\nabla \times \mathbf{r})\ \mathrm{d}A - \iint_{\Omega_b} \mathbf{r} \times \nabla p\, \mathrm{d}A. \end{aligned}$$

Since $\nabla \times \mathbf{r} = \mathbf{0}$, we arrive at

$$\mathbf{M_p} = -\iint_{\Omega_b} \mathbf{r} \times \nabla p\, \mathrm{d}A. \tag{3.16}$$

If we introduce a scalar function φ_3 defined as

$$\varphi_3 = \begin{cases} 1, & \forall\,(x, y) \in \Omega_b \\ 0, & \text{elsewhere} \end{cases} \tag{3.17}$$

we can express the pressure forces and moment in terms of surface integrals over the complete domain of computation Ω as

$$\boldsymbol{F_p} = -\iint_{\Omega} (\nabla p)\varphi \, \mathrm{d}A \tag{3.18}$$

$$\boldsymbol{M_p} = -\iint_{\Omega} (\mathbf{r} \times \boldsymbol{\nabla} p)\varphi \, \mathrm{d}A. \tag{3.19}$$

The viscous forces cannot be treated this way because the viscous stress tensor defined in (3.14) is not continuous across the body boundary. The spatial derivatives of the velocity field has a finite value at the outer side of the boundary, while the gradient of the artificial velocity field in the interior of the body is zero. This is because a uniform velocity field equal to the rigid body velocity is imposed on the interior of the body. Hence, this might explain the rather poor convergence properties for the skin friction forces when using the surface integral representation, as reported by Hu and Kashiwagi (2004).

3.7 Equations of motion for the floating body

When the forces and moments acting on the floater are found, the body motions in an inertial frame of reference Oxy are obtained by means of integration of Newton's second law. The motion equations for the floater for planar motion are

$$m\ddot{x}_c = F_x \tag{3.20}$$

$$m\ddot{y}_c = F_y \tag{3.21}$$

$$I\ddot{\theta} = M, \tag{3.22}$$

where m is the structural mass per unit length of the body, $\ddot{x}_c$ and $\ddot{y}_c$ are the body accelerations at the center of gravity in the horizontal direction and vertical direction, respectively. Further, I is roll inertia about the center of gravity, $\ddot{\theta}$ is roll acceleration, while F_x, F_y and M are the total forces in the horizontal and vertical direction and the roll moment about COG, in that order.

3.8 Wave characteristics and wavemaker theory

Some basic properties of progressive water waves, which are frequently utilized in the present work, are described below. For intermediate and deep water relative to the wave length, water is a dispersive medium. This means that the celerity or phase speed C of water waves is frequency dependent. The celerity is simply given by $C = \omega/k$, where ω is wave angular frequency and k is wave number defined as $k = 2\pi/\lambda$, with λ being the wave length. A relation between ω and k, known as the dispersion relation, is from potential flow theory found as

$$\omega^2 = gk \tanh kh, \tag{3.23}$$

where g is the acceleration of gravity and h is a constant water depth. The group velocity C_g of the wave train is an important parameter, which will be used e.g. when constructing the domain of the numerical wave-tank or when evaluating if wave reflections in the flume are likely to be contaminating the measurements. The group velocity is according to linear potential flow theory expressed as

$$C_g = \frac{\mathrm{d}\omega}{\mathrm{d}k} = \frac{C}{2}\left[1 + \frac{2kh}{\sinh 2kh}\right]. \tag{3.24}$$

When generating waves either experimentally in a physical wave-flume or numerically in an NWT, it is convenient to know what wavemaker paddle motion that yields a given wave height of the waves generated. Such a relation between the wavemaker paddle motion and the resulting steady state wave height H far away from the wavemaker can be found e.g. from linear potential flow theory (Hughes 1993). For the piston type wavemaker where the paddle is acting from the bottom of the flume to the free surface, the wave height-to-stroke ratio is

$$\frac{H}{S_0} = \frac{4\sinh^2 kh}{\sinh 2kh + 2kh}, \tag{3.25}$$

where S_0 is the piston stroke. Further, h is water depth and k the wave number found from the dispersion relation (3.23). For the flap type wavemaker hinged at a distance l from the bottom of the flume, the wave height-to-stroke ratio is

$$\frac{H}{S_0} = \frac{4\sinh kh}{\sinh 2kh + 2kh}\left[\sinh kh + \frac{(1-\cosh kh)}{k\,(h+l)}\right]. \tag{3.26}$$

For the flap type wavemaker, the stroke S_0 is defined as two times the horizontal motion amplitude of the paddle at the mean free surface.

Chapter 4

Numerical model

4.1 Discretization of the Navier-Stokes equations

In the previous chapter we established a mathematical model for our physical problem. The obtained mathematical model, which is governed by the time-dependent incompressible Naviér-Stokes equations with proper initial- and boundary conditions, must be solved numerically. Hence, a suitable discretization method must be found. By discretization method is meant a method to approximate the differential equations with a set of algebraic equations for the flow variables at a discrete set of points in time and space. A numerical grid defining these points or nodes of computation must then be specified. However, also grid-less methods for solving the incompressible N-S equations exists. An example here is the Smoothed particle hydrodynamics (SPH) method (Gingold and Monaghan 1977; Monaghan 1992). We apply a grid method for our numerical wave tank. How the grid is organized is described in the following.

4.1.1 The numerical grid

For grid methods, there is a vast number of ways to arrange the numerical grid. Some concepts will now be described. First of all, the grid can be fixed in space (Eulerian) or it can move with the flow (Lagrangian). Further, the grid can be structured (regular), block-structured or unstructured (irregular). Block-structured grids, which are composed of some regions (blocks) in where the grid is regular. Some block-structured grids may have overlapping blocks. Such arrangements where e.g. a body-fitted grid (which can be moving) is overlapping a fixed grid are called *composite* or *Chimera* grids. These types of grids have shown to be advantageous for flow computations with moving bodies (Ferziger and Peric' 2002), since the body boundary condition then easily can be imposed. A new type of grid which has been used in combination with the CIP-method is the so-called *soroban* grid, introduced by Takizawa et al. (2006). For the soroban grids, the grid points can be moved in a systematic manner, similarly as the beads on an abacus. In fact, soroban is the Japanese word for abacus.

The presence of the air-water interface is a complicating factor in our problem, and must be considered when deciding which type of grid arrangement to apply. Typically when dealing with free surface flows, we separate between domain dividing methods and domain embedding methods. Domain dividing methods apply Lagrangian type of grids which adept to the free surface. Hence, regridding is required as the free surface evolves

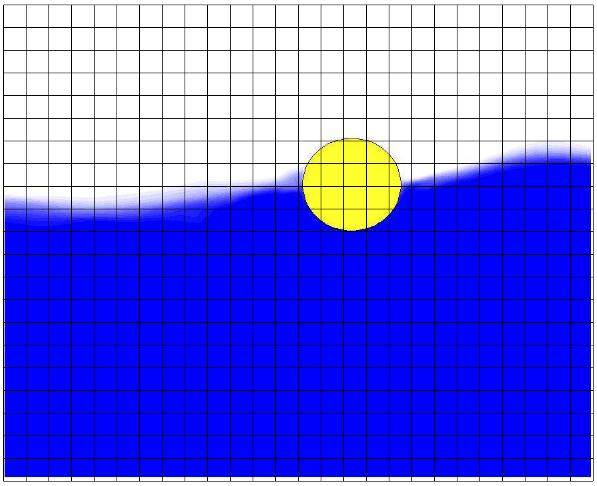

Figure 4.1: Illustration of the domain embedding method. A fixed Cartesian grid is used which does not conform to the free surface or the floating body. The grid covers the air, the water and the floating body.

with time. For violent free surface flows where large distortions and even fragmentation of the free surface may occur, the regridding process can be very cumbersome and time consuming. For such flow problems it is more common to apply a domain embedding method which is characterized by a fixed grid that extends from the liquid phase into the air, as illustrated in Fig. 4.1. Since the grid does not conform to the free surface and covers both air and water, an interface capturing method must be used in order to locate the free surface within the domain. Due to the good performance for violent free surface flows, we will base our numerical model on a domain embedding method, i.e. using a fixed grid. We have already established a mathematical model where the governing equations are expressed in Cartesian coordinates. Thus, when constructing the finite difference schemes, it is convenient that also the computational nodes are arranged in a Cartesian manner, i.e. that the nodes are aligned in the coordinate directions. Hence, a fixed Cartesian grid will be applied on a rectangular domain. We will use the indices i and j to represent the node number in the horizontal and vertical direction, respectively.

4.1.2 Staggered grid arrangement

One may think that it is convenient to use a grid where all the primary variables, i.e. horizontal velocity u, vertical velocity v and pressure p, are calculated in the same set of points. Such grids are referred to as collocated grids. Drawbacks of collocated grids are difficulties with the pressure-velocity coupling which then requires interpolation, in addition comes problems with unphysical oscillations of the pressure (Ferziger and Peric' 2002). This has motivated for other arrangements of Cartesian grids. Harlow and Welch (1965) introduced an arrangement where a separate grid was used for each primary variable and where each primary variable was computed at different sets of points. This resulted in a set of staggered grids. The staggered grids can be explained by having one set of grid cells where horizontal velocity nodes are located on vertical cell faces, vertical velocity nodes are located on horizontal cell faces while pressure nodes are located at the geometrical cell centres, as depicted in Fig. 4.2. We use Δx_i to represent the grid line spacing in the horizontal direction for the grid cell containing pressure node with index (i, j). Similarly is Δy_j representing the grid line spacing in the vertical direction for the same grid cell. Application of grid stretching causes the grid line spacings Δx_i and Δy_j to differ from the spacings between cell centres. For convenience, we introduce the parameters Δxc_i and Δyc_j to represent the horizontal and vertical spacing between cell centres, respectively. The relation between the two are $\Delta xc_i = 0.5(\Delta x_i + \Delta x_{i+1})$ and $\Delta yc_j = 0.5(\Delta y_j + \Delta y_{j+1})$.

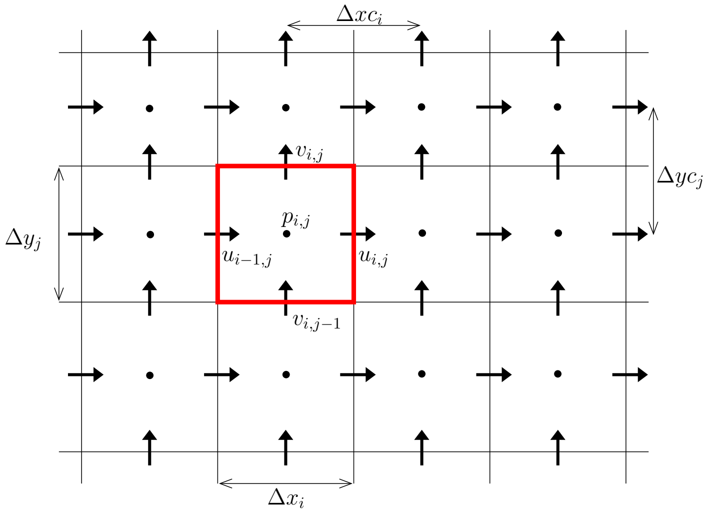

Figure 4.2: Definitions of the Cartesian staggered grid which is used in the present numerical model. Pressure nodes are marked with circles, while horizontal and vertical arrows represents horizontal velocity nodes and vertical velocity nodes, respectively. We use Δx_i and Δy_j to represent spacing between grid lines, while Δxc_i and Δyc_j represents spacing between cell centres.

For the primary variables, we use $u_{i,j}$ to represent an approximation to the horizontal velocity $u(x_i, yc_j)$ where (x_i, yc_j) are the coordinates of the horizontal velocity node considered. Further, $v_{i,j}$ represents $v(xc_i, y_j)$ and $p_{i,j}$ represents $p(xc_i, yc_j)$.

4.1.3 Temporal discretization

The discretized momentum equations must be integrated in time to obtain the velocity field at a later time step. Many methods exists for integrating the Naviér-Stokes equations in time. Methods classified as *Fractional step approaches* as first suggested by Harlow and Welch (1965) and Chorin (1968) are perhaps the most popular class of methods. For these approaches, the terms of the N-S equations representing different physical effects are stepped forward in time separately. In the fractional step approach by Chorin, a tentative velocity field is obtained by integrating an incomplete version of the momentum equations where the pressure term is excluded. This tentative velocity field is then not necessarily divergence free, meaning the velocity field might not satisfy the continuity equation (3.4). Then, in order to obtain a divergence free velocity field at the next time step, an orthogonal projection of the tentative velocity field onto the plane of zero divergence is performed. Hence, such methods are referred to as projection methods. Chorin's method has later been modified for use with finite volume methods and staggered grid arrangements by Kim and Moin (1985). The Harlow and Welch approach has lead to the fully implicit method *SIMPLE* by Patankar (1980), where all terms are solved simultaneously and iterates are performed until a velocity field free of divergence is reached. This method was originally developed for solving the steady-state Naviér-Stokes equations but has also been used for solving unsteady problems. We will use a projection method similar to that proposed by Kim and Moin, but instead of using finite volumes for the spatial discretization we will apply finite differences.

The notation $\boldsymbol{u}^n$ will be used to represent an approximation to the velocity field $\boldsymbol{u}(t^n)$, where the time $t^n = n\Delta t$ with n being the time step and Δt the time increment. However, adaptive time stepping will sometimes be used. Then the solution time is $t^n = \sum_{k=1}^{n} \Delta t_k$.

4.1.4 The adopted fractional step approach

Fractional step methods are time-splitting schemes where approximate factorizations of the Naviér-Stokes equations are applied, such that each term of the equations can be treated separately. The underlying method for time integration of the different terms can be either implicit or explicit. Here, time integration will be performed using the first order explicit Euler method.

Projection methods can be divided into *pressure-free projection methods* as that introduced by Kim and Moin (1985) and *incremental-pressure projection methods* as described by Brown et al. (2001). In the pressure-free projection method, the advection and diffusion terms are solved to obtain a tentative velocity field which is projected onto a divergence free plane. Hence, no pressure gradient is included in the tentative velocity field. In the latter method the pressure field from the former time step is used to get a better estimate of the velocity field before a projection step of the incremental change in pressure from time t^n to t^{n+1} is performed. The incremental pressure projection method will be used here. Using the explicit Euler method for time integration, the fractional step approach with incremental pressure projection can be expressed as

$$\boldsymbol{u}^{n+1} = \boldsymbol{u}^n + \left(\boldsymbol{C}^n + \boldsymbol{D}^n + \boldsymbol{P}^{n+1}\right)\Delta t \tag{4.1}$$

where $\boldsymbol{C}$ represents the convective terms, $\boldsymbol{D}$ represents diffusive terms, the body forces and the pressure gradient from time t^n. Finally, $\boldsymbol{P}$ is the gradient of the incremental pressure change from time t^n to t^{n+1}. This leads to a three step approach for integrating the N-S equations, with the following steps

$$\boldsymbol{u}^{*} = \boldsymbol{u}^n + \left(\boldsymbol{C}^n\right)\Delta t \tag{4.2}$$

$$\boldsymbol{u}^{**} = \boldsymbol{u}^{*} + \left(\boldsymbol{D}^n\right)\Delta t \tag{4.3}$$

$$\boldsymbol{u}^{n+1} = \boldsymbol{u}^{**} + \left(\boldsymbol{P}^{n+1}\right)\Delta t. \tag{4.4}$$

The different steps will be referred to as the advection step, non-advection step and incremental-pressure correction step, respectively. The non-advection step will be further divided into a diffusion step and a pressure correction step. In the incremental-pressure correction step, the velocity is updated with the incremental change in the pressure, which leads to a divergence free velocity field. This incremental-pressure correction is unknown and must be found using a projection method leading to a Poisson type equation for the incremental pressure.

4.2 The CIP-method

When solving the advection step, a method with small numerical diffusion is favorable. Numerical diffusion is due to artificial diffusion terms that are caused by truncation errors of the discretization. Although numerical diffusion stabilizes the numerical scheme, it is unphysical and may cause erroneous solutions. A typical example is rapid decay of the wave amplitude in simulations of propagating surface waves. A method with small numerical diffusion that has shown to work well for fluid-structure interaction problems (Hu and Kashiwagi 2004; Hu et al. 2005) is the CIP-method. The CIP-method was first introduced by Takewaki et al. (1985) as a solver for one-dimensional hyperbolic-type equations, then with CIP being the abbreviation for Cubic Interpolated Pseudo-particle method. This method uses the values of the advected variable and its spatial derivatives to construct an interpolating profile, usually a cubic polynomial, to represent the advected variable in the upstream cell. Then the solution is found by moving the interpolation profile in a Lagrangian manner. The CIP-method has been extended to apply for multi-dimensional problems, and also other interpolating functions than the cubic polynomial have been used. To construct a cubic polynomial, four constraints are needed in the 1D-formulation, while ten constraints are needed in 2D. This could be done by using information from more than one upwind cell. However, in the CIP-method the spatial derivatives of the advected variable are introduced as free variables. This yields a compact scheme where information from only one upwind cell is used. Thus, to account for other types of interpolating functions, the first definition of the CIP-method has been changed to the Constrained Interpolation Profile method. The CIP-method has been incorporated into N-S solvers where time-splitting algorithms are used (Toro 1999) as a solver for the advection step. CIP has also been used in multiphase flow simulations for solving the advection equation for density functions, which appear when interface capturing methods are used. A review of the CIP-method for multiphase flow simulations is presented in Yabe et al. (2001).

In order to explain the CIP-method, it is convenient to start out with the 1D-formulation. Then, a 2D-formulation which are used in our numerical model will be presented. Some mathematical background relevant for the CIP-method is presented in Appendix A.1.1.

4.2.1 One-dimensional CIP-formulation

The one-dimensional linear advection equation can be written as

$$\frac{\partial f}{\partial t} + u\frac{\partial f}{\partial x} = 0. \tag{4.5}$$

and describes a function $f(x,t)$ which is advected with the velocity u. For the special case of constant velocity $u = u_0$, the advected function $f(x,t)$ retains its initial shape and is only shifted along the x-axis with time. Then the relation of $f(x,t)$ between two different time instants Δt apart is $f(x, t+\Delta t) = f(x - u_0\Delta t, t)$, as illustrated in Fig. 4.3. For

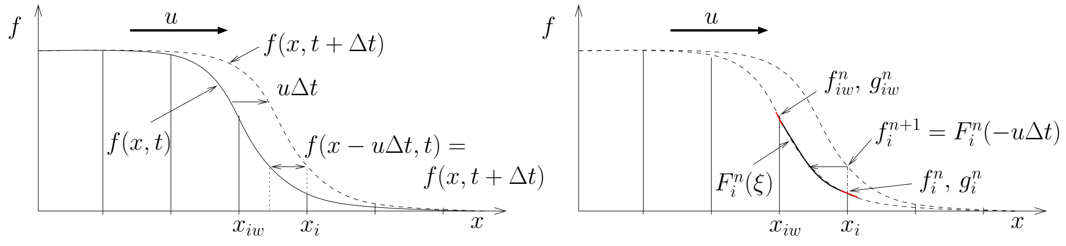

(a) (b)

Figure 4.3: Relation between the advected function $f(x,t)$ and the same function at a later time $f(x,t+\Delta t)$ when the advection velocity u is constant is shown in (a). In (b) the advected variable $f(x,t)$ in the upwind cell of x_i is approximated by a cubic polynomial $F_i^n(\xi)$. The solution f_i^{n+1} is then found by moving $\xi = -u\Delta t$ along the profile F_i^n.

the general case where $u = u(x,t)$, also the shape of $f(x,t)$ will be affected during the advection process. The CIP-method makes use of the spatial derivative of the advected function, which are introduced as additional free variables. Then, for the 1D-problem we need one additional equation for the time evolution of the spatial derivative $g = \partial f/\partial x$. Differentiating (4.5) with respect to x and substituting $\partial f/\partial x = g$ yields

$$\frac{\partial g}{\partial t} + u(x,t)\frac{\partial g}{\partial x} = -\frac{\partial u}{\partial x}g. \tag{4.6}$$

Equations (4.5) and (4.6) are the governing equations for the one-dimensional CIP-method. Due to the source term on the RHS, eq. (4.6) is solved by a two-step time-splitting method. First we solve eq. (4.6) with the RHS equal to zero to obtain a tentative g^*. Then, g^* is updated by the source term on the RHS of (4.6) to obtain g^{n+1}.

The solution procedure is as follows. We consider the node x_i, for which u_i^n, f_i^n and g_i^n are known. We want to find f_i^{n+1} and g_i^{n+1}. First, the upwind node index is found as $iw = i - sign(u)$, where the function $sign$ is defined as

$$sign(x) = \begin{cases} 1, & x \geq 0 \\ -1, & x < 0 \end{cases} \tag{4.7}$$

Then, a cubic polynomial $F_i^n(\xi)$, where $\xi = x - x_i$, is constructed to represent $f(x,t^n)$ in the upwind cell, i.e. in the interval $[x_i,\, x_{iw}]$. The cubic polynomial and the corresponding differentiated profile is

$$F_i^n(\xi) = C_3\xi^3 + C_2\xi^2 + C_1\xi + C_0 \tag{4.8}$$

$$G_i^n(\xi) = 3C_3\xi^2 + 2C_2\xi + C_1, \tag{4.9}$$

where $G_i^n = \mathrm{d}F_i^n/\mathrm{d}\xi$. The four unknown coefficients are now found using the known values of f^n and g^n in the two nodes of the upwind cell as constraints. Details of the derivation of these coefficients can be found in Appendix A.1.2. When the coefficients are found, the interpolation profiles are shifted the distance $u_i\Delta t$ to obtain the new values

$$f_i^{n+1} = F_i^n(-u_i\Delta t) \tag{4.10}$$

$$g_i^* = G_i^n(-u_i\Delta t). \tag{4.11}$$

The spatial derivative g^* is updated with the source term on the RHS of (4.6) as

$$g_i^{n+1} = g_i^* - \Delta t \left(\frac{u_{i+1}^n - u_{i-1}^n}{\Delta x_i + \Delta x_{i+1}} \right) g_i^* . \tag{4.12}$$

We note that (4.10), (4.11) and (4.12) are consistent with the analytical solutions to (4.5) and (4.6) for the case when u is a linear function in space and constant in time, which is given in appendix A.1.1 (equations (A.6) and (A.10), respectively).

Stability of the 1D CIP-method

When solving the advection equation (4.5) numerically, there is usually an upper limit on the time-step in order to obtain a stable solution. This criterion on the time-step for a stable solution is expressed in terms of the Courant-Friedrichs-Lewy (CFL) number, which for the 1D case is defined as $CFL = U\Delta t/\Delta x$. Here U is the maximum fluid velocity in the domain, Δt is the time-step and Δx is the spatial increment. A commonly used stability criterion for the CIP-method is $CFL < 1$. For a given spatial discretization and a given transport velocity, we then get $\Delta t < \Delta x/U$ as a constraint for a stable calculation. Although no rigorous stability analysis is performed to verify the stability criterion, we note that $CFL = 1$ marks the limit between interpolation ($CFL < 1$) and extrapolation ($CFL > 1$) on the constrained polynomial defined by (4.8).

4.2.2 Two-dimensional CIP-formulation

Several variants of the CIP method has been developed for advection calculations in two- and three- space dimensions, as described by Zhu (2006). In the methods referred to as C-type and M-type CIP, directional splitting techniques are used such that the two- or three-dimensional problem is reduced to a set of one-dimensional problems which are then solved by the 1D-solution procedure. We will in the following use what is called the A-type CIP method. This method does not apply directional splitting. Instead, a polynomial surface is constructed as the interpolation function representing the advected variable. This will now be explained.

We want to solve the linear advection equation in two spatial dimensions, which can be expressed as

$$\frac{\partial f}{\partial t} + u\frac{\partial f}{\partial x} + v\frac{\partial f}{\partial y} = 0. \tag{4.13}$$

Differentiating (4.13) with respect to the spatial coordinates and introducing the new variables $g = \partial f/\partial x$ and $k = \partial f/\partial y$, we obtain

$$\frac{\partial g}{\partial t} + u\frac{\partial g}{\partial x} + v\frac{\partial g}{\partial y} = -\frac{\partial u}{\partial x}g - \frac{\partial v}{\partial x}k \tag{4.14}$$

$$\frac{\partial k}{\partial t} + u\frac{\partial k}{\partial x} + v\frac{\partial k}{\partial y} = -\frac{\partial v}{\partial y}k - \frac{\partial u}{\partial y}g. \tag{4.15}$$

The hyperbolic equations (4.14) and (4.15) describing the evolution of spatial derivatives g and k, are coupled due to the source terms on the right hand side (RHS). In order to solve these equations, a two-step time-splitting technique is used. First, pure advection of the derivatives are computed by setting the RHS to zero. Then the spatial derivatives are updated due to the source terms.

The upwind cell for a given node is determined by the sign of the two velocity components for the node considered. Since the nodes for the horizontal and vertical velocity components are not collocated on a staggered grid (cf. Fig. 4.2), interpolation of the velocities to the node considered is necessary. For advection of horizontal momentum the vertical velocity component has to be interpolated to the horizontal velocity node, while for advection of vertical momentum the horizontal velocity component must be interpolated to the vertical velocity node. When advection of the color function is computed, both velocity components must be interpolated to the cell centre. The advection velocity components will be referred to as u_c and v_c referring to the horizontal and vertical component, respectively. Now the upwind cell for a given node (i, j) is determined based on the sign of the velocity components u and v. More precisely, the upwind node indices for the horizontal and vertical direction is found as $iw = i - sign(u)$ and $jw = j - sign(v)$, respectively. The upwind cell is defined as the area limited by the four nodes (i, j), (iw, j), (i, jw) and (iw, jw).

When the upwind cell is found, the next step in the A-type CIP-method is to approximate the advected variable $f(x, y, t^n)$ in the upwind cell with a cubic polynomial surface $F^n(\xi, \eta)$, where $\xi = x - x_i$ and $\eta = y - y_j$ are the local cell coordinates. If the grid spacings Δx_i and Δy_j are of the same order of magnitude, i.e. ξ and η are of the same order, a complete cubic polynomial surface is described by

$$\begin{aligned} F^n_{i,j}(\xi, \eta) = {} & C_{30}\xi^3 + C_{21}\xi^2\eta + C_{12}\xi\eta^2 + C_{03}\eta^3 + C_{20}\xi^2 + C_{11}\xi\eta + C_{02}\eta^2 \\ & + C_{10}\xi + C_{01}\eta + C_{00}, \end{aligned} \tag{4.16}$$

where by complete is meant that all terms up to third order of ξ and η are included. Further, the differentiated profiles $G^n(\xi, \eta) = \partial F^n/\partial\xi$ and $K^n(\xi, \eta) = \partial F^n/\partial\eta$ are found as

$$G^n_{i,j}(\xi, \eta) = 3C_{30}\xi^2 + 2C_{21}\xi\eta + C_{12}\eta^2 + 2C_{20}\xi + C_{11}\eta + C_{10} \tag{4.17}$$

$$K^n_{i,j}(\xi, \eta) = C_{21}\xi^2 + 2C_{12}\xi\eta + 3C_{03}\eta^2 + C_{11}\xi + 2C_{02}\eta + C_{01}. \tag{4.18}$$

The polynomial in (4.16) contains ten unknown coefficients that must be determined. These coefficients are found using the constraints $F^n(\xi_p, \eta_q) = f^n_{p,q}$, with (p, q) being the indices of the four nodes describing the upwind cell and ξ_p and η_q the corresponding cell coordinates. Further, $G^n(\xi_p, \eta_q) = g^n_{p,q}$ and $K^n(\xi_p, \eta_q) = k^n_{p,q}$ are used for the three nodes $(p, q) = (i, j), (iw, j)$ and (i, jw). This yields a total of ten constraints. If also the spatial derivatives at the fourth node (iw, jw) were used, we would have twelve constraints but only ten unknowns. Thus, two more terms must be added to the polynomial (4.16) if the spatial derivatives at the fourth node are to be used. However, the additional terms would be of fourth order and are neglected in our numerical model. When the interpolation profile $F^n_{i,j}$ is found, the solution to the linear advection equation (4.13) is obtained as

$$f^{n+1}_{i,j} = F^n_{i,j}(-u\Delta t, -v\Delta t) \tag{4.19}$$

For the spatial derivatives, a two-step time-splitting approach is used as follows. First, due to pure advection of the spatial derivatives we get

$$g^*_{i,j} = G^n_{i,j}(-u\Delta t, -v\Delta t) \tag{4.20}$$

$$k^*_{i,j} = K^n_{i,j}(-u\Delta t, -v\Delta t), \tag{4.21}$$

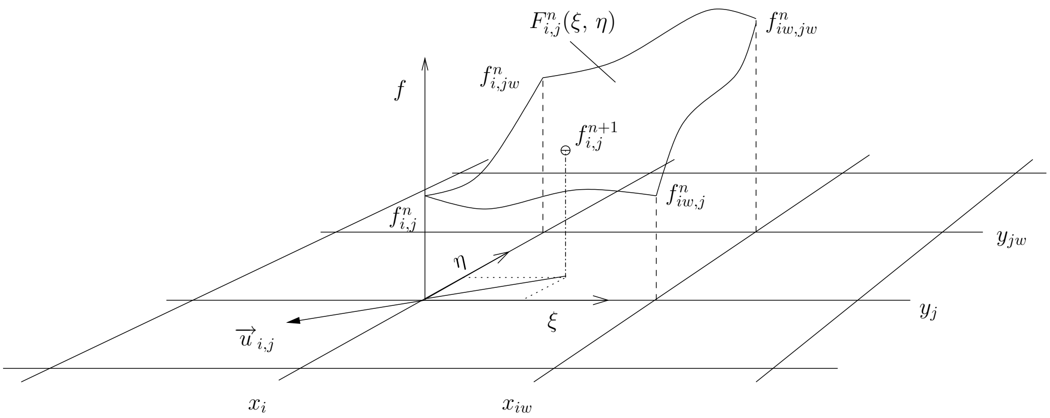

Figure 4.4: CIP-method in two-dimensions where a cubic polynomial surface $F^n_{i,j}(\xi,\,\eta)$ is constructed using ten constraints and then shifted according to the solution of the constant coefficient linear advection equation to obtain $f^{n+1}_{i,j}$.

which conserves the shape of the differentiated profile. However, due to the varying velocity field the shape of the differentiated profile will be modified. This is represented by the source terms on the RHS of (4.14) and (4.15). Updating the derivatives for the source terms yields

$$g^{n+1}_{i,j} = g^*_{i,j} - \Delta t\left(\frac{\partial u}{\partial x}\tilde{g}^n_{i,j} + \frac{\partial v}{\partial x}\tilde{k}^n_{i,j}\right) \tag{4.22}$$

$$k^{n+1}_{i,j} = k^*_{i,j} - \Delta t\left(\frac{\partial u}{\partial y}\tilde{g}^n_{i,j} + \frac{\partial v}{\partial y}\tilde{k}^n_{i,j}\right), \tag{4.23}$$

where the spatial derivatives of the velocity is evaluated using central differences. Due to the staggered grid, the actual stencil for differentiation depends on which variable is being advected. The A-type CIP-method is illustrated in Fig. 4.4. As for the 1D CIP-method, no rigorous stability analysis is performed for the 2D CIP-scheme. However, the 1D stability criterion ($CFL < 1$) is used for each of the two spatial directions. Usually, $CFL < 0.5$ is used in practice.

Generally, both the 1D and 2D approach can be summarized as follows. For each node of computation:

1. Locate upwind cell based on the total velocity in the node considered

2. Approximate the advected variable in the upwind cell by constructing a cubic polynomial curve/surface using the node values of the advected variable and its spatial derivatives as constraints

3. Shift the approximated profile according to the analytical solution of the linear constant coefficient advection equation

4. Find new spatial derivatives by shifting the differentiated profile and adding source terms

5. Update variables

4.3 Solving the Navier-Stokes equations

The Naviér-Stokes equations are solved using finite differences on a Cartesian staggered grid. A fractional step approach with an incremental pressure-projection method is applied to step the solution forward in time, as already described. The different steps will be explained more in detail in the following.

4.3.1 Advection step

The first task in the fractional step approach used here is to solve the advection equation for the horizontal and vertical velocity component. The advection of fluid momentum implies we have to solve the following nonlinear advection equations

$$\frac{\partial u}{\partial t} + u\frac{\partial u}{\partial x} + v\frac{\partial u}{\partial y} = 0 \tag{4.24}$$

$$\frac{\partial v}{\partial t} + u\frac{\partial v}{\partial x} + v\frac{\partial v}{\partial y} = 0. \tag{4.25}$$

These equations are hard to solve. However, if we use the method of frozen coefficients (see e.g. Strikwerda (2004)), we can approximate the nonlinear equations (4.24) and (4.25) to obtain the linear equations

$$\frac{\partial u}{\partial t} + \overline{u}\frac{\partial u}{\partial x} + \overline{v}\frac{\partial u}{\partial y} = 0 \tag{4.26}$$

$$\frac{\partial v}{\partial t} + \overline{u}\frac{\partial v}{\partial x} + \overline{v}\frac{\partial v}{\partial y} = 0, \tag{4.27}$$

where $\overline{u}$ and $\overline{v}$ are constant in time during the small time interval of length Δt. The velocity components $\overline{u}$ and $\overline{v}$ are evaluated at the node of computation, using the velocity field $\boldsymbol{u}^n$. For the evolution of the spatial derivatives of the advected velocity components, we solve (4.14) and (4.15). Then, using Eqs.(4.19-4.23) the advected variable $\boldsymbol{u}^*$ and its spatial derivatives $\boldsymbol{g}^*$ and $\boldsymbol{k}^*$ after advection are found.

4.3.2 Diffusion step

Due to the viscosity of the fluid, diffusion of fluid momentum will occur. Central differences are used for the spatial discretization of the viscous stress terms. When using the non-conservative formulation of the Naviér-Stokes equations, the diffusion equations for the two spatial directions are coupled. For this we introduce the indices E, W, N, S referring to points to the East, West, North and South relative to the node of computation. At these points, the kinematic viscosity coefficient ν and the derivatives of the horizontal and vertical velocity components are to be computed. First we consider diffusion of the horizontal velocity component, which can be written

$$\begin{aligned}\tilde{u}^{**}_{i,j} = u^*_{i,j} + \frac{\Delta t}{\rho_c}\Bigg(&\frac{2}{\Delta x c_i}\left(\mu_E \frac{\partial u^*}{\partial x}\bigg|_E - \mu_W \frac{\partial u^*}{\partial x}\bigg|_W\right)\\ &+ \frac{1}{\Delta y_i}\left(\mu_N\Big(\frac{\partial u^*}{\partial y}\bigg|_N + \frac{\partial v^*}{\partial x}\bigg|_N\Big) - \mu_S\Big(\frac{\partial u^*}{\partial y}\bigg|_S + \frac{\partial v^*}{\partial x}\bigg|_S\Big)\right)\Bigg).\end{aligned} \tag{4.28}$$

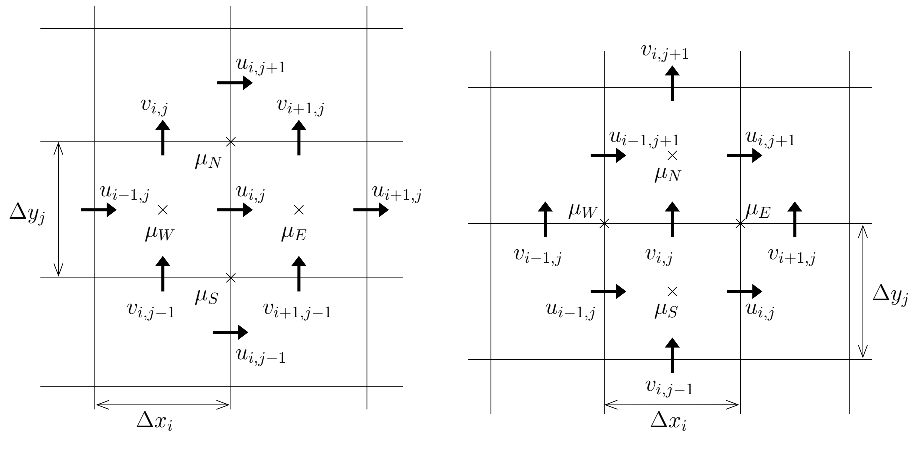

(a) (b)

Figure 4.5: Variables involved in the diffusion calculation for (a) the horizontal velocity component and (b) the vertical velocity component. The dynamic viscosity coefficient is approximated at the points marked with a cross.

Similarly, for the vertical velocity component we get the following expression for the diffusion calculation, including the effect of gravity,

$$\begin{aligned}\tilde{v}^{**}_{i,j} = v^*_{i,j} + \frac{\Delta t}{\rho_c}\Bigg(&\frac{1}{\Delta x_i}\left(\mu_E\left(\frac{\partial u^*}{\partial y}\bigg|_E + \frac{\partial v^*}{\partial x}\bigg|_E\right) - \mu_W\left(\frac{\partial u^*}{\partial y}\bigg|_W + \frac{\partial v^*}{\partial x}\bigg|_W\right)\right)\\ &+ \frac{2}{\Delta yc_i}\left(\mu_N\frac{\partial v^*}{\partial y}\bigg|_N - \mu_S\frac{\partial v^*}{\partial y}\bigg|_S\right)\Bigg) - g\Delta t,\end{aligned} \tag{4.29}$$

where g is the acceleration of gravity. Details on the evaluation of the kinematic viscosity and the velocity derivatives are given in appendix A.2. The computational stencils corresponding to (4.28) and (4.29) are illustrated in Fig. 4.5.

When the explicit Euler method is used to time step the effect of the diffusion equation, there is a stability constraint that must be satisfied. This stability constraint can be found from a von Neumann analysis (Roache 1976; Strikwerda 2004). However, due to the change of material properties across the free surface, this is not an easy task. If we consider the different phases separately, the following stability constraint for the diffusion step is obtained

$$\frac{\mu\Delta t}{\rho}\left(\frac{1}{\Delta x^2_{min}} + \frac{1}{\Delta y^2_{min}}\right) \leq \frac{1}{2}. \tag{4.30}$$

This constraint on the stability of the solution can be removed by using an implicit method for the time integration, like the second order Crank-Nicolson method.

4.3.3 Pressure coupling

In the pressure projection method suggested by Chorin, a Poisson equation for the total pressure is solved. Then the pressure is used to project the velocity field onto a plane of zero divergence. For methods classified by Brown et al. (2001) as incremental pressure projection methods, the velocity field is first updated with the old pressure field p^n to obtain a better prediction of the velocity field before the projection is performed. Updating the velocity field with the old pressure is done by

$$u^{**}_{i,j} = \tilde{u}^{**}_{i,j} - \frac{\Delta t}{0.5(\rho_{i,j} + \rho_{i+1,j})} \frac{p^n_{i+1,j} - p^n_{i,j}}{\Delta xc_i} \tag{4.31}$$

$$v^{**}_{i,j} = \tilde{v}^{**}_{i,j} - \frac{\Delta t}{0.5(\rho_{i,j} + \rho_{i,j+1})} \frac{p^n_{i,j+1} - p^n_{i,j}}{\Delta yc_i}. \tag{4.32}$$

Then the projection step is done with the incremental change in pressure $\delta p^{n+1} = p^{n+1} - p^n$ from time step n to the next time step $n+1$. Consider the velocity update due to the incremental pressure gradient, which is

$$\frac{\boldsymbol{u}^{n+1} - \boldsymbol{u}^{**}}{\Delta t} = -\frac{1}{\rho} \nabla \delta p^{n+1} \tag{4.33}$$

Now, taking the divergence of (4.33) and imposing the continuity constraint $\nabla \cdot \boldsymbol{u}^{n+1} = 0$, the unknown velocity $\boldsymbol{u}^{n+1}$ is removed from the equation and we obtain a Poisson equation for the incremental pressure δp^{n+1} as

$$\frac{\nabla \cdot \boldsymbol{u}^{**}}{\Delta t} = \nabla \cdot \left(\frac{1}{\rho} \nabla \delta p^{n+1} \right). \tag{4.34}$$

Due to the one-fluid formulation which implies that the fluid density in the domain is non-constant, Eq. (4.34) is more precisely a variable-coefficient Poisson equation. Hence, the coefficient matrix must be calculated for each time step. When the Poisson equation for the incremental pressure is solved using a suitable solver (which will be described more in detail below), the tentative velocity field $\boldsymbol{u}^{**}$ is updated using the incremental pressure gradient to give the velocity field at the next time step $\boldsymbol{u}^{n+1}$. Hence,

$$u^{n+1}_{i,j} = u^{**}_{i,j} - \frac{\Delta t}{0.5(\rho_{i,j} + \rho_{i+1,j})} \frac{\delta p^n_{i+1,j} - \delta p^n_{i,j}}{\Delta xc_i} \tag{4.35}$$

$$v^{n+1}_{i,j} = v^{**}_{i,j} - \frac{\Delta t}{0.5(\rho_{i,j} + \rho_{i,j+1})} \frac{\delta p^n_{i,j+1} - \delta p^n_{i,j}}{\Delta yc_i}. \tag{4.36}$$

The new velocity field $\boldsymbol{u}^{n+1}$ will now satisfy the continuity equation (3.4). Further is the pressure for the next time step found as

$$p^{n+1}_{i,j} = p^n_{i,j} + \delta p^{n+1}_{i,j}. \tag{4.37}$$

4.3.4 Solving a Poisson equation for the incremental pressure

The variable-coefficient incremental-pressure Poisson equation can be discretized to give

$$\frac{1}{\Delta x_i} \left(\frac{\delta p_{i+1,j} - \delta p_{i,j}}{\rho_{i+1/2,j} \Delta xc_i} - \frac{\delta p_{i,j} - \delta p_{i-1,j}}{\rho_{i-1/2,j} \Delta xc_{i-1}} \right) + \frac{1}{\Delta y_j} \left(\frac{\delta p_{i,j+1} - \delta p_{i,j}}{\rho_{i,j+1/2} \Delta yc_j} - \frac{\delta p_{i,j} - \delta p_{i,j-1}}{\rho_{i,j-1/2} \Delta yc_{j-1}} \right) = \frac{1}{\Delta t} \left(\frac{u^{**}_{i,j} - u^{**}_{i-1,j}}{\Delta x_i} + \frac{v^{**}_{i,j} - v^{**}_{i,j-1}}{\Delta y_j} \right) \tag{4.38}$$

where $\rho_{i+1/2,j}$ is the fluid density evaluated at the velocity node at the right cell boundary, i.e. at the velocity node $u_{i,j}$. Similarly, $\rho_{i-1/2,j}$ corresponds to the density at $u_{i-1,j}$, while $\rho_{i,j+1/2}$ and $\rho_{i,j-1/2}$ corresponds to the density at the velocity nodes $v_{i,j}$ and $v_{i,j-1}$, respectively. The Poisson equation is an elliptical equation, which means that boundary conditions for the incremental pressure must be specified. We consider two types of boundary conditions. These are the Neumann condition for which the normal velocity is specified on boundary, and the Dirichlet condition where the pressure is specified on the boundary. By setting $\boldsymbol{n} \cdot \boldsymbol{u}^{**} = \boldsymbol{n} \cdot \boldsymbol{u}^{n+1}$ on the boundary, the Neumann condition is expressed as $\boldsymbol{n} \cdot \nabla(\delta p^{n+1}) = 0$. This is applied for the rigid wall boundaries. At the upper boundary, the pressure is atmospheric, meaning the imposed pressure on the boundary is constant in time, i.e. $p^{n+1} = p^n$. This leads to the Dirichlet boundary condition $\delta p^{n+1} = 0$.

Equation (4.38) represents the linear system

$$\mathbf{Ax} = \mathbf{b}, \tag{4.39}$$

where $\mathbf{x}$ is a vector of the unknown pressure increment, $\mathbf{A}$ is the coefficient matrix due to the discretization and $\mathbf{b}$ is the divergence of the tentative velocity field, i.e. the right hand side of (4.38). How to obtain the coefficient matrix $\mathbf{A}$ is described in appendix A.3. The system of equations can be very large, which implies that a direct solver would be inefficient. Thus, an iterative solver is used to solve (4.39). Further, the coefficient matrix $\boldsymbol{A}$ will due to the discretization be non-symmetric when nonuniform grids are used. This puts additional requirements to the iterative solver. An efficient solver that is able to handle systems where the coefficient matrix is non-symmetric is the Bi-CGSTAB algorithm (van der Vorst 1992), which will be used here. Due to the moving free surface and the fact that the coefficient matrix depends on the fluid density, the coefficient matrix must be calculated at every time step. Another aspect of the moving free surface is that the large variation of the density causes the eigenvalues λ_i of the coefficient matrix $\boldsymbol{A}$ to be wide spread along the real axis. Hence, the condition number $\kappa = |\lambda_{max}/\lambda_{min}|$ is large and the system is called stiff which means hard to solve. In order to gain faster convergence of the iteration process, preconditioning of the equation system is favorable. Preconditioning means that instead of solving the system represented by (4.39), we solve a modified system

$$\mathbf{M^{-1}Ax} = \mathbf{M^{-1}b}, \tag{4.40}$$

where $\boldsymbol{M}$ is a preconditioning matrix that approximates $\boldsymbol{A}$ and where the inverse matrix $\boldsymbol{M}^{-1}$ is easy to compute. We will use a simple precondition algorithm called D-ILU that has shown to work well with Bi-CGSTAB (Barrett et al. 1994). Algorithms for the preconditioned Bi-CGStab method and the D-ILU preconditioner are given in appendix A.3.

4.4 Free surface capturing

When solving two-phase flow with a one-fluid model using an embedded grid method, the free surface must be captured for each time step to know the material properties in the node of computation. There exist several methods for free surface capturing. The MAC scheme (Harlow and Welch 1965) is such a method which can treat complex phenomena like wave breaking. In the MAC scheme, marker particles which are advected with the flow are used to capture the free surface. However, the computational effort is large since one has to keep track on a large number of marker particles. Another popular method is the Volume of Fluid (VOF) method by Hirt and Nichols (1981). This method makes use of a density function which numerical value is the area fraction occupied by the liquid in each cell. The density function is then used to give a cell-averaged estimate of the mass density and viscosity of the fluid. A transport equation for the evolution of density function is solved for the whole domain to locate the free surface. The momentum and mass conservation equations are then solved for the liquid phase only. A problem with such methods is that due to the discontinuity of the density function at the interface, the density function will be smeared out here when using a low-order method to solve the transport equation. Using higher-order methods may lead to over-shoot or under-shoot of the density function. This problem is avoided by the *level-set* method introduced by Osher and Sethian (1988). In the level-set method, a distance function is introduced. The distance function is a scalar function which value is the shortest distance to the free surface which is in the normal direction to the surface. An advantage of the signed distance function is that it is smooth such that problems related to numerical diffusion and over- or undershoot, which are typical issues for methods applying pure density functions, are avoided. Applications and further details of the level-set method are described in Osher and Fedkiw (2003).

In the present work, we have used *color functions* for free surface capturing. This is a similar approach as the VOF-method.

4.4.1 Color functions

Similar as the density function in the VOF-method, also the color function can be considered as a cell averaged density function. We will use one color function for each phase present in the domain, here represented by the water (liquid phase), the air (gas phase) and the floating body (solid phase). The color functions for the water, the air and the floater are denoted φ_1, φ_2 and φ_3, respectively. As the node value of a color function represents the area fraction of a grid cell that is occupied by a given phase, all color functions takes a value $\varphi_k \in [0, 1]$, where $k = 1, 2, 3$. Further, the following condition is enforced

$$\sum_{k=1}^{3} \varphi_k = 1. \tag{4.41}$$

The color function can be considered as a cell averaged material property for the phase it represents and thus the color function for water φ_1 is advected with the flow. This means that the time evolution of φ_1 is described by (3.7), which is solved using the CIP-method. The color function for the solid body is found directly when the position and orientation of the solid body are known. This is described more detailed in the next section. When the color functions φ_1 and φ_3 are found, the color function for the air φ_2 can be obtained from (4.41).

When advecting a step-like function with the CIP-procedure, the advected function will smear out at the step due to numerical diffusion and due to representation of a discontinuous function by a cubic polynomial. This smearing may also cause a wrong phase speed of the contour represented by $\varphi_1 = 0.5$, which defines the free surface. To reduce this effect, the color function φ_1 is replaced by a transformed color function $\Phi(\varphi_1)$

when solving (3.7). After the advection calculation, the color function φ_1 is recovered by the inverse transform $\varphi_1 = \Phi^{-1}$. Different transforms are used in the literature. Yabe et al. (2001) introduced a tangent transform and its inverse function defined as

$$\Phi = \tan\left(\pi(1-\varepsilon)(\varphi_1 - 0.5)\right) \tag{4.42}$$

$$\varphi_1 = \frac{\tan^{-1}\Phi}{\pi(1-\varepsilon)} + 0.5. \tag{4.43}$$

Here ε is a small positive constant which is used to tune the thickness of the air-water interface. Usually, $\varepsilon = 0.02$ is used. Since the tangent function represents an additional computational cost, a simpler linear transform was proposed by Hu et al. (2005)

$$\Phi = 0.5 + \alpha(\varphi_1 - 0.5) \tag{4.44}$$

$$\varphi_1 = 0.5 + (\Phi - 0.5)/\alpha, \tag{4.45}$$

with the tuning parameter $\alpha = 1.2$. Both the tangent transform and the linear transform are implemented in our numerical model. However, in all cases presented the linear transform is used. A parameter study for different color function transforms used in free surface capturing with the CIP-method is presented in Vestbøstad (2009).

After advection of the transformed color function Φ and when the inverse transform has been applied to obtain φ_1^{n+1}, eventually overshoots or undershoots of φ_1^{n+1} that usually occur when advecting a step-like function using a higher order method are removed. This is done by setting $\varphi^{n+1} = 1$ if $\varphi^{n+1} > 1$ and $\varphi^{n+1} = 0$ if $\varphi^{n+1} < 0$. Then, the density and viscosity of the fluid in a given cell is computed as

$$\rho = \sum_{k=1}^{3} \rho_k \varphi_k \quad \text{and} \quad \mu = \sum_{k=1}^{3} \mu_k \varphi_k, \tag{4.46}$$

where ρ_k and μ_k are the mass density and dynamic viscosity coefficients for the phase k, respectively. For the grid cells occupied by the solid body, fictitious coefficients for the mass density and dynamic viscosity are used with values equal to those of water.

4.5 Introduction of the floating body

Introduction of a solid body with arbitrary geometry into the computational domain needs special treatment when a Cartesian grid is used. Since the Cartesian grid cannot conform to an arbitrary geometry, the velocity nodes will in general not be located on the body surface. This means that imposing the body boundary condition on the floating body would require special treatment. Methods that deals with the problem of imposing boundary conditions on arbitrary geometries when using Cartesian grids are called *immersed boundary methods* and was first introduced by Peskin (1972) for representing the effect of an elastic membrane of a heart valve on the blood flow. The main feature of immersed boundary methods is that an extra body force is added to the momentum equations in the vicinity of the body boundary to represent the effect of the solid body on the fluid flow. Other approaches using the same concept have later been introduced, and today immersed boundary methods are widely used for many applications. Review of immersed boundary methods are given by Mittal and Iaccarino (2005) and de Tullio et al. (2006).

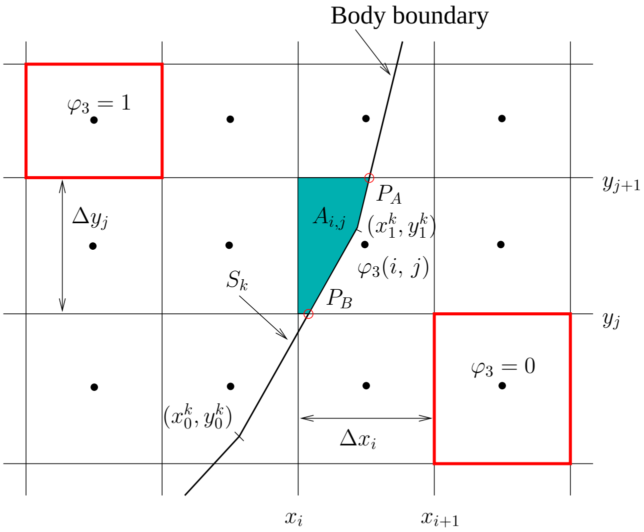

Figure 4.6: Computation of the color function $\varphi_3(i, j)$ representing the solid body. The intersection points P_A and P_B between the body geometry and the Cartesian grid, which are found by parametrization of the body geometry, is used to compute the area fraction $A_{i,j}$ of the grid cell (i, j) covered by the body.

Mittal and Iaccarino (2005) divides the group of immersed boundary methods into two main approaches, namely *continuous forcing approach* and *discrete forcing approach* depending on how the effects of the immersed boundary are introduced into the governing equations for the fluid flow. In the continuous forcing approach, the forcing is incorporated into the continuous momentum equations before discretization. However, this method involves user-specified parameters in the forcing which is undesirable in addition to problems with instability issues for rigid boundaries. In the discrete forcing approach, the forcing is introduced after the equations are discretized and this method has the major advantage that user-specified parameters in the forcing are avoided. Here we will use a discrete forcing approach similar as the direct forcing method introduced by Mohd-Yusof (1997). Further, we will make use of color functions in the representation of the solid body. This is described in the following.

4.5.1 Representing the solid body using color functions

We use the color function φ_3 to represent the solid body. In the same manner as for the color function φ_1 representing water, the value of $\varphi_3(i, j)$ is defined as the area fraction of the cell with indices (i, j) that is covered by the solid body divided by the total area of the cell. This means $\varphi_3 \in [0, 1]$. Mathematically speaking

$$\varphi_3(i, j) = \frac{A_{i,j}}{\Delta x_i \Delta y_j}, \tag{4.47}$$

where $A_{i,j}$ is the area of cell (i, j) covered by the solid body, as shown in Fig. 4.6. The body geometry is represented by a discrete number of straight line segments S_k with $k = 1, 2, ..., N$. Each line segment is described by the two end points (x_0^k, y_0^k) and (x_1^k, y_1^k). In order to compute the area fraction A of the cell occupied by the solid body, we first need to locate the intersection points (x_c, y_c) between the grid lines and the body boundary. This is done by "walking" along the curve defining the geometry. Each line segment S_k is parametrized using the parameter $t = [0, 1]$, which means that all points located on the line segment S_k is defined by

$$x = x_0^k + (x_1^k - x_0^k)t \tag{4.48}$$

$$y = y_0^k + (y_1^k - y_0^k)t. \tag{4.49}$$

We now find all horizontal grid lines y_j between y_0^k and y_1^k, and all vertical grid lines x_i between x_0^k and x_1^k. These are the grid lines intersected by the line segment S_k. If a vertical grid line is intersected, we know that the horizontal coordinate of the intersection point is $x_c = x_i$. The parameter $t = t_c$ for the intersection point is then found as $t_c = (x_i - x_0^k)/(x_1^k - x_0^k)$ and subsequently the vertical coordinate of the same intersection point is found from (4.49) with $t = t_c$. Similarly, for the intersection of horizontal grid lines $y_c = y_j$ which yields $t_c = (y_j - y_0^k)/(y_1^k - y_0^k)$ and then x_c is found from (4.48) with $t = t_c$. An index vector which tells whether the intersection is with a horizontal grid line or with a vertical grid line is also stored. Now the order of the intersection points as they appear on the line segment can be found by sorting t_c in ascending numerical order. We use a sorting algorithm based on Shell's method for this purpose (Press et al. 1992). Hence, using the sorted vector of intersection indices, we can now follow the curve defining the body geometry through all the intersected cells and compute φ_3 using (4.47). Since the intersection points P_A and P_B are now found, calculation of $A_{i,j}$ is only a matter of geometry.

4.5.2 The body boundary condition

We want to impose the no-slip body boundary condition (3.9) on the immersed boundary, using the direct forcing method similar as that proposed by Mohd-Yusof (1997). The method can be described as follows. Discretized in time with the first order Euler method, the momentum equations (3.5) and (3.6) can in compact form be written as

$$\frac{\boldsymbol{u}^{n+1} - \boldsymbol{u}^n}{\Delta t} = RHS^n, \tag{4.50}$$

where RHS^n contains the convective terms, the viscous terms and the pressure gradient evaluated at time step n. In order to account for the presence of a solid body in the domain, we modify (4.50) by adding a body force $\boldsymbol{f}^n$ on the right hand side, according to the immersed boundary method. This force is nonzero only in the vicinity of the body boundary. This yields,

$$\frac{\boldsymbol{u}^{n+1} - \boldsymbol{u}^n}{\Delta t} = RHS^n + \boldsymbol{f}^n \tag{4.51}$$

Now the question is what this force $\boldsymbol{f}^n$ should be? We note that the purpose of adding $\boldsymbol{f}^n$ to (4.50) is to satisfy $\boldsymbol{u}^{n+1} = \boldsymbol{u}_{\boldsymbol{b}}^{n+1}$ on the body boundary at the new time step $n+1$, where $\boldsymbol{u_b}$ is the rigid body velocity. By substituting $\boldsymbol{u}^{n+1}$ with $\boldsymbol{u}_{\boldsymbol{b}}^{n+1}$ in (4.51) and rearranging, the force $\boldsymbol{f}^n$ is found as

$$\boldsymbol{f}^n = -RHS^n + \frac{\boldsymbol{u}_{\boldsymbol{b}}^{n+1} - \boldsymbol{u}^n}{\Delta t}. \tag{4.52}$$

Implicitly, this means that the effect of the immersed boundary is incorporated by simply updating the velocity nodes of the grid cells that is partly or totally occupied by the solid body according to the rigid body velocity. Different interpolation techniques can be used for this purpose as described by Fadlun et al. (2000). We will use a volume fraction weighting approach, also used by Hu et al. (2005), where the color function φ_3 representing the solid body is utilized to update the velocity nodes of the grid cells occupied by the floating body. This is done by

$$u^{n+1} = \tilde{\varphi}_3 u_b^{n+1} + (1 - \tilde{\varphi}_3) u^{**} \tag{4.53}$$

$$v^{n+1} = \tilde{\varphi}_3 v_b^{n+1} + (1 - \tilde{\varphi}_3) v^{**}, \tag{4.54}$$

where $\tilde{\varphi}_3$ is the color function for the solid body interpolated linearly to the velocity node considered.

It is after the velocity field has been updated according to (4.53) that the projection step is performed and the incremental pressure change δp is found, as described in 4.3.3. When updating the velocity field due to this incremental pressure correction using (4.35) and (4.36), the fluid velocity at the body boundary may be changed such that the body boundary condition is violated. More simply, the obtained pressure correction might cause the fluid to flow through the body surface, yielding an incorrect solution. This has to do with the fact that the force $\boldsymbol{f}^n$ is found using the tentative velocity field $\boldsymbol{u}^{**}$ (Fadlun et al. 2000). However, it has been shown that the pressure corrections at the immersed boundary are always small and that this error can be reduced to round-off by two or three iterations of the time advancement scheme (de Tullio et al. 2006). The iteration process is simply that after the first update of the velocity field due to the incremental pressure correction, the body boundary condition is again imposed using (4.53) before a final pressure projection step for the incremental pressure is performed. Our experience is that two iterations are sufficient for this approach.

4.6 Pressure loads on the solid body

When the pressure field at the new time step is known, the pressure forces and moments on the solid body can be computed using a discretized version of (3.18) and (3.19), respectively, with φ being the color function describing the solid body, φ_3. In the mathematical formulation of the pressure force given by Eq. (3.18), the integral is over the complete domain. However, since $\varphi_3 = 0$ outside the solid body boundary, we can make the numerical procedure more efficient by taking the double sum only over a sub-domain enclosing the solid body. This sub-domain is limited by the indices $(i1, i2)$ in the horizontal direction and $(j1, j2)$ in the vertical direction. For the pressure forces, this leads to

$$F_x^n = -\sum_{i=i1}^{i2} \sum_{j=j1}^{j2} \frac{\partial p^n}{\partial x}\Big|_{i,j} \varphi_{i,j} \, \Delta x_i \Delta y_j, \tag{4.55}$$

$$F_y^n = -\sum_{i=i1}^{i2} \sum_{j=j1}^{j2} \frac{\partial p^n}{\partial y}\Big|_{i,j} \varphi_{i,j} \, \Delta x_i \Delta y_j, \tag{4.56}$$

where

$$\left.\frac{\partial p^n}{\partial x}\right|_{i,j} = \frac{\Delta xc_i\, p^n_{i+1,j}}{\Delta xc_{i+1}(\Delta xc_{i+1} + \Delta xc_i)} - \frac{(\Delta xc_{i+1} - \Delta xc_i)\, p^n_{i,j}}{\Delta xc_i \Delta xc_{i+1}} + \frac{\Delta xc_{i+1}\, p^n_{i-1,j}}{\Delta xc_i(\Delta xc_{i+1} + \Delta xc_i)}$$

$$\left.\frac{\partial p^n}{\partial y}\right|_{i,j} = \frac{\Delta yc_j\, p^n_{i,j+1}}{\Delta yc_{j+1}(\Delta yc_{j+1} + \Delta yc_j)} - \frac{(\Delta yc_{j+1} - \Delta yc_j)\, p^n_{i,j}}{\Delta yc_j \Delta yc_{j+1}} + \frac{\Delta yc_{j+1}\, p^n_{i,j-1}}{\Delta yc_j(\Delta yc_{j+1} + \Delta yc_j)}.$$

Here, the pressure gradients are correct to $\mathcal{O}(\Delta x^2)$ and $\mathcal{O}(\Delta y^2)$ on a stretched staggered grid. The roll moment due to the fluid pressure acting on the body surface is calculated as

$$M^n = -\sum_{i=i1}^{i2}\sum_{j=j1}^{j2}\left((xc_i - x_b)\left.\frac{\partial p^n}{\partial y}\right|_{i,j} - (yc_j - y_b)\left.\frac{\partial p^n}{\partial x}\right|_{i,j}\right)\varphi_{i,j}\,\Delta x_i \Delta y_j, \tag{4.57}$$

where (x_b, y_b) are the coordinates of the centre of gravity of the solid body.

4.6.1 Rigid body motions

The instantaneous body position and orientation is defined by the coordinates of the geometrical center of the body (x_b, y_b) and the roll angle θ. If the center of gravity is located at the geometrical center of the body, the rigid body translatory motions can be found upon integration of (3.20) and (3.21). Further is the roll angle found by integration of (3.22). Assuming the pressure forces and moments are constant during a time interval $\Delta t = t^{n+1} - t^n$, we find the instantaneous rigid body velocities in heave sway and roll as

$$U_b^{n+1} = U_b^n + \Delta t F_x^n/m \tag{4.58}$$
$$V_b^{n+1} = V_b^n + \Delta t F_y^n/m \tag{4.59}$$
$$\dot\theta^{n+1} = \dot\theta^n + \Delta t M^n/I, \tag{4.60}$$

where m is the structural mass per unit length of the body while I is the roll inertia about the center of gravity. If we assume constant body accelerations during the time step Δt, this implies that the body velocities in the same time interval are linearly varying. Hence, using the trapezoidal rule of integration, we find the coordinates of the mass center of the body (x_b, y_b) at the next time step t^{n+1} as

$$x_b^{n+1} = x_b^n + \frac{\Delta t}{2}\left(U_b^{n+1} + U_b^n\right) \tag{4.61}$$
$$y_b^{n+1} = y_b^n + \frac{\Delta t}{2}\left(V_b^{n+1} + V_b^n\right) \tag{4.62}$$
$$\theta^{n+1} = \theta^n + \frac{\Delta t}{2}\left(\dot\theta^{n+1} + \dot\theta^n\right) \tag{4.63}$$

Now we can find the instantaneous position of the discrete set of points (x_k^{n+1}, y_k^{n+1}) describing the body boundary at time step t^{n+1} as

$$x_k^{n+1} = x_b^{n+1} + (x_k^0 - x_b^0)\cos\theta^{n+1} - (y_k^0 - y_b^0)\sin\theta^{n+1} \tag{4.64}$$
$$y_k^{n+1} = y_b^{n+1} + (x_k^0 - x_b^0)\sin\theta^{n+1} + (y_k^0 - y_b^0)\cos\theta^{n+1}, \tag{4.65}$$

where (x_k^0, y_k^0) are the initial (reference) positions of the set of points defining the body boundary, and (x_b^0, y_b^0) is the initial position of the body centre.

4.7 Time-stepping of the spatial derivatives in the CIP flow solver

When the advection step in the adopted fractional step method is performed, a tentative velocity field $\boldsymbol{u}^*$ and a corresponding set of tentative spatial derivatives $\boldsymbol{g}^*$ and $\boldsymbol{k}^*$ of the velocity field are obtained, where $\boldsymbol{g} = \partial \boldsymbol{u}/\partial x$ and $\boldsymbol{k} = \partial \boldsymbol{u}/\partial y$. After the advection step, the velocity field is updated due to the diffusion step, the pressure coupling and due to the presence of the floater, before the velocity field $\boldsymbol{u}^{n+1}$ for the new time step is obtained. These updates of the velocity field imply possible changes to the spatial derivatives of the velocity field. As the spatial derivatives of the velocity field are used as constraints when constructing the interpolation polynomial in the CIP-method, the spatial derivatives $\boldsymbol{g}^*$ and $\boldsymbol{k}^*$ must be updated according to the modifications of the velocity field to obtain $\boldsymbol{g}^{n+1}$ and $\boldsymbol{k}^{n+1}$, before a new advection step can be made. Time-stepping of the spatial derivatives are performed using the explicit Euler method. For the case of $\boldsymbol{g}$, we can formally write the time stepping as $\boldsymbol{g}^{n+1} = \boldsymbol{g}^* + \Delta t \left(\frac{\partial \boldsymbol{g}}{\partial t}\right)$. As the new velocity field $\boldsymbol{u}^{n+1}$ is known, we can approximate the time derivative as $\frac{\partial \boldsymbol{g}}{\partial t} = \frac{1}{\Delta t}\left[\left(\frac{\partial \boldsymbol{u}}{\partial x}\right)^{n+1} - \left(\frac{\partial \boldsymbol{u}}{\partial x}\right)^{*}\right]$. The same approach is used for the time-stepping of $\boldsymbol{k}$. Hence, we obtain

$$\boldsymbol{g}^{n+1} = \boldsymbol{g}^* + \left[\left(\frac{\partial \boldsymbol{u}}{\partial x}\right)^{n+1} - \left(\frac{\partial \boldsymbol{u}}{\partial x}\right)^{*}\right] \tag{4.66}$$

$$\boldsymbol{k}^{n+1} = \boldsymbol{k}^* + \left[\left(\frac{\partial \boldsymbol{u}}{\partial y}\right)^{n+1} - \left(\frac{\partial \boldsymbol{u}}{\partial y}\right)^{*}\right]. \tag{4.67}$$

Central differences are used to compute the spatial derivatives inside the parenthesis directly from the tentative velocity field $\boldsymbol{u}^*$ and from the new velocity field $\boldsymbol{u}^{n+1}$. The discretized expressions for time-stepping of the spatial derivatives are given in appendix A.4.

4.8 Numerical modelling of a wave tank

A damping zone is introduced by an adding a volume force f_y to the momentum equation for the vertical direction (Hu and Kashiwagi 2004). This force is calculated as

$$f_y = \frac{1}{2\Delta t}\left(\frac{xc_i - x_s}{x_e - x_s}\right)^4 \left(1 - \left|\frac{y_j - h}{H}\right|\right) v_{i,j}^n, \tag{4.68}$$

where x_s and x_s is the start and end points of the damping zone in the horizontal direction, while H is the height of the domain, h is the water depth and (xc_i, y_j) is the coordinates of the vertical velocity node.

The wavemaker is modelled in a linear manner by setting the nodes of the horizontal velocity at the wavemaker boundary equal to the paddle velocity. Thus, when the wavemaker is located on the left side of the domain, we get

$$u_{0,j}^{n+1} = u_{wm}^{n+1}. \tag{4.69}$$

The wavemaker velocity is imposed on the total height H of the domain, i.e. for $y = [0, H]$.

Chapter 5

Verification studies

Verification studies are important activities in the process of developing a CFD-code, and rigorous testing of the flow solver is the key to obtain a reliable code. A validation study of the verified computer program is also necessary before the code is applied to real problems. In this chapter, the most important verification tests performed in the development of the present code are presented. Before we go on with presenting the different test studies, we will explain what is meant by verification and validation and what is the difference between the two. Guidelines for validation and verification of CFD-codes were proposed in ITTC (1990) with the following definitions of verification and validation:

Verification of a computer program means to check that the program is actually a correct representation of the mathematical model that forms the basis for it.

Validation is the demonstration that the verified computer program is an adequate representation of the physical reality.

This means that validation is a broader activity which includes verification. Other definitions of verification and validation presented by Roache (1976) are that verification "is the process of demonstrating that a computer program has solved its equations correctly", while validation "is the process of demonstraing that a computer code is solving the correct equations". The latter is with respect to the physical problem being studied. Thus, verification is a purely mathematical exercise that does not address the physics.

We will in the following present some of the verification test studies that have been performed for testing the present numerical code.

5.1 Error norms and order of convergence

In the process of verifying the implemented flow solver, each step in the numerical algorithm represented by the fractional step procedure, is studied separately. For each case, ideal time-dependent problems where analytical or exact solutions exist are solved numerically and compared with the exact solution at a fixed time instant $T = N\Delta t$. We will let $\hat{\mathbf{u}}^N$ refer to the numerical solution to the given problem at a discrete set of points in space for the time instant T, while $\mathbf{u}^N$ is the corresponding exact solution for the same set of points at this time instant, which we want to approximate well. The local error $\mathbf{E}^N$ for the solution time $T = N\Delta t$ is defined as

$$\mathbf{E}^N = \hat{\mathbf{u}}^N - \mathbf{u}^N. \tag{5.1}$$

In order to quantify this error, a norm in which to measure the error must be chosen. The global error can be found by integration of the local error over the domain of computation.

5.1.1 Choice of error norms

To measure the error of a numerical solution obtained with some finite difference scheme relative to an exact solution, the standard $p-$norms are most commonly used (LeVeque 2002). For one-dimensional space, these are

$$\left\|\mathbf{E}^N\right\|_p = \left(\sum_i |\hat{u}_i^N - u_i^N|^p \Delta x_i\right)^{1/p}. \tag{5.2}$$

We will in the following use the 1-norm, which is obtained by setting $p = 1$ in (5.2), as a measure of the global error when solving the linear and nonlinear advection equation. For verification of the diffusion step and the pressure solver, the 2-norm (obtained by setting $p = 2$) will be used. In 2D, the global error is found by integration the local error over the domain of computation as

$$\left\|\mathbf{E}^N\right\|_p = \left(\sum_j \sum_i |\hat{u}_{ij}^N - u_{ij}^N|^p \Delta x_i \Delta y_j\right)^{1/p}. \tag{5.3}$$

To simplify the notation, we will let ε_p refer to the error measure $\left\|\mathbf{E}^N\right\|_p$.

5.1.2 Order of convergence

As an indicator for how fast the numerical solution approach the true solution, we speak of the order of convergence. We can apply the concept of order of convergence if the time increment Δt is related to the spatial increment Δx in a fixed manner. Hence, when solving the advection equation, the time step Δt is chosen such that the Courant-Friedrichs-Lewy (CFL) number is kept constant when the grid is refined. Here, the CFL-number is defined as $\mathrm{CFL} = u\Delta t/\Delta x$, with u being some reference velocity. Then the order of convergence of the solution $\hat{\mathbf{u}}^N$ is defined to be the number r, if it exists, such that the errors ε_p vanish like $\mathcal{O}(\Delta x^r)$ or as $\mathcal{O}(\Delta t^r)$ (Strikwerda 2004). This implies that the error can be described as $\varepsilon_p = C\Delta x^r$, with C being a constant. Taking the natural logarithm of both sides yields

$$\ln(\varepsilon_p) = \ln(C) + r\ln(\Delta x). \tag{5.4}$$

To find the order of convergence r, we must get rid of the unknown coefficient C. Let ε_p^1 be the error of the numerical solution obtained on a grid represented by the grid increment Δx_1. Further, let ε_p^2 be the error obtained from the finer grid represented by Δx_2. The unknown coefficient C can now be removed by subtracting Eq. (5.4) expressed in terms of ε_1 and Δx_1 from the same equation with ε_2 and Δx_2. Then, the order of convergence in 1D is found as

$$r = \frac{\ln\left(\varepsilon_p^2/\varepsilon_p^1\right)}{\ln(\Delta x_2/\Delta x_1)}. \tag{5.5}$$

For the 2D case, we assume that the vertical discretization is related to the horizontal discretization as $\Delta y = K\Delta x$, where K is a constant. Then, the order of convergence in 2D can be expressed as

$$r = \frac{\ln\left(\varepsilon_p^2/\varepsilon_p^1\right)}{2\ln\left(\Delta x_2/\Delta x_1\right)}. \tag{5.6}$$

5.2 Verification of the 1D CIP-method

Although the 1D-formulation of the CIP-method is not used as a part of the present flow-solver, it has been implemented in order to get a better understanding of the CIP-method in general before going on with the CIP-method in two spatial dimensions. Two verification tests of the 1D CIP-method are presented in the following. First, a linear advection problem is studied, while thereafter a non-linear advection problem is addressed.

5.2.1 Linear advection

First we will consider the case of linear advection where a function $f(x,t)$ is transported with the velocity u along the $x-$axis. By linear advection is meant that the transport velocity u is independent of the advected variable f. The spatial derivative $g = \partial f/\partial x$ is introduced as an additional free variable. We will investigate how the function f and its spatial derivative g evolves while being advected with the velocity $u(x) = x$. Consider the initial condition $f(x,0) = f_0(x)$ being defined as

$$f_0(x) = \begin{cases} \sin^2(2\pi x), & 0 < x < 0.5 \\ 0, & \text{otherwise} \end{cases} \tag{5.7}$$

which means that $g(x,0) = g_0(x)$ is described by

$$g_0(x) = \begin{cases} 4\pi\sin(2\pi x)\cos(2\pi x), & 0 < x < 0.5 \\ 0, & \text{otherwise.} \end{cases} \tag{5.8}$$

The governing equations for the problem are the linear advection equation (4.5) and the corresponding equation of evolution for the spatial derivative (4.6). Taking the material derivative of the function $f(x,t)$ along a curve $\mathcal{C}$ in the $x,t-$plane yields

$$\frac{\mathrm{d}f}{\mathrm{d}t} = \frac{\partial f}{\partial t} + \frac{\partial f}{\partial x}\frac{\mathrm{d}x}{\mathrm{d}t}. \tag{5.9}$$

Thus, by choosing $\frac{\mathrm{d}x}{\mathrm{d}t} = u(x)$ in (5.9), (4.5) is through (5.9) reduced to the following pair of ODE's

$$\frac{\mathrm{d}f}{\mathrm{d}t} = 0, \quad f(x,0) = f_0(x) \tag{5.10}$$

$$\frac{\mathrm{d}x}{\mathrm{d}t} = x, \quad x(0) = \xi. \tag{5.11}$$

Equation (5.10) means that the f is constant along curves described by the solution of (5.11). Thus, for a curve that initially passes through the point $x = \xi$, the solution to

(5.10) is simply $f(x,t) = f_0(\xi)$ (see Whitham (1974) for more details). By solving (5.11) we obtain

$$\xi = x\mathrm{e}^{-t} \tag{5.12}$$

Thus, the exact solution to (4.5) for the given initial conditions is

$$f(x,t) = \begin{cases} \sin^2(2\pi x\mathrm{e}^{-t}), & 0 < x < 0.5\mathrm{e}^{t} \\ 0, & \text{otherwise} \end{cases} \tag{5.13}$$

The exact analytical solution for $g(x,t)$ is then found by differentiating (5.13) with respect to x as

$$g(x,t) = \begin{cases} 4\pi\mathrm{e}^{-t}\sin(2\pi x\mathrm{e}^{-t})\cos(2\pi x\mathrm{e}^{-t}), & 0 < x < 0.5\mathrm{e}^{t} \\ 0, & \text{otherwise} \end{cases} \tag{5.14}$$

Equations (5.13) and (5.14) are used to verify the implementation of the 1D CIP-method. Hence, Eq. (4.5) with the above mentioned initial conditions is solved numerically using the 1D CIP-method (see Sec. 4.2.1) and compared with the analytical solution. We choose the domain of computation to be $x \in [0, 2\mathrm{m}]$ and $t = [0, T]$, where $T = \ln(4)$ is the time it takes for the point defined by $f_0(0.5)$ (and thus also $g_0(0.5)$) to reach the end of the domain ($x = 2$m). All computations are performed under the same $CFL-$condition, which is chosen to be $\mathrm{CFL}_{\max} = u_{\max}\Delta t/\Delta x = 0.5$. With the largest advection velocity $u_{\max} = 2$m/s and the spatial increment Δx given, this means that the time increment is obtained as $\Delta t = 0.5\Delta x/u_{\max}$. Obtained numerical results are compared with the exact analytical solution (5.13) and the corresponding global error ε_1 are found from (5.2) with $p = 1$. Errors of the numerical solutions obtained with the 1D CIP-method from calculations with four different grids are presented in Tab. 5.1. To study the performance of the CIP-method on a linear problem relative to a more conventional numerical scheme for advection calculations, relative errors and order of convergence obtained with the classical first order upwind-scheme (Roache 1976) are presented in Tab. 5.1 for comparison. Comparison of the obtained numerical results with the exact analytical solution to the linear advection problem are presented in Fig. 5.1, which shows that the results obtained with the present CIP-solver are in good agreement with the analytical solution while results obtained using the first order upwind-scheme differs somewhat from the analytical solution.

5.2.2 Nonlinear advection

In order to study the performance of the 1D CIP-model when applied to a nonlinear advection problem, we consider Burger's equation which is defined as

$$\frac{\partial u}{\partial t} + u\frac{\partial u}{\partial x} = \mu\frac{\partial^2 u}{\partial x^2}, \tag{5.15}$$

where μ is a constant. The non-linearity in Burger's equation is that the advected variable also defines the transport velocity, which means the transport velocity is a priory unknown. As can be seen from the right hand side (RHS) of (5.15), Burger's equation also contains a diffusion term. The diffusion term has a stabilizing effect which counteracts the shock-formation that may occur for the inviscid Burger equation, which is defined by (5.15)

Table 5.1: Convergence test of linear advection calculations with the 1D CIP-method and the first order upwind method. Global errors ε_1 relative to the exact analytical solution at solution time $T = \ln(4)$, obtained from (5.2) with $p = 1$, are presented. The time increment Δt is chosen such that $\text{CFL}_{\text{max}} = 0.5$. N is total number of time steps.

			CIP		Upwind	
Δx [m]	Δt [s]	N	ε_1	Order (r)	ε_1	Order (r)
1/50	1.00×10^{-2}	138	1.48×10^{-2}		2.06×10^{-1}	
1/100	5.00×10^{-3}	277	7.10×10^{-3}	1.06	1.23×10^{-1}	0.750
1/200	2.50×10^{-3}	554	3.50×10^{-3}	1.02	6.83×10^{-2}	0.846
1/400	1.25×10^{-3}	1109	1.74×10^{-3}	1.01	3.63×10^{-2}	0.910

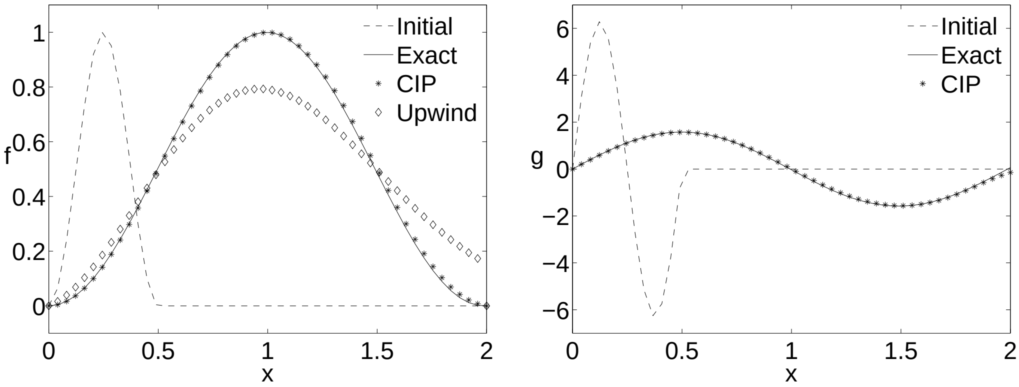

Figure 5.1: Verification of the implemented 1D CIP-method. Numerical solution to the linear advection problem obtained with the CIP-scheme when $\Delta x = 1/50$ are compared with the exact analytical solution for the solution time $t \approx 1.39$s. Results obtained with the first order upwind-scheme are added for comparison.

with $\mu = 0$ (see (LeVeque 1992)). An exact analytical solution to (5.15) on the domain $x = [0, 1\text{m}]$ with the initial condition

$$u_0(x) = \frac{2\mu\pi \sin(\pi x)}{a + \cos(\pi x)}, \tag{5.16}$$

with a being a constant, and boundary conditions

$$u(0,t) = 0 \quad \text{and} \quad u(1,t) = 0, \tag{5.17}$$

is given by Wood (2005) as

$$u(x,t) = \frac{2\mu\pi \exp\left(-\pi^2 \mu t\right) \sin\left(\pi x\right)}{a + \exp\left(-\pi^2 \mu t\right) \cos\left(\pi x\right)}. \tag{5.18}$$

Equation (5.15) is solved numerically in the domain defined by $x = [0, 1\text{m}]$ using the 1D CIP-method, with initial- and boundary conditions defined by (5.16) and (5.17), respectively. Due to the presence of the diffusion term on RHS of (5.15), a two-step time-splitting technique is applied. First an advection step is solved using the 1D CIP-method. Then, a diffusion step is solved using central differences in space. The first order explicit Euler method is used for time-stepping of the diffusion equation. Since the CIP-method applies the spatial derivative of the advected variable $g(x,t) = \frac{\partial u}{\partial x}$ in its formulation, an initial condition for $g(x,0) = g_0$ is also needed. This is simply found by differentiation of (5.16) with respect to the spatial variable x, which yields

$$g_0(x) = \frac{2\mu\pi^2 \cos(\pi x)\left(a + \sin(\pi x) + \cos(\pi x)\right)}{\left(a + \cos(\pi x)\right)^2} \tag{5.19}$$

In order to verify the evolution in time of the new variable $g(x,t)$, the exact solution is found by differentiation of (5.18) as

$$g(x,t) = \frac{2\mu\pi^2 \cos(\pi x) \exp\left(-2\pi^2 \mu t\right)\left(a + \sin(\pi x) + \cos(\pi x)\right)}{\left(a + \exp\left(-\pi^2 \mu t\right) \cos(\pi x)\right)^2}. \tag{5.20}$$

We easily verify that $g(x,0) = g_0(x)$ by setting $t = 0$ in (5.20). The boundary conditions for g can now be found from (5.20) as

$$g(0,t) = \frac{2\mu\pi^2 \exp\left(-2\pi^2 \mu t\right)}{a+1} \quad \text{and} \quad g(1,t) = \frac{2\mu\pi^2 \exp\left(-2\pi^2 \mu t\right)}{1-a} \tag{5.21}$$

We will in the following consider this case using $\mu = 10^{-4}\text{s}^{-1}$ and $a = 1.1$, which yields the maximum initial velocity $u^0_{\max} = \max\left[u(x,0)\right] = 1.37\times10^{-3}\text{m/s}$. For a given discretization of the spatial domain with constant spacing Δx between the nodes, the time increment Δt is here chosen such that $\text{CFL}_{\max} = 0.1$, initially. The time increment is then found as $\Delta t = 0.1\Delta x / u^0_{\max}$. Error of numerical solutions obtained using the 1D CIP-method and the upwind method for the solution time $t = 100\text{s}$, relative to the exact analytical solution are presented in Tab. 5.2. Order of convergence of the numerical solutions are also shown. The advected variable u and its spatial derivative g obtained with the implemented 1D CIP-scheme for the time instant $t = 100\text{s}$ are compared with the analytical solution in Fig. 5.2.

Table 5.2: Convergence test of nonlinear advection calculations with the 1D CIP-method and the first order upwind method. Global errors ε_1 relative to the exact analytical solution at solution time $T = 100$s, obtained from (5.2) with $p = 1$, are presented. The time increment Δt is chosen such that $\mathrm{CFL}_{\max} = 0.1$. N is total number of time steps.

			CIP		Upwind	
Δx [m]	Δt [s]	N	ε_1	Order (r)	ε_1	Order (r)
1/10	7.30	14	1.51×10^{-5}		2.32×10^{-5}	
1/20	2.36	42	1.07×10^{-6}	3.81	1.34×10^{-5}	0.799
1/40	0.787	127	4.20×10^{-7}	1.35	8.03×10^{-6}	0.735
1/80	0.262	381	8.52×10^{-8}	2.30	4.24×10^{-6}	0.921

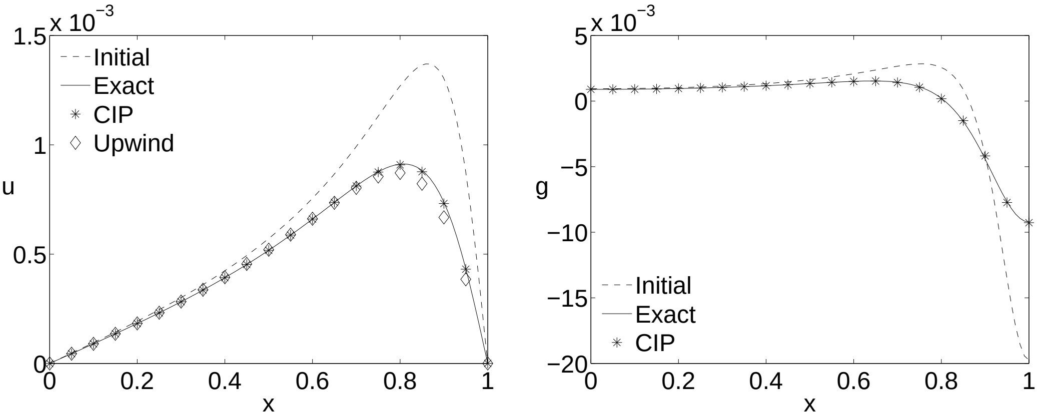

Figure 5.2: Application of the 1D CIP-method to nonlinear advection. Comparison between the exact solution and numerical solution at time $t = 100$s. The numerical solution is obtained using time-splitting with the 1D CIP-method for the advection step and central differences for the diffusion step for the case when $\Delta x = 1/20$. Results obtained with the first order upwind-scheme are plotted for comparison.

5.3 Verification of the 2D CIP-method

In this section verification tests of the implemented 2D CIP-scheme, which is used in the present flow solver, are presented. Two test cases are considered, with the first case being linear advection of a smooth function while the second case is linear advection of a discontinuous function. In both cases, the domain of computation is $(x, y) = [0, 1]$.

5.3.1 Linear advection of a smooth function

The linear problem represented by a smooth function $f(x, y, t)$ with initial condition $f(x, y, 0) = f_0(x, y)$ being advected due to a uniform, constant velocity field $\boldsymbol{u} = [u, v]$ is considered, since analytical solutions are available for such cases. The equation describing the evolution of f in time and space is the 2D linear advection equation (4.13), with the coefficients u and v being constants. When solving (4.13) using the CIP-method, we also need to solve for the spatial derivatives $\partial f/\partial x = g$ and $\partial f/\partial y = k$, as they are introduced as free variables used as constraints for the interpolation function $F(x, y)$, which is defined in (4.16). The equations of evolution for the spatial derivatives g and k for the case of a uniform velocity field are (4.14) and (4.15), respectively, with the right hand side set to zero in both equations. The exact analytical solution to (4.13) is $f(x, y, t) = f_0(x - ut, y - vt)$, meaning the initial profile f_0 is shifted a distance ut in the horizontal direction and vt in the vertical direction. The shape of the advected profile f is conserved.

We have considered the case where the initial condition for the advected function is given as

$$f_0(\xi, \eta) = \begin{cases} \cos(\pi\xi)^2 \cos(\pi\eta)^2, & \forall \quad (\xi, \eta) \in [-0.5, 0.5; -0.5, 0.5] \\ 0, \quad \text{elsewhere} \end{cases} \tag{5.22}$$

where $\xi = 4x/L - 3/2$ and $\eta = 4y/H - 3/2$. Here, $L = 1\text{m}$ and $H = 1\text{m}$ is the length and height of the computational domain, respectively. The velocity field was uniform and constant, and defined as $u = v = 0.2\text{m/s}$. Computations with the two different CFL-conditions CFL $= 0.1$ and CFL $= 0.5$ were performed. Since the CFL-number reflects the relative position on the interpolation function F^n from where the new value f^{n+1} is obtained, the CFL-number is an important parameter. With the velocity field and the spatial discretization given, the time step was adjusted to give the wanted CFL-number. Convergence of the numerical solution towards the exact solution for the solution time $t = 2$ were tested using four different grids. The global error of the numerical solution relative to the exact solution was computed using (5.3) with $p = 1$, while the order of convergence was computed from (5.6). Obtained global errors and corresponding orders of convergence are presented in Tab. 5.3. The results shows that the order of convergence for the present problem is $r \approx 1.3$. A comparison between the numerical solution and the exact solution for a horizontal cut through the domain at $y = 0.775\text{m}$ is presented in Fig. 5.3. The cut goes through the point where the solution at time $t = 2\text{s}$ has its maximum value. Undershoots of the numerical solution relative to the exact solution are observed in regions where the gradient of the advected profile is large, as is seen in the zoomed view in Fig. 5.3. This is a typical problem for many higher order numerical methods for hyperbolic problems, including the present CIP-method, and is(5.2) with $p = 1$ further discussed in the next section.

Table 5.3: Convergence test of linear advection calculations with the 2D CIP-method. At solution time $t = 2$s, global errors ε_1 relative to the exact analytical solution and orders of convergence r are obtained from (5.3) with $p = 1$ and (5.6), respectively. The time increment Δt is chosen to give the wanted CFL-condition for the given velocity field and spatial discretization.

	CIP, CFL = 0.1			CIP, CFL = 0.5		
Δx, Δy [m]	Δt [s]	ε_1	Order (r)	Δt [s]	ε_1	Order (r)
1/25	0.0200	4.15×10^{-3}		0.1000	2.73×10^{-3}	
1/50	0.0100	8.91×10^{-4}	1.11	0.0500	5.95×10^{-4}	1.10
1/100	0.0050	1.52×10^{-4}	1.28	0.0250	9.85×10^{-5}	1.30
1/200	0.0025	2.58×10^{-5}	1.28	0.0125	1.63×10^{-5}	1.30

5.3.2 Linear advection of a non-smooth profile

The color function which is used to define the water in the computational domain in the present numerical wave tank appear initially as discontinuous Heaviside functions. Generally, the traditional CIP-method is not adequate for such problems, as the solution is assumed to be described by a cubic polynomial function. To test the implemented 2D CIP-method for linear advection of non-smooth functions, a step-like function is advected in the uniform velocity field $u = v = 0.2$m/s. The initial condition for the advected function is

$$f_0(\xi, \eta) = \begin{cases} 1, & \forall \quad (\xi, \eta) \in [-0.5, 0.5; -0.5, 0.5] \\ 0, & \text{elsewhere} \end{cases} \tag{5.23}$$

where $\xi = 4x/L - 3/2$ and $\eta = 4y/H - 3/2$. Dimensions of the computational domain are $L = 1$ and $H = 1$ for the $x-$ and $y-$direction, respectively. Numerical solutions obtained from four different grids are compared with the exact analytical solution for the solution time $t = 2$. Global error ε_1 is computed from (5.3) with $p = 1$, and the order of convergence r is estimated from (5.6). Results are presented in Tab. 5.4. As expected, convergence properties of the numerical solution towards the exact discontinuous solution is poor. Contour plots of the initial profile and the numerical solution after 400 time steps are presented in Fig. 5.4, and shows that numerical diffusion occur as the contour lines

Table 5.4: Convergence test of linear advection of a non-smooth function using the 2D CIP-method. Global errors ε_1 relative to the exact analytical solution at solution time $t = 2$ and order of convergence r are obtained from (5.3) with $p = 1$ and (5.6), respectively. The time increment Δt is chosen such that CFL = 0.5. N is total number of time steps.

			CIP	
Δx, Δy [m]	Δt [s]	N	ε_1	Order (r)
1/25	0.1000	25	2.61×10^{-2}	
1/50	0.0500	50	1.12×10^{-2}	1.22
1/100	0.0250	100	8.80×10^{-3}	0.35
1/200	0.0125	200	5.26×10^{-3}	0.74

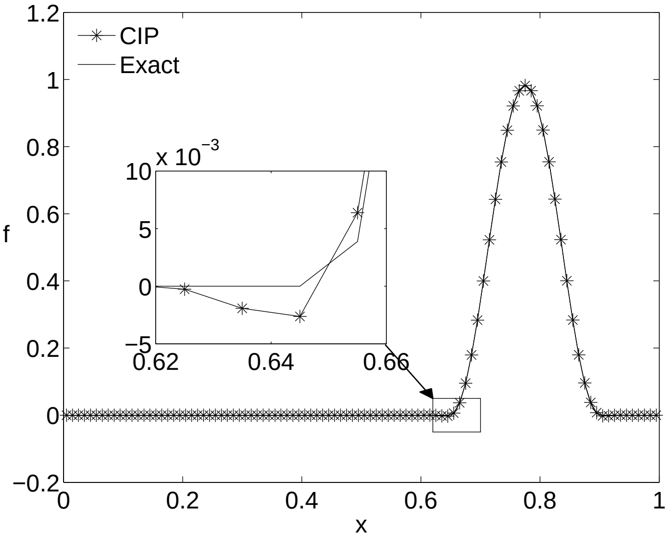

Figure 5.3: Verification of the 2D CIP-method when $\Delta x = \Delta y = 1/100$m and CFL $= 0.5$. Comparison with exact solution at time $t = 2$s for a horizontal cut through the domain at $y = 0.775$m. This is where the solution has its maximum value. Undershoot of the numerical solution relative to the exact solution is observed.

of the solution after 400 time steps are more spread than the contour lines of the initial profile. The numerical solution for the case when $\Delta x = \Delta y = 1/100$ and CFL $= 0.5$ are compared with the exact solution for a horizontal cut through the domain at $y = 0.775$ at the solution time $t = 2$s in Fig. 5.5. Over- and undershoots of the numerical solution relative to the exact solution are observed to be more pronounced for this case than for the case with linear advection of a smooth profile presented in Fig. 5.3.

5.4 Verification of the diffusion calculation

Linear laminar boundary layer flows generally represent good test cases for verification of the diffusion step in our CFD-code, because they are simple to model and the fact that analytical solutions exist. An example of laminar boundary layer flow is the second Stokes problem, which describes the flow of a viscous fluid above an oscillating wall. The fluid is set into motion due to viscous shear forces in the fluid. The analytical steady state solution of the second Stokes problem can be found in many text books e.g. Schlichting and Gersten (2000). When solving Stokes second problem numerically using a time-domain flow solver, it is convenient from a modelling point of view to start with the fluid being at rest initially. Thus, in order to compare the numerically obtained velocity field with the steady state solution, one must be sure that the numerical solution has reached a steady state. However, there also exists an analytical solution for the transient start-up of Stokes second problem (Panton 1968) which would be better suited for verification purposes of the time-dependent flow solver. We will in the following section use the transient second Stokes problem as a verification test for the implementation of the diffusion terms in our numerical code.

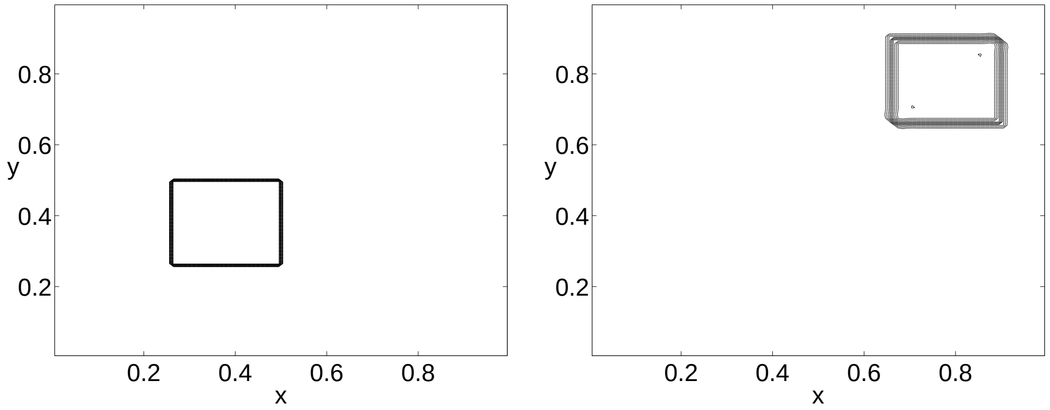

Figure 5.4: Linear advection in 2D for a uniform velocity field $u = v = 0.2\mathrm{m/s}$. Left, initial contour. Right, contour after 400 time steps. $\Delta x = \Delta y = 1/100\mathrm{m}$ and $\mathrm{CFL} = 0.5$.

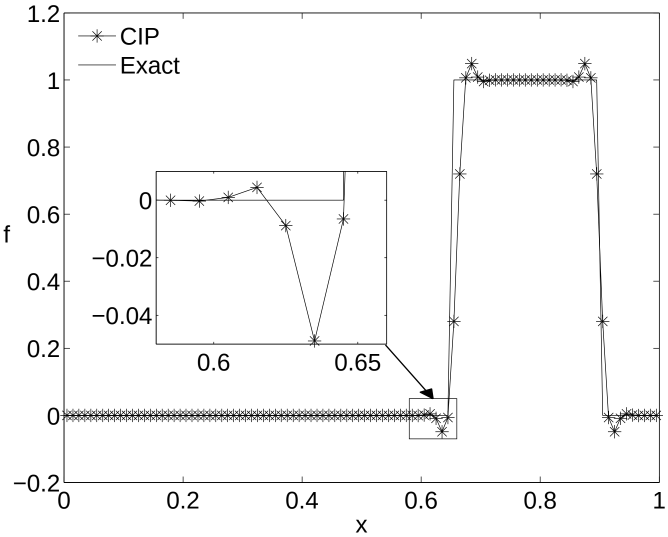

Figure 5.5: Linear advection in 2D of a step-like function in a uniform velocity field $u = v = 0.2\mathrm{m/s}$. Comparison with exact solution at time $t = 2\mathrm{s}$ for a horizontal cut through the domain at $y = 0.775\mathrm{m}$. $\Delta x = \Delta y = 1/100\mathrm{m}$ and $\mathrm{CFL} = 0.5$. Both undershoots and overshoots are observed near the step.

5.4.1 The transient second Stokes problem

First, we will give a brief description of the mathematical problem. Consider a semi-infinite domain bounded an impermeable wall along the $x-$axis ($y = 0$), where the upper half plane is occupied by a viscous fluid. Initially, the fluid is at rest. At time $t = 0$ the wall abruptly starts to move with an oscillatory motion in the horizontal direction. Due to adhesion forces between the fluid and the wall, a no-slip condition is applied on the wall. Together with viscous shear forces in the fluid, the no-slip condition will cause energy to be transferred from the wall into the fluid domain. The surrounding fluid is then set into an oscillatory motion. The infinite length of the wall means there are no end-effects present, and the horizontal fluid velocity u is only a function of the normal distance from the wall y in addition to time t. The vertical fluid velocity component is zero due to continuity. The mathematical problem is defined by the time-dependent diffusion equation

$$\frac{\partial u}{\partial t} = \nu \frac{\partial^2 u}{\partial y^2}, \tag{5.24}$$

where $\nu = \mu/\rho$ is the kinematic viscosity coefficient, with μ and ρ being the dynamic viscosity coefficient and the mass density of the fluid, respectively. When finding the analytical solution to (5.24) the time dependent velocity field $u(y, t)$ is divided into a steady-state part U^s and a transient part U^t as

$$u(y, t) = U^s + U^t, \tag{5.25}$$

where the analytical steady state solution obtained from Prandtl's boundary layer equations is given as

$$U^s(\eta, T) = U_0 \exp(-\eta) \sin(T - \eta), \tag{5.26}$$

with the non-dimensional parameters $T = \omega t$ and $\eta = y\sqrt{\frac{\omega}{2\nu}}$ (see Appendix). The analytical solution to the transient part presented by Panton (1968) is

$$\begin{aligned} U^t(\eta, T) = U_0 \Im \Big\{ &-0.5 \exp\left[C\eta - iT\right] \operatorname{erfc}\left[\sqrt{0.5T}(C + \eta/T)\right] \\ &+ 0.5 \exp[-C\eta - iT] \operatorname{erfc}\left[\sqrt{0.5T}(C - \eta/T)\right] \Big\}, \end{aligned} \tag{5.27}$$

where $\Im\{z\}$ refers to the imaginary part of a complex argument $z = x + iy$. Further, *erfc* is the complementary error function with complex argument due to the complex constant $C = 1 - i$ (see Appendix for further details).

Numerically we cannot handle unbounded or semi-infinite domains. Hence we consider a limited rectangular domain of length L along the wall and height H in the normal direction from the wall. As in the mathematical formulation, the computational domain is limited by an impermeable wall at the lower boundary ($y = 0$), where a no-slip condition is applied. The remaining three boundaries are the top boundary at $y = H$, and the side boundaries at $x = 0$ and $x = L$, which are all open boundaries. To minimize end-effects on the resulting velocity field due to the limited computational domain, the dimensions of the domain are chosen to be large compared to a characteristic length of the problem. The boundary layer thickness for steady-state is defined as

$$\delta_{0.99} = 4.6\sqrt{\frac{2\nu}{\omega}}, \tag{5.28}$$

Table 5.5: Parameters used in the numerical solution of Stokes second problem. Material properties of the fluid are those representative for water.

Parameter	Symbol	Value	Unit
Frequency of oscillation	ω	5.317	rad/s
Wall velocity amplitude	U_0	0.025	m/s
Mass density	ρ	1000	kg/m^3
Dynamic viscosity	μ	1.52×10^{-3}	kg/(ms)

with ω being the oscillation frequency of the wall, is a suitable measure of characteristic length (Schlichting and Gersten 2000). This is the normal distance from the wall to where the absolute value of the fluid velocity in the steady state solution is reduced to 1% of the wall velocity amplitude U_0. For later purposes, the frequency of oscillation of the wall was choosen equal to the natural frequency for the first mode of a standing wave in a 1m long tank with 0.5m water depth. For the kinematic viscosity coefficient, respectively, representative values for water are used. The parameters used in the calculations are listed in Tab. 5.5. Using the data from Tab. 5.5, the boundary layer thickness is found to be $\delta_{0.99} = 0.0035$. With the boundary layer thickness in mind, the domain-length and -height are chosen to be $L = 0.5$m and $H = 0.025$m, respectively. Hence, the distance between the mid-point of the oscillating wall and the ends of the domain are more than $70 \times \delta_{0.99}$, which is believed enough to avoid end effects. Further, the distance to the upper boundary of the domain is about $7 \times \delta_{0.99}$. Although the distance from the wall to the upper boundary is ten times shorter than the distance to the end-boundaries, it is assumed that the upper boundary will have no influence on the boundary layer flow, as the velocity at the upper boundary is zero.

In order to efficiently resolve the viscous flow inside the thin boundary layer, grid stretching is applied in the $y-$direction where the grid is divided into three regions. In these regions, different gridding techniques are used. Since the envelope of the velocity profile of the boundary layer flow is exponential, we use an exponential distribution of grid points in the $y-$direction inside the boundary layer. Far away from the wall, constant grid spacing is used, while a quadratic distribution is used to match the exponential grid region with the constant grid region. Constant grid spacing is applied in the $x-$direction. More details on the grid generation for this case is presented in appendix B.1.3.

Grid convergence

Convergence tests of the numerical solution are performed, where three grids with different boundary layer resolution were tested. Grid parameters for the three grids are given in Tab. B.1.3. The error of the numerical solution relative to the analytical solution at the solution time $t/T = 1.07$, where T is the period of oscillation of the wall, is computed for a cut along the $y-$axis in the middle of the domain. The error ϵ_2 is computed using the 1D error norm defined in (5.2) with $p = 2$, but with using $\Delta y_j = \Delta y_1$ which is the grid spacing at the wall. When calculating the error norm, the sum is taken only over the velocity nodes located inside the boundary layer ($y < \delta_{0.99}$). The time $t/T = 1.07$ for when the error is computed is when the largest error $\epsilon_2(t)$ is obtained with the finest. The order of convergence r of the numerical solution is estimated using (5.5). Obtained error estimates and corresponding order of convergence towards the analytical solution are presented in Tab. 5.6. Results presented in Tab. 5.6 shows that the order of convergence is $r \approx 2$. Snapshots from the transient start-up phase of Stokes second problem are presented in Fig. 5.6 where the numerical solution for the case when $N_{bl} = 8$ is compared with the analytical solution. N_{bl} is the number of grid points inside the boundary layer in the cut from where the error ϵ_2 is computed. Good comparison between the numerical and analytical solution is shown. Note the overshoot of the transient solution relative to the envelope of the steady state solution.

Table 5.6: Test of grid convergence for the transient second Stokes problem for the horizontal velocity inside the boundary layer. Solutions are compared at time $t/T = 1.07$. The error ε_2 is computed from eq.(5.2) with $p = 2$ and using Δy_1 which is the grid increment at the wall as a reference. N_{bl} is number of grid points inside the boundary layer.

N_{bl}	Δy_1 [m]	ε_2	Order (r)
6	2.55×10^{-4}	9.54×10^{-6}	
8	1.54×10^{-4}	3.52×10^{-6}	1.98
15	6.27×10^{-5}	6.27×10^{-7}	1.92

5.5 Verification of the pressure solver

In order to verify the implementation of our pressure solver, we first consider the Poisson equation with constant coefficients which formally can be written

$$\nabla^2 f = h, \tag{5.29}$$

where $f(x, y)$ is unknown while $h(x, y)$ is a known forcing. For one-phase flow problems where the mass density of the fluid is constant, (5.29) is the equation to be solved in order to find the pressure at the new time step when projection methods are used. To test our Poisson solver, we utilize trigonometric test functions to define a Poisson problem for which analytical solutions easily are obtained. This will now be discussed.

Consider a square domain where $[x, y] \in [0, 1\text{m}]$. Further, assume the mass density of the fluid is constant with $\rho = 1$ throughout the domain. Then we consider a test function of the form

$$f(x, y) = \cos(\pi x) \sin(\pi y) \tag{5.30}$$

with the Dirichlet boundary condition $f(x, y) = 0$ on $y = [0, 1\text{m}]$ and Neumann boundary condition $\partial f/\partial x = 0$ on $x = [0, 1\text{m}]$. Then, inserting (5.30) into (5.29) yields the following expression for the forcing

$$h(x, y) = -2\pi^2 \cos(\pi x) \sin(\pi y). \tag{5.31}$$

We discretize the square domain into N_x and N_y number of points in the $x-$ and $y-$direction, respectively. Further, eq. (5.29) is discretized as described in section 4.3.4 to yield the linear system of equations $\boldsymbol{Ax} = \boldsymbol{b}$ where the elements of $\boldsymbol{b}$ are obtained as the values of h at the node points. Solving this Poisson problem with the given boundary

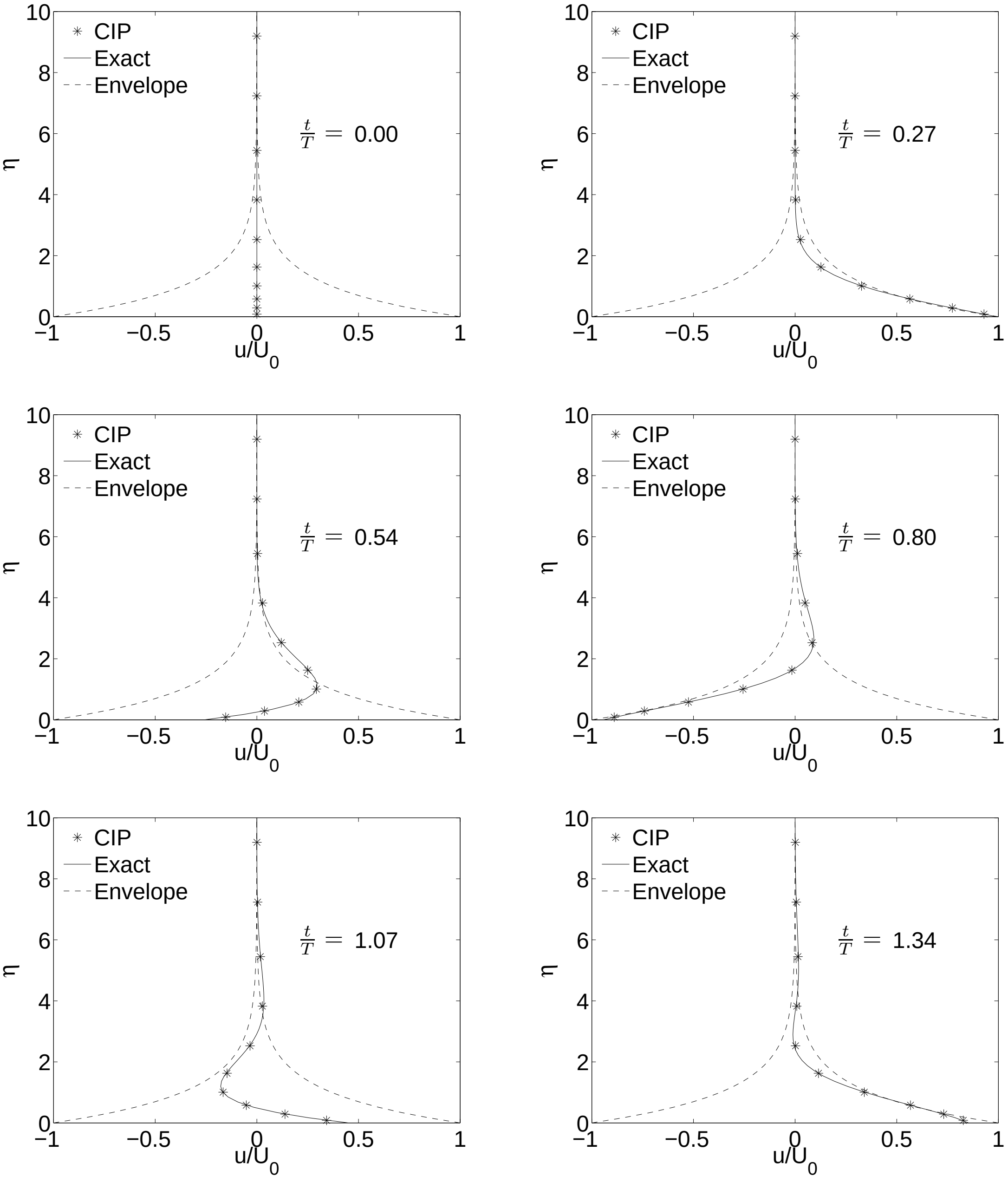

Figure 5.6: Comparison of numerical solution to the transient second Stokes problem obtained with the present flow solver and the analytical solution. Number of elements inside the boundary layer in the normal direction from the wall is $N_{bl} = 8$. The envelope of the steady state solution is shown by the stippled lines.

conditions, the solution vector $\boldsymbol{x}$ should be equal to the values of (5.30) at the node points. This Poisson problem is solved both on a uniform grid and on a nonuniform (stretched) grid, using the present implementation of the Bi-CGSTAB algorithm. For the nonuniform grid, the grid spacings Δx_i are obtained as

$$\Delta x_i = \frac{L\,(1 - \beta \cos^2(\pi t_i))}{\sum_{i=1}^{Nx} (1 - \beta \cos^2(\pi t_i))} \tag{5.32}$$

where $L = 1\text{m}$ is the length of the domain, $\beta = 0.9$ is a stretching coefficient and $t_i \in [0, 1\text{s}]$. The vertical grid spacings Δy_j is found in the same way. Convergence tests are performed for both the uniform grid and the nonuniform grid. As a measure of error in the numerical solution when testing for convergence, we use the normalized error

$$\varepsilon = \frac{\|\boldsymbol{x}_{ex} - \boldsymbol{x}_{num}\|}{\|\boldsymbol{b}\|}. \tag{5.33}$$

Results for both the uniform grid case and the nonuniform grid case are presented in Tab. 5.7. The rate of convergence towards the exact solution is found to be of second order for both cases.

Table 5.7: Convergence of the Poisson solver applied on a non-uniform grid. The obtained rate of convergence is of second order. The convergence rate depends on how the grid stretching is performed relative to the nature of the solution. The normalized error ε is defined in (5.33).

	Uniform grid		Stretched grid	
$N_x \times N_y$	ε	Order	ε	Order
8×8	7.02×10^{-4}		6.66×10^{-4}	
16×16	1.49×10^{-4}	2.24	1.46×10^{-4}	2.19
32×32	3.15×10^{-5}	2.24	3.15×10^{-5}	2.21
64×64	6.40×10^{-6}	2.30	6.50×10^{-6}	2.28

5.6 Verification of the flow solver for one-phase flow

In the previous sections, the implementation of the main parts of the flow solver has been verified separately. Next step is to verify the complete flow solver for one-phase flow with no interior body inside the domain. For this purpose, the classical lid-driven cavity flow problem presented by Ghia et al. (1982) has been studied.

5.6.1 Lid-driven cavity flow

The lid-driven cavity flow problem is a good verification test case for one-phase flow solvers due to simple boundary- and initial conditions, and the fact that all terms in the Navier-Stokes equations matter for this case. The physical domain of computation has length $L = 1\text{m}$ and height $H = 1\text{m}$ and is completely filled with a viscous and incompressible fluid with density ρ and dynamic viscosity μ. A no-slip boundary condition is applied on all boundaries. There is no effect of gravity. Initially, the fluid is at rest. At time $t = 0$ the top boundary abruptly starts to move with a constant velocity $U = 1\text{m/s}$ in the positive $x-$direction. As the flow is driven by viscous shear forces in the fluid, the Reynolds number is an important parameter characterizing the flow. Here, the Reynolds number is defined as $\text{Rn} = UL/\nu$ where $nu = \mu/\rho$ is the kinematic viscosity coefficient while U and L are velocity and length of the top boundary, respectively. We consider the case with $Rn = 100$. Thus, the density and the dynamic viscosity are chosen such that $\nu = 0.01$. Numerically, the moving top boundary is modelled by imposing $u_{i,N} = 2.0 - u_{i,N-1}$ at the horizontal velocity nodes of the top boundary ghost cells. Further, the spatial derivatives are set to $g_{i,N} = -g_{i,N-1}$ and $k_{i,N} = k_{i,N-1}$ in the same ghost cells.

As the domain is totally enclosed by rigid non-permeable walls, the pressure is unknown at all boundaries and the Poisson equation for the pressure represents a complete Neumann problem. In the discretized problem, this implies that the coefficient matrix for the linear system of equations is singular. To overcome this problem, an artificial pressure is specified in one grid cell inside the domain at the bottom boundary.

Three uniform grids are tested. The spatial increments and corresponding time increment used in the simulations are listed in Tab. 5.8. At time $t = 25\text{s}$ of simulation, the fluid motion has converged to a steady state where a primary vortex is rotating clockwise and two secondary vortices at the lower corners are rotating counter clockwise as shown in Fig. 5.7. Location of the vortex center of the primary vortex is compared with numerical results by Ghia et al. (1982) in Tab. 5.9. Results obtained with the present flow solver seems to converge towards the comparison data. However, results obtained with the finest grid with the present flow solver deviates from the comparison data for the same grid by 1.4% and 2.1% for the horizontal and vertical coordinate, respectively.

Table 5.8: Spatial- and time increments used in the computations.

$N_x \times N_y$	Δx [m]	Δy [m]	Δt [s]
20×20	0.05	0.05	0.02
64×64	0.0156	0.0156	0.002
129×129	0.0078	0.0078	0.001

Table 5.9: Convergence test for the steady state position of the vortex center (x_c, y_c) of the primary vortex.

	$N_x \times N_y$	$x_c[m]$	$y_c[m]$
Present	20×20	0.6699	0.8001
-	64×64	0.6375	0.7673
-	129×129	0.6258	0.7500
Ghia et al. (1982)	129×129	0.6172	0.7344

5.6.2 Circular cylinder in uniform cross flow

To verify the implementation of the immersed boundary method used for introducing a solid body inside the computational domain, a case with a fixed circular cylinder subject

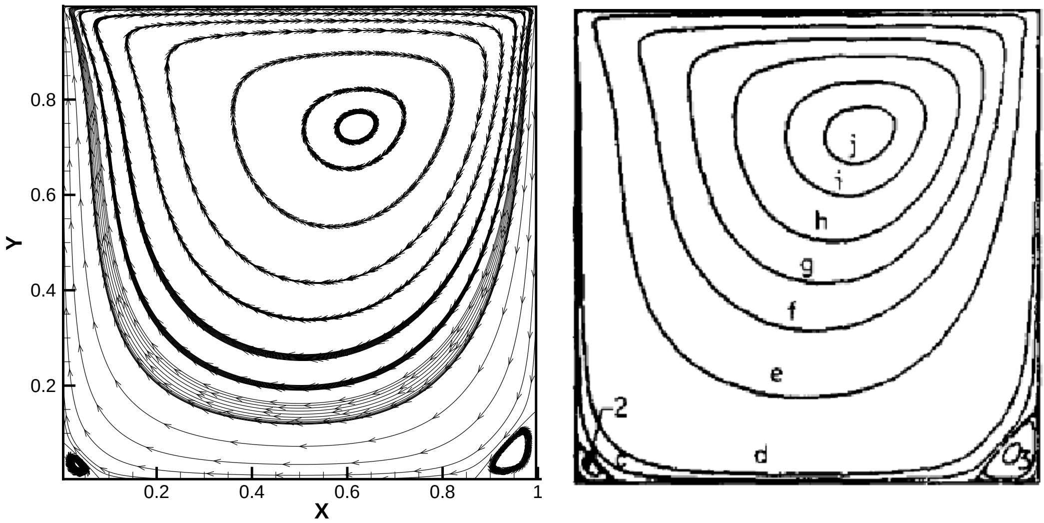

Figure 5.7: Computed stream-lines for the lid-driven cavity flow with $Rn = 100$ at time $t = 25$s obtained from simulation with the finest grid using the present code is shown to the left. Corresponding results presented by Ghia et al. (1982) for $Rn = 100$ is shown to the right. Secondary vortices at each of the two lower corners of the domain are observed in the present results as in results by Ghia et al.

to an incident uniform flow is studied. The cylinder has a diameter $D = 1.0$m and is fixed inside a rectangular domain of length $L = 45D$ and height $H = 20D$. The position of the cylinder axis is $X = 10D$ and $Y = 10D$ measured from the lower left corner of the domain. Initially, the fluid is at rest. At time $t = 0$ a uniform velocity $U = 1.0$m/s in the $x-$direction and $V = 0$ in the $y-$direction is imposed on the left, bottom and top boundaries of the domain. An outlet boundary condition is applied at the right hand boundary, where a uniform reference pressure is specified. A no-slip condition is imposed on the cylinder surface. The computational domain with boundary conditions is depicted in Fig. 5.8.

The non-dimensional parameter describing the flow for this case is the Reynolds number $Rn = UD/\nu$. We consider the case with $Rn = 100$, which is obtained by using the kinematic viscosity coefficient $\nu = 0.01\text{m}^2/\text{s}$. The boundary layer flow on the cylinder surface is laminar for this Reynolds number.

The computational grid

A good resolution of the boundary layer on the cylinder surface is necessary for an accurate prediction of the flow separation points. The position of the separation points on the cylinder surface is important for the lift and drag forces on the cylinder. From the study of the second Stokes problem in section 5.4.1 we found that a number of 6-10 grid cells inside the boundary layer in the normal direction from the no-slip boundary was sufficient in order to capture the oscillating flow in the boundary layer. We assume that 10 grid cells inside the boundary layer is sufficient also for this case. The boundary layer thickness is estimated as $\delta \approx D/\sqrt{\text{Rn}}$. For the case when $Rn = 100$, this yields $\delta = 0.1D$. Hence, the cylinder is discretized by 100 grid cells over the diameter in both the $x-$ and $y-$direction.

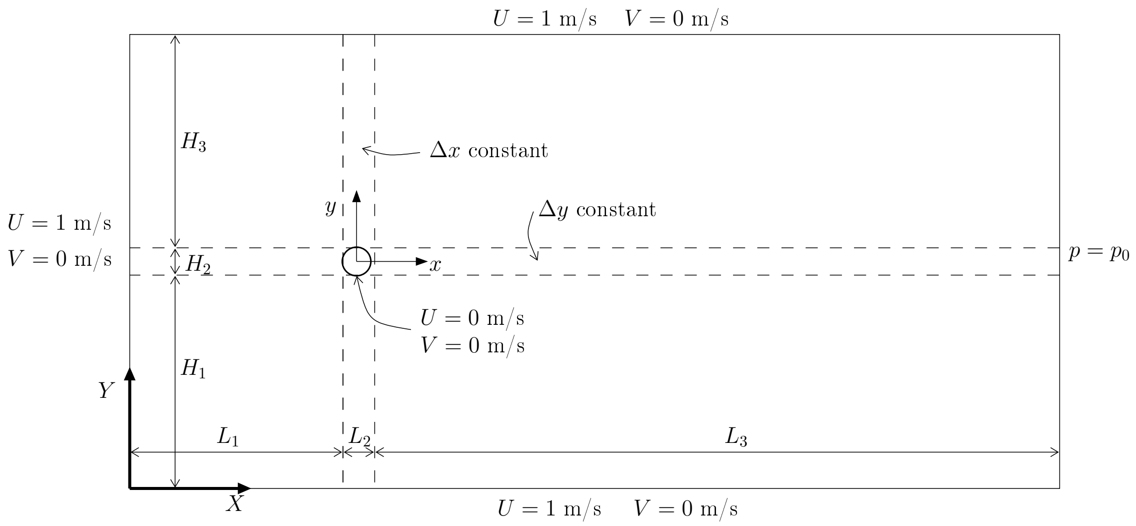

Figure 5.8: Domain and boundary conditions used for simulation of a circular cylinder in uniform cross flow. The cylinder axis is located at $X = Y = 10D$, where D is the cylinder diameter. Different grid zones are indicated by stippled lines.

In order to keep the CPU-time on an acceptable level, stretching of the computational grid is applied. The computational domain is divided into three regions in both the $x-$ and $y-$direction as indicated by the stippled lines in Fig. 5.8. Constant grid line spacing is used in L_2 and H_2, while a quadratic variation of the spatial increments is used in the remaining regions. Smooth variation of the grid increments are ensured between the constant grid zones and the quadratic grid zones.

Table 5.10: Number of grid cells in $x-$ and $y-$direction for the different regions of the domain. This yields a total of 100,000 grid cells in the domain.

	L_1	L_2	L_3	H_1	H_2	H_3
N	100	100	200	75	100	75

Results and discussion

In the beginning, the flow is symmetric with a growing recirculation zone behind the cylinder. A close view of the cylinder at this stage is shown in Fig. 5.9. The no-slip condition on the cylinder surface is verified by inspection of the computed velocity field. Symmetry of the flow in the early stage of the simulation supports a correct implementation of the body boundary condition. After some time of simulation (here at $Ut/D \approx 80$), inception of flow instability occur in the wake. This causes vortices to be shed from the cylinder surface, yielding a so-called von Karman street in the wake flow. Such vortex shedding leads to an oscillating pressure on the cylinder surface, which yields a time-dependent force on the cylinder. This force is decomposed into an in-line force component F_x (drag), and a transverse force component F_y (lift). The drag- and lift forces due to the pressure are computed from (4.55) and (4.56), respectively. In addition comes contributions from skin friction forces on the cylinder surface. An expression for the drag coefficient

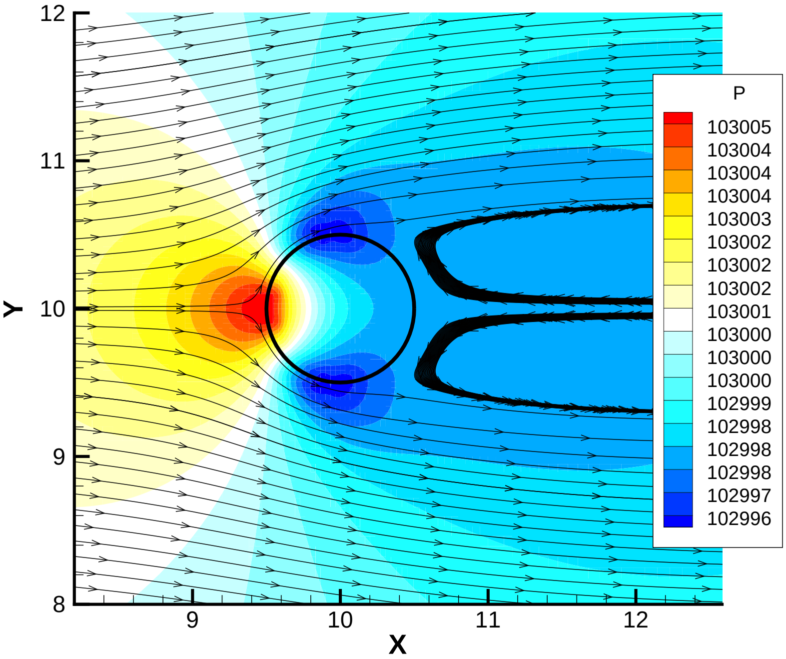

Figure 5.9: Pressure-field and stream traces obtained from simulation of cylinder in uniform cross-flow at time $t = 56$s with $Rn = 100$. This is before vortex shedding occur. We note that the artificial pressure field inside the cylinder is smooth.

due to skin friction on a smooth circular cylinder in uniform cross-flow was presented by Henderson (1995) as $C_{d,v}(Rn) = 2.5818/Rn^{0.4369}$, as a fit to his numerical results. For $Rn = 100$, this yields $C_{d_v} = 0.345$. Skin friction is not included in the present code. The lift force oscillates with the vortex shedding frequency f, while the drag force oscillates with the frequency $2f$. When the flow has reached a steady state, the mean pressure drag coefficient $C_{D,p}$ and the peak-to-peak lift coefficient C_L are obtained as

$$C_{D,p} = \frac{\overline{F_x}}{0.5\rho U^2 D} \quad \text{and} \quad C_L = \frac{F_y^{A+} + \left|F_y^{A-}\right|}{0.5\rho U^2 D}, \tag{5.34}$$

where $\overline{F_x}$ is the mean pressure drag force, while F_y^{A+} and F_y^{A-} are the mean positive and mean negative lift force amplitudes, respectively. Obtained drag and lift coefficients are compared with numerical results presented by Berthelsen and Faltinsen (2008) and Henderson (1995) in Tab. 5.11.

Table 5.11: Computed mean drag coefficient C_D and peak-to-peak lift coefficient C_L due to pressure forces only, for the case of a circular cylinder in uniform cross flow with $Rn = 100$. Skin friction forces are not included.

Source	$C_{D,p}$	C_L
Berthelsen and Faltinsen (2008)	1.028	0.596
Henderson (1995)	1.005	-
Present	1.015	0.580

The Strouhal number, which is the non-dimensional vortex shedding frequency, is found as

$$St = \frac{fD}{U}, \tag{5.35}$$

where f is calculated as the zero up-crossing frequency from the computed time-series of the lift force. For the present case, $St = 0.170$ is obtained. This is in agreement with numerical results found in the literature (Engelman and Jamnia 1990; Herfjord 1996; Berthelsen and Faltinsen 2008).

The presently obtained results are in agreement with numerical results from the literature, which indicate that the adopted immersed boundary method and the force calculation routines are correctly implemented.

5.7 Verification of the flow solver for two-phase flow

So far we have only considered one-phase flow in our verification tests. Next step is to verify the implemented flow solver for two-phase flow problems. Here the two phases are represented by water and air. A numerical issue is numerical diffusion associated with the finite thickness air-water interphase. We continue our verification study by considering the two-phase problem of small amplitude sloshing in a square tank. Free surface flow problems inside tanks are also referred to as sloshing and has many applications in marine hydrodynamics.

5.7.1 Small amplitude sloshing

The free decay of a small amplitude standing wave inside a square tank is studied, with the objective to investigate the effect of numerical diffusion in our flow solver. This problem was introduced as a verification test case by Vestbøstad et al. (2007). Viscous dissipation of energy in the boundary layers along the tank bottom and side walls will cause the amplitude of the standing wave to decrease with time. However, when this problem is solved numerically there can also be dissipation of energy caused by numerical diffusion, which is unphysical. This is an important issue for a numerical wave tank, as numerical diffusion may cause the generated waves to have an unphysical decay in amplitude. Hence, in order to rely on results to be obtained with our numerical wave tank, we must verify that the numerical dissipation of energy is negligible relative to the physical dissipation of energy. The cause of numerical energy dissipation can be discretization errors or smearing of the color functions at the interphase between the different phases.

Numerical setup

Consider a square tank of length $L = 1$m and height $H = 1$m. The tank has vertical side walls, open tank top and is partially filled with water and air. The fill level is 50%, yielding a water depth $h = 0.5$m. We define a coordinate system Oxy with origin in the calm free surface with a distance $L/2$ from the side walls. The $y-$axis is pointing upwards. Consider a free standing wave represented by the first natural mode. The wave length of the first mode is $\lambda = 2L$ and thus the wave number is $k = \pi/L$. According to linear potential flow theory, the wave frequency is found to be $\omega = 5.32$rad/s from the dispersion relation for finite water depth (3.23). The corresponding wave period is

$T = 1.18$s. Further, the free surface profile $\zeta(x,t)$ and the corresponding velocity potential $\phi(x,y,t)$ for a standing wave of the fist mode with amplitude ζ_A is

$$\zeta(x,t) = \zeta_A \sin kx \sin \omega t \tag{5.36}$$

$$\phi(x,y,t) = \frac{g\zeta_A}{\omega}\frac{\cosh k(y+h)}{\cosh kh}\sin kx \cos \omega t. \tag{5.37}$$

The horizontal- and vertical velocity components are derived from the velocity potential as

$$u(x,y,t) = \frac{\partial \phi}{\partial x} = \omega\zeta_A \frac{\cosh k(y+h)}{\sinh kh}\cos kx \cos \omega t \tag{5.38}$$

$$v(x,y,t) = \frac{\partial \phi}{\partial y} = \omega\zeta_A \frac{\sinh k(y+h)}{\sinh kh}\sin kx \cos \omega t \tag{5.39}$$

Using Bernoulli's equation, the linear hydrodynamic pressure is found to be

$$p_D(x,y,t) = -\rho\frac{\partial \phi}{\partial t} = \rho g \zeta_A \frac{\cosh k(y+h)}{\cosh kh}\sin kx \sin \omega t. \tag{5.40}$$

At time $t = 0$ the free surface profile obtained from (5.36) is $\zeta(x,0) = 0$. This provides a simple implementation. Further, from (5.40) we see that the hydrodynamic pressure is zero, initially. Hence the initial pressure field is described by the hydrostatic pressure $p_s = -\rho g y$ below the calm free surface. The initial velocity field is found from (5.38) and (5.39) using $\zeta_A = 0.025$m.

Theoretical decay rate of the wave amplitude

In order to quantify the numerical energy dissipation, we must know what is the physical dissipation of energy in the tank. A theoretical estimate of the physical energy dissipation is obtained as follows. Linear potential flow theory is used to derive the inviscid velocity field in the water, as defined in (5.38) and (5.39). This yields the velocity outside the boundary layers along the tank bottom and side walls. For small amplitude waves, the boundary layer flow along the tank walls will be laminar. This means we can utilize the second Stokes problem to obtain an estimate of the rate of viscous energy dissipation inside the boundary layers. The theoretical decay rate for the amplitude of the standing wave is found to be

$$\frac{\zeta_A}{\zeta_{A0}} = \exp\big(-\frac{\alpha}{T}t\big), \tag{5.41}$$

where

$$\alpha = \pi\sqrt{\frac{2\nu}{\omega L^2}}\left(1 + \frac{k(L-2h)}{\sinh 2kh}\right). \tag{5.42}$$

The computational grid

There are basically two cautions to take when constructing the grid for this problem. One is the resolution of the boundary layer and the other is the resolution of the finite thickness air-water interphase. Good resolution of the boundary layers at the tank bottom and side walls are necessary in order to capture the physical energy dissipation. Further, to minimize the numerical dissipation of energy due the finite thickness air-water interphase,

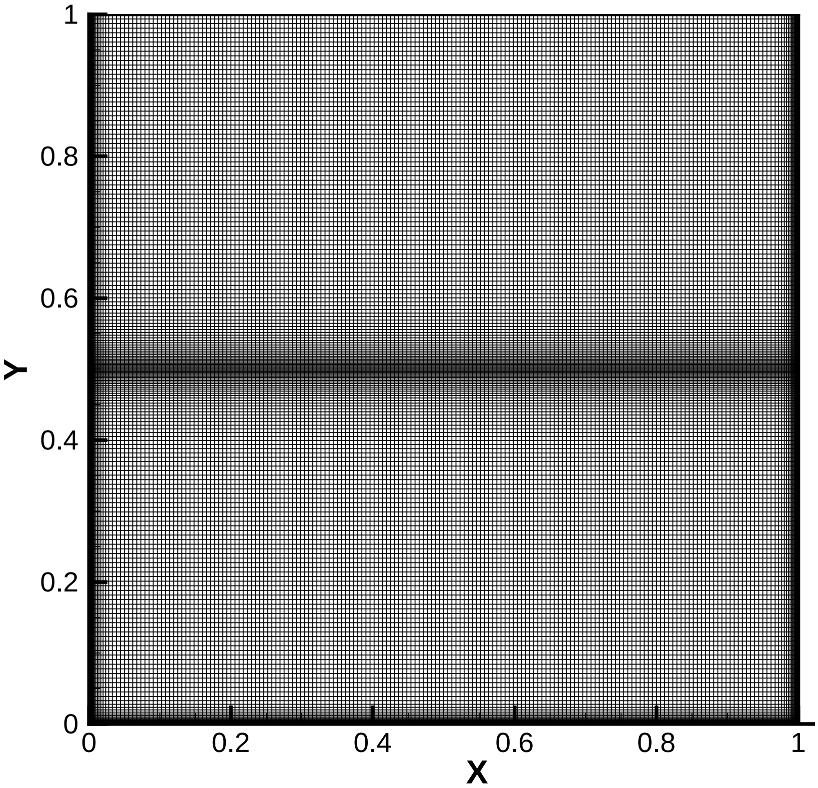

Figure 5.10: Complete grid with grid refinement in the interphase zone used for simulating small amplitude sloshing.

the interphase should be kept as thin as possible. This means also the free surface zone needs to be well resolved by the grid.

Discretization of laminar boundary layers in oscillatory flow was discussed when solving the second Stokes problem in section 5.4.1. By using an exponential variation of grid increments in the normal direction from the wall inside the boundary layer, good results were obtained for the boundary layer flow. Hence, an exponential variation of the grid increments inside the boundary layer is used also for the present problem. However, here the exponential grid is extended outside the boundary layer to match the coarser constant grid in the main bulk of the domain without a quadratic matching zone as used for the second Stokes problem.

To obtain a fine grid at the air-water interphase, a squared cosine variation of the vertical grid increments is used in the interphase zone. The grid increments here are found as

$$\Delta y_j = \Delta y_0 (1 - \beta \cos^2(0.5\pi s_j)), \tag{5.43}$$

where Δy_0 is the vertical grid increment in the constant grid zone, $\beta < 1$ is a clustering coefficient and $s \in [-1, 1]$ is a linearly spaced parameter. A complete grid with a squared cosine variation of grid increments in the wave zone and exponential variation of grid increments in the boundary layers is shown in Fig. 5.10.

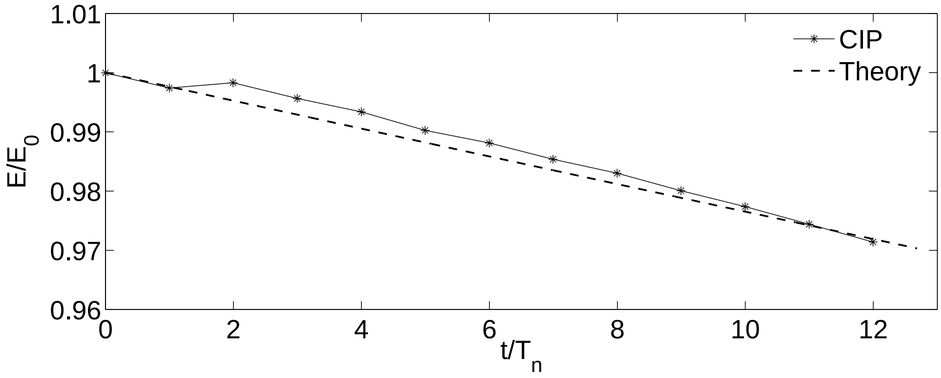

Figure 5.11: Comparison between theoretical and computed energy dissipation of the first sloshing mode. The domain is resolved by 200 grid cells in both the $x-$ and the $y-$direction. The boundary layers are resolved by 8 grid cells in the normal direction from the boundary, while an interphase zone of height $h_{wz} = 0.35$ centered about the mean free surface is resolved by 86 grid cells.

Results

During the simulation, the potential- and kinetic energy in the water is computed. The kinetic energy in the wave is found as

$$E_k = \frac{\rho_w}{2} \sum_{i=1}^{N_x} \sum_{j=1}^{N_y} \left(\hat{u}_{i,j}^2 + \hat{v}_{i,j}^2 \right) \varphi_{i,j} \Delta x_i \Delta y_j, \tag{5.44}$$

where $\varphi = \varphi_1$ is the color function for the water and

$$\hat{u}_{i,j} = 0.5(u_{i,j} + u_{i-1,j}) \tag{5.45}$$

$$\hat{v}_{i,j} = 0.5(v_{i,j} + v_{i,j-1}) \tag{5.46}$$

are the fluid velocity components in the cell center. Further, is the potential energy in the wave found as

$$E_p = \rho_w g \sum_{i=1}^{N_x} \sum_{j=1}^{N_y} \left(yc_j - 0.5h \right) \varphi_{i,j} \Delta x_i \Delta y_j. \tag{5.47}$$

The total energy in the wave is then computed as $E = E_k + E_p$. Initially, the total energy of the standing wave is given as $E_0 = \rho_w g \zeta_A^2/4$. The decay of the total energy from a simulation with a 200×200 grid and time step $\Delta t = 0.0015$s is averaged over one period of oscillation and compared with the theoretical decay rate in Fig. 5.11. Oscillations of the computed total energy of the wave is observed. This can be due to transfer of energy between the water and air, or due to effects of the finite thickness air-water interphase. However, the trend of the computed energy decay rate seems to be in agreement with the theoretical decay rate.

5.8 Verification of forced motions

In order to verify the adopted immersed boundary method for moving boundaries, simulations of forced heave motions of cylinders in the free surface were performed with the present code. Two geometries were tested, one circular and one rectangular, for which the added mass and damping coefficients were obtained from the computed pressure forces on the body. The oscillation amplitudes of the heave motion were small, such that linear potential flow theory could be used for an adequate comparison of the obtained coefficients. The hydrodynamic coefficients obtained from the simulations were also compared with data from model tests by Vugts (1968).

5.8.1 Added mass and damping coefficients in heave

For the 2D hydrodynamic problem of a body performing forced oscillatory heave motions in the free surface, the vertical hydrodynamic force acting on the heaving body can according to linear potential flow theory be expressed as

$$F_3^{HD} = -a_{33}\ddot{\eta}_3 - b_{33}\dot{\eta}_3. \tag{5.48}$$

Here, a_{33} and b_{33} are the 2D coefficients in heave for added mass and potential damping, respectively. Further, $\ddot{\eta}_3$ is the heave acceleration and $\dot{\eta}_3$ is the heave velocity of the body. The hydrodynamic coefficients a_{33} and b_{33} can be found from linear potential flow theory by solving a boundary value problem for the velocity potential ϕ using e.g. a boundary element method (BEM). Then, the hydrodynamic pressure is according to Bernoulli's equation found from the velocity potential as $p = -\rho\frac{\partial\phi}{\partial t}$, where ρ is the density of water and t is time. By integrating the hydrodynamic pressure over the mean wetted surface of the body F_3^{HD} is obtained, from which the added mass and damping coefficients can be determined. When expressing the equation of motion for the body, also the hydrostatic restoring force $F_3^{HS} = -c_{33}\eta_3$ must be included. η_3 is the heave motion and $c_{33} = \rho g B$ is the 2D restoring coefficient in heave, where B is the mean wetted beam of the body. According to Newton's second law, the equation describing the heave motion of the body is

$$m\ddot{\eta}_3 = F_3^{HD} + F_3^{HS} + F_3^{E}, \tag{5.49}$$

with m being the 2D structural mass and F_3^E the external force applied to the body in order to perform steady harmonic oscillations.

If the added mass and damping coefficients are to be found from experiments, usually the force F_3^E applied to the model is measured. Let the body motion be expressed as $\eta_3(t) = \eta_{3a}\cos\omega t$, where η_{3a} is the motion amplitude and ω is frequency of oscillation. Further, assume the measured force applied to the body is $F_3^E = F_{3a}\cos(\omega t + \delta)$, where F_{3a} is the force amplitude per unit length of the body and δ is the phase angle between the measured force and the body motion. Then, from (5.48) and (5.49), the 2D added mass and damping coefficients in heave are found as

$$a_{33} = -\frac{F_{3a}\cos\delta - c_{33}\eta_{3a}}{\omega^2\eta_{3a}} - m \tag{5.50}$$

$$b_{33} = \frac{F_{3a}\sin\delta}{\omega\eta_{3a}}. \tag{5.51}$$

The experiments by Vugts

Hydrodynamic coefficients obtained from an extensive set of model tests with forced oscillations of cylinders in the free surface was presented by Vugts (1968). Several cross-sectional geometries were tested and the added mass and damping coefficients due to small amplitude oscillations were deduced. Test parameters were the frequency of oscillation and oscillation amplitude. The experiments were conducted in the main basin of the Delft Shipbuilding Laboratory, which measures 142m of length and 4.2m of width. Here, we have only considered tests with a circular model and a rectangular model. The circular model had a diameter of 0.300m with draft 0.150m at the mean position, such that the cylinder axis was located in the calm free surface. The rectangular model had breadth 0.400m and draft 0.200m at the mean position. Further, the rectangular model had rounded bilges with bilge radius $r = 0.0025$m. The water depth for all tests was in the range 1.80m - 2.25m. However, the exact water depth for the individual test runs was not reported.

Numerical setup

Simulations in 2D of bodies in the free surface when forced to oscillate in heave have been performed with the present numerical code. A circular body and a rectangular body were tested, where the body dimensions corresponded to that of the circular cylinder and the rectangular cylinder tested by Vugts. However, the rectangular body in the numerical simulations had sharp corners and not rounded bilges as the rectangular model in Vugts experiments. Dimensions of the circular and the rectangular body are presented in Tab. 5.12. The length of the computational domain used in the simulations was $L = 76$m, which is shorter than the actual length of the basin in where Vugts experiments were conducted. By application of damping zones, wave reflections from the side boundaries of the domain were avoided. The efficiency of the damping zones depends on their length L_{dz} relative to the wave length λ of the wave to be damped. When constructing the damping zone, $\lambda = 2\pi/k$ was estimated using the dispersion relation (3.23) for the oscillation frequency tested. For all simulations $L_{dz} = 3\lambda$ was used, except for the lowest oscillation frequency tested where the length of the damping zone was $L_{dz} = 2\lambda$. The height of the domain was 3.00m and the water depth was $h = 1.80$m for all tests, which corresponded to the smallest water depth reported in the experiments by Vugts. A sketch of the computational domain is presented in Fig. 5.12. For each of the two bodies, six different oscillation frequencies of the heave motion were tested corresponding to the non-dimensional frequencies $\omega\sqrt{B/2g} = [0.25, 0.50, 0.75, 1.00, 1.25, 1.50]$. For each test frequency, the three oscillation amplitudes $\eta_{3A} = 0.01$m, $\eta_{3A} = 0.02$m and $\eta_{3A} = 0.03$m were tested. The simulations started from calm conditions with $\eta_3(0) = \eta_{3a}$ and $\dot{\eta}_3(0) = 0$, being the initial vertical body position and velocity, respectively.

Table 5.12: Dimensions of the circular model and rectangular model used in the numerical simulations. The model dimensions are equal to those for the models tested by Vugts (1968).

	Rectangle	Circle
Breadth (B)	0.40 m	0.30 m
Draft (d)	0.20 m	0.15 m

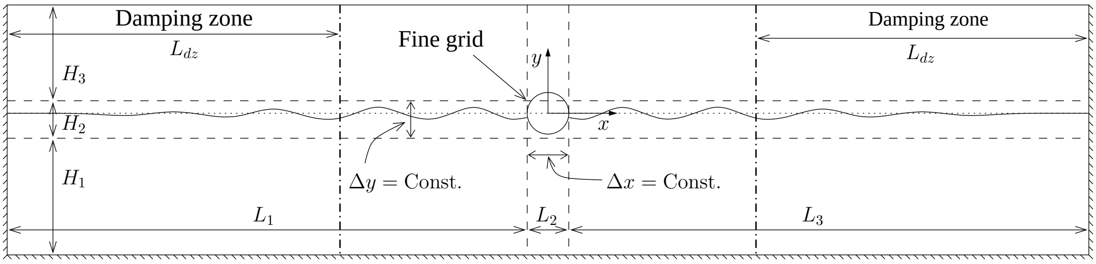

Figure 5.12: Domain used for the numerical solution to the hydrodynamical problem of a circular cylinder which is forced to oscillate in heave. The cylinder is situated in the air-water interphase. Damping zones are introduced to avoid wave reflections.

The numerical grid

A non-uniform numerical grid was constructed as follows. By dividing the computational domain into sub-regions where different gridding strategies were used, a fine grid region was created at the body position. More precisely, both the $x-$axis and the $y-$axis were divided into the three sub-regions L_i and H_i where $i = 1, 2, 3$ as shown in Fig. 5.12. The horizontal grid line spacings Δx were small and constant in L_2. Similarly, the vertical grid line spacings Δy were small and constant in H_2. Stretching of the grid by a quadratic function was performed outside the fine grid regions for both the horizontal and vertical direction, such that the grid became coarser when moving away from the free surface in the vertical direction and away from the floater position for the horizontal direction. A smooth variation of the grid spacings was ensured. The computational domain was discretized using 500 grid cells in the horizontal direction and 200 grid cells in the vertical direction. The time increment was $\Delta t/T = 1/2000$, with $T = 2\pi/\omega$ being the period of oscillation. Grid parameters for the actual grid are presented in Tab. 5.13.

Table 5.13: Grid parameters for the fine grid zone used when simulating forced heave motions of the circular and rectangular body. B is the mean wetted beam of the body and d is the mean draft. Δx and Δy are the constant grid increments in L_2 and H_2, respectively.

	$\Delta x/B$	$\Delta y/d$
Circular body	0.0100	0.0133
Rectangular body	0.0075	0.0100

High frequency viscous damping

Potential flow theory was used for comparison with the numerical results. For high frequencies of oscillation, the potential damping approaches zero as no waves are generated. However, for the rectangular body, flow separation from the bilges yields a damping force. In the following, a theoretical high frequency viscous damping is presented.

For linear potential flow theory, the kinematic- and dynamic free surface conditions for harmonic steady state oscillations can be combined to give $-\omega^2\phi + g\partial\phi/\partial y = 0$, where ϕ is the velocity potential. Taking the limit $\omega \rightarrow \infty$, we obtain $\phi = 0$ on the free surface. This means no waves are generated and the fluid velocity on the free surface is only vertical. From symmetry properties of the forced high frequency heave problem, we can by mirroring the submerged part of the body about the mean free surface, transform our problem into the problem of the double body oscillating in infinite fluid. Now, one may argue that due to vortex separation at the corners of the cylinder, the assumption of irrotational flow is violated. However, by assuming that all vorticity is compressed into thin free shear layers we can still use potential flow theory with the asymptotic free surface condition outside the free shear layers. The analogy between the rectangular cylinder in the free surface and the double body in infinite fluid makes it possible to use Morison's equation (5.52) to estimate the vertical hydrodynamic forces for high frequencies of oscillation. For the double body we get

$$F_y^{2D} = \rho A C_M \ddot{\eta}_3 + 0.5 \rho B C_D |\dot{\eta}_3| \dot{\eta}_3. \tag{5.52}$$

Here, A is the area of the cross-section of the double body, C_M is the mass coefficient, $\ddot{\eta}_3$ is heave acceleration of the body, B is the breadth, C_D is the drag coefficient and $\dot{\eta}_3$ is the heave velocity of the body. First term on the right hand side of (5.52) is the added mass force while the second term is the viscous drag force due to flow separation. Equivalent linearization of the drag term gives $F_D = B_v |\eta_A| \omega \frac{8}{3\pi} \dot{\eta}_3$ (Faltinsen 1990), where the viscous damping coefficient is $B_v = 0.5 \rho C_D B$. By assuming that the drag force on the heaving body in the free surface is half the value of the drag force on the double body in infinite fluid, we obtain the linear damping coefficient $b_{33}^v = 0.5 F_D / \dot{\eta}_3$. The non-dimensional damping coefficient for high frequencies is then

$$\lim_{\omega \to \infty} \frac{b_{33}^v}{\rho A} \sqrt{\frac{B}{2g}} = \frac{2 C_D}{3 \pi d} \hat{\omega} \eta_{3a} \tag{5.53}$$

where d is the mean draft of the cylinder and $\hat{\omega} = \omega \sqrt{B/2g}$. The drag coefficient is in general dependent on Keulegan-Carpenter number $KC = UT/B \approx 2\pi \eta_{3a}/B$ and on the Reynolds number for oscillatory flow $\mathrm{Rn} = U_m^2/\omega\nu$, where U_m is maximum velocity outside the boundary layer. For low KC-number flow ($KC < 10$), the drag coefficient for an oscillating facing square cylinder in infinite fluid is $C_D \approx 3.0$, found from experiments by Bearman et al. (1985). Using the present test parameters for the rectangular body, $KC < 0.5$ was obtained. Hence, $C_D = 3.0$ was used in (5.53) to obtain the non-dimensional viscous damping coefficient. This high frequency viscous damping was used for comparison with the damping coefficients obtained from the numerical simulations and the damping coefficients presented by Vugts.

Results and discussion

From the numerical simulations, the fully nonlinear vertical force F_y^p on the oscillating body due to the total pressure was computed. As we wanted to compare obtained added mass and damping coefficients with those from linear potential flow theory, band-pass filtering of the fully nonlinear forces time-series were performed such that the linear harmonic component was retained. Band-pass filtered was performed using $0.8/T$ and $1.5/T$ as the low and high cut-frequencies, respectively. Here, T is the oscillation period of the body for the case considered. As the vertical force obtained from the numerical simulations was found by integration of the total pressure over the body boundary, the computed force corresponded to the sum of the hydrodynamic force F_y^{HD} and the hydrostatic force F_y^{HS} from potential flow theory. Hence, the hydrostatic force was subtracted from the computed force time-series F_y^p to obtain F_y^{HD}, from which the added mass and damping coefficients could be deduced. The hydrodynamic coefficients obtained from the present numerical simulations were compared with the coefficients according to linear potential flow theory for infinite water depth. The potential flow theory results for infinite water depth were provided by Skejic (2008), where the hydrodynamic coefficients for the rectangular body were obtained with a sharp-edged body. Also the coefficients presented by Vugts (1968) were used for comparison. Added mass and damping coefficients for the circular cylinder are presented in Figs. 5.8.1 and 5.8.1, respectively. Results from simulations with the rectangular cylinder are presented in Figs. 5.8.1 and 5.8.1.

Obtained coefficients from simulations with the circular model were in good agreement with both experiments and theory, except for the lowest frequencies where some deviations from the potential flow theory were observed. This was also observed for the results obtained with the rectangular body. Deviations in the low frequency range are believed to be due to effects of finite water depth in both the experiments and in the numerical simulations. The lowest test frequency in the simulations was $\omega\sqrt{B/2g} = 0.25$. Using the dispersion relation (3.23) where $k = 2\pi/\lambda$, this means that the wave length λ of the wave generated for this oscillation frequency is $\lambda = 13.7$m for the rectangular cylinder and $\lambda = 11.42$m for the circular cylinder. Taking the uncertainty of the actual water depth h in Vugts experiments into account, $h/\lambda = 0.132 - 0.165$ and $h/\lambda = 0.158 - 0.197$ for the rectangular and circular cylinder, respectively. Using $h/\lambda = 0.5$ as the deep water limit, we should expect an effect of finite water depth for both cylinders at the lowest test frequency and also for $\omega\sqrt{B/2g} = 0.50$. This may explain the deviations between simulations and experiments for the lowest frequencies. In addition, Vugts (Vugts 1968) reported experimental inaccuracies, especially for the added mass in the low frequency range ($\omega\sqrt{B/2g} < 0.50$).

The damping coefficients for the rectangular body obtained from both experiments and simulations show some scatter in the high frequency range ($\omega\sqrt{B/2g} > 1.40$) and deviates considerably from the potential (wave making) damping, which goes to zero when the frequency of oscillation goes to infinity. This is explained by vortex shedding from the sharp edges of the rectangular body. The high frequency viscous damping coefficient obtained from (5.53) was added to the non-dimensional potential damping coefficient in Fig. 5.8.1. The high frequency theory shows reasonable agreement with experiments. The numerically obtained damping coefficients deviates some from this high frequency theory and the deviations increase for decreasing amplitude of oscillation. For low KC-numbers, the vortices separated from a sharp edged body are small compared to the dimension of the body (Bearman et al. 1985). We also note that the edges of our rectangle is not perfectly sharp, while the high frequency theory is for a sharp edged body. According to Faltinsen (1990), the bilge radius becomes important for the drag at small $KC-$values. This means that effects of finite bilge radius may contribute to the deviation between the numerically obtained damping coefficient and that from the high-frequency theory. However, we believe that the main explanation for the deviation between the numerical results and the high frequency theory is related to the fact that the same grid was used for all tested amplitudes of the body motion. Hence, the grid resolution relative to the motion of the body decreases for decreasing motion amplitude, such that the viscous flow might not be fully resolved by the grid for the smallest heave amplitudes tested. As expected, viscous flow separation was not observed for the circular body, where the small heave amplitudes yielded $KC < 1.0$.

Skin friction was not included in the numerical model. However, the numerical results has shown to be able to give good estimates of the hydrodynamic forces on oscillating cylinders in the free surface for the frequency range $0.75 < \hat{\omega} < 1.25$.

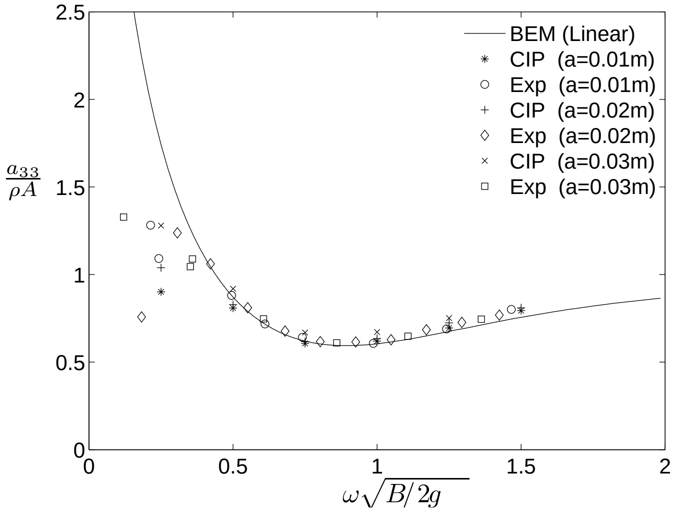

(a) Added mass

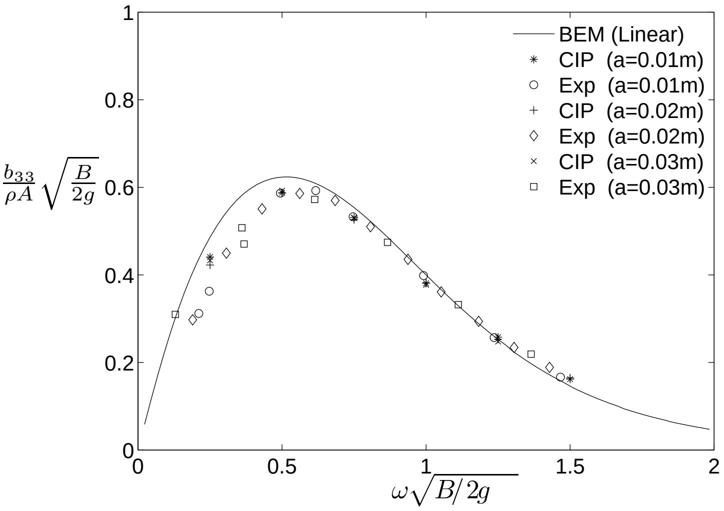

(b) Damping

Figure 5.13: Added mass and damping coefficients in heave for the semi-submerged circular cylinder with diameter $D = 0.3$m. Obtained results with the present numerical code are compared with experiments (Vugts, 1968) and linear deep water potential flow theory results (Skejic, 2007). Here, $A = \pi B^2/8$ is area of the semi-submerged circular cross-section. In the figure, a is the heave motion amplitude.

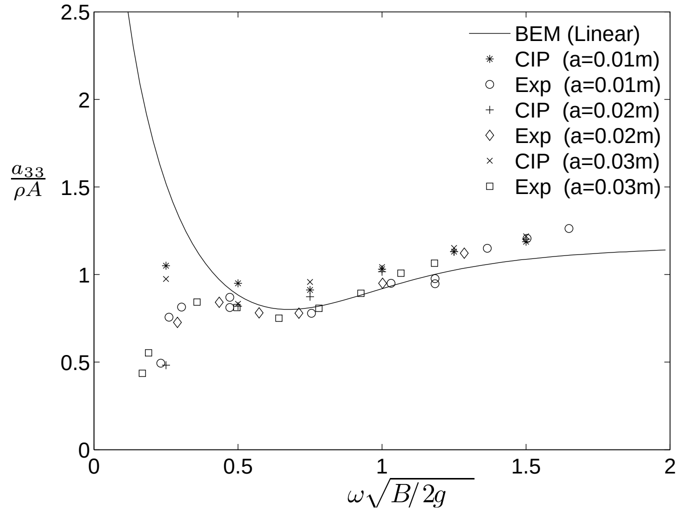

(a) Added mass

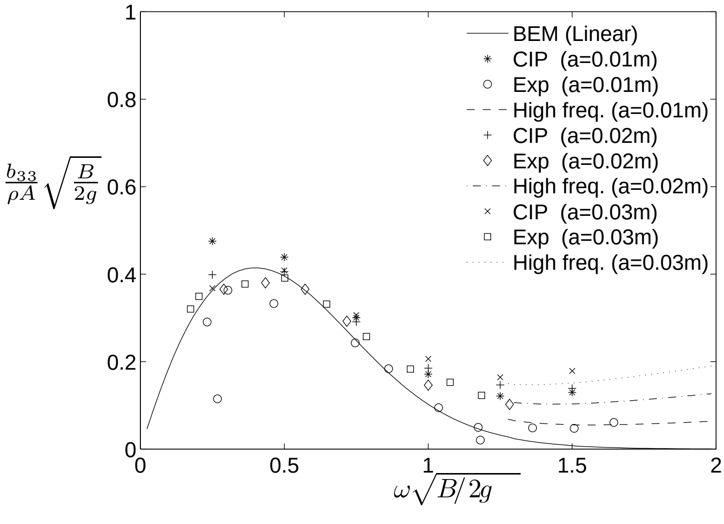

(b) Damping

Figure 5.14: Added mass and damping coefficients for the rectangular cylinder obtained with the present code compared with experiments by Vugts (1968) and linear deep water potential flow theory by Skejic (2007). Here, $A = Bd$ is the area of the semi-submerged rectangular cross-section. Beam-to-draft ratio is $B/d = 2$. In the figure, a is the heave motion amplitude.

5.9 Verification of free motions

In order to verify the numerical model for computation of free motion of floaters, i.e. the implementation of the equations of motions for the floater, we have studied free decay tests of the heave mode of motion. Free decay tests for the sway mode are considered in Chapter 8. Both a rectangular body and a circular body are tested in the simulations with free decay of the heave motion, and the computed heave motions were compared with potential flow theory results. Simulations of the rectangular body floating at equilibrium were considered.

Numerical setup and grid arrangement

The computational domain was rectangular with height H and length L, as illustrated in Fig. 5.15. The domain was partially filled with water and air. The water depth h was varied in the tests and is specified for each case considered. A coordinate system Oxy was defined in the middle of the domain with origin in the calm free surface. Positive $x-$direction was defined to the right, while positive $y-$direction was upwards. Simulations where a rectangular floater or a circular floater was introduced into the domain were performed. The rectangular floater had breadth $B = 2.0$m and height $H_b = 1.0$m, while the diameter of the circular floater was $D = 2.0$m. The mass of the floater was specified as input to the simulations, and the center of gravity (COG) was defined to be at the area center of the body. Heave motion of the body $\eta_3(t)$ was then defined to be the vertical coordinate of the instantaneous position of the COG for the body tested. A no-slip condition for the fluid velocity was imposed on the bottom boundary and on the side boundaries of the domain. No-slip was also imposed on the body boundary. The top boundary of the computational domain was modelled open with a constant reference pressure equal to the atmospheric pressure.

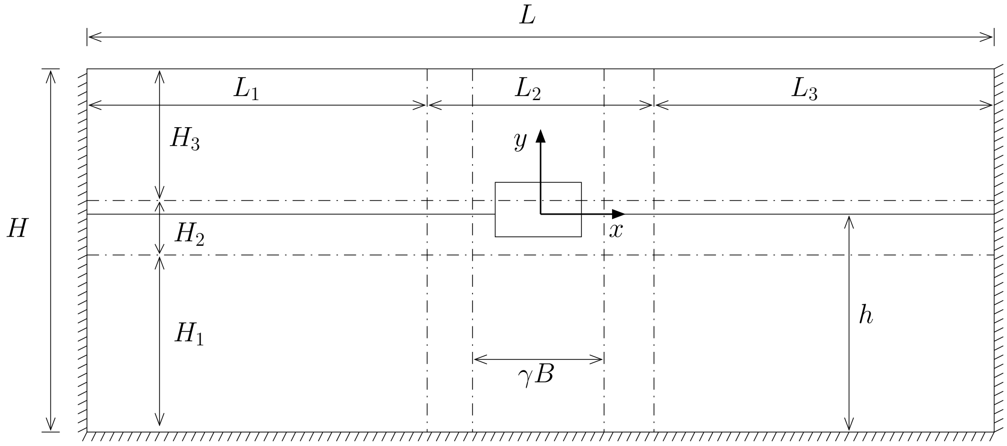

Figure 5.15: Grid arrangement used for numerical simulations of freely floating bodies. Constant grid spacing Δx was applied at the body position in the region of length γB, and in L_1 and L_3. Grid stretching was used to merge the fine grid at the model position with the coarser grid at L_1 and L_3. In the vertical direction, grid stretching is applied over H_1 and H_2, while a fine grid with constant spacing is applied over H_2.

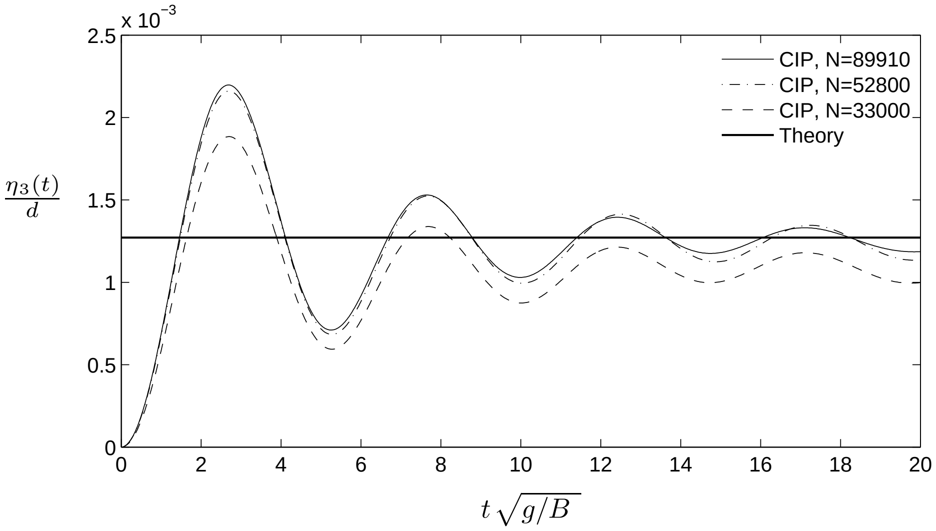

Figure 5.16: Vertical position $\eta_3(t)$ of COG of the floater obtained from numerical simulations with theoretical equilibrium position as the initial position. Results suggests that the numerical equilibrium position converges to the theoretical equilibrium position. The heave motion is normalized by $H/2$ of the floater.

Grid stretching was applied in order to reduce the CPU time for the simulations. As for the grids used in the simulations of bodies with forced motions in the previous section, the computational domain was also here divided into regions L_i and H_i with $i = 1, 2, 3$, where different gridding strategies were applied. The different grid zones are depicted in Fig. 5.15. The horizontal grid line spacing Δy was kept constant in the free surface zone H_2, while the grid line spacing was described by an exponential function in H_1 and H_3. The spacings between the vertical grid lines, Δx, was constant over a region γB at the model position. Away from the model position, in L_1 and L_3, constant but larger grid line spacings were used. Stretching of the grid was used in L_2 to merge the fine grid at the model position with the coarser grid in L_1 and L_3. Smooth variations of the grid increments Δx and Δy were ensured.

5.9.1 Test of equilibrium

First we consider the most simple verification test case for a freely floating body, which is the hydrostatic problem of a body floating at its equilibrium position. The rectangular body was placed with the COG at the origin, i.e. $\eta_3(0) = 0$. As the COG was placed at the area center of the body, the initial draft was $d = 0.5$m. For this to be the draft at equilibrium of the body, the body mass was estimated using Archimedes law. Archimedes law states that the weight of a body floating in water is equal to the weight of the water displaced by the body. Hence, the body mass was found as $m = \rho_w B d$, where ρ_w is the mass density of water. Numerical simulations with the given initial conditions were performed on three grids of different resolution in order to check for grid convergence of the computed equilibrium position. Computed time-series of the vertical position $\eta_3(t)$ of the COG of the rectangular body are compared in Fig. 5.16. The results shows that the floater starts to oscillate as in a free decay test. This means that the initial position of the body does not correspond to the equilibrium position of the body with the given mass. Although a steady state condition of the vertical position was not reached within the length of the simulations, the computed heave motion η_3 seemed to converge towards a positive value less than 1mm or 0.15% relative to the draft. This can be explained as follows. Due to the mass density of the air, ρ_a, also the part of the computational domain occupied by the air represents a pressure gradient field. Hence, also displacement of air by the body yields a buoyancy force. Balance of static forces on the rectangular body floating with zero roll angle at equilibrium with draft d_e can be expressed as $mg = \rho_a g B(H_b - d_e) + \rho_w g B d_e$, where g is acceleration of gravity. Thus, the theoretical draft of the rectangular body when floating with zero roll angle at equilibrium is

$$d_e = \frac{m - \rho_a A}{B(\rho_w - \rho_a)}, \tag{5.54}$$

where $A = BH_b$ is the area enclosed by the body boundary. The theoretical equilibrium position is then $\eta_3(t \to \infty) = d - d_e$, which is shown in Fig. 5.16 as the straight horizontal line. We observe that the heave motion of the rectangular body seems to converge towards a value in agreement with the theoretical equilibrium position.

5.9.2 Free decay of the heaving motion

When simulating free decay tests in heave of the floaters, we wanted the draft at equilibrium for the rectangular body and the circular body to be $d_e = 0.5H_b$ and $d_e = 0.5D$, respectively. Based on the above discussion, the body mass for the free decay tests was obtained as $m = 0.5A(\rho_a + \rho_w)$ where $A = BH_b$ for the rectangular floater and $A = \pi D^2/4$ for the circular floater. Then $\eta_3 = 0$ corresponds to the equilibrium position.

Simulations were performed with the floaters initially being positioned in the free surface with a vertical offset from the equilibrium position and with $x = 0$ as the horizontal coordinate of the COG. At time $t = 0$ the floater was released and started an oscillatory heave motion until equilibrium was reached. The frequency of oscillation approached the heave natural frequency for the model considered. For the case of the rectangular floater with beam to draft ratio $B/d = 4$ at equilibrium, the natural period in heave is $T_n = 2.195$s according to potential flow theory.

The oscillation amplitude of the vertical motion obtained from numerical simulations will decay due to wave radiation damping and due to viscous effects from flow separation at the sharp corners of the model.

Skin friction may also have contributed to the damping of the heave motion, but is not included in the numerical model.

Obtained time series of the heaving motion of the floaters are compared with potential theory results provided by Yeung (1982) for the case of a rectangular model, and results by Maskell and Ursell (1970) based on previous work by Ursell (1964) for the case of the circular model. The data used for comparison are obtained from deep water conditions.

Influence of water depth

Three simulations where the water depth h is varied from $h/\lambda = 0.5$ to $h/\lambda = 1.0$ are compared with data from Yeung (1982) in Fig.5.18. Here λ is the wave length of the linear deep water wave with wave frequency is equal to the natural frequency of the heaving

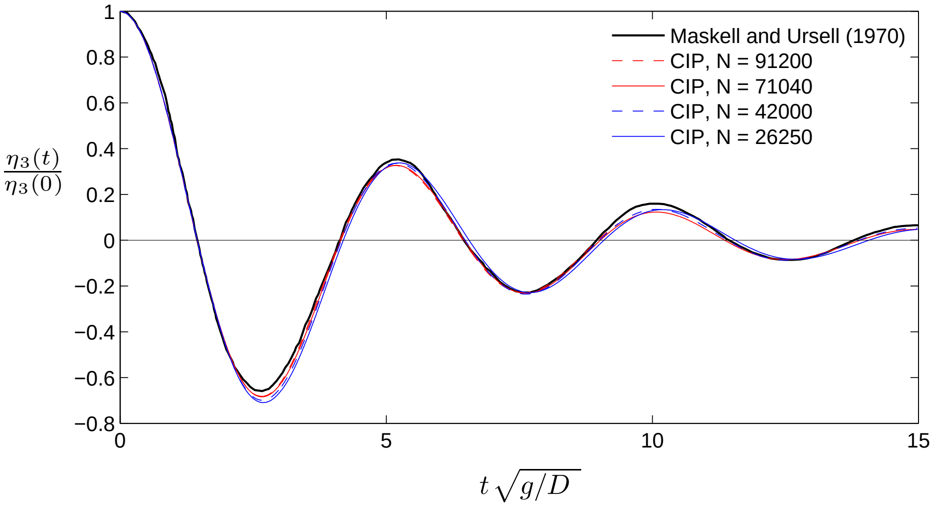

Figure 5.17: Vertical motion $\eta_3(t)$ of COG of the circular floater obtained from numerical free decay tests. The vertical motion is normalized by the initial vertical offset from equilibrium position, which is 5% of the radius of the cylinder.

motion of the floater. The resulting time series of the vertical motion shows that a water depth of $h = 0.5\lambda$, which is commonly used as a limit for deep water conditions, is not sufficient to give a water depth-independent solution. The length of the domain is here set to $L = 7\lambda$.

Influence of domain length

Initially when the floater starts to move, all wave frequencies will be excited theoretically. This means there is a possibility for some of the radiated waves to travel to the end of the computational domain and reach back to the model position within the time window of simulation. Further is the data used for comparison for the free decay tests obtained from BEM-calculations with deep water conditions. Hence the length of the computational domain and the water depth are physical parameters that will influence the results of the heaving motion if they are taken too small. A parameter study is performed for the case of the heaving rectangular cylinder, where the length of the computational domain and the water depth is varied systematically. This is discussed in the following.

Now, the water depth is kept constant at $h/\lambda = 1.0$, while the length of the domain is varied. The grid spacing Δx is held constant when the length of the domain is extended, such that the resolution of the radiated waves is not affected by the domain elongation. Results for the heaving motion of the rectangular cylinder obtained using three different domain lengths $L = [5\lambda, 7\lambda, 9\lambda]$ are presented in Fig.5.19. The obtained time series deviates from the theory towards the end of the simulation. Since this deviation depends on the domain length, it is reasonable to believe that wave reflections from the side walls of the domain influence the results.

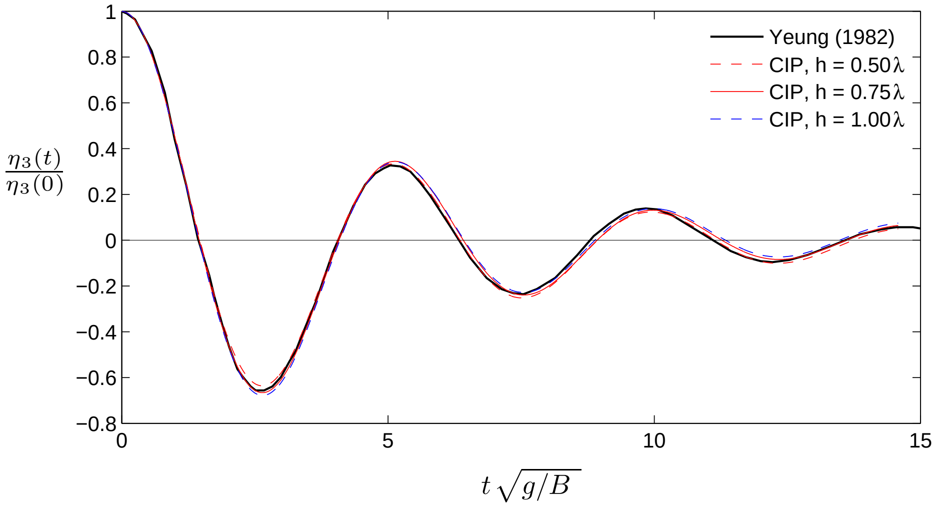

Figure 5.18: Vertical motion $\eta_3(t)$ of COG of the rectangular floater obtained from numerical simulations of free decay tests for different water depths h. The vertical motion is normalized by the initial vertical offset from equilibrium position, which is 2.5% of the draft.

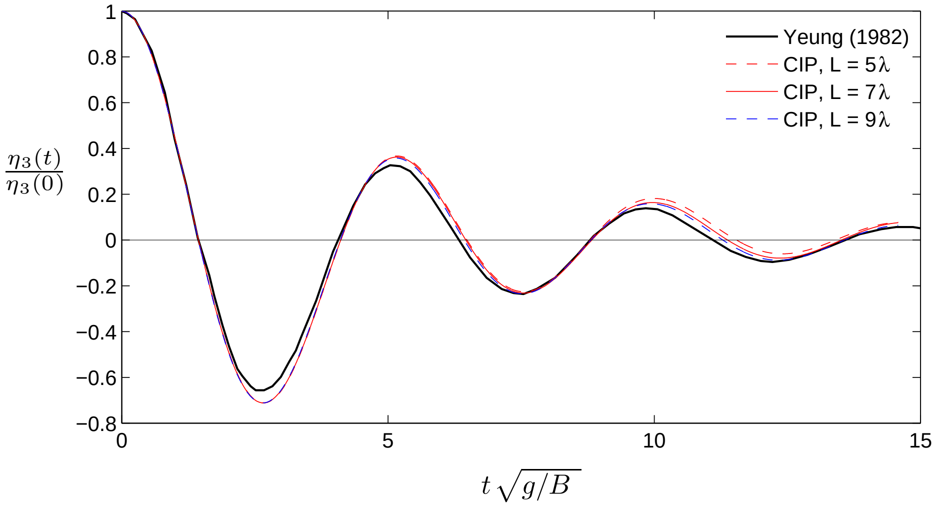

Figure 5.19: Vertical motion $\eta_3(t)$ of COG of the rectangular floater obtained from numerical simulations of free decay tests for different lengths L of the domain of computation. The vertical motion is normalized by the initial vertical offset from equilibrium position, which is 2.5% of the draft.

5.10 Summary of the verification tests

In this chapter, we have presented many of the cases that have been tested to verify the implementation of the present numerical model. First, the different steps of the adopted fractional step method were tested separately, where we concluded that the implementation of all steps was correct as obtained results were in agreement with theory. Then, the complete flow solver was tested for one-phase flow and for two-phase flow problems. The introduction of a solid body inside the domain was tested, and satisfaction of the no-slip boundary condition on the body boundary was checked. The implemented method for calculation of pressure forces on the body was verified. Further, the heave equation of motion for the body was verified through simulations of free decay tests.

Based on the results from all of these verification tests, we feel confident that our numerical model is correctly implemented. Hence, if our mathematical model is an adequate representation of the reality, we believe that our numerical wave tank (NWT) will be a good tool for investigation of wave forces and wave induced motions of the floaters of fish farms.

Chapter 6

Model tests

As a part of the present study, two sets of model tests have been conducted. The first set was accomplished in November 2006 and the other in September-October 2008. In both experiments the models tested were cylinders oriented with the cylinder axis horizontally in the free surface zone and subjected to regular waves. Two-dimensional flow conditions were sought, such that measurements could be compared with results from numerical simulations with the 2D numerical wave tank.

In the model tests conducted in 2006, the wave loads on fixed horizontal cylinders in the free surface were studied. Focus were put on nonlinear effects like wave over-topping on the models and how such events influence the wave loading. Measurements were intended for use as validation data to the 2D NWT for computations of wave loads on fixed bodies in the free surface. Results from these experiments have been published in two conference papers (Kristiansen and Faltinsen 2008a; Kristiansen and Faltinsen 2008b). Some results have also been utilized by Vestbøstad et al. (2007).

The experiments from 2008 were addressing the wave induced motions of a moored circular cylinder in regular waves. Again we wanted to obtain validation data for the NWT, but now with respect to the computation of nonlinear wave-induced body motions. Results from these experiments were published in Kristiansen and Faltinsen (2009).

6.1 Over-topping on fixed horizontal cylinders in waves

Model tests addressing wave loads on fixed horizontal cylinders in regular waves were conducted in November 2006. Wave excitation forces on the models in the horizontal in-line direction and in the vertical direction were measured. Also measurements of the wave elevation at some positions in the flume were performed. As the measurements were to be used for comparison with results from numerical simulations with the 2D NWT, we wanted the flow conditions in the model tests to be two-dimensional. We found that an appropriate wave flume for our model tests was the narrow wave flume at the Division of Marine Civil Engineering, NTNU. This flume is 26.5m long and 0.60m wide and has sidewalls of transparent Plexiglas, which is beneficial for good visual observation of the waves. The maximum possible water depth in the flume is 0.65m. The flume is equipped with a piston-type wavemaker from DHI (www.dhi.com), with the wave-board ranging from the bottom of the flume to above the free surface. An active wave absorber control system (AWACS) is included in the wavemaker software, which absorbs the waves reflected from

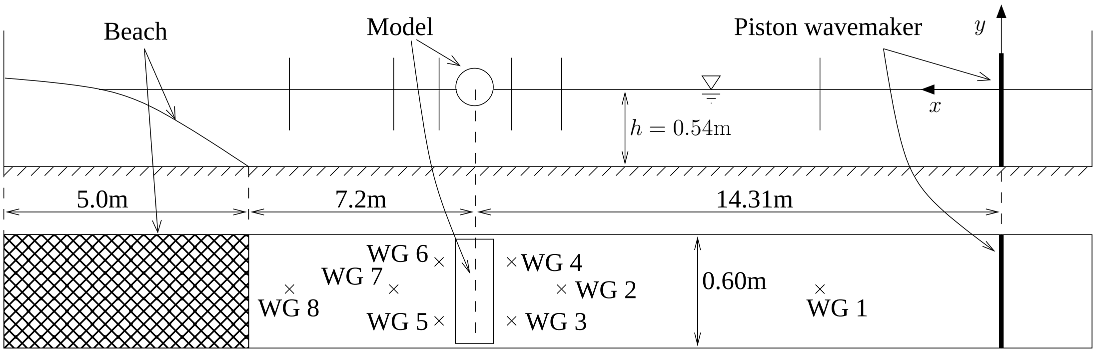

Figure 6.1: Schematic view of the test setup in the flume from the model tests in 2006. On top a side view of the flume is shown, while a top view is depicted below. Positions of the eight wave gauges (WG) are marked by vertical lines and "×".

Table 6.1: Main dimensions of the two models used in the experiments. Both models are made of aluminium and are stiff structures.

	Quantity	Symbol	Value
Circular cylinder:	Diameter [m]	D	0.300
	Length [m]	l	0.590
Rectangular cylinder:	Breadth [m]	a	0.300
	Height [m]	b	0.250
	Length [m]	l	0.590

the model to the wavemaker. This allows for long test runs without the time limitation caused by waves being reflected from the model to the wavemaker and back to the model position. In addition, the AWACS showed to be effective for damping out waves and making the water surface calm after each test run, reducing the waiting time between the runs. At the opposite end of the flume from the wavemaker a 5m long parabolic beach is mounted for wave absorption. The beach is covered by a rough, porous mat to increase its energy dissipation ability. A qualitative sketch of the flume is presented in Fig. 6.1. The wavemaker software applies linear wavemaker theory to estimate the necessary stroke of the wave board for generating waves with a given wave height. However, the predicted stroke is often not sufficient for generating waves with the input wave height. One explanation of this problem is leakage around the wave board, which causes a reduced efficiency of the wavemaker (Hughes 1993). To compensate for the reduced efficiency, the software provides a fudge factor C_s for tuning the stroke of the wave board such that the input wave height is obtained.

6.1.1 Models, test setup and instrumentation

Two cylindrical models were tested. One model had a circular cross-section, while the other had a rectangular cross-section. The length (transverse dimension) of both models was $l = 0.590$m, leaving a 5mm clearance to both side-walls of the flume to avoid contact. Model dimensions are listed in Tab. 6.1. The model tested was fixed at a distance $L_m = 14.31$m from the wavemaker, measured from the mean position of the paddle to

Figure 6.2: From the wave laboratory. The circular model, seen to the far left, is mounted to the rig. The photo is taken towards the wavemaker side of the flume.

the cylinder axis. This means the distance from the model to the start of the beach was about 7.2m. It was ensured that the cylinder axis was perpendicular to the side walls of the flume and hence parallel to the wave crests of the incoming waves. The water depth during all tests was $h = 0.54$m.

Choice of test parameters

Test parameters were the wave period T, wave steepness ε and model draft d. Only regular waves were considered. Ten wave periods were deduced from wave lengths λ_0 of deep water waves, linearly spaced from 5 to 15 times the beam of the models. This yielded wave periods in the range from 0.98s to 1.70s. Three wave steepnesses were tested. The wave steepness were based on deep water waves as $\varepsilon = H_0/\lambda_0$, where H_0 is the deep water wave height. For long waves relative to the water depth, effects of finite water depth will influence on the wave height and the wave length and make a wave generally steeper than the corresponding deep water wave. This causes the actual wave steepness in the flume to differ, increasingly with the wave period, from the corresponding deep water wave steepness. Ten wave periods and three wave steepnesses yielded 30 different wave conditions, which are presented in Tab. 6.2. Each model was tested at three different drafts for all wave conditions. The non-dimensional parameter κ was introduced, which is the draft normalized by the height of the model cross-section. This means that for the circular cylinder $\kappa = d/D$, while for the rectangular cylinder $\kappa = d/b$. For both models and all the wave conditions, $\kappa = [0.2, 0.5, 0.8]$ were tested. A test matrix was made based on the three test parameters which was wave period, wave steepness and model draft. A run index was composed of four numbers, where the first one was used to specify

Table 6.2: Characteristics of the test waves. Due to effects of finite water depth, the height, length and hence also the steepness of the generated waves will be modified. $\varepsilon = H_0/\lambda_0$ is the deep water wave steepness, while H and λ are the computed wave height and wave length from linear potential flow theory for finite water depth ($h = 0.54$m).

			$\varepsilon = 1/50$		$\varepsilon = 1/30$		$\varepsilon = 1/20$	
T [s]	λ_0 [m]	λ [m]	H [m]	H/λ	H [m]	H/λ	H [m]	H/λ
0.981	1.503	1.474	0.029	0.0197	0.048	0.0329	0.073	0.0493
1.084	1.835	1.760	0.035	0.0198	0.058	0.0329	0.087	0.0494
1.179	2.170	2.026	0.041	0.0200	0.068	0.0333	0.101	0.0499
1.266	2.502	2.267	0.046	0.0204	0.077	0.0339	0.115	0.0509
1.348	2.837	2.492	0.052	0.0209	0.088	0.0348	0.130	0.0522
1.425	3.170	2.701	0.058	0.0214	0.097	0.0357	0.145	0.0536
1.498	3.504	2.898	0.064	0.0221	0.107	0.0368	0.160	0.0552
1.568	3.839	3.082	0.070	0.0228	0.117	0.0380	0.176	0.0569
1.634	4.169	3.256	0.076	0.0235	0.127	0.0391	0.191	0.0587
1.698	4.502	3.423	0.083	0.0242	0.138	0.0403	0.207	0.0605

geometry and submergence, except for the 8000-series which is the wave calibration tests. The second number indicated the wave steepness while the third referred to the wave period. Finally, the last number in the run index was reserved for repetition tests or re-runs. Some causes of re-runs were *deleted values* during data acquisition because the measured forces or wave elevation caused voltage signals that were out of range relative to that specified in the calibration file for the logging system software. The test matrix is presented in Tab. C.1 in appendix C.1.

Data acquisition

Wave excitation forces on the model for the vertical direction and the horizontal in-line direction were measured. Free surface elevation was also measured. Data acquisition was performed as described below.

Surface elevation was measured with eight wave gauges distributed in the flume. The wave gauges are denoted WG 1 - WG 8 and their position in the flume are qualitatively shown in Fig. 6.1. The wave gauges were of the capacitance type and composed of two parallel steel rods, each 3mm thick, 7mm apart. Close to the model, two wave gauges were placed at the same longitudinal position but at different positions in the transverse direction in order to check for two-dimensionality of the waves. This was done on both the wavemaker side and the beach side of the model.

Wave run-up was measured using two strips of copper tape that were glued onto the model surface on the side facing the wavemaker. The copper tape was 12mm wide and the strips were separated by 7mm.

Excitation forces were measured as the clamping forces of the models. For this purpose, three force transducers (force rings) were mounted between two 12 mm thick aluminium plates. All three force transducers were aligned in the same direction. Each force transducer was able to measure forces in three directions. Due to lack of channels on the amplifier, forces were only measured in the vertical direction and in the horizontal in-line direction.

Local free surface elevation at the model position were captured by a high speed camera of type IDT, using a sampling frequency of 200 frames per second (fps). For each run, 600 frames were recorded, which for the given sampling frequency covers 3 seconds in real time. During recording with the high speed camera, a voltage signal was sent to the logging system such that the exact time window of the recording within the test run could be obtained.

Wavemaker piston motion was logged. At start-up, the wave-board had a linear gain up of the piston motion, lasting for 5 seconds, until full gain was reached.

A Hottinger-Balwin KWS amplifier was used to amplify the voltage signals from the force transducers, while a separate Hottinger amplifier was used for the wave probes. A DHI Filter Cabinet 154/IF was used for analog to digital conversion of the signals. No filtering of the signals was performed before logging. Acquisition data were stored with a sampling frequency of 200Hz by the DHI Wave Synthesizer software, except from the wave-maker motion which was logged with a sampling frequency of 60Hz. Typical test duration (duration of data acquisition) was 60 seconds. That includes 10 seconds of data acquisition before the linear gain up of the wave maker.

6.1.2 Measurements and observations

All measurements were band pass filtered with $f_{low} = 0.35$Hz and $f_{high} = 6.0$Hz as the lower and higher cut-off frequencies, respectively. A one sided Gaussian envelope was used at the cut-off frequencies in order to avoid beating effects in the reproduced time series. The linear-, second- and third order harmonic components of the measured signals were studied. Repetition tests were conducted for five of the test conditions, where five repetitions were performed for each test. To quantify the repeatability of a measured variable, the relative error defined as $\sigma/\mu \cdot 100\%$ was used, where μ is the mean value and σ is the standard deviation of the variable considered. Relative error of the force amplitude in the steady state regime was less than 1.5%, even for cases where wave overtopping on the model occured. For the measured wave elevation, the relative error was 4% or less. Thus, the obtained time series showed good repeatability. Statistics from the repetition tests are presented in appendix C.1.1. Measured stroke of the steady state piston motion S and the resulting fully non-linear wave amplitudes ζ_A^+ and ζ_A^- measured with wave gauge WG3 from the wave calibration tests are listed in Tab. 6.3. Here, ζ_A^+ and ζ_A^- refer to the positive and the negative wave amplitude, respectively. WG 3 is located 0.356m from the cylinder axis towards the wavemaker. The fudge factor $C_s = 1.1$ in the wave maker software was necessary in order to obtain the wanted wave height. The need for scaling of the piston stroke estimated by linear potential flow theory (linear wavemaker theory) is explained by energy loss due to leakage through the gap between the wave board and the flume walls (Hughes 1993).

Fully non-linear force amplitudes A^+ and A^- (positive and negative respectively) in the

Table 6.3: Measured wave maker stroke S and measured resulting fully non-linear wave amplitudes (positive ζ_A^+ and negative ζ_A^-) at wave gauge 3 from the wave calibration tests. H_0/λ_0 is the corresponding deep water linear wave steepness.

		$H_0/\lambda_0 = 1/50$			$H_0/\lambda_0 = 1/30$			$H_0/\lambda_0 = 1/20$		
T_p [s]	λ [m]	S [m]	ζ_A^+ [m]	ζ_A^- [m]	S [m]	ζ_A^+ [m]	ζ_A^- [m]	S [m]	ζ_A^+ [m]	ζ_A^- [m]
0.981	1.472	0.017	0.015	-0.014	0.030	0.025	-0.023	N.A.	N.A.	N.A.
1.084	1.760	0.023	0.018	-0.017	0.038	0.032	-0.027	0.057	0.051	-0.039
1.179	2.024	0.029	0.020	-0.019	0.048	0.036	-0.032	0.072	0.059	-0.044
1.266	2.267	0.034	0.024	-0.022	0.057	0.041	-0.034	0.086	0.064	-0.049
1.348	2.491	0.041	0.025	-0.023	0.069	0.042	-0.038	0.103	0.072	-0.050
1.425	2.700	0.048	0.027	-0.026	0.080	0.047	-0.042	0.121	0.081	-0.054
1.498	2.896	0.055	0.030	-0.027	0.092	0.051	-0.044	0.139	0.088	-0.057
1.568	3.081	0.063	0.032	-0.028	0.104	0.057	-0.045	N.A.	N.A.	N.A.
1.634	3.257	0.070	0.034	-0.030	0.117	0.065	-0.044	0.176	0.096	-0.065
1.698	3.424	0.079	0.038	-0.031	0.131	0.063	-0.052	N.A.	N.A.	N.A.

steady state regime for the circular cylinder are plotted in Fig. 6.3 and for the rectangular cylinder in Fig. 6.4. Measured forces are normalized by the hydrostatic buoyancy force $F_B = \rho g V_0$ corresponding to the fully submerged model. Thus, $V_0 = (\pi/4)D^2 l$ for the circular cylinder and $V_0 = abl$ for the rectangular cylinder. Figures 6.5 and 6.6 show that when $\kappa = 0.5$, the measured forces are nearly linear with respect to the wave steepness for both models. Nonlinearities of the wave excitation forces are observed when $\kappa = 0.2$ and $\kappa = 0.8$. The nonlinearities are most pronounced for the circular cylinder.

Over-topping did occur on both models for all wave periods when $H_0/\lambda_0 = 1/20$ and $\kappa = 0.8$. For the circular cylinder, the over-topping wave was attached to the model surface during the whole over-topping process as shown in Fig. 6.7. Over-topping on the rectangular cylinder was somewhat different. The over-topping wave had a dam-break like behaviour, until the front of water separated at the leeward top edge of the model.

6.1.3 Discussion of possible errors

When using model tests for validation of numerical models, it is easy, but dangerous, to consider model test results as the “true story”. Generally, as for numerical computations, also model test results may contain some or considerable errors. Thus it is important to identify the possible sources of errors in the experiments and quantify these. We distinguish between precision errors and biased errors. Precision errors are somewhat easy to handle since they are stochastic of nature and can be estimated by repetition tests. From the computed relative error in the repetition tests presented, we see that precision errors are small. Biased errors are systematic errors that can be difficult to discover. However, there are general procedures for how to proceed in order to discover biased errors. One procedure is to repeat the experiment at different replication levels (Ersdal 2004), e.g. by repeating the experiment after re-rigging, or by repeating the experiment in a different laboratory. We will now discuss some possible sources to errors in the experiments.

Two-dimensional flow conditions were sought in the tests. This means 3D flow effects may lead to biased errors in the measured free surface elevation as well as in the measured

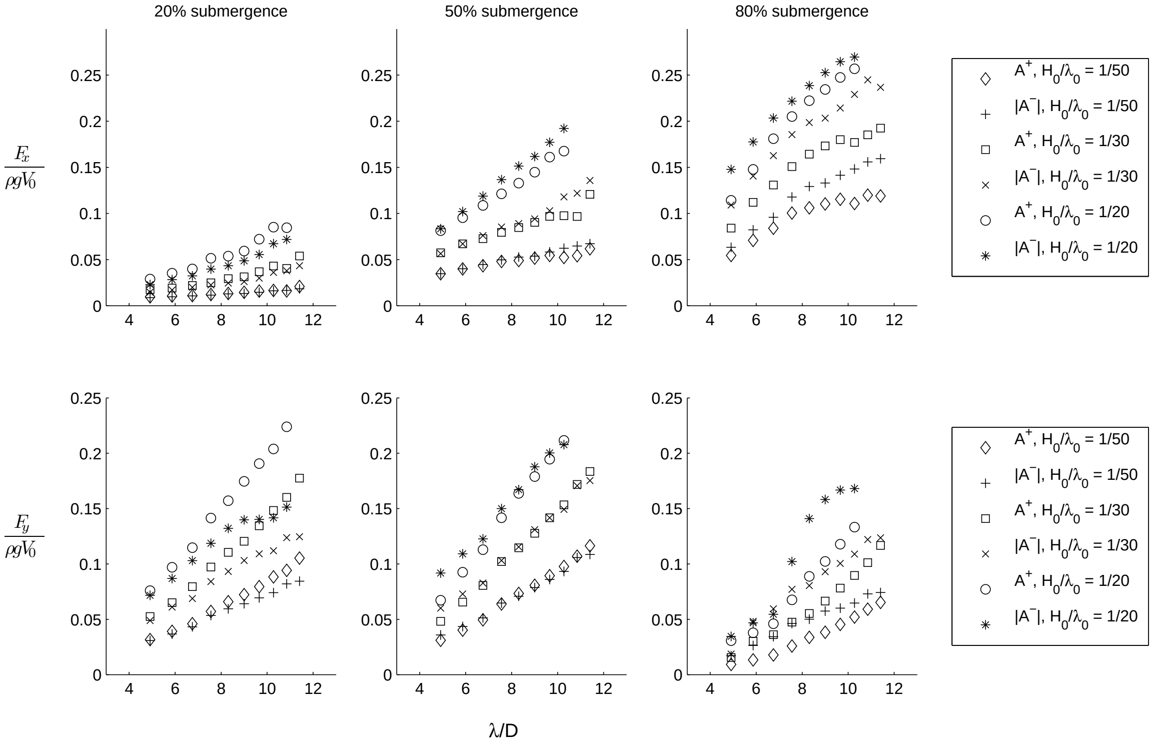

Figure 6.3: Measured positive and negative fully non-linear force amplitudes from experiments with the circular cylinder. Here, $V_0 = (\pi/4)D^2 l$. F_x is the measured in-line horizontal force in the positive wave propagation direction, while F_y is the measured vertical force positive upwards.

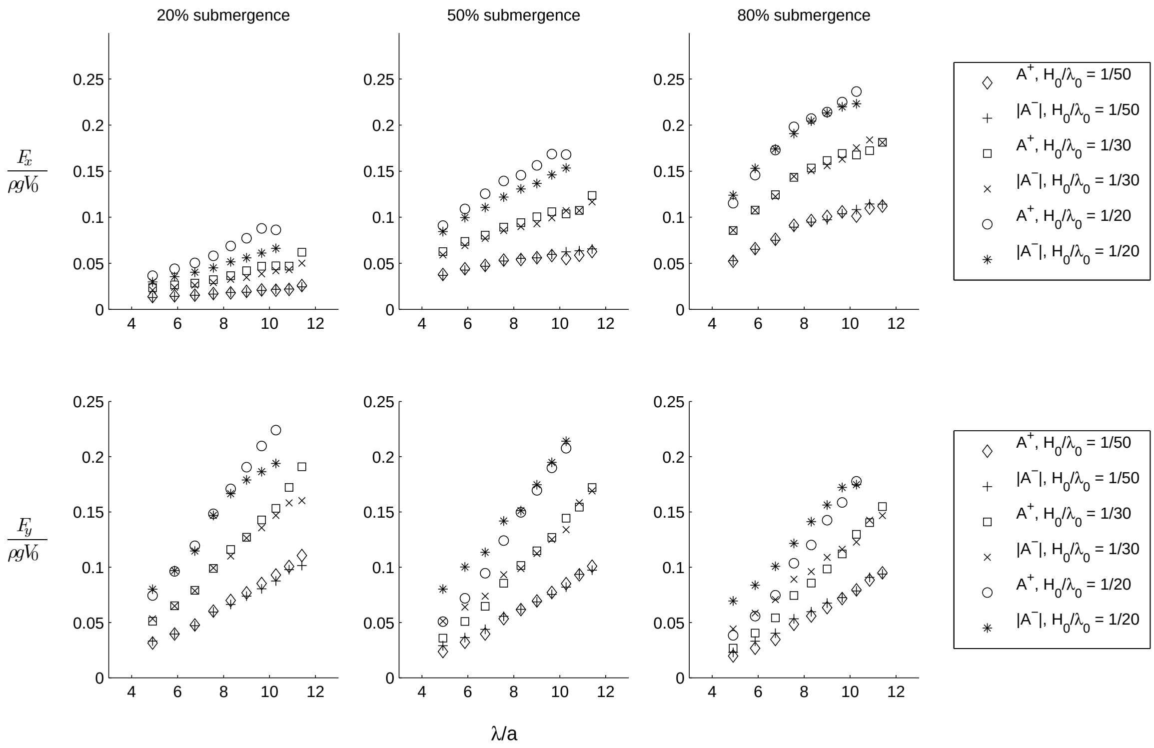

Figure 6.4: Measured positive and negative fully non-linear force amplitudes from experiments with the rectangular cylinder. $V_0 = abl$. F_x is the measured in-line horizontal force in the positive wave propagation direction, while F_y is the measured vertical force positive upwards.

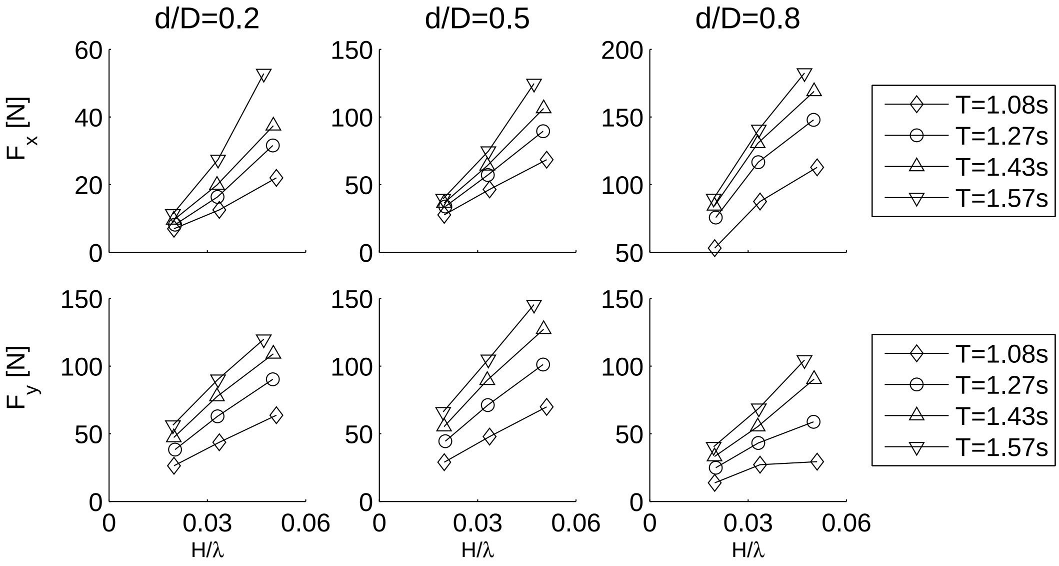

Figure 6.5: Mean peak-to-peak force amplitudes for the circular cylinder as function of mean incident wave amplitude. Nonlinearities of the measured forces are observed when the normalized draft is $d/D = 0.2$ and $d/D = 0.8$.

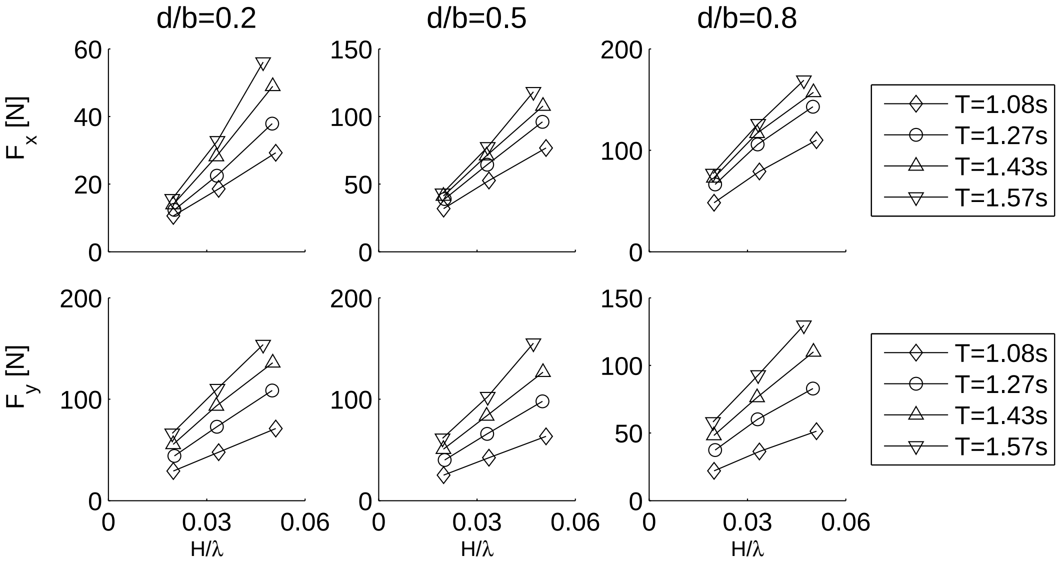

Figure 6.6: Mean peak-to-peak force amplitudes for the rectangular cylinder as function of mean incident wave amplitude.

forces. Examples of such 3D effects are transverse sloshing, which is standing waves in the transverse direction of the flume. The natural periods of the first, second and third sloshing mode is $T_1^t = 0.880$s, $T_2^t = 0.620$s and $T_3^t = 0.506$s. These sloshing periods are all smaller than the test wave periods. However, these natural periods could still be excited by higher harmonic components of the tested waves in combination with imperfections of the wavemaker or the model. An example of such imperfections are the gaps between the model and the side walls of the flume, which may cause disturbances on the free surface. There is also a gap between the wave-board and the tank walls which is of order 1cm that may excite the transverse sloshing. To check if transverse sloshing did appear in the experiments, two wave gauges were distributed in the transverse direction of the flume close to the model position. This was done on both sides of the model (cf. Fig. 6.1). Transverse sloshing was observed for some of the tests with the steepest waves ($\varepsilon = 1/20$). The second sloshing mode was observed for some tests with the wave periods $T = 1.43$s and $T = 1.50$s. The first sloshing mode was observed for some tests with wave period $T = 1.57$s, which is close to two times the sloshing period for the first mode. Sloshing can also occur in the longitudinal direction of the flume. The first sloshing mode for the longitudinal direction is referred to as seiching. Due to the length of the flume relative to the water depth, seiching is characterized by a shallow water wave. The seiching period of the flume (first natural period of longitudinal sloshing) is $T_1^s = 23$s. No seiching of significance was observed in the experiments.

6.1.4 Summary of results

Wave calibration tests was performed for all test wave conditions and a fudge factor of $C_s = 1.1$ to scale the stroke of the wave board was needed to obtain the input wave height. The generated waves showed good repeatability, with a relative error less than 4% for the wave heights measured from the repetition tests. Waves overtopping on the

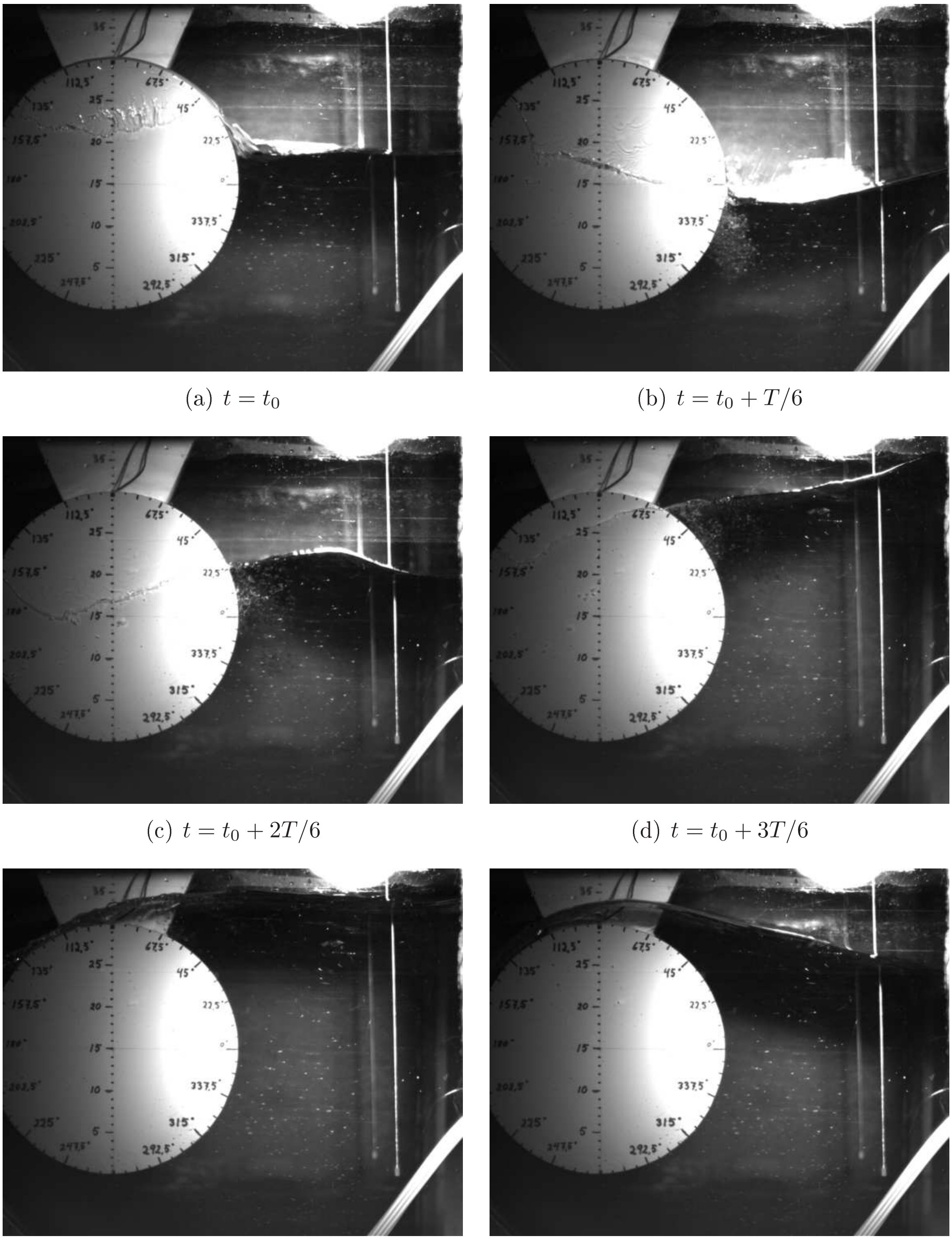

(a) $t = t_0$

(b) $t = t_0 + T/6$

(c) $t = t_0 + 2T/6$

(d) $t = t_0 + 3T/6$

(e) $t = t_0 + 4T/6$

(f) $t = t_0 + 5T/6$

Figure 6.7: Over-topping on the circular cylinder for $d/D = 0.8$, $T = 1.348$s and $H_0/\lambda_0 = 1/20$. The wave is propagating from the right to the left. In (b), air is sucked from the surface into the water domain due to a low pressure zone at the right hand side of the model. The surface of the over-topping wave is smooth and the wave does not separate from the body.

models occured for some of the test conditions. However, no out-of-water event was observed. Also the repeatability of the measured forces were good with relative errors less than 1.5%, even for the tests with overtopping.

6.2 Wave induced motions of a moored horizontal cylinder

Model tests were performed in the turn of the month from September to October 2008 with the purpose to study the wave induced motions of a moored horizontal cylinder, and to obtain validation data for the NWT. Only regular waves were considered.

We wanted to investigate the wave-induced motions of floaters of fish farms. There exist many configurations of floaters and floating collars for fish farms, so we decided to choose a geometry for our model which was representative for fish farms. Hence our choice felt on a cylinder with a circular cross-section. The model scale was based on an existing steel-structure fish farm designed for exposed locations. This structure is characterized by square floating collars that are formed by four circular cylinders that are rigidly connected. The diameter of the cylinders in full scale is 1m. The global structure is elastic, and typical values for the wet natural period of the first elastic mode of the floater are in the order of 2-3 seconds (Lien 2009). This is considered when deciding the characteristics of the mooring line system in the experiments.

6.2.1 The laboratory, model and test setup

The experiments were conducted in a narrow wave flume at the Department of Marine Technology, NTNU. The flume is constructed from steel frames with glass-plates for the walls and bottom. This makes the flume very suitable for visual observations of waves, which in addition to availability and low cost was the main reason for choice of laboratory. Further, the fact that the flume is narrow makes it also beneficial for tests where 2D flow conditions are wanted. The flume measures 13.67m of length, 0.60m of breadth and 1.30m of height, and is designed for a water depth of 1.0m. For wave generation, the flume is equipped with a single-flap wavemaker where the paddle is hinged 10cm above the bottom of the flume and extends through the free surface. The wavemaker is computer-controlled and capable of generating regular waves as well as irregular waves. Unfortunately, the wavemaker software do not provide an active wave absorption control system. This put a limit on the duration of the test runs. At the opposite end from the wavemaker, a conventional beach with a parabolic-arc shape is mounted for wave absorption.

The model scale was 1/10 and a cylindrical model with a circular cross-section of diameter $D = 0.100$m was tested. The model was composed of a 0.580m long circular pipe of transparent plexi-glass with a inner core of divinycell. Wall thickness of the pipe was 3.1mm. The model was considered rigid. We wanted the model mass to be constant during the tests, which means we had to avoid water to enter the interior of the model. Since divinycell absorbs water, the pipe had to be sealed at the ends. For this purpose tight plugs of polyethylene were cut on the lathe such that they perfectly entered the pipe. In addition, waterproof clay was used for sealing the joints. Due to the transparency of the pipe, any leakage would easily be discovered. However, control weighing of the model after several hours in water was performed to check for waterproofness. To reduce 3D-flow effects at the ends of the model, end-plates made from transparent plexi-glass were applied. The end-plates were 5mm thick and shaped circular with diameter of 0.30m. This means the overall length of the model with the end-plates was $L = 0.590$m and a 5mm gap was obtained between the end-plates and the tank walls to avoid contact. The

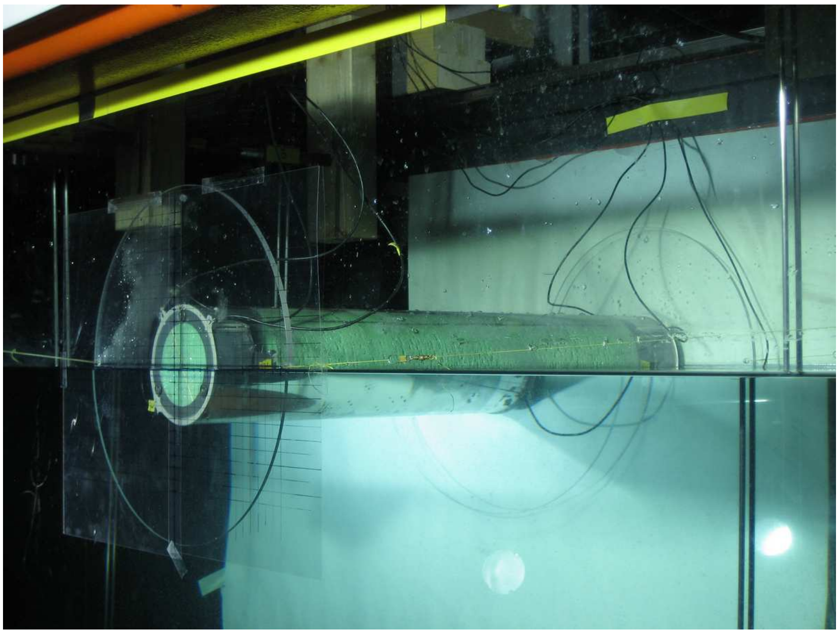

Figure 6.8: The model when moored and ready for testing. The black cables are connected to the accelerometers inside the model.

dry mass of the model was measured to be $M = 2.50\text{kg}$.

The model was placed a distance 6.50m from the hinge of the wave paddle and kept on its position by four mooring lines. A picture of the moored floating model in place at the desired location is shown in Fig. 6.8. The mooring lines were fastened to the edge of the end-plates of the model, yielding an increased stiffness in roll. Two lines were applied on the wave maker side of the model, while for the side of the model facing the beach, two lines which were attached to the model met to form a crowfoot. Thus, the total number of mooring lines attached to the rig was three. Each mooring line were pointing nearly horizontally from the model position, making an angle $\alpha = 3.2^\circ$ with the calm water surface. Three pulleys were used to direct the mooring lines upwards before they were attached to linear springs. The springs were then loaded in the vertical direction. This was to avoid transverse dynamics due to the mass of the spring, which could have contaminated the force measurements. Although not observed, transverse dynamics of the springs could still occur due to Mathieu-instability (McLachlan 1964). The upper end of the springs were mounted to force transducers of type Hottinger Baldwin (18kg). A qualitative sketch of the mooring system is given in Fig. 6.9.

6.2.2 Choice of test conditions

We wanted the test waves in the experiments to be representative for a typical design wave condition for floating fish farms. Design wave conditions for floating fish farms are described in section 2.2. Only regular waves were considered. For the most extreme design waves presented in Tab. 2.2, the waves are long compared to the cylinder diameter. This means that if the full scale floater was exposed to such waves, the floater would be in the stiffness dominated regime of the heave response curve and only float on top of the waves. This is not very interesting from a hydrodynamic point of view. More interesting are the

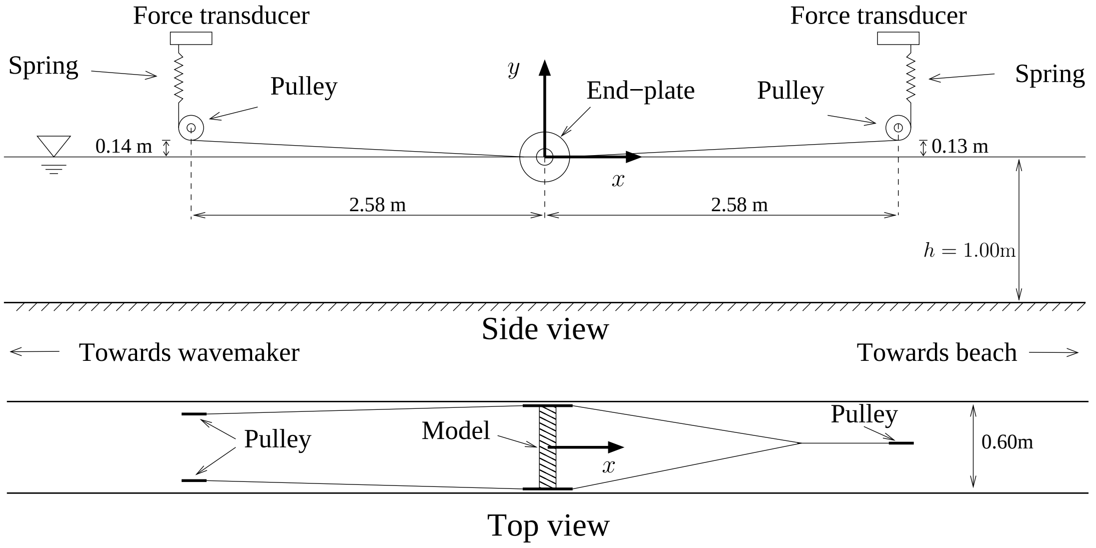

Figure 6.9: Model test setup for the floating circular cylinder. The model is kept on its location by mooring lines attached to springs. Spring forces are measured by force transducers. Pulleys are used to direct the mooring lines to the cylinder while keeping the springs oriented vertically.

wave periods that leads to resonant motion of the floater. The test waves were chosen to cover the regions where resonance of the heave motion and the sway motion occur. The natural periods in heave and sway for the model were estimated using linear potential flow theory and were found as the peaks of the response curve for the considered mode of motion. The response curves were found as follows. We assumed that the heave and sway modes were uncoupled, such that the uncoupled linear equations of motion could be used. Further, roll is negligible as the center of gravity (COG) of the body is located at the cylinder axis, meaning that the pressure forces on the cylinder surface cannot yield a roll moment about the COG. This yielded the following expression for the response amplitude η_{ka} relative to the incident wave height H,

$$\frac{\eta_{ka}}{0.5H} = \frac{F_{ka}/\left(0.5H\right)}{\sqrt{\left(c_{kk} - \omega^2\left(m + a_{kk}\right)\right)^2 + \omega^2 b_{kk}^2}}, \tag{6.1}$$

with $k = 2, 3$ referring to the sway and heave mode of motion, respectively. Further, m is the structural mass of the model per unit length, a_{kk} and b_{kk} are the frequency dependent 2D added mass and damping coefficients from potential flow theory (Skejic 2008), c_{kk} is the 2D restoring coefficient, ω is wave frequency, ρ is mass density of water while g is the acceleration of gravity. The 2D excitation force amplitude F_{ka} is related to the potential damping coefficient b_{kk} as $F_{ka} = 0.5H\sqrt{\rho g^2 b_{kk}/\omega}$ (Newman 1962). The restoring coefficient for heave is $c_{33} = \rho g D$, where D is the cylinder diameter. The natural period in heave was predicted to be $T_{n3} = 0.518$s, when the effect of the mooring lines was neglected. For sway, the 2D restoring coefficient is found by dividing the sum of the given spring coefficients by the model length as $c_{22} = (k_1 + k_2 + k_3)/L_m$. In order to obtain a natural frequency in sway representative for the elastic modes of a steel type fish farm, the spring stiffnesses were chosen to be $k_1 = 43.7$N/m and $k_2 = 43.5$N/m for the two springs at the wavemaker side, while for the spring on the beach side the stiffness was

$k_3 = 88.2$N/m. Using the given spring coefficients in the sway natural period of the model was found to be $T_{n2} = 1.09$s. Based on the obtained response curves for heave and sway of the model, ten test wave periods were chosen. For each wave period, the two wave steepnesses $H/\lambda = 1/14$ and $H/\lambda = 1/10$ were tested. This yielded a total of twenty test wave conditions which are tabulated in Tab. 6.4.

Table 6.4: Characteristics of the waves used in the experiments with the moored floating circular cylinder. Ten different wave periods and two wave steepnesses yielded twenty test wave conditions.

		$H/\lambda = 1/14$	$H/\lambda = 1/10$	
T [s]	λ [m]	H [m]	H [m]	C_G [m/s]
0.423	0.279	0.020	0.028	0.330
0.457	0.326	0.023	0.033	0.357
0.497	0.386	0.028	0.039	0.388
0.544	0.462	0.033	0.046	0.425
0.601	0.564	0.040	0.056	0.469
0.672	0.705	0.050	0.071	0.525
0.761	0.904	0.065	0.090	0.594
0.878	1.204	0.086	0.120	0.686
1.038	1.680	0.120	0.168	0.813
1.132	1.993	0.142	0.199	0.891

6.2.3 Instrumentation and measurements

The main purpose with the experiments was to study the wave-induced motions of the moored cylinder. However, the motions of the cylinder were not measured directly, but had to be deduced from recorded time-series of the body accelerations. The accelerations of the model in heave, sway and roll were measured using six accelerometers. These accelerometers were mounted in grooves that were carved in the polyethylene end-plugs of the cylinder. Three accelerometers were placed at each end of the model in order to verify that the motion was 2D. A sketch that shows the positions of the three accelerometers relative to the body-fixed coordinate system $Ox'y'$ in a cross-sectional cut of the model is presented in Fig. 6.10(a), where r_1, r_2 and r_3 are the normal distances from the cylinder axis to the position of the accelerometers. The relation between the body-fixed coordinate system and the Earth-fixed coordinate system Oxy defined in Fig. 6.9 is shown in Fig. 6.10(b). For the Earth-fixed coordinate system, the $x-$axis is in the calm water surface and points in the wave propagation direction while the $y-$axis is the vertical coordinate with positive direction upwards. The $z-$axis represents the transverse coordinate with positive direction given by the right hand rule. We wanted the body motion to be planar and described by heave, sway and roll in the $xy-$plane.

Tension in the mooring lines were measured by Hottinger Baldwin (18kg) force transducers that were fixed to the rig. These force transducers proved to be very accurate and stable.

Traditional capacitance wave gauges were used for measuring the free surface elevation at six positions in the flume. As for the model tests in 2006, close to the model position two

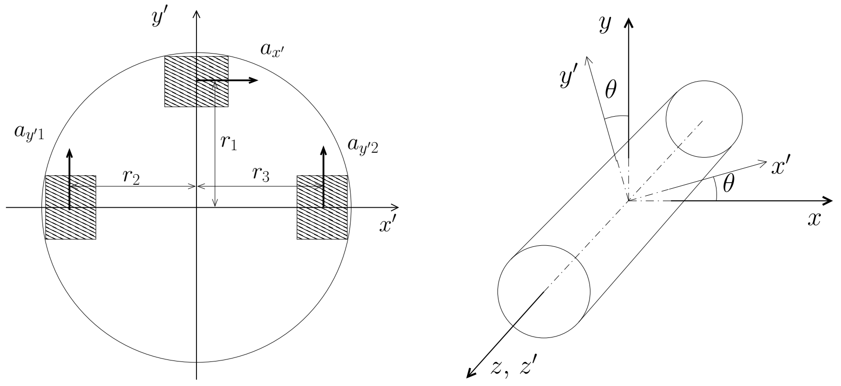

(a) Position of accelerometers (b) Coordinate systems

Figure 6.10: The accelerometers are positioned in the cross-section as shown to the left. Relation between the Earth-fixed coordinate system $Oxyz$ and body-fixed coordinate system $Ox'y'z'$ is shown in the right figure. It is only the angular motion of the body-fixed coordinate system that has influence on the measured accelerations relative to the Earth-fixed frame of reference.

wave gauges were placed at the same longitudinal ($x-$)position but at different positions in the transverse ($z-$) direction in order to check for two-dimensionality of the waves. This was done on both the wavemaker side and the beach side of the model. Positions of the six wave gauges used are listed in Tab. 6.5. For the longitudinal direction, the position of the wave gauges are given both relative to the wavemaker x_{wm} and relative to the model position x.

Table 6.5: Position of wave gauges in the flume relative to the mean position of the wavemaker x_{wm} and relative to the initial model position x.

Wave gauge	x_{wm} [m]	x [m]	z [m]
WG 1	4.00	-2.50	0.000
WG 2	6.00	-0.50	-0.155
WG 3	6.00	-0.50	0.155
WG 4	7.00	0.50	-0.145
WG 5	7.00	0.50	0.145
WG 6	9.00	2.50	0.000

Recordings of the model with a high-speed camera of type IDT Dantec Dynamics were performed, using an image sampling ratio of 50 frames per second. The reason for the rather low sampling frequency was to obtain longer recordings in real-time. For all test cases, a time-window of 30 seconds was recorded, starting from calm water conditions such that the transient build up of the body motions was captured.

The measured signals from all sensors went through a Hottinger Baldwin amplifier of type MGCplus and the data acquisition was performed with a sampling frequency of 300Hz. All signals were filtered using an analog Butterworth low-pass filter with cut-off frequency 80Hz. The Hottinger Baldwin software Catman was used for logging of the measured data. All sensors were calibrated before measurements.

6.2.4 Post-processing of measured accelerations

Since the accelerometers are fixed to the moving body, they will measure accelerations $a_{x'}$ and $a_{y'}$ in the directions given by the body-fixed coordinate system (x', y') as shown in Fig. 6.10(a). Here, $a_{y'} = 0.5\,(a_{y'2} + a_{y'1})$. To obtain the body accelerations at the center of gravity of the body in the Earth-fixed coordinate system Oxy, the measured time-series of acceleration must be mapped from the directions given by the body-fixed coordinate system into the Earth-fixed frame of reference (see Fig. 6.10(b)). The effect of angular (roll) acceleration $\ddot{\theta} = 0.5\,(a_{y'2}/r_3 - a_{y'1}/r_2)$ must be accounted for. Further, if the body-fixed coordinate system is rotated with a roll angle θ relative to the Earth-fixed coordinate system, the measured accelerations must be corrected for the acceleration of gravity g. The instantaneous roll angle θ is found from time-integration of the roll acceleration $\ddot{\theta}$. Accelerations in the Earth-fixed reference frame, a_x and a_y referring to the horizontal and vertical component respectively, are then calculated as

$$\begin{bmatrix} a_x \\ a_y \end{bmatrix} = \begin{bmatrix} \cos\theta & -\sin\theta \\ \sin\theta & \cos\theta \end{bmatrix} \begin{bmatrix} a_{x'} \\ a_{y'} \end{bmatrix} + g \begin{bmatrix} \sin\theta \\ \cos\theta - 1 \end{bmatrix} + \ddot{\theta} \begin{bmatrix} r_1 \\ r_2 - r_3 \end{bmatrix}, \tag{6.2}$$

Details on the derivation of these expressions are given in Appendix C.2.1.

Obtaining the body motions

The body motions were obtained by time integration of the measured body accelerations. One important aspect with integration of measured accelerations is that measured time records usually contain noise at all frequencies. Especially low-frequency noise is a problem when measured accelerations are used to deduce the body motions. This is exemplified in the following. Assume the measured horizontal acceleration can be described by a Fourier series as $\ddot{x}(t) = \sum_{j=1}^{N} (A_j + \epsilon_j) \cos(\omega_j t + \delta_j)$, where A_j is the Fourier amplitude for the frequency interval represented by ω_j of the model acceleration, ϵ_j is the Fourier amplitude due to noise in the measured signal and δ_j is the phase angle. Then, by integration we obtain the position $x(t) = -\sum_{j=1}^{N} \omega_j^{-2} (A_j + \epsilon_j) \cos(\omega_j t + \delta_j)$. For low frequencies $\omega_j \ll 1$, it is clear that noise in the measured acceleration will have a major effect on the error of the computed position if the noise amplitude ϵ_j is of the same order of magnitude as the physical Fourier amplitude A_j. This means filtering of the recorded accelerations prior to integration is necessary. An estimate of the noise in the measured accelerations is obtained by taking the Fourier transform of the recordings in a time-window before the wavemaker is started and while the model is at rest. The noise level for the different frequencies are compared with the Fourier transform of the complete time-series of the accelerations. This is then used to judge which lower cut-frequency to apply when filtering, which is the lowest frequency where the Fourier amplitude of the noise is of comparable order as the Fourier amplitude obtained from the total time-series. By inspection of the Fourier transforms, we found that a lower cut-frequency $f_{cut} = 0.65 f_w$, where f_w is the wave frequency, yielded good results for most cases (Fig. 6.11(a)). The exception was when sub-harmonic response did occur at nearly half the wave frequency. Then a lower cut-frequency $f_{cut} = (0.65 f_w)/2$ was used, such that the physical sub-harmonic components of the response were not removed when filtering the signals (Fig. 6.11(b)). When the measured time-series of acceleration is band-pass filtered as described above, the acceleration of the model in an Earth-fixed frame of reference is found using (C.1).

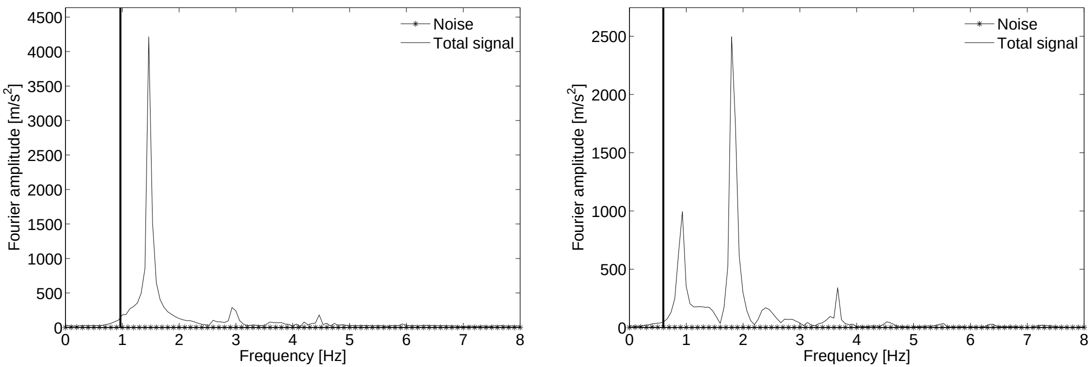

(a) No sub-harmonics (b) With sub-harmonics

Figure 6.11: Fourier amplitude spectra used when choosing the lower cut-frequency. When there is no sub-harmonic response, the lower cut-frequency is taken as $f_{cut} = 0.65 f_w$ which is represented by the vertical line in (a). For cases when sub-harmonic response occur, the cut-frequency $f_{cut} = (0.65 f_w)/2$ is used as shown in (b).

The obtained body acceleration $\ddot{\mathbf{x}}(t) = [a_x, a_y]^T$, where T is the transpose operator, is then integrated numerically using the trapezoidal rule (Kreyszig 1999) with the initial condition $\dot{\mathbf{x}}(0) = \mathbf{0}$ to obtain the velocity of the model. The time-series of the model velocity is then band-pass filtered, using the same pass-band as for the accelerations. Repeating the integration procedure with initial condition $\mathbf{x}(0) = \mathbf{x_0}$, the body motion is obtained.

An estimate of the sway motion could also be obtained by dividing the measured mooring line tension with the spring coefficient for the mooring line considered. Due to small angles between the mooring lines and calm water surface and the fact that the mooring lines were long relative to the cylinder diameter (cf. Fig. 6.9), this would yield a good estimate of the sway motion. As the mooring line forces and the body accelerations are measured independently, this provides a possibility to cross-check the computed sway motion and to verify our procedure for calculating the body motions from the measure accelerations. Applying the same band-pass filter for the spring forces as for the accelerations, an estimation of the horizontal position of the model is found as $\eta_2 = F_s/k$, where F_s is the measured mooring line tension and k is the spring coefficient corresponding to the mooring line considered. Time series of the obtained sway motion from the two different approaches presented are compared in Fig. 6.12 and shows good agreement. More precisely, the mean difference of the estimated motion amplitudes (both positive and negative) in the time window $t = 15$s to $t = 25$s is less than 1% for the case considered. The obtained body motions were also verified by comparison with images from the high-speed camera recordings.

6.2.5 Discussion of errors in the experiments

Possible sources of systematic errors in the experiments could be wave reflections from the beach or from the wavemaker or 3D flow effects, e.g. due to excitation of transverse sloshing modes in the flume. The natural periods for the first and second transverse

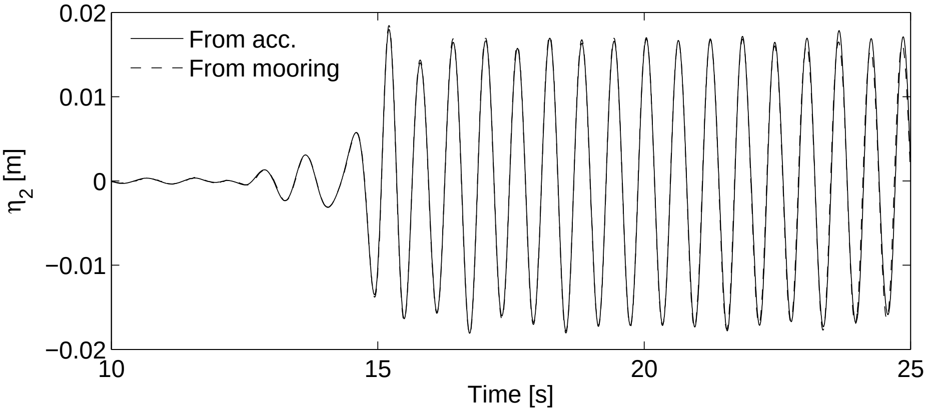

Figure 6.12: Comparison of sway motion obtained from integration of measured horizontal accelerations with that obtained from measured mooring line tensions. The test wave period and wave steepness was $T = 0.601$s and $H/\lambda = 1/14$, respectively.

sloshing mode was $T_1^t = 0.877$s and $T_2^t = 0.620$s, respectively. Large transverse standing waves (similar to the second sloshing mode) were seen close to the model in the tests with wave period $T = 0.544s$ and steepness $H/\lambda = 1/10$, although this wave period does not correspond to the sloshing period for the second mode.

Contact between model and tank walls

Since we wanted a 2D flow condition in the experiments, the gap between the model and the side walls of the flume should be as small as possible. However, a narrow gap increases the possibility of contact between the model and the tank walls. Wall contact will introduce unknown forces to our system which is highly unwanted. Unfortunately, for some tests where the model motion became large and violent, wall contact was visually observed. Hence, before we could use the measurements for validation purposes, we had to be able to detect with a high level of confidence if and eventually when contact did occur. A good indicator for sudden contact between the flume walls and the model is the time derivative of the measured acceleration time-series. This parameter is also known as jerk (Boore and Bommer 2005). Figure 6.13 shows the measured acceleration of the model and the corresponding jerk for a test case where contact between model and tank walls was observed. Contact is seen as spikes in the jerk time-series.

Effects of the mooring system

The pulleys used for the mooring system may have an effect on the motions of the model. As the pulleys have a finite mass, the inertia of the pulleys will add to the total inertia of the system in motion. The effect of the pulley inertia is quantified by performing free decay tests in sway of the model suspended in air. As the added mass effect due to the air is small compared to the structural mass and can be neglected, the system can be simply modelled as a harmonic oscillator represented by a mass and a spring. The mass is the structural mass of the model while the spring is the effective spring stiffness due to the mooring lines. Hence, the natural period of the system can be estimated. Practically,

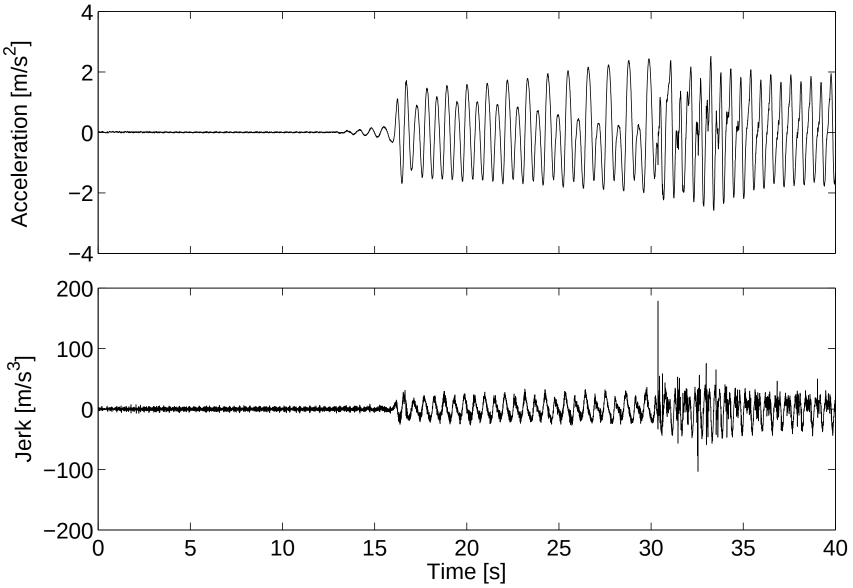

Figure 6.13: Example of wall contact identification by the use of jerk. Sudden contact between the model and the tank walls leads to spikes in the jerk time-series.

free decay in air was done by suspending the model in a long line such that the model appeared as a long pendulum. The natural period of the pendulum had to be far higher than the natural period due to the mooring lines. The natural period of the pendulum motion is for small amplitudes of oscillation found as $T_n^p = 2\pi\sqrt{L/g}$, where $L = 2.20$m is the length of the pendulum and g is acceleration of gravity. This yielded a natural period $T_n^p = 2.98$s for the pendulum motion. The natural period due to the restoring forces from the mooring lines when the model is suspended in air is found as

$$T_n = 2\pi\sqrt{\frac{M}{k_{eff}}}, \tag{6.3}$$

where $k_{eff} = (k_1 + k_2) + k_3 =$ is total effective spring stiffness. For the given spring stiffnesses used, the effective spring stiffness is found to be $k_{eff} = 176.4$N/m. The mass of the cylinder is $M \approx 2.500 \pm 0.005$kg. This approximate description of the structural mass is due to the cables connecting the accelerometers to the logging system and the uncertainty of how much of the cables weight that contributes to the oscillating mass. This yields a dry natural period in the range $T_n^{dry} = 0.747\text{s} - 0.749\text{s}$. The measured natural period from free decay tests in air was found to be $T_n = 0.778$s, which is 3.8% higher than the theoretical value where the mass of the pulleys is excluded. This difference between measured and theoretical natural period means the mass of the pulleys contributes 8.2% to the oscillating mass. Hence, the natural period in sway in the model tests is modified due to the inertia of the pulleys. However, when the model is oscillating in water the added mass will be of the order of the structural mass of the model. This means that the relative importance of the pully inertia is significantly reduced. There is also an effect of friction in the ball bearings of the pulleys. This effect is discussed in Chapter 8.

We wanted the springs in the mooring line system to be linear, meaning that there is a linear relation between the force applied to the spring and its resulting elongation. Linearity of the springs were tested by loading the springs using known weights and measuring the spring elongation. Results from this test are shown in Appendix C.2. All springs proved to be linear when loaded below their reported floating limit, which for all three springs was 30N.

Precision errors of the incident wave heights and model response amplitudes are estimated from repetition tests, which were conducted for some of the test wave periods. For the incident waves, an average wave height $\overline{H}$ is found from the steady state region of the wave elevation time-series for each test run. Then a measure for the random error of the generated wave heights is the relative error $\varepsilon_{rel} = \hat{\sigma}_H/\hat{\mu}_H$, where the experimental mean $\hat{\sigma}_H$ and experimental standard deviation $\hat{\mu}_H$ of the average wave heights obtained from N repetition tests are defined as

$$\hat{\mu}_H = \sum_{i=1}^{N} \frac{\overline{H}_i}{N}, \tag{6.4}$$

$$\hat{\sigma}_H = \left[\sum_{i=1}^{N} \frac{(\overline{H}_i - \hat{\mu}_H)^2}{N-1} \right]^{1/2}. \tag{6.5}$$

Mean of the averaged wave heights and corresponding relative errors obtained from the wave calibration tests are listed in Tab. 6.6. The relative error ε_{rel}^{tot} of the mean total wave height $\overline{H}$ is less than 2% for all wave periods where repetition tests are conducted.

Table 6.6: Mean averaged wave height $\hat{\mu}_H$ and relative error ε_{rel} of the total, linear- and second harmonic component of the wave height obtained from five repetition tests at steady state condition.

T [s]	H_{input} [m]	$\hat{\mu}_H$ [m]	ε_{rel}^{tot}	$\varepsilon_{rel}^{1.harm}$	$\varepsilon_{rel}^{2.harm}$
0.497	0.028	0.029	1.46×10^{-2}	1.57×10^{-2}	4.83×10^{-2}
0.761	0.065	0.069	2.45×10^{-3}	1.65×10^{-3}	3.74×10^{-2}
1.132	0.142	0.137	1.83×10^{-2}	1.26×10^{-2}	1.09×10^{-2}

6.2.6 Summary of results

Wave calibration tests were conducted for all test wave periods and both wave steepnesses. The quality of the generated wave profiles for the two shortest wave periods was less good, due to some transverse disturbances on the free surface. This was observed to be mainly caused by the gap between the wavemaker paddle and the side-walls of the flume, which measured about 2cm on each side of the paddle. For larger wave periods, these disturbances were less pronounced.

Steady-state of the cylinder motion was reached in all the test runs, except for the tests for which the wave period was $T = 0.544$s. For these tests, the response amplitudes of the sway mode of motion were observed to increase in an instability-like manner. For some tests, the sway motion was limited due to contact between the model and the side walls of the flume. Measured sway motion from repetition tests with the wave period

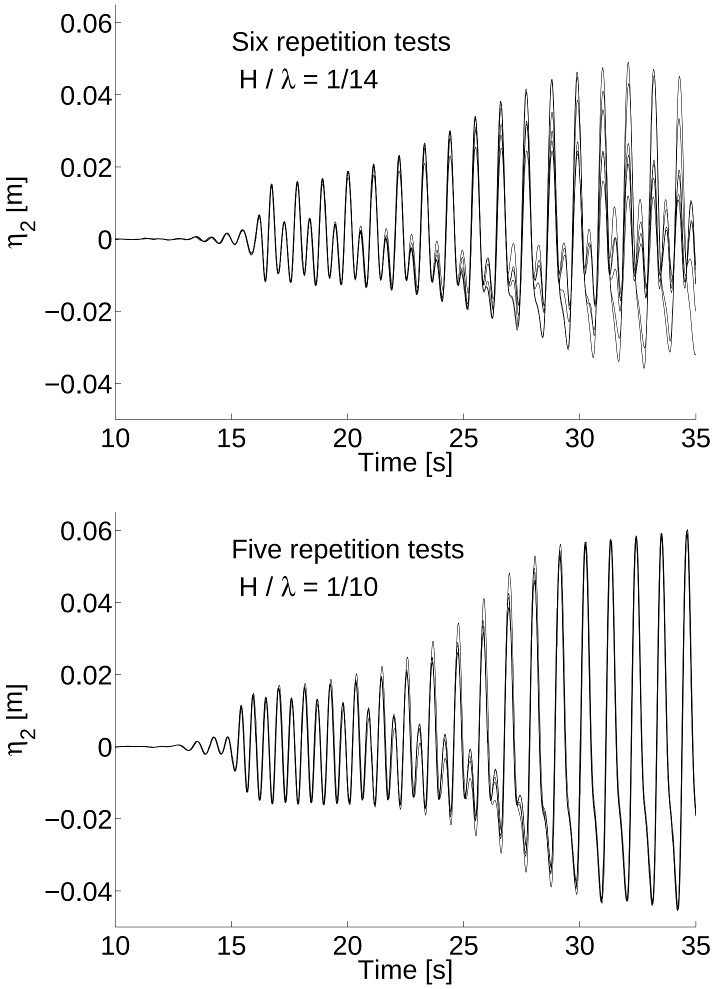

Figure 6.14: Experimentally obtained sway response from repetition tests when the moored circular cylinder is subject to regular beam sea waves with wave period $T = 0.544$s. Differences between obtained time-series seen after 25s for when $H/\lambda = 1/14$ are explained by wall-contact problems.

$T = 0.544$s are compared in Fig. 6.14. The repetition tests shows that this characteristic sway motion was repeatable until wall-contact occurred. Resulting sway motion for this wave period are observed to be slightly different for the two wave steepnesses tested, as shown in Fig. 6.14. This instability-like phenomenon was observed to be characterized by a final shift in the sway response frequency. In the first stage after the wave train has reached the model, the cylinder started to oscillate in heave and sway with period equal to the wave period, as expected. However, after a build-up through 18 - 20 wave periods, the sway motion frequency had become half the wave frequency, such that the frequency of the sway motion was equal to the natural frequency in sway. Trace plots of the model motion in heave and sway for this case are presented in Fig. 6.15.

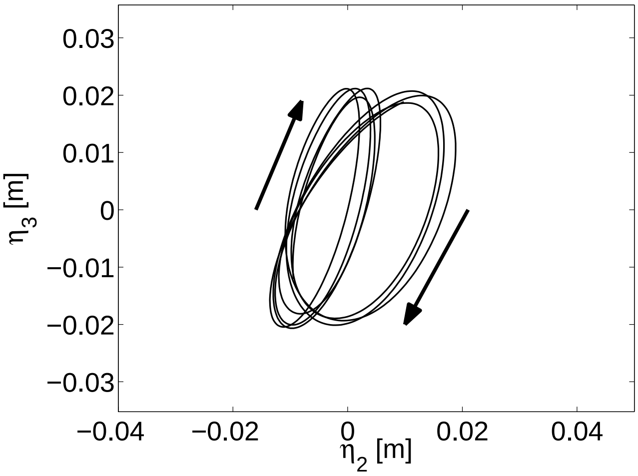

(a) $t = (17\text{s}, 21\text{s})$

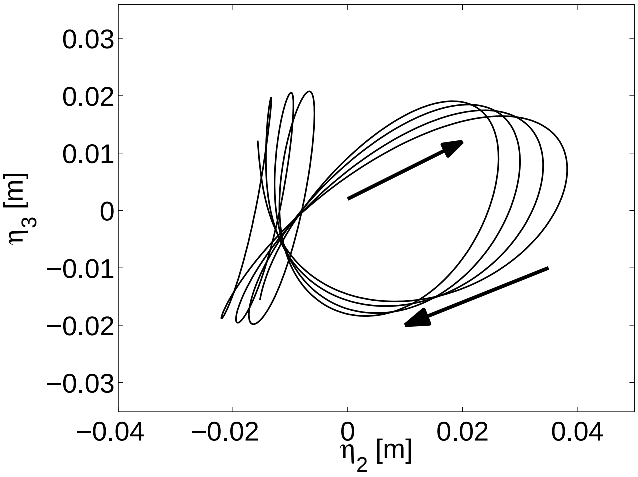

(b) $t = (23\text{s}, 27\text{s})$

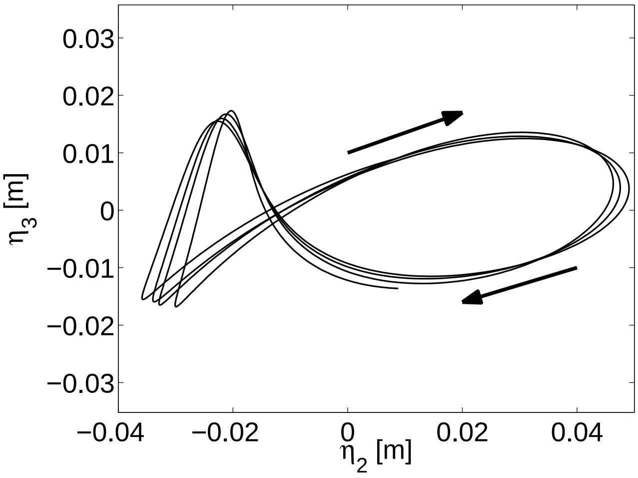

(c) $t = (29\text{s}, 33\text{s})$

Figure 6.15: Trace plots of the cylinder motion from three different time windows for the case when sway instability occurs (cf. Fig. 6.14). Wave period and wave steepness is $T = 0.544\text{s}$ and $H/\lambda = 1/14$, respectively.

Chapter 7

A study of fixed cylinders in regular waves

In this chapter results from our study on horizontal cylinders which are fixed in the free surface zone and subject regular waves are presented. The study is based on the model tests from 2006. Numerical simulations with our 2D NWT has been performed, where the test conditions from the experiments was modelled. The wave excitation forces due to regular waves where studied, with focus on the nonlinear effects. Nonlinearities are associated with model geometry and model dimensions relative to the amplitude of the incoming waves.

In order to perform adequate comparisons of time-series for the computed wave forces with the measured wave forces, it was necessary to verify that the wave conditions simulated with the NWT were in agreement with the actual wave conditions in the experiments. This was done by performing numerical wave calibration tests with the NWT. Comparisons of the measured and computed time-series of free surface elevation are presented. Convergence studies of the generated waves from the numerical wave calibration tests and the computed wave forces from simulations with the model present were performed. In addition to direct comparison of time-series from the measured and computed wave forces on the models, Fourier analysis of both the measured and computed wave forces are performed and obtained Fourier amplitudes are compared. At the end of this chapter, a generalized Morison type of model is proposed and applied to some of the test conditions from the model tests.

Our study on fixed horizontal cylinders in regular waves has resulted in two publications (Kristiansen and Faltinsen 2008a; Kristiansen and Faltinsen 2008b).

7.1 Numerical modelling of the 2006-experiments

In order to perform numerical simulations of fixed horizontal cylinders subject to regular waves with the same test conditions as in the experiments from 2006, a numerical model of the physical wave flume was constructed using the presently developed 2D flow solver. Definition of the computational domain and arrangement of the numerical grids used in the calculations will now be described.

7.1.1 The computational domain

The narrow wave flume used in the experiments from 2006 is modelled numerically with our 2D flow solver on a rectangular domain. At the right hand boundary of the domain a piston-type wavemaker was introduced. The wavemaker was modelled linearly, meaning the piston velocity was imposed on the horizontal velocity nodes located at the boundary which was fixed in space. The piston velocity was imposed over the total height of the domain. A numerical beach or damping zone was applied at the left end of the domain to damp out the waves that reached the end of the flume.

Ideally, the length of the NWT should be equal to the length of the physical flume. However, this was not beneficial from a computational point of view. First of all, since we did not have any wave absorption system for the wavemaker in our NWT, we had to make sure that the distance from the wavemaker to the model was sufficient to avoid the diffracted waves from the model towards the wavemaker being reflected back to the model. Next, in order to properly resolve the generated waves with the numerical grid, a certain number of grid cells are needed relative to the wave length and wave height. Hence, if the domain of computation has the dimensions of the physical flume and we require that all test waves are equally resolved with respect to wave length, a large number of elements will be needed for simulation of the shortest waves compared to that needed to simulate the longest waves. Based on these arguments, we found it convenient to define the length of the NWT in terms of the wave length λ, which was predicted by linear potential flow theory as the wave length corresponding to the test wave period T for the actual water depth in the flume. The water depth in the NWT was $h = 0.543$m, as in the experiments.

For simulations where a body was present in the NWT, there was a limit on the simulation time due to wave reflections reaching the model position. Since a damping zone was applied at the far end of the flume while there was no wave absorption on the wavemaker, it was reflections from the wavemaker of the diffracted waves from the model that limited the simulation time. Theoretically, all wave frequencies will be excited during the transient start-up of the wavemaker. This causes small disturbances to be generated in the fluid which for the case of an incompressible fluid propagate at an infinite velocity. However, the surface waves containing energy of significance are gravity waves which are bounded by the wave front propagating with a finite velocity C_g, known as the group velocity. This means that the limit of the simulation time before waves were reflected back to the model position could be estimated as $t_r \approx 3L_{wm}/C_g$, with L_{wm} being distance from the wavemaker to the cylinder axis. Alternatively, given a wanted simulation time t_r, an estimate of the necessary length L_{wm} to avoid wave reflections reaching the model position within the time window considered could be found. However, for steep waves the group velocity will be higher than that predicted by linear potential flow theory. Further, due to nonlinear effects, some of the wave frequencies associated with the transient wave front will also propagate faster than the linear group velocity. The estimated time for reflections t_r was only used as a guideline when choosing the length of the domain. In the simulations with fixed models, $L_{wm} = 4.5\lambda$ was used. Hence, for deep water waves where $C_g = 0.5\lambda/T$ according to linear potential flow theory, we obtain $t_r \approx 27T$. When effects of finite water depths matter, t_r will be less. The distance from the cylinder axis to the far end boundary of the NWT, including the damping zone, was 5.5λ. The efficiency of the damping zone depends on its length L_{dz} relative to the wave length of the wave that is to be damped. For the damping zone applied in our NWT, $L_{dz} = 4\lambda$ was sufficient to avoid

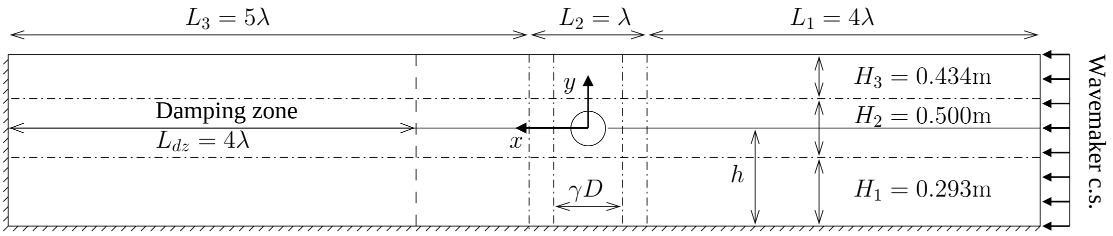

Figure 7.1: Arrangement of the grid in the NWT. A fine grid region is applied at the floater position. Grid stretching is used to reduce the CPU time while keeping the grid resolution high in regions where large variations of the flow occur.

wave reflections. As our flow solver applies a one-fluid model and a surface capturing method to simulate surface waves, also the air above the free surface had to be included in the computational domain. Total height of the domain for all tests was 1.23m. With the given water depth, the distance from the calm water surface to the upper boundary, where an outlet boundary condition was applied, was 0.68m. Due to the large difference in mass density between air and water, the air flow has negligible influence on the flow of water. Hence, modifications of the air flow caused by the outlet boundary has minor effect on the hydrodynamic problem. For the bottom boundary, a no-slip condition is applied. The two bodies tested the NWT had geometry and dimensions as the cross-sections of the cylindrical models used the experiments. Hence, the diameter of the circular model was $D = 0.300\text{m}$, while the breadth and the height of the rectangular model were $a = 0.300\text{m}$ and $b = 0.250\text{m}$, respectively. Both models were rigid and fixed at a given position in the free surface zone. A no-slip condition was imposed on the model surface. The different boundary conditions are defined in section 3.5. Based on the previous discussion, the computational domain depicted in Fig. 7.1 was used for simulations of fixed bodies in regular waves.

7.1.2 The numerical grid

We use a non-uniform Cartesian staggered grid as defined in 4.1.1 for discretization of the computational domain. As our problem is characterized by several flow effects with large differences in associated length scales, special attention is needed when constructing the numerical grid. Examples of length scales here are the length of the generated waves which is of the order of meters, the model dimensions in the order of centimeters, and the boundary layer thickness on the model surface which is of the order of millimeters. Grid stretching is applied to keep the grid resolution relatively high in the regions of the domain where large variations of the flow is expected, which is locally at the model position in addition to the free surface zone in general. Important grid parameters relative to the waves are the ratio between the wave length λ and the horizontal grid spacing Δx_i and the ratio between the wave height H and the vertical grid spacing Δy_j. As Cartesian grids were used, a complicating factor was how to obtain a fine grid resolution at the model position, which should be based on the dimensions of the model (or the boundary layer on the model surface) and not on the waves. When using a single Cartesian grid and when the model was located in the wave zone, it was not possible to keep the relation between the grid parameters $H/\Delta y_j$ and $b/\Delta y_j$ constant for the different test wave conditions.

Hence, the structure of the grids did vary slightly from test to test.

The grid was constructed as follows. For each spatial direction, the domain of computation was divided into three sub-regions where different gridding strategies were applied. These sub-regions are denoted L_i for the horizontal direction and H_i for the vertical direction with $i = 1, 2, 3$, as illustrated in Fig. 7.1. For the horizontal discretization starting from the wavemaker boundary, the grid increment Δx_i was constant and expressed in terms of the wave length λ in the sub-region $L_1 = 4\lambda$. In the sub-region $L_2 = \lambda$ centered about the model position, a cosine squared stretching of the grid was used to merge a fine grid region of length γD inside L_2 with the coarser grid on each side of L_2. Here, the parameter $\gamma = 2$ was used. In the fine grid region, Δx_i was constant and based on the model breadth. A parabolic stretching of the grid was applied in L_3, such that Δx_i was increasing when moving in the positive $x-$direction. This was in order to increase the numerical diffusion of energy in the damping zone. For the vertical direction, a fine grid with constant grid spacings Δy_j was applied in the interface zone defined by H_2. The height of the interface zone H_2 was two times the height of the model tested. Parabolic grid stretching was used outside H_2, such that Δy_j was increasing when moving away from the interface zone. All grid stretching was performed such that the grid increments Δx_i and Δy_j varied smoothly over the domain.

The following grid parameters are introduced for describing the numerical grid. N_B is the number of vertical grid lines relative to the beam of the model cross-section, N_λ is the number of vertical grid lines per wave length and N_I is number of horizontal grid lines in the air-water interface zone H_2. Four different grids were constructed for each test condition in order to perform convergence tests. Grid parameters describing these grids are listed in Tab. 7.1. Grid 3 was used as the base case grid.

Table 7.1: Grid parameters for the four grids used in convergence tests. N_B is number of grid cells over the breadth of the model, N_λ number of grid cells per wave length, while N_I is number of grid cells vertically in the interface zone. Grid 3 is used as the base case grid.

Name	N_B	N_λ	N_I	N_x	N_y
Grid 1	60	40	80	431	120
Grid 2	80	45	100	512	145
Grid 3	90	50	120	572	170
Grid 4	110	60	130	690	185

7.2 Numerical wave calibration tests

Numerical wave calibration tests were performed in order to verify that the waves generated in our NWT for some given input wave period and wave height were is in agreement with the measured wave elevation in the wave calibration tests from the experiments in 2006. By numerical wave calibration we mean numerical simulations of wave generation without any model present in the domain. This was performed using wave parameters for the test wave conditions in the experiments as input to our NWT. The input parameters were wave period and wave height. However, as for wave-making in the physical flume, the height of the waves generated with the NWT could not be prescribed directly, but was controlled indirectly through the imposed velocity at the wavemaker boundary. From potential flow theory, a linear relation between the stroke of a piston-type wavemaker and the resulting wave height far away from the wave board can be found as given in (3.25). To obtain a smooth wave front a linear ramp of the piston motion amplitudes were used during the first 5 seconds of simulation, before full gain of the wavemaker was reached.

Three of the wave periods from the steepest waves ($H/\lambda = 1/20$) tested in the experiments in 2006 were chosen, for which numerical wave calibration tests were performed with the NWT. These were also the wave conditions used when simulations with the models were performed. Since the computational domain was defined in terms of the wave length λ, three different domains had to be constructed. For each domain, four grids were created using the grid parameters from Tab. 7.1. The grid used in numerical wave calibration for a given wave condition was identical to the grid used when simulations with the models for this wave condition were performed. Temporal discretization was related to the input wave period T. Typically, a time step $\Delta t = T/1000$ was used. However, adaptive time stepping was applied to avoid numerical instabilities and break-down of the simulations. Obtained wave heights from the numerical wave calibration tests are presented in Tab. 7.2.

Table 7.2: Input wave periods T, wave heights H_{input} and associated amplitude S_a of the piston wavemaker. Resulting mean wave heights $\overline{H}$ obtained by the NWT and and $\overline{H}_e$ from the experiments, are also given.

T [s]	H_{input} [m]	S_a [m]	$\overline{H}$ [m]	$\overline{H}_e$ [m]
1.084	0.087	0.026	0.079	0.088
1.348	0.130	0.050	0.120	0.121
1.568	0.176	0.082	0.156	-

7.2.1 Grid convergence of the generated waves

Grid convergence are tested for numerical wave calibration with the wave period $T = 1.568$s, using the four grids defined in Tab. 7.1. Computed time-series of the free surface elevation were band-pass filtered using the low cut-frequency $f_{\text{low}} = 0.4/T$ and the high cut-frequency $f_{\text{high}} = 8/T$. The band-pass filtered time-series of the wave elevation at $x = 0.342$m obtained with the different grids are compared in Fig. 7.2. For this wave period, this is 17.29m from the wavemaker boundary. Fourier transforms of the computed wave elevation time-series are found from the time window $t = [18\text{s}, 28\text{s}]$ using FFT. Resulting Fourier amplitudes are compared in Fig. 7.3. Both the second- and third harmonic components are observed in addition to the linear harmonic. No significant differences are observed between the transforms of the time-series obtained with the four grids. In order to test for grid convergence of the calculations, a measure of the error is needed. For this purpose we use the mean wave height $\overline{H}$ from a time window where the solution is close to steady state. An error measure is defined as the difference between $\overline{H}$ and the corresponding mean wave height obtained with the finest grid $\overline{H}^*$. The error is normalized with the mean wave height from the finest grid. Hence, a normalized error is defined as

$$\varepsilon_H = \frac{\overline{H} - \overline{H}^*}{\overline{H}^*}. \tag{7.1}$$

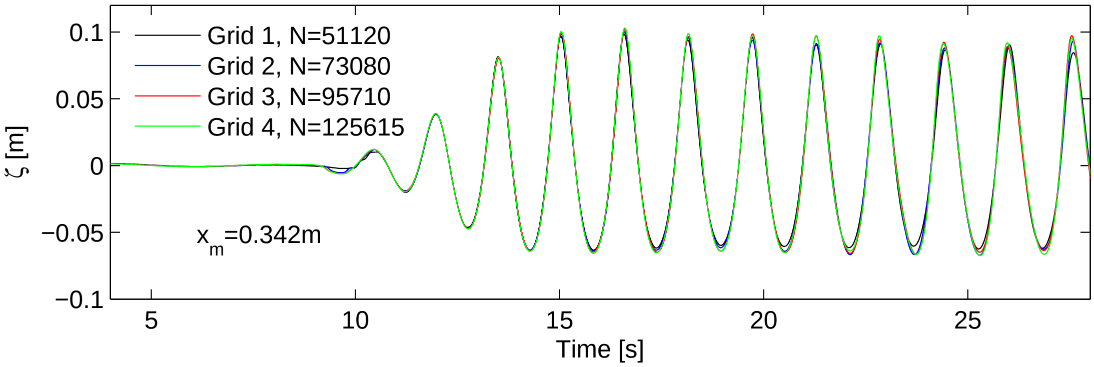

Figure 7.2: Comparison of time-series of the free surface elevation at $x = 0.342$m, obtained from convergence testing of the incident waves. The wave period is $T = 1.568$s and input wave steepness is $H_0/\lambda_0 = 1/20$. N is the total number of grid cells.

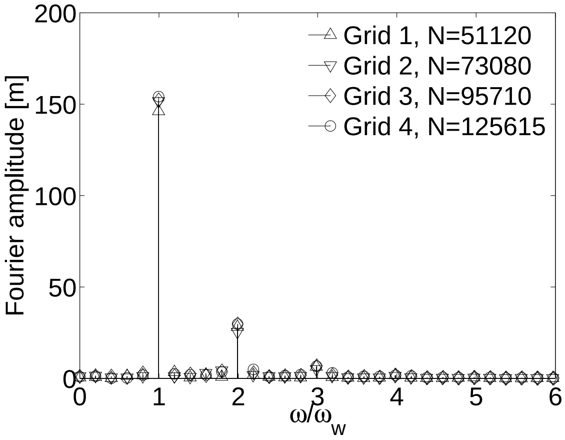

Figure 7.3: Convergence test of computed free surface elevation at $x = 0.342$m from numerical wave calibration with wave period $T = 1.568$s and wave steepness $H_0/\lambda_0 = 1/20$. Fourier amplitudes are obtained using FFT for the time window $t = [18\text{s}, 28\text{s}]$ of the computed time-series. The frequency is normalized by the wave frequency $\omega_w = 2\pi/T$.

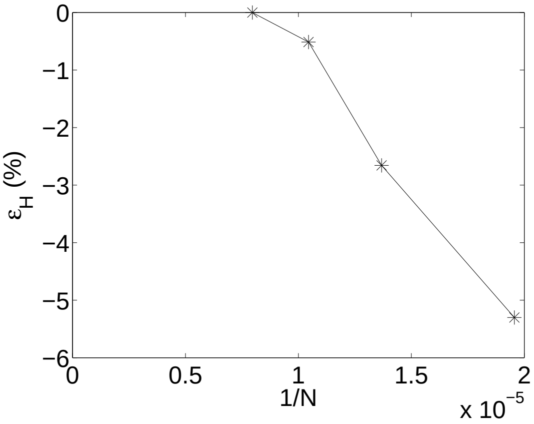

Figure 7.4: Convergence rate for the mean wave height $\overline{H}$ from wave calibration with wave period $T = 1.568$s and wave steepness $H/\lambda = 1/20$.

Normalized errors ε_H of the computed waves for the time interval $t = [18\text{s}, 28\text{s}]$ obtained with the four different grids, are presented in Fig. 7.4. The difference between the normalized error obtained with the base case grid (grid 3) relative to that obtained with the finest grid is only 0.5%. Although we cannot conclude that the computed waves are fully converged, we observe that the differences of the results from the simulations with the two finest grids are small.

7.2.2 Comparisons with the experiments

Now, as we have verified that the grid sensitivity of the generated waves is small for the base case grid, the computed time-series of the free surface elevation can adequately be compared with the free surface elevation measured in the physical wave calibration tests. Due to the difference in length of the NWT and the physical flume, the waves will reach the fine grid region where the model is to be placed at different times. We use the starting time of the wavemaker in the NWT as the reference time when time-series from the numerical simulations are compared with the measured time-series.

First, results from numerical and physical wave calibration for the wave with period $T = 1.084$s and input wave height $H_{\text{input}} = 0.087$m are considered. The base case grid is used in the simulation. Figure 7.5 shows time-series of the free surface elevation calculated at the position $x = -0.356$m in the NWT compared with the measured free surface elevation by WG 3 from the experiments. In the physical flume, WG 3 was located 13.96m from the wavemaker. The comparison shows some deviation between the computed time-series from that measured, in particular for the wave front. It is also observed that the computed wave heights towards the end of the simulated time window is somewhat lower that the corresponding measured wave heights. The frequency contents of the simulated and measured wave elevation was obtained from the Fourier transforms of the time-series presented in Fig. 7.5. To avoid leakage when computing the discrete Fourier transform from the wave elevation time-signal, the Fourier transform was computed from an integral number of wave periods from the time interval $t = [15\text{s}, 20\text{s}]$ (Ambardar 1995). The Fourier amplitudes obtained from the simulated time-series are compared with those obtained from the measurements in Fig. 7.6, which shows a 8.2% underprediction of

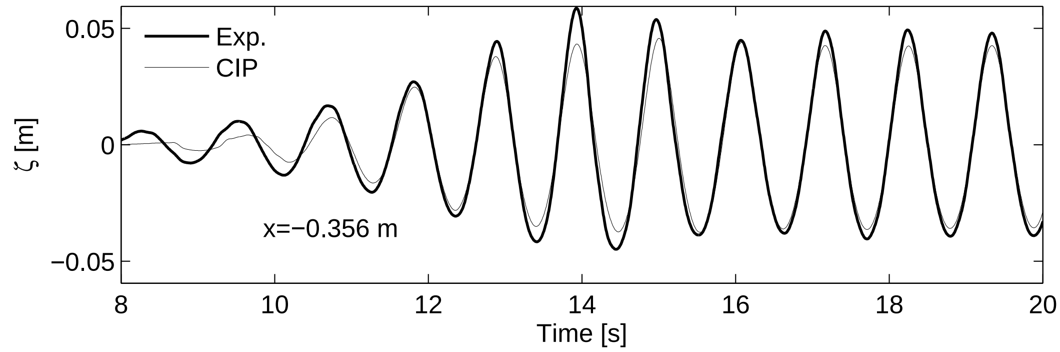

Figure 7.5: Time-series of the free surface elevation obtained with the NWT compared with measured free surface elevation from experiments. Wave period is $T = 1.084$s and input wave height is $H_{\text{input}} = 0.087$m.

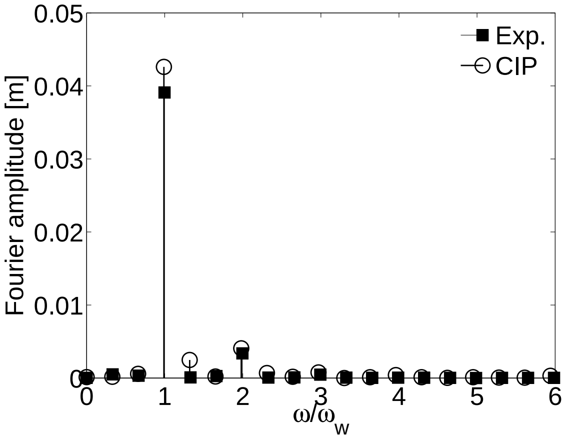

Figure 7.6: Comparison of Fourier amplitudes obtained from FFT of measured and computed free surface elevation in the wave calibration tests. The FFT is computed from the time window $t = [15\text{s}, 20\text{s}]$. The frequency is normalized with the input wave frequency $\omega_w = 2\pi/T$. Wave period is $T = 1.084$s and input wave height is $H_{\text{input}} = 0.087$m.

the linear harmonic component from the computed time-series relative to that from the measured time-series. Good agreement between simulations and measurements is observed for the second harmonic component of the free surface elevation.

Next, we consider results from wave calibration tests for the wave period $T = 1.348$ and input wave height $H_{\text{input}} = 0.130$m. Time-series of computed free surface elevation at $x = -0.356$m are compared with measured waves from WG 3 in Fig. 7.7. The computed free surface elevation is obtained from simulation with the base case grid. Corresponding Fourier amplitudes calculated from the time window $t = [16\text{s}, 24\text{s}]$ are presented in Fig. 7.8. The Fourier amplitude of the linear harmonic component obtained from the simulation is 2.6% smaller than the corresponding Fourier amplitude obtained from the measurements. Computed free surface elevation shows good agreement with measurements for this case. However, some deviations are observed for the wave front.

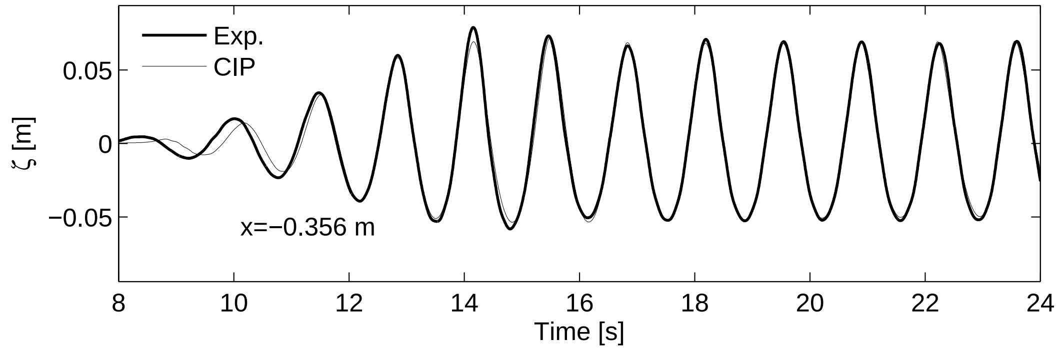

Figure 7.7: Time-series of the free surface elevation obtained with the NWT compared with measured free surface elevation from experiments. Wave period is $T = 1.348\text{s}$ and input wave height is $H_{\text{input}} = 0.130\text{m}$.

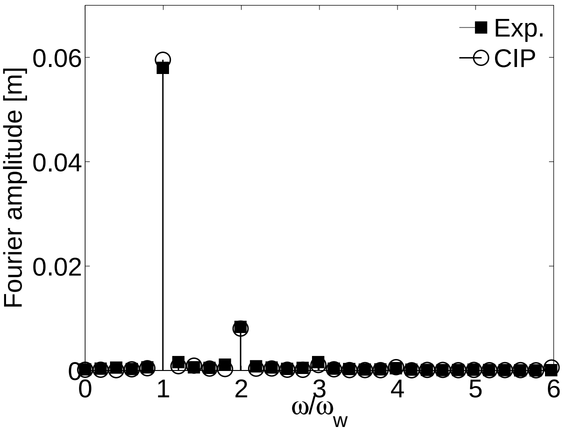

Figure 7.8: Comparison of Fourier amplitudes obtained from FFT of measured and computed free surface elevation time-series in the wave calibration tests. The FFT is computed from the time window $t = [16\text{s}, 24\text{s}]$. The frequency is normalized with the input wave frequency $\omega_w = 2\pi/T$. Wave period is $T = 1.348\text{s}$ and input wave height is $H_{\text{input}} = 0.130\text{m}$.

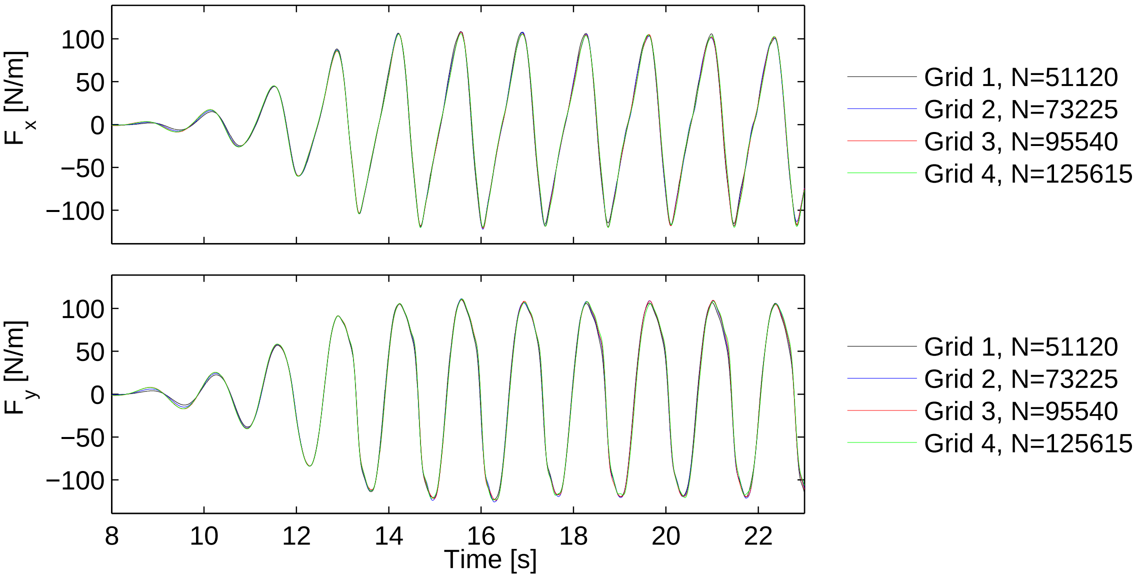

Figure 7.9: Convergence test of wave forces for case with wave period $T = 1.348$s, $H_0/\lambda_0 = 1/20$. N is total number of grid cells.

7.3 Nonlinear wave forces on fixed cylinders

The incident waves have been studied by means of wave calibration tests, both numerically and experimentally. If the kinematics of the incident waves obtained from simulations agree with the measured waves, accordingly, also the computed wave forces should agree with the measurements if our model representation of the physical experiments is adequate and the numerical results are converged. Thus, in the same manner as we confirmed that the grid sensitivity for the incident waves are small, we must also verify that the computed wave forces are converged. This is done in the following. The horizontal and vertical force components are denoted F_x and F_y, respectively. Further, we define the horizontal force component to be positive in the wave propagation direction, while the vertical force component is defined positive upwards.

7.3.1 Grid convergence for the computed wave forces

A convergence study of the computed wave forces are presented for the case of the circular model with draft $d/D = 0.5$ when subjected to waves with period $T = 1.348$s and incident height $H = 0.120$m as found from the numerical wave calibration test. In the same manner as for the convergence tests of the incident waves, four grids are constructed using the grid parameters from Tab. 7.1. Time-series of the computed wave forces obtained with the four grids are compared in Fig. 7.9, which shows that the resulting time-series are almost identical. As a measure for convergence, we use the mean peak-to-peak force amplitudes $\overline{F}$ which are computed from the time interval $t = [17\text{s}, 23\text{s}]$ where the time-series appear to be close to steady state. We define the relative error of the computed mean peak-to-peak force amplitudes as the deviation from the mean peak-to-peak force amplitude obtained from simulation with the finest grid $\overline{F}^*$. Similarly as for the wave heights, the normalized

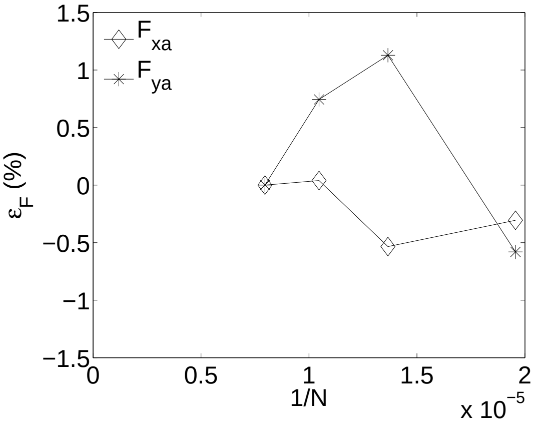

Figure 7.10: Test on convergence of mean peak-to-peak force amplitudes obtained from the time window $t = [17, 23]$s for tests with the circular cylinder with submergence $d/D = 0.5$, $T = 1.348$s and $H_0/\lambda_0 = 1/20$.

error for the peak-to-peak force amplitudes is then defined as

$$\varepsilon_F = \frac{\overline{F} - \overline{F}^*}{\overline{F}^*}. \tag{7.2}$$

Resulting normalized errors ε_F corresponding to the time-series shown in Fig. 7.9 obtained with the four grids are presented in Fig. 7.10. Although no monotone convergence is obtained, the peak-to-peak force amplitudes obtained with the different grids are all within 1.3% from that obtained with the finest grid. Hence, we conclude that the grid sensitivity for the computed wave forces is small.

The free surface elevation at three positions in the NWT obtained with the four grids are compared in Fig. 7.11. We see that diffracted waves from the model clearly interact with the incoming waves. It is mainly where the incoming waves and the diffracted waves forms anti-nodes, and the resulting waves become locally steep, that the largest differences in the computed free surface elevation are observed. This can be explained by wave breaking which is not adequately modelled by the smeared air-water interface.

7.3.2 Discussion of viscous effects

We will now try to estimate what flow behaviour we should expect at the model position. The incoming waves cause an oscillatory flow around the model. An important parameter for cylinders in oscillatory flow is the Keulegan-Carpenter number $KC = UT/B \approx \pi H/B$, where H is wave height and B is the model breadth. This yields $KC < 2.0$ for all wave conditions in Tab. 6.3. Thus, we assume the flow is attached for the circular cylinder and that the vortex shedding from any edge of the rectangular cylinder is small compared to the model dimensions (Bearman et al. 1985). Another important parameter is the Reynolds number for oscillatory flow defined as $\mathrm{Rn} = U_m^2/\omega\nu$, where U_m is the maximum tangential velocity outside the boundary layer. For a fully submerged circular cylinder in attached flow we get $\mathrm{Rn} \approx 4\omega\zeta_A^2/\nu$, where ζ_A is the mean wave amplitude. Here we have neglected the exponential decay with depth of the fluid particle velocity due to the waves. Transition from laminar to turbulent boundary layer flow occur at

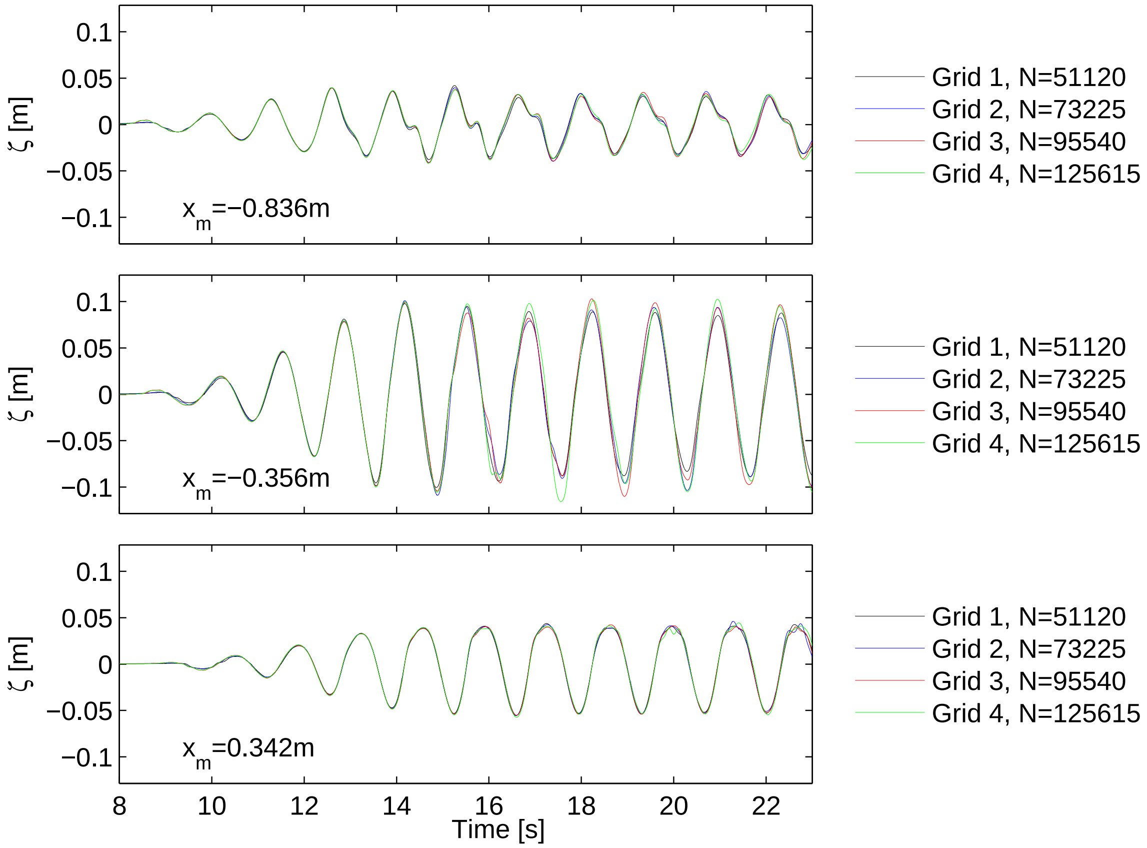

Figure 7.11: Convergence test of free surface elevation with wave period $T = 1.348$s, $H_0/\lambda_0 = 1/20$.

$\mathrm{Rn}_{crit} \approx 10^5$ for a smooth circular cylinder in infinite fluid. Data from Tab. 6.3 yields at most $\mathrm{Rn} \approx 7.9 \cdot 10^4 < \mathrm{Rn}_{\mathrm{crit}}$. Due to effects of roughness at the cylinder surface the actual Rn_{crit} will be lower. Hence, transition to turbulence may still occur. However, we have assumed laminar boundary layer flow. Then the boundary layer thickness in steady-state condition is found from $\delta_{0.99} = 4.6\sqrt{2\nu/\omega}$ (Schlichting and Gersten 2000). Table 6.3 yields $\delta_{0.99} = 3.2 \cdot 10^{-3} - 4.2 \cdot 10^{-3}\mathrm{m}$, which is about 1% of the beam of the circular cylinder. For the case of the rectangular cylinder, turbulence will always develop in the free shear layers separated from the sharp edges.

Estimation of skin friction force on the circular model

As the skin friction forces are not computed with our numerical model, an estimate the order of magnitude of the skin friction force on the circular cylinder is found. First consider a fully submerged circular cylinder in oscillatory flow. We assume laminar boundary layers and that the flow is attached. This problem was studied thoroughly by Stokes (1851). Here we follow a procedure from Faltinsen (1990). A similar approach was also used by Molin (2004) to compute the frictional damping in roll of ship sections. Here, we consider the boundary layer flow $u(y,t)$ due to an oscillating current above a fixed wall. Assume the outer flow is only a function of time and described by $U(t) = U_\infty \cos(\omega t)$. Substituting $u(y,t) = U(t) - \tilde{u}(y,t)$ in the boundary layer equations a diffusion equation for $\tilde{u}$ is obtained. The solution procedure is the same as for the classical Second Stokes problem (Schlichting and Gersten 2000). The steady state solution of the velocity profile in the boundary layer is described by $u(y,t) = U_\infty\big[\cos(\omega t) - \exp(-\eta)\cos(\omega t - \eta)\big]$, where $\eta = y\sqrt{\omega/2\nu}$. The wall shear stress on an impermeable wall is given by $\tau_w = \mu \partial u/\partial y|_{y=0}$, and we get $\tau_w = \mu U_\infty \sqrt{\omega/\nu}\cos(\omega t + \frac{\pi}{4})$. Long wave approximation yields the local velocity distribution outside the boundary layer expressed in polar coordinates as $U_\infty(\theta) = 2U_A \sin(\theta)$. The velocity amplitude in the waves is $U_A \approx \omega H/2$. This yields the in-line skin friction force per unit length of the cylinder

$$F_v = \frac{\pi}{2}\mu\omega H D\sqrt{\frac{\omega}{\nu}}\cos(\omega t + \frac{\pi}{4}). \tag{7.3}$$

The skin friction force takes its largest value for the highest frequency. Using data from Tab. 6.3 in (7.3) gives $F_v/(\rho g V_0) = 0.012$ for a fully submerged circular cylinder. Assuming the skin friction for $d/D = 0.5$ is $F_v/(\rho g V_0) \approx 0.5 \cdot 0.012$ and comparing this estimate with measured forces from model tests, we see that the estimated skin friction is at most 7.3% of the measured horizontal force.

7.3.3 Comparison of computed and measured wave forces

We will now investigate how the computed wave forces obtained from simulations with our NWT agree with the measured clamping forces from the experiments. This is done by comparing time-series of the wave forces directly. Also the Fourier amplitudes from the discrete Fourier transforms of the computed and measured force time-series, which are found using FFT, are compared. In the following, results from the different test cases will be discussed.

Circular cylinder with $d/D = 0.2$

First we consider the circular floater being fixed with draft $d/D = 0.2$. Computed and measured time-series of the horizontal in-line wave force F_x and the vertical wave force F_y are compared in Fig. 7.12. The corresponding Fourier amplitudes, found using FFT over an integral number of wave periods in the time interval $t = [16\text{s}, 21\text{s}]$ are compared also compared in the figure. After 16 seconds of simulation time we see from the time-series of computed and measured wave forces that the system is close to a steady state. In this "steady state" regime, the horizontal wave force amplitudes obtained from simulations with our NWT are somewhat larger than the horizontal force amplitudes measured. This is also observed from the Fourier transforms, which shows an over-prediction of the linear harmonic component from the computed horizontal force relative to the measured horizontal force. The computed vertical force component shows in the steady state regime a better agreement with the measurements. However, in the transient phase, larger deviations are seen for the vertical force than for the horizontal force. In the Fourier transforms of the horizontal force, we observe that there in addition to the linear harmonic component is a pronounced second harmonic component. With pronounced is here meant that the magnitude of the second harmonic component is significant relative to magnitude of the linear harmonic component. A non-zero second harmonic component of the Fourier amplitudes is also present for the vertical force. Although the magnitude of this second harmonic is of comparable order as that for the horizontal force (61% for the measured forces), its magnitude relative to the linear harmonic of the vertical force is marginal. The free surface elevation measured at three positions close to the model are compared with the free surface elevation from the present simulation in Fig. 7.13. Here, the horizontal position of the wave gauge x_m is given relative to the model position which is represented by the cylinder axis. The agreement is satisfactory.

Now we consider the tests with wave period $T = 1.348\text{s}$ for the same draft $d/D = 0.2$ and wave steepness $H_0/\lambda_0 = 1/20$. Force time-series obtained from the model test and from the simulation are compared in Fig. 7.14(a). The corresponding Fourier amplitudes of the horizontal and vertical forces, calculated from the time interval $t = [18\text{s}, 24\text{s}]$, are presented in 7.14(b) and 7.14(c), respectively. The time-series are in good agreement, although some differences of the peak-to-peak force amplitudes are observed. When we consider the Fourier amplitudes for the horizontal force component presented in Fig. 7.14(b), we see that also for this wave period there is a significant contribution from the second harmonic component on the total force. In addition, a third harmonic component is also present. Both the linear harmonic and second harmonic component of the computed horizontal forces are larger than the corresponding harmonic components obtained from the experiments. In the time-series of the horizontal force component, this is seen as the differences in the peak-to-peak force amplitudes.

The largest period simulated for the circular cylinder with draft $d/D = 0.2$ is $T = 1.568\text{s}$. Obtained time-series of the computed wave forces for this case are compared with the measured forces in Fig. 7.15(a). The computed and measured force time-series shows the same trends, but the computed peak-to-peak force amplitudes, in particular for the horizontal force component, are considerably larger than those in the measured force time-series. This deviation is also reflected by the Fourier amplitudes presented in Fig. 7.15(b), which are calculated from the time interval $t = [17\text{s}, 24\text{s}]$.

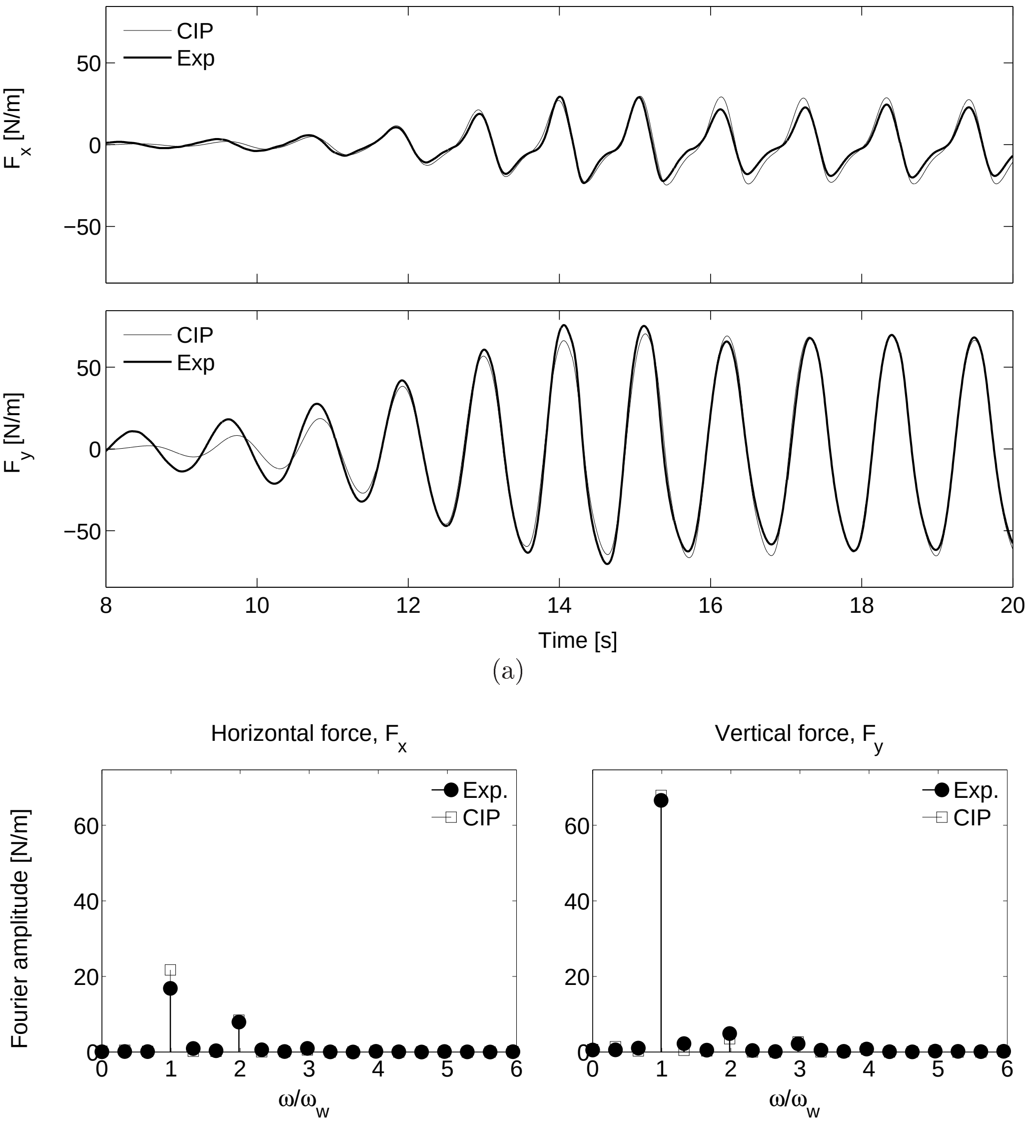

(a)

(b)

(c)

Figure 7.12: Comparison of time-series and corresponding Fourier amplitudes of wave forces on the circular cylinder obtained from simulations and model tests. The test parameters are $d/D = 0.2$, $T = 1.084$s and $H_0/\lambda_0 = 1/20$.

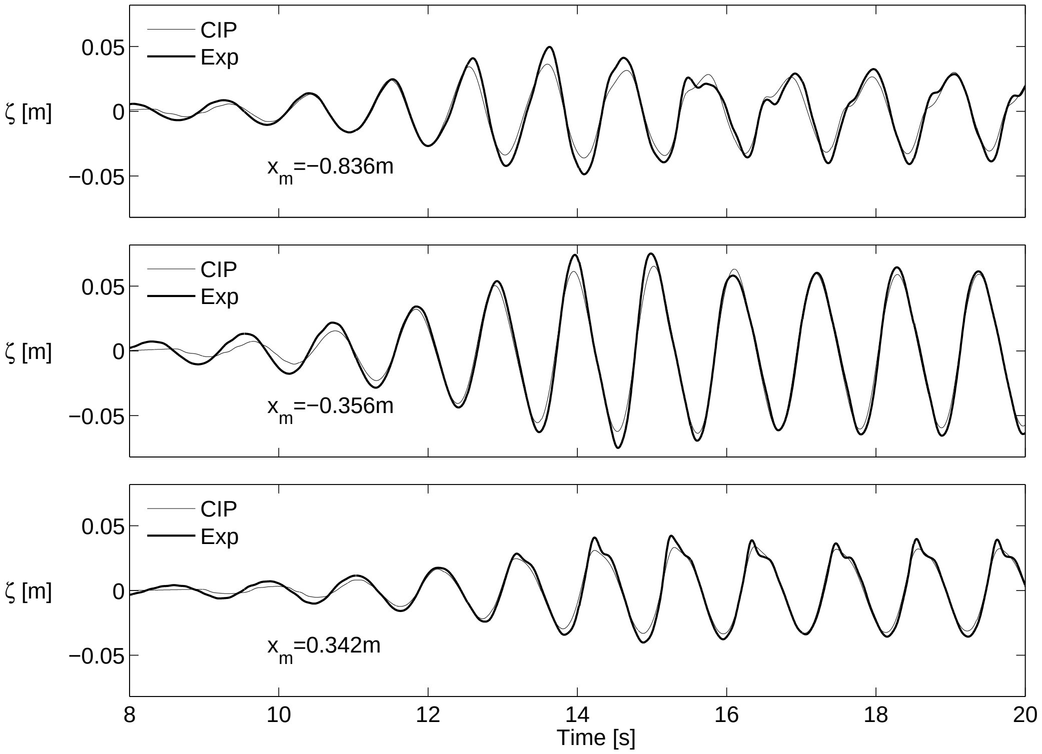

Figure 7.13: Computed and measured free surface elevation at WG 2, WG 3 and WG 5 from tests with the circular cylinder with draft $d/D = 0.2$. Wave period is $T = 1.084$s and corresponding deep water wave steepness is $H_0/\lambda_0 = 1/20$.

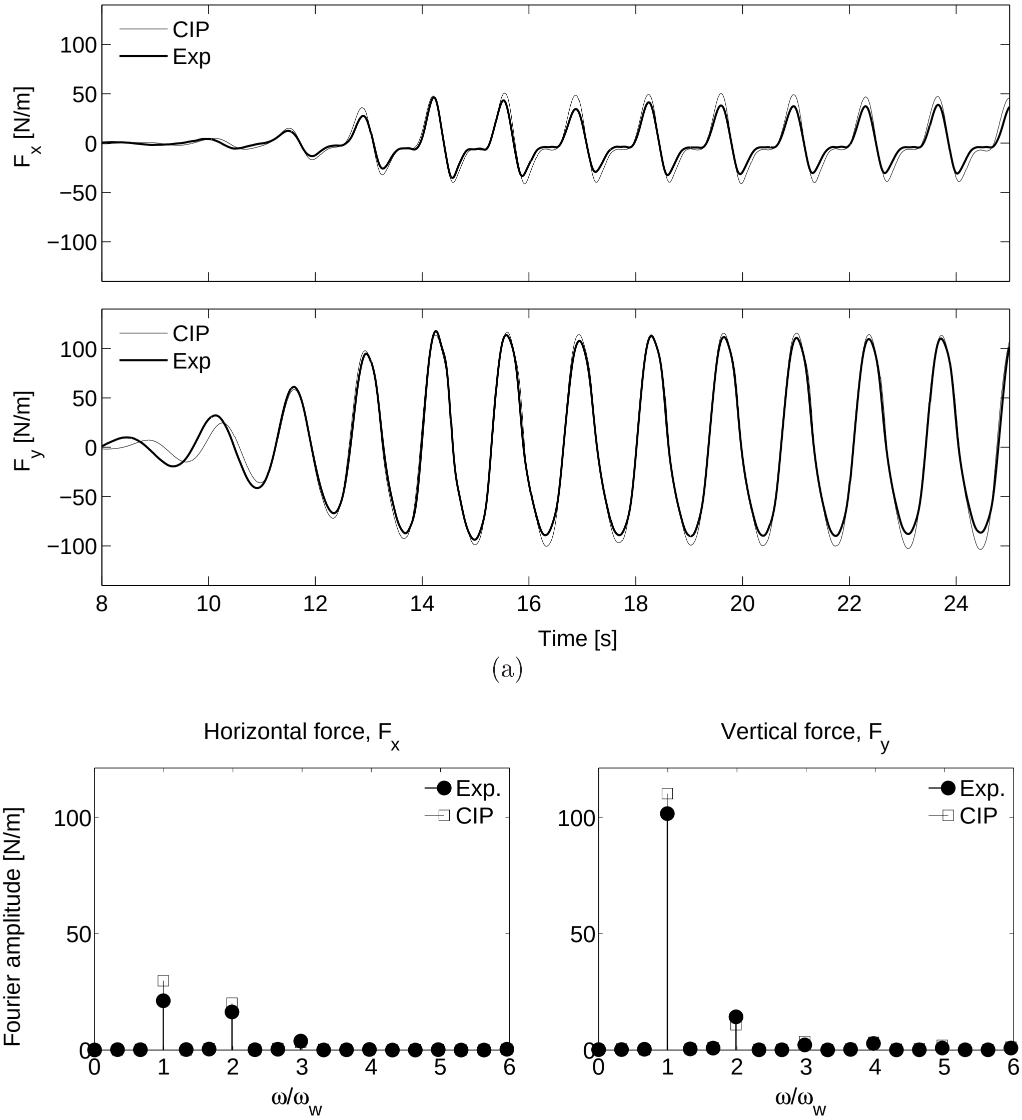

(b) (c)

Figure 7.14: Comparison of time-series and corresponding Fourier amplitudes of wave forces on the circular cylinder obtained from simulations and model tests. Test parameters are $d/D = 0.2$, $T = 1.348$s, $H_0/\lambda_0 = 1/20$.

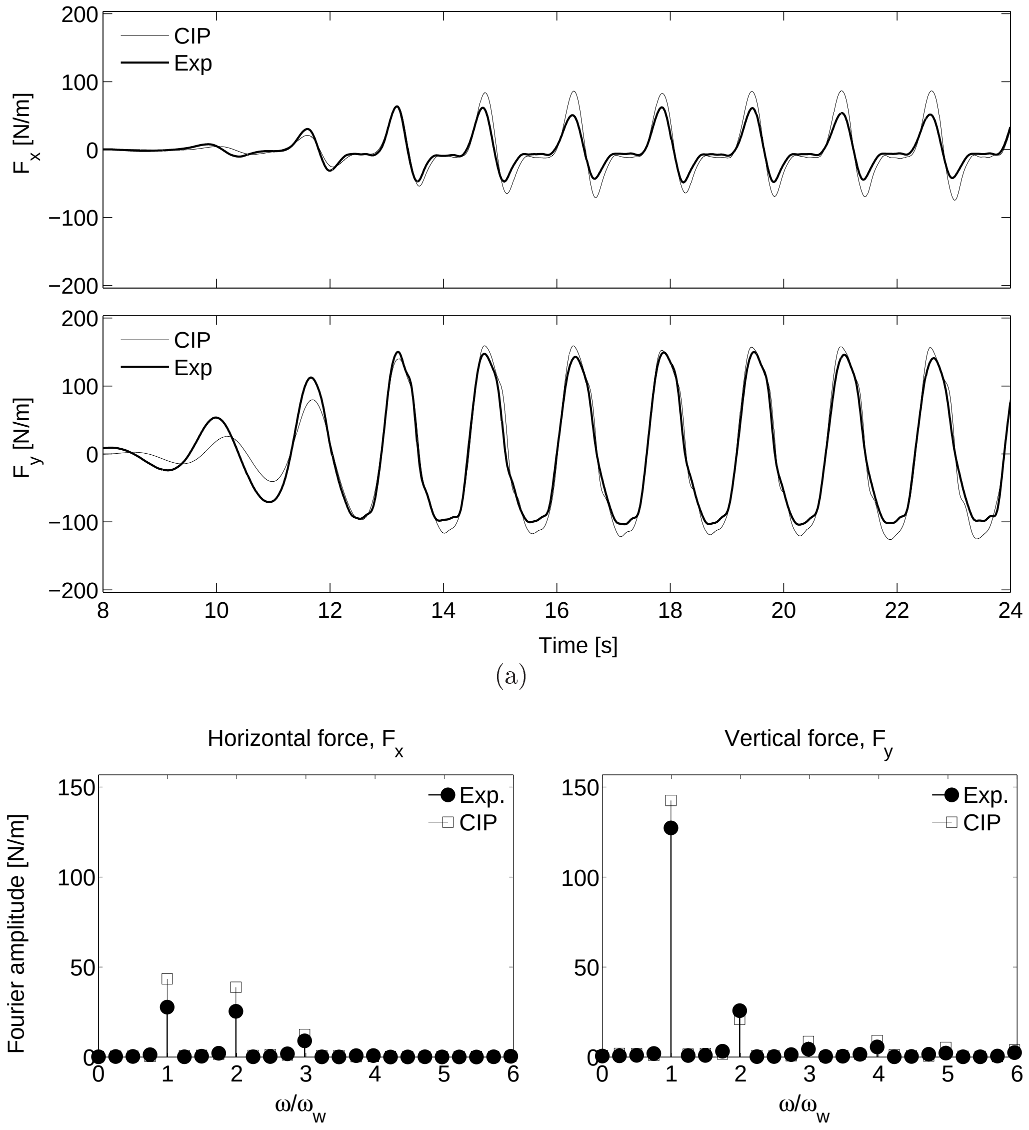

(a)

(b)

(c)

Figure 7.15: Comparison of time-series and corresponding Fourier amplitudes of wave forces on the circular cylinder obtained from simulations and model tests. Test parameters are $d/D = 0.2$, $T = 1.568$s, $H_0/\lambda_0 = 1/20$.

Circular cylinder with $d/D = 0.5$

We continue on the study of the circular cylinder, but now with the draft being increased to $d = 0.5D$. The same wave periods and wave heights as tested in the previous case are also tested here. Comparisons of force time-series are shown in Fig. 7.16(a) while corresponding Fourier amplitudes of the horizontal force and vertical force are presented in Figs. 7.16(b) and 7.16(c), respectively, for the test when the wave period is $T = 1.084$s. The Fourier amplitudes are obtained from the interval $t = [16\text{s}, 21\text{s}]$ of the time-series presented. For this case, the Fourier amplitude spectrum calculated from the time-series of the horizontal force and vertical force are very similar. The amplitude of the second harmonic component relative to the amplitude of the linear harmonic is 15% for both the horizontal force and for the vertical force, based on the measured data. A small third harmonic component is also present in the vertical force signal.

The force time-series obtained from the experiments and simulations with wave period $T = 1.348$s are compared in Fig. 7.17(a) which shows good agreement, although the computed force amplitudes of the horizontal force are somewhat larger than the measured amplitudes. In the Fourier amplitude spectra presented in Figs. 7.17(b) and 7.17(c), we observe that while the amplitude of the second harmonic component of the horizontal force has increased, the same component has nearly vanished from the amplitude spectrum of the vertical force. In fact, for the measured vertical force, the amplitude of the third harmonic component exceeds the amplitude of the second harmonic.

Circular cylinder with $d/D = 0.8$

Finally, we consider the circular cylinder at the largest draft $d = 0.8D$ subject to regular waves of period $T = 1.348$s and steepness $H_0/\lambda_0 = 1/20$. For this case, wave over-topping on the floater was observed both in the experiments and in the numerical simulations. A comparison of computed and measured wave excitation forces are presented in Fig. 7.19(a), which shows good agreement. We note from the time-series (Fig. 7.19(a)) that the vertical force component has two local maxima's for each wave load cycle in the steady state regime. This is associated with the over-topping wave. When the free surface elevation at the model position increases, the model experience a positive vertical force due to the hydrodynamic pressure. When the wave elevation becomes so large that over-topping occur, the pressure due to the water running on top of the model causes a negative vertical force that counteracts the positive force from the hydrodynamic pressure on the lower side of the model. As we see from the Fourier amplitude spectrum of the vertical force component in Fig. 7.19(c), over-topping leads to large nonlinearities of the vertical wave loads. However, the horizontal force component for which the Fourier amplitudes are presented in Fig. 7.19(b), is almost entirely described by the linear harmonic. Snapshots of the local flow kinematics at two time instants from simulations with our NWT are presented in Figs. 7.20 and 7.21 showing the velocity magnitude and the $z-$vorticity, respectively. We observe that vorticity is induced in the water due to flow separation from the boundary layer on top of the cylinder during over-topping. Further, vorticity is generated both in front of and behind the body at the end of the over-topping process, when the water runs off the body on both sides. The induced vortex at the right hand side of the body is rotating clock-wise, while the vortex generated on the left side is rotating counter clock-wise. In addition, some vorticity is observed close to the body

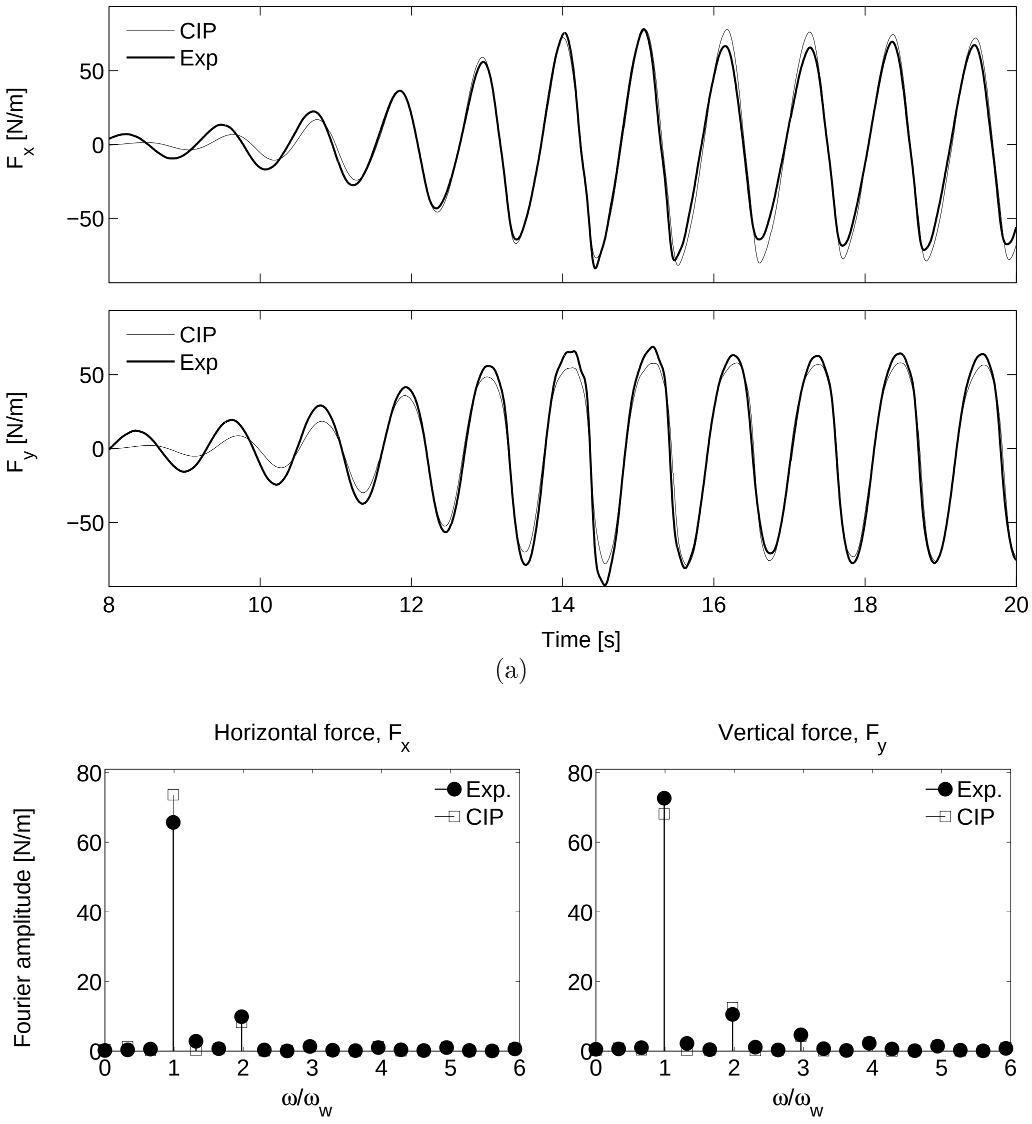

(a)

(b)

(c)

Figure 7.16: Comparison of time-series and corresponding Fourier amplitudes of wave forces on the circular cylinder obtained from simulations and model tests. Test parameters are $d/D = 0.5$, $T = 1.084$s, $H_0/\lambda_0 = 1/20$.

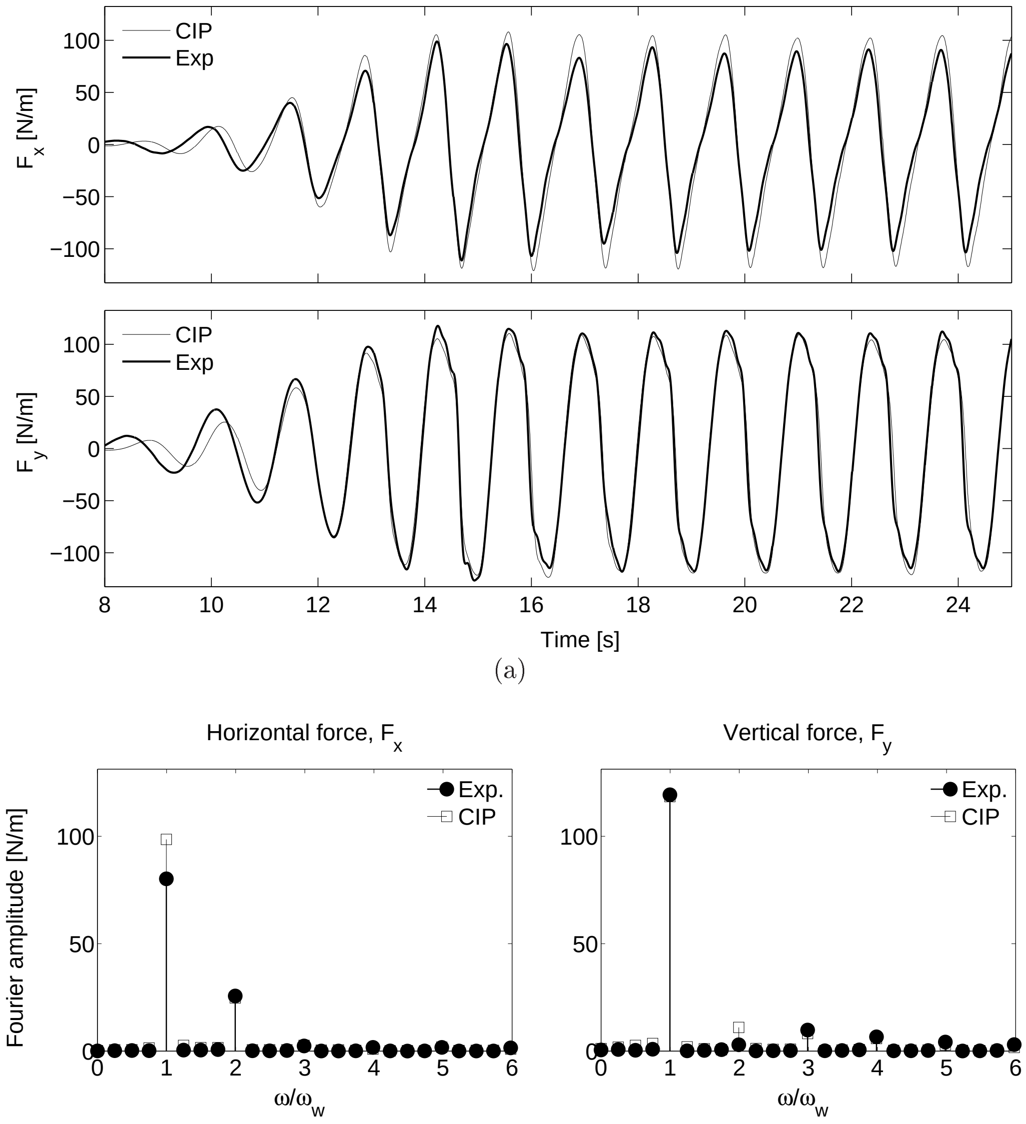

(a)

(b) (c)

Figure 7.17: Comparison of time-series and corresponding Fourier amplitudes of wave forces on the circular cylinder obtained from simulations and model tests. Test parameters are $d/D = 0.5$, $T = 1.348\text{s}$, $H_0/\lambda_0 = 1/20$.

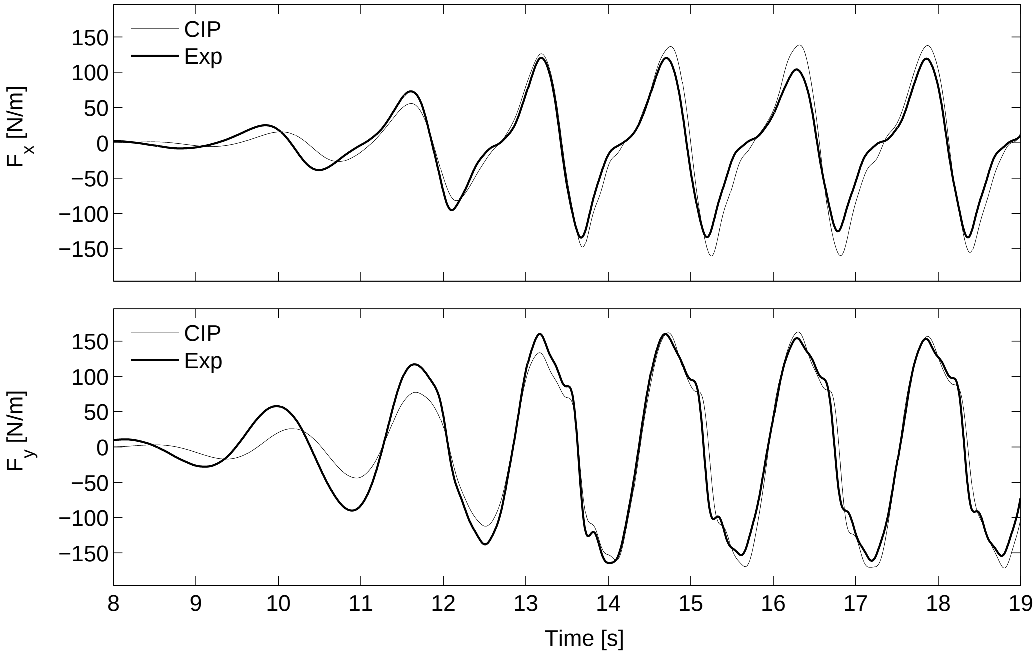

Figure 7.18: Computed and measured clamping forces from tests with circular cylinder at $d/D = 0.5$, $T = 1.568$s, $H_0/\lambda_0 = 1/20$.

boundary due to the no-slip condition and some close to the free surface away from the model. By comparing the numerical results against the recorded movies from the model test experiment, the latter is assumed to be a false effect due to the finite thickness of the air-water interface.

Rectangular cylinder with $d/b = 0.2$

Simulations are performed with the NWT for the rectangular model with draft $d/b = 0.2$ when subjected to waves with period $T = 1.348$s and steepness $H_0/\lambda_0 = 1/20$. Time series of the computed wave excitation forces forces are compared with time series of the measured clamping forces in Fig. 7.22(a). The computed force amplitudes of the horizontal force are observed to be larger than the measured force amplitudes. Corresponding Fourier amplitudes obtained from the time window $t = [15\text{s}, 20\text{s}]$ of the computed and measured wave forces are compared in Figs. 7.22(b) and 7.22(c) for the horizontal force and vertical force, respectively. The Fourier amplitude of the second harmonic component of the horizontal force is of the same order of magnitude as the Fourier amplitude of the linear harmonic component for this case. A pronounced second harmonic component of the horizontal force was also observed in tests with the circular cylinder for $d/D = 0.2$. However, the total vertical force amplitude is much larger than the total horizontal force amplitude. This is because the projected pressure area in the vertical direction is proportional to the model breadth, while the projected pressure area in the horizontal direction is proportional to the model draft which is less than 20% of the breadth.

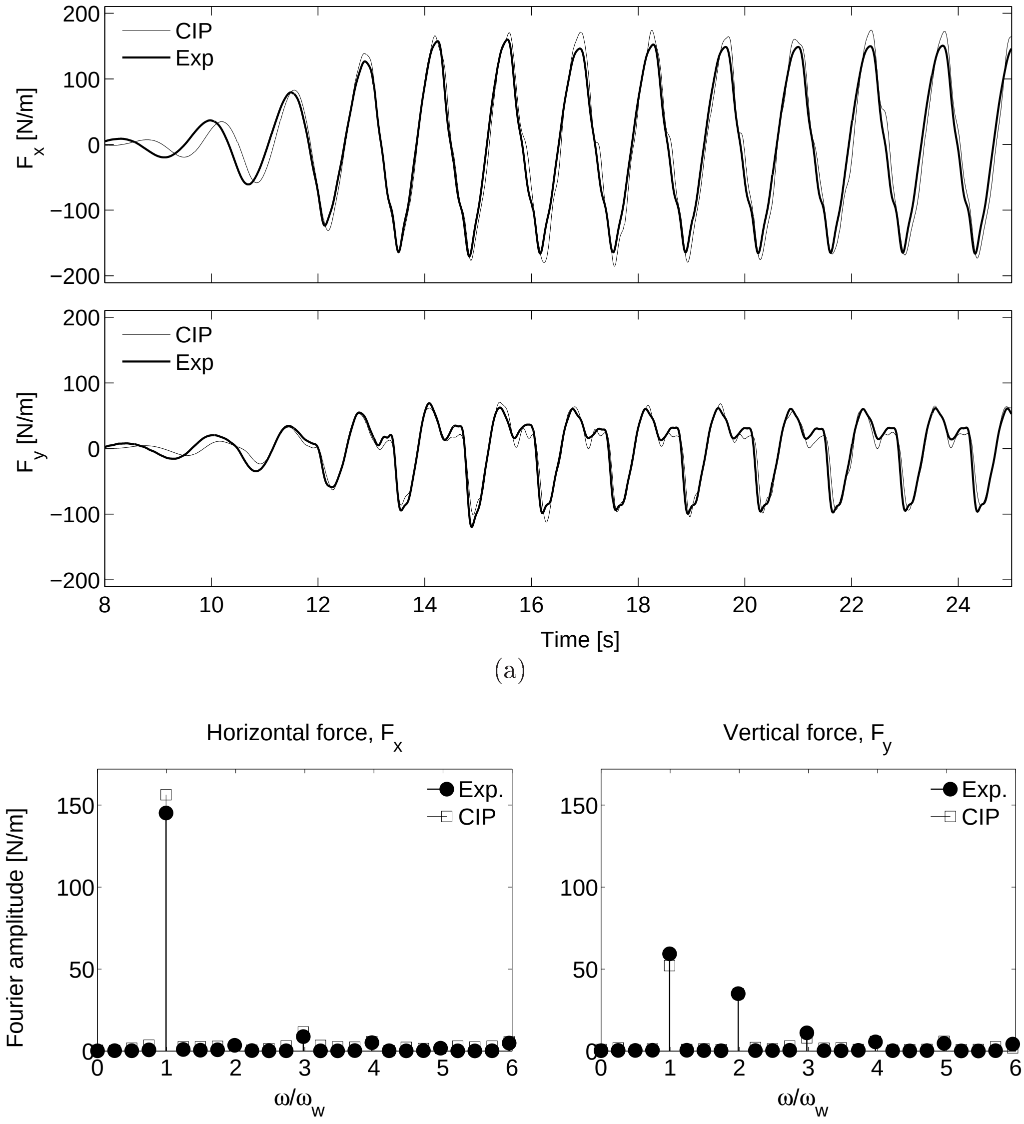

(a)

(b) (c)

Figure 7.19: Comparison of time-series and corresponding Fourier amplitudes of wave forces on the circular cylinder obtained from simulations and model tests. Test parameters are $d/D = 0.8$, $T = 1.348$s, $H_0/\lambda_0 = 1/20$.

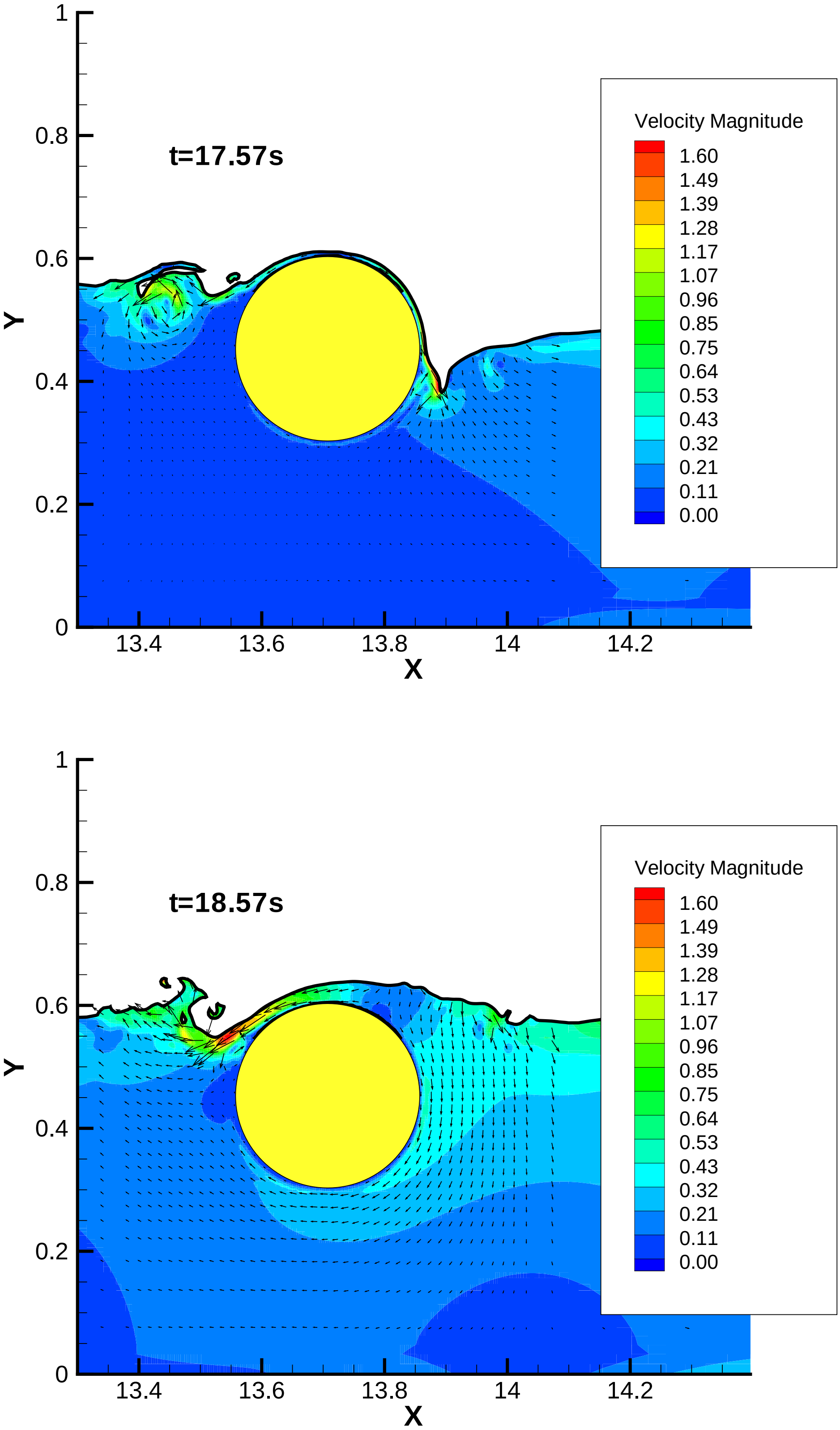

Figure 7.20: Snapshots of the local flow near the fixed model. The air-phase is excluded. Test parameters here are $d/D = 0.8$, $T = 1.348$s, $H_0/\lambda_0 = 1/20$. The contour values for the velocity are given in units of meters per second.

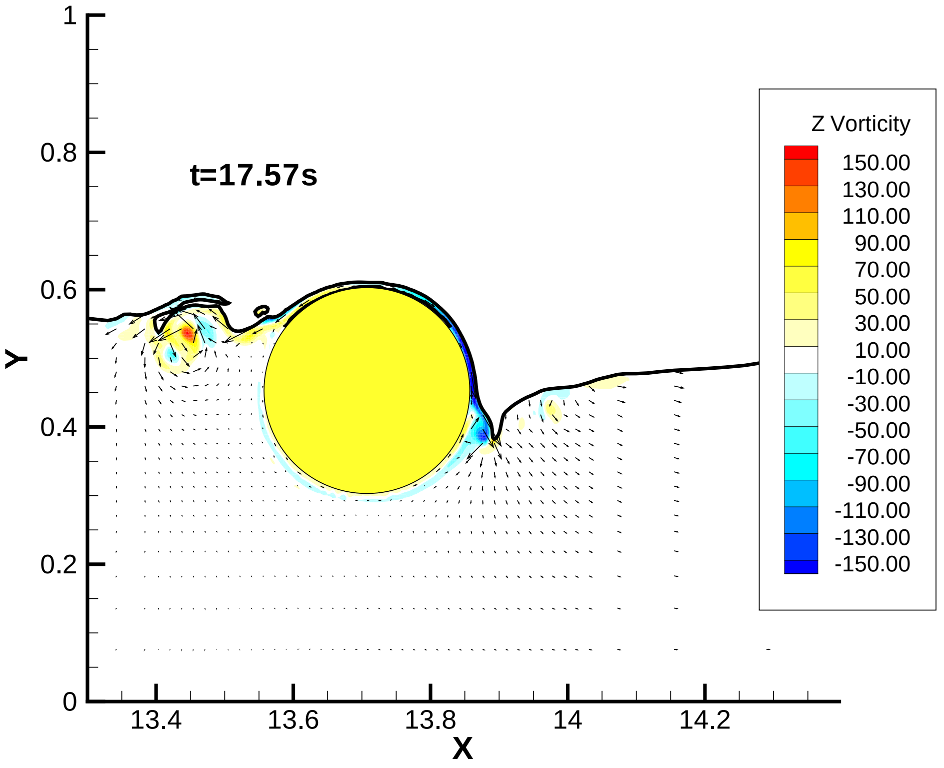

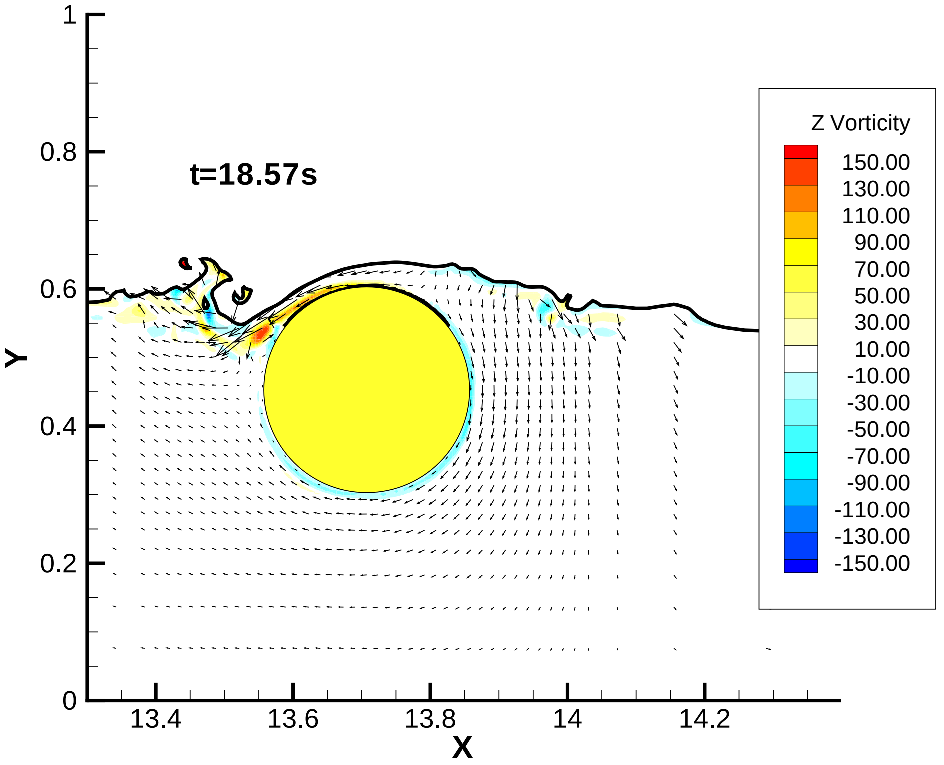

Figure 7.21: Snapshots of the $z-$vorticity in the local flow near the fixed model. The air-phase is excluded. Test parameters here are $d/D = 0.8$, $T = 1.348$s, $H_0/\lambda_0 = 1/20$. Contour values for the $z-$vorticity are given in 1/s.

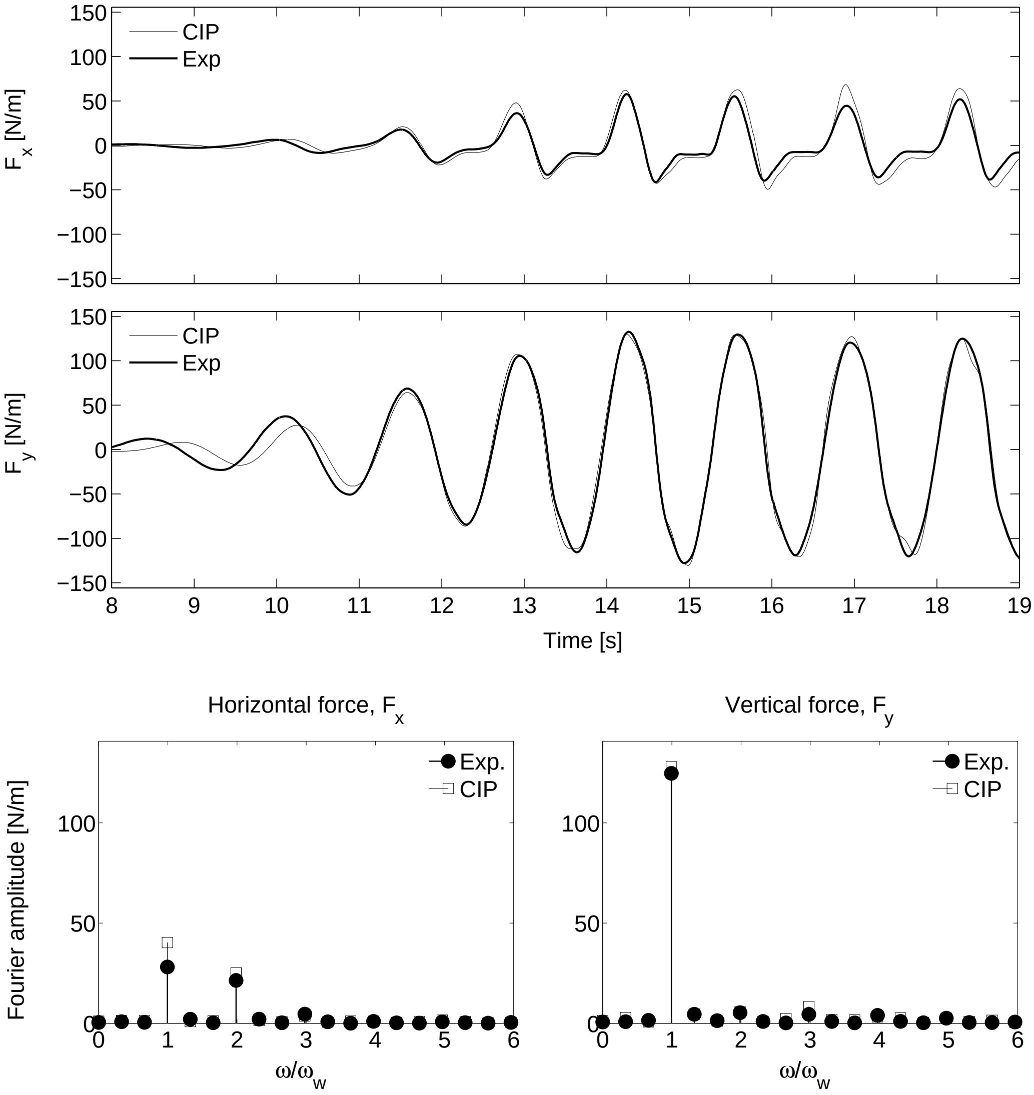

Figure 7.22: Comparison of time-series and corresponding Fourier amplitudes of wave forces on the rectangular cylinder obtained from simulations and model tests. Test parameters are $d/b = 0.2$, $T = 1.348\text{s}$, $H_0/\lambda_0 = 1/20$.

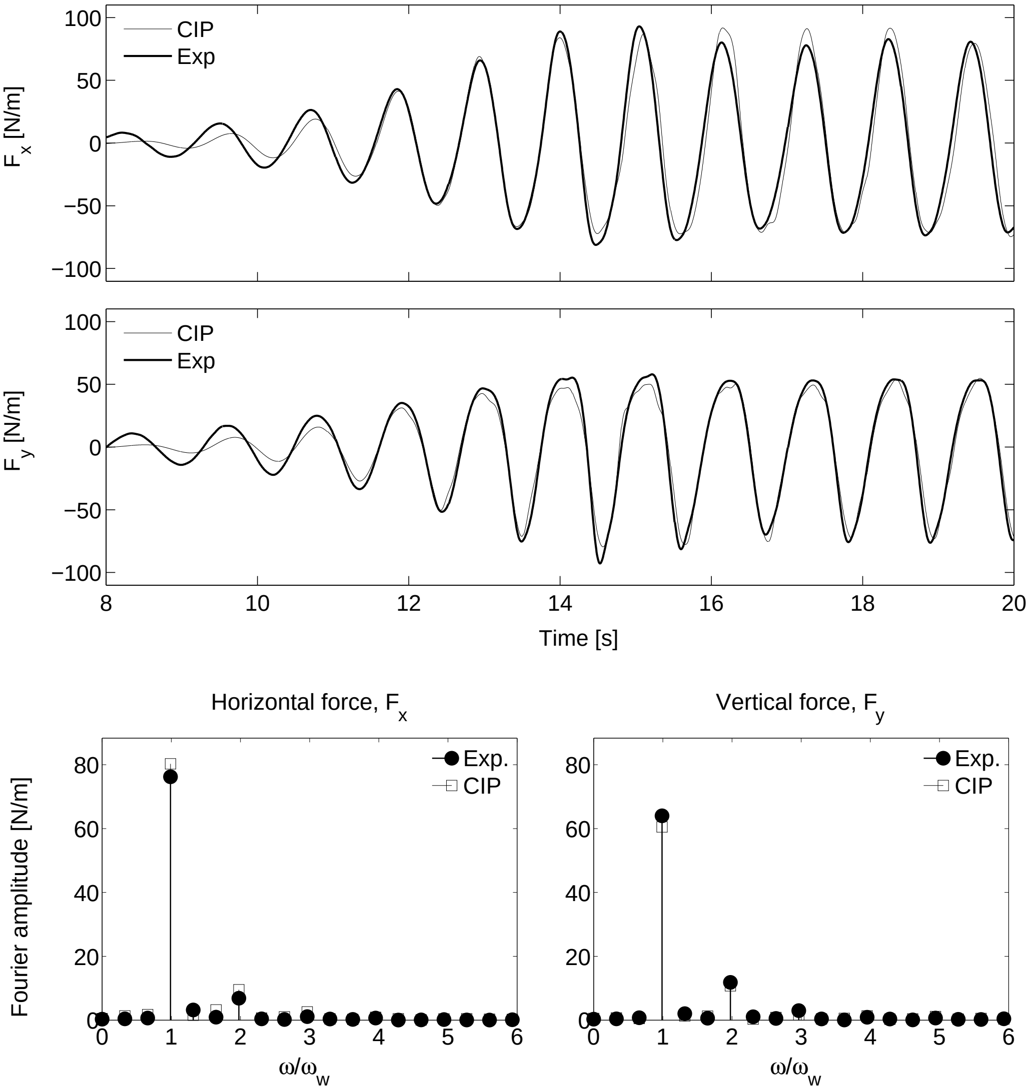

Figure 7.23: Comparison of time-series and corresponding Fourier amplitudes of wave forces on the rectangular cylinder obtained from simulations and model tests. Test parameters are $d/b = 0.5$, $T = 1.084$s, $H_0/\lambda_0 = 1/20$.

Rectangular cylinder with $d/b = 0.5$

Time-series of computed wave forces on the rectangular cylinder with draft $d/b = 0.5$ due to waves with period $T = 1.084$s and steepness $H_0/\lambda_0 = 1/20$ is compared with corresponding measured forces in Fig. 7.23(a). Corresponding Fourier amplitudes obtained from the time interval $t = [16\text{s}, 21\text{s}]$ are presented in Figs. 7.23(b) and 7.23(c). The linear harmonic component dominates for both the horizontal force and the vertical force. Good agreement between measured and computed forces are observed for this case.

Rectangular cylinder with $d/b = 0.8$

Finally, we consider the rectangular cylinder with draft $d/b = 0.8$ when subjected to waves with period $T = 1.084$s and steepness $H_0/\lambda_0 = 1/20$. Wave over-topping on the model was observed both in the experiments and in the numerical simulation with the NWT for this test condition. Time series of the computed and measured wave excitation forces are compared in Fig. 7.24(a). Obtained Fourier amplitudes of the horizontal and vertical forces are compared in Figs. 7.24(b) and 7.24(c), respectively. Due to short length of the time series from the numerical simulation, the Fourier transform of the force time-series are relatively coarse. However, we observe that the horizontal force is almost entirely described by the linear harmonic component. Further, we observe for the vertical force that the importance of the second harmonic component relative to the linear harmonic component increases when over-topping occur.

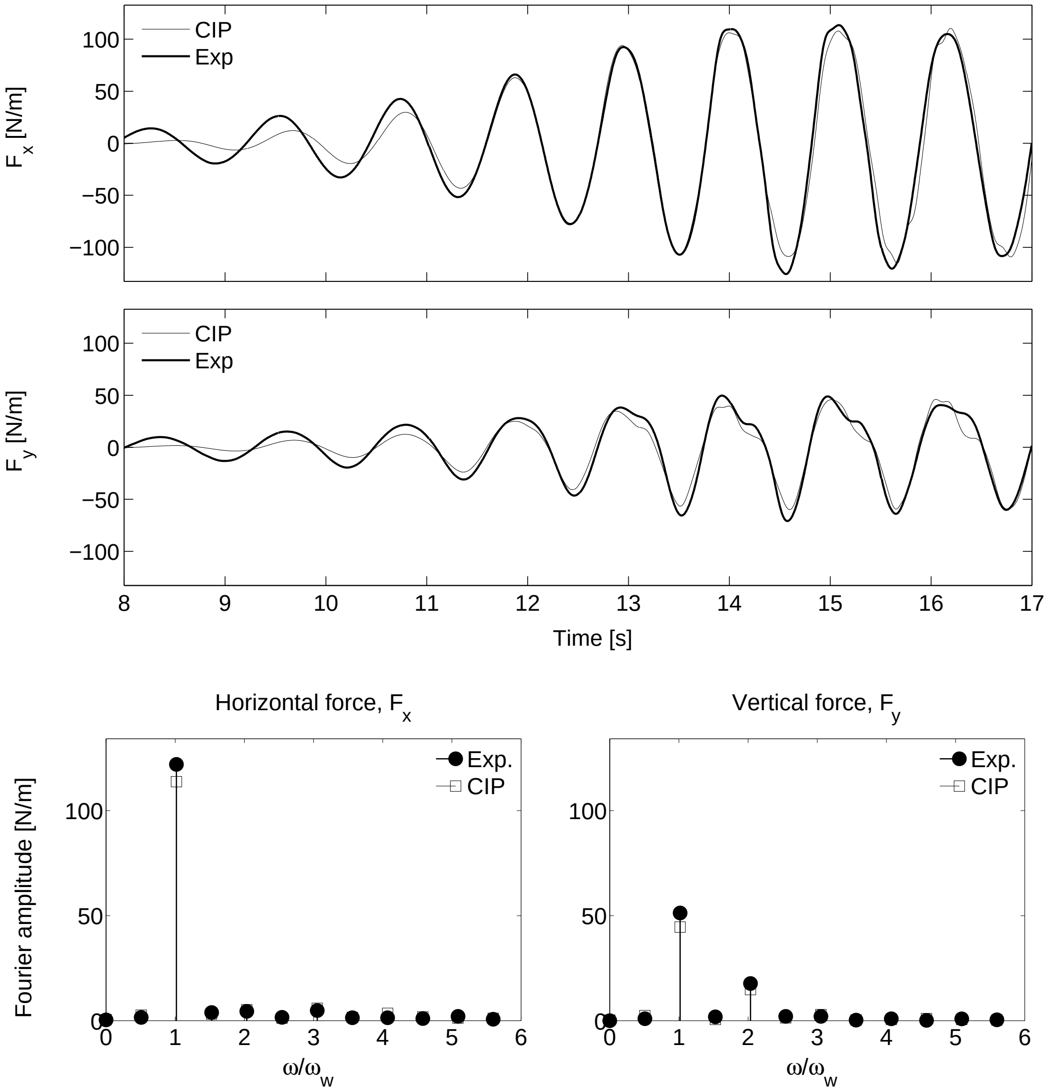

Figure 7.24: Comparison of time-series and corresponding Fourier amplitudes of wave forces on the rectangular cylinder obtained from simulations and model tests. Test parameters are $d/b = 0.8$, $T = 1.084$s, $H_0/\lambda_0 = 1/20$. Over-topping is observed in the model test and in the simulation. Due to short time series, the resolution of the discrete Fourier transform is coarse.

7.4 A generalized Morison model

In the following, a simplified numerical model for computation of wave forces on cylinders are discussed. It is common engineering practice to apply the Morison's equation when wave excitation forces on vertical cylinders are sought, which yields the in-line hydrodynamic force on the cylinder. Morison's equation is expressed in terms of a mass coefficient C_M and a drag coefficient C_D which generally has to be determined empirically. Further, Morison's equation applies for large wave lengths λ relative to the cross-sectional dimension D of the cylinder. For a vertical cylinder, the wave is considered long if $\lambda/D > 5$. A consequence of this is that both acceleration and velocity in the incident wave do not vary much over the cross-section of the cylinder and can be evaluated at the cylinder axis as if the cylinder was not there. The mass coefficient in Morison's equation has two components. One component is due to the undisturbed pressure field which yields the Froude-Kriloff force, while the other component is due to the diffraction effect of the cylinder. We propose a generalization of Morison's equation where the term including the mass coefficient is replaced by an explicit expression for the diffraction force and the Froude-Kriloff force as

$$F_i = F_i^D + F_i^{FK} + \frac{1}{2}\rho C_D D \left|u_i\right| u_i, \tag{7.4}$$

where F_i^D and F_i^{FK} is the 2D diffraction force and the 2D Froude-Kriloff force, respectively, on the cylinder cross-section. The index i indicates the direction of the force, where $i = 2$ refers to the horizontal $(x-)$ direction and $i = 3$ refers to the vertical $(y-)$ direction. Further, ρ is mass density of water, D is the projected dimension of the cylinder in the force direction and u_i is the fluid particle velocity evaluated at the position of the cylinder axis as if the cylinder was not there. This approach is consistent with the linear potential flow analysis of a semi-submersible as described by Faltinsen (1990). How the different terms in (7.4) are obtained are discussed in the following.

Froude-Kriloff forces

The Froude-Kriloff forces are found by integrating the hydrodynamic pressure p from the incident wave over the wetted surface S of the cylinder, i.e.

$$F_i^{FK} = -\int_S p n_i \mathrm{d}S. \tag{7.5}$$

Here n_i is the i-th component of the unit normal vector $\mathbf{n}$ pointing into the fluid domain. To first order in the wave slope $\varepsilon = k\zeta_A$, the Froude-Kriloff force is found by integrating the linear hydrodynamic pressure $p_1 = -\rho\frac{\partial\phi_1}{\partial t}$, found from Bernoulli's equation, over the mean wetted surface of the cylinder S_0. Here ϕ_1 is the first order velocity potential of a regular wave. Moving to second order in ε, the hydrodynamic pressure is from Bernoulli's equation found to be $p_2 = -\rho\frac{\partial\phi_2}{\partial t} - 0.5\rho\left|\nabla\phi_1\right|^2$, where ϕ_2 is the velocity potential correct to second order (see e.g. Dean and Dalrymple (1991)). Integrating the second order pressure over the mean wetted surface yields a second order force. We must also account for the time-varying wetted surface of the cylinder, which is done by integrating the linear hydrodynamic pressure from $y = 0$ to $y = \zeta_1(x,t)$. ζ_1 is the first order free surface elevation. By Taylor expansion of Bernoulli's equation from $y = 0$, the linear hydrodynamic pressure in the wave zone is found to be $p_1 = \rho g\left(\zeta_1 - y\right)$. This yields the total Froude-Kriloff force correct to $\mathcal{O}(\varepsilon^2)$. It should be noted that it is questionable to separate out a nonlinear Froude-Kriloff force from a nonlinear analysis as described above.

Diffraction forces

Due to the presence of the cylinder, the hydrodynamic pressure field in the incident wave will be modified. This yields the diffraction force. The diffraction potential can be found either numerically of analytically and then used to calculate the diffraction forces directly. We will use a simpler approach as described by Newman (1977). By means of consistency with calculation of the Froude-Kriloff forces, also the diffraction forces should be evaluated to $\mathcal{O}(\varepsilon^2)$ and the nonlinear interaction with the incident waves should be considered. Despite of this, a linear approach is used here for the diffraction forces. Using linear potential flow theory, the diffraction potential can be related to the incoming wave potential and the radiation potentials through the Haskind relation. This means the diffraction forces on a section of the cylinder can be written in terms of two-dimensional added mass and damping coefficients as

$$F_i^D = a_{ii}\dot{u}_i + b_{ii}u_i. \tag{7.6}$$

Here, $\dot{u}_i$ and u_i is the particle acceleration and particle velocity of the incident wave in the i-th direction, respectively. One important question here is: where do we evaluate the velocity and acceleration for a horizontal cylinder in the free surface? To answer this question, one should go back to the derivation of the Haskind relation. Then one should focus on what are the relations between the body boundary condition in the diffraction problem and the body boundary condition in the radiation problem. Intuitively, the velocity and acceleration used should represent the body boundary conditions in the diffraction problem. But, since both particle acceleration and velocity is space-varying under a wave, representative values should be used. Hence, for the vertical diffraction force component on the rectangular cylinder, the velocity and acceleration is evaluated at $[x, y] = [0, -d]$ where d is the model draft. For the horizontal diffraction force component, the velocity and acceleration is found from a weighted average over the center-plane of the model, i.e. by integrating the depth dependency of the acceleration and velocity from $y = -d$ to $y = 0$. The added mass and damping coefficients are a priory unknown and has to be found either by means of tabulated values or from computations. Since we assume 2D flow in the xy-plane, this implies we have to solve the radiation problem in heave and surge to find the added mass and damping coefficients. Added mass and damping are generally dependent on the frequency of oscillation, body geometry and the water depth. The radiation problem for heave and sway motion of a rectangular cylinder at finite water depth is solved using a linear time domain boundary element method (BEM) computer program. Dimensionless coefficients are listed in Table 7.3. Locally near the model, the free surface elevation will be modified due to the presence of the cylinder. Amplification of the local free surface elevation due to diffraction effects may cause the incoming wave to over-top on the rectangular cylinder, even when the incident wave amplitude is smaller than the freeboard. Over-topping will naturally have an effect on the vertical force time history of the wave excitation force which will be dependent on the nature of the over-topping wave (see Greco et al. (2007)). Over-topping is not modelled explicitly by our model.

Table 7.3: Non dimensional added mass and damping coefficients in heave and sway for a rectangular cylinder with beam B and draft d oscillating with the non-dimensional frequency $\omega\sqrt{B/g} = 1.014$ at finite water depth $h/B = 1.81$.

B/d	h/d	$\frac{a_{33}}{\rho Bd}$	$\frac{b_{33}}{\rho\omega Bd}$	$\frac{a_{22}}{\rho Bd}$	$\frac{b_{22}}{\rho\omega Bd}$
2.40	4.43	0.8850	0.5592	0.9108	1.0401
1.50	2.72	0.6512	0.6737	0.2392	1.5109

Viscous drag forces

Since the pressure distribution on the cylinder is modified due to separation of vortices at the sharp edged corners of the rectangular cylinder, the cylinder will experience a drag force. This drag force is represented by the last term in (7.4). The Reynolds number and surface roughness dependence of C_D for sharp edged bodies can be neglected. However, the KC-number dependence should be assessed. For a facing square cylinder in infinite fluid at low KC-number flow ($KC < 10$), experiments shows that the drag coefficient $C_D \approx 3.0$, i.e. KC-independent (Bearman et al. 1984). Viscous drag force is included in the horizontal direction for the whole wave cycle, and in the vertical direction only when the vertical velocity at the cylinder centre is negative.

7.4.1 Comparisons with CFD-simulations and experiments

To test the proposed method, two test conditions from the experiments in 2006 are considered. The first case considered is where the rectangular cylinder with draft $d = 0.125$m is subject to regular waves with period $T = 1.084$s and wave height $H = 0.088$m. This means $KC \approx \pi H/B = 0.92$. Over-topping was not observed in the experiments for this case. Numerical simulation with the CIP-based NWT using the base case grid and the same input parameters as in the experiments has been performed. The vertical forces computed with the NWT was in good agreement with experiments, meaning the difference between computed force amplitudes and measured force amplitudes is less than 5%. Comparing peak-to-peak force amplitudes ($(F_y^+ + |F_y^-|)/2$) shows that the NWT underpredicts the measured values from experiments by 1.5%. When it comes to horizontal forces obtained with the NWT, the agreement with experimental results is less good. Computed horizontal force amplitudes differ from the measured horizontal force amplitudes by 15%. Peak-to-peak force amplitudes differ by 14%. One should note here that the time series of the forces obtained with the NWT are relatively short, meaning forces from 2-3 wave cycles are used for comparison. This is due to the length of the computational domain and the fact that no wave absorber is used on the wave maker in the simulations to take care of the reflected waves from the model, which puts a limit on the simulation time. Hence, computed forces with the NWT might not give a good representation of the steady-state values. In addition comes the effect of increased water depth during the simulation due to the linear imposition of boundary condition on the wave maker. As in the experiments, overtopping was not observed in the numerical simulation with the NWT for this case. The generalized Morison model (GMM) gives a good representation of the measured forces, relative to the simplicity of the model. The difference in vertical force amplitudes obtained with the GMM compared to experiments is less than 5.5%. This is also the case for the horizontal force amplitudes. According

Table 7.4: Measured and computed wave excitation force amplitudes ([N/m]) in sway and heave for the test case 1 and 2 with the rectangular model. Beam-to-draft ratio for case 1 is $B/d = 2.4$, while for case 2 $B/d = 1.5$.

	Case 1				Case 2			
	F_x^+	F_x^-	F_y^+	F_y^-	F_x^+	F_x^-	F_y^+	F_y^-
Experiments	80.27	-73.26	53.03	-73.52	107.7	-111.8	41.85	-60.53
CIP	92.30	-82.34	51.73	-76.66	118.0	-117.9	43.66	-53.32
Gen. Morison	84.65	-70.23	50.61	-69.60	116.8	-98.90	37.04	-52.21
Newman, eq. (7.7)	89.96	-89.96	65.95	-65.96	137.2	-137.2	54.56	-54.56

to Newman (1962), the wave excitation force amplitude for the mode given by $k = 2, 3$, referring to the sway and heave mode respectively, can be related to the potential flow damping coefficient b_{kk} for the mode in question as

$$F_{ka} = 0.5H\sqrt{\rho g^2 b_{kk}/\omega}. \tag{7.7}$$

This relation yields force amplitudes in sway and heave which are at most 25% off the measured value in the experiments for the present case. Force amplitudes, both positive and negative, of the in-line horizontal force and the vertical force obtained from measurements and from the different numerical methods are given in Table 7.4. Time series of the free surface elevation at the model position from wave calibration tests and the forces measured in the experiments, are compared with corresponding numerically obtained time series from the CIP-based NWT and the generalized Morison model in Figure 7.25. The computed force time history show the same behaviour as the measured time series from experiments.

In the second case the draft was increased to $d = 0.200$m, yielding a free-board of 0.050m. The cylinder was subject to regular waves with the same wave parameters as in Case 1. Over-topping was observed in the experiments for this case, despite the fact that the incident wave amplitude was lower than the free-board. This means local diffraction effects are important. The over-topping wave had a dam-breaking-like behaviour. Simulations with the CIP-based NWT was performed with the draft increased to $d = 0.200$m using the same grid, computational domain and wave maker signal input as for Case 1. Over-topping was also seen in the numerical simulations, with the same dam-breaking-like behaviour as observed in the model test. An effect of over-topping on the wave excitation forces is seen to be a bump on the positive half cycles of the vertical force time history, associated with the pressure from the over-topping wave on the top-side of the cylinder. This effect of over-topping on the vertical force is captured by our NWT. As in Case 1, the generalized Morison model is applied to obtain force time series for Case 2. Resulting time series of measured and computed forces for the case of $d/H_m = 0.8$ are compared in Figure 7.26. Since the incident wave amplitude is lower than the freeboard of the cylinder, the generalized Morison model obviously does not predict over-topping. This explains why the obtained time series of the vertical wave excitation force from the GMM do not show the same trend as the measured time series and time series obtained with the CIP-based NWT of the vertical force. Positive and negative wave excitation force amplitudes are compared in Tab. 7.4. The generalized morison model is not tested for the circular model.

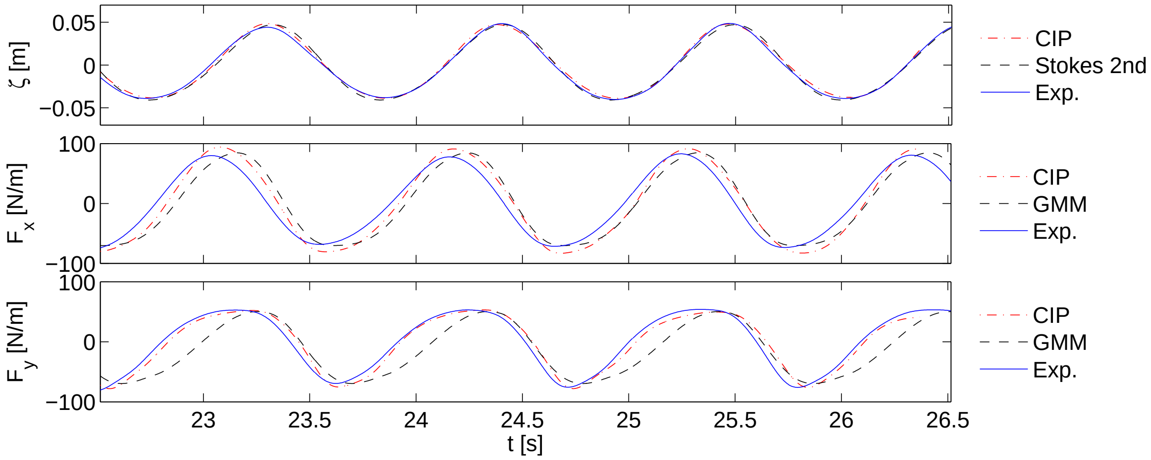

Figure 7.25: Comparison of incident free surface elevation at the model position and resulting horizontal in-line and vertical forces on the rectangular cylinder when $d/H_m = 0.5$, obtained from experiments and numerical simulations. Overtopping is not observed.

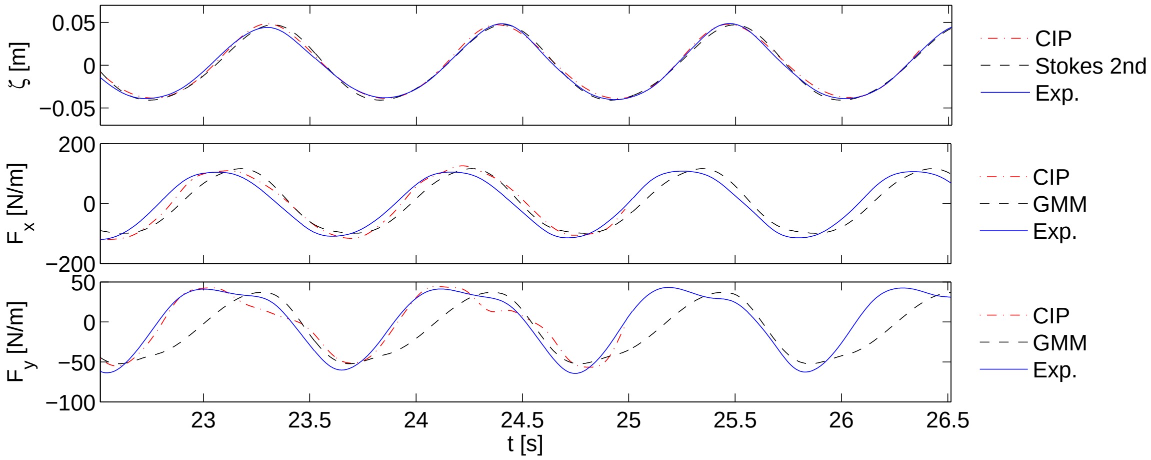

Figure 7.26: Comparison of incident free surface elevation at the model position and resulting horizontal in-line and vertical forces on the rectangular cylinder when $d/H_m = 0.8$, obtained from experiments and numerical simulations. Overtopping is observed in experiments and in the simulations with the CIP-based NWT.

7.5 Summary

Our study on horizontal cylinders fixed in the free surface zone and subject to large amplitude regular waves has been presented. Numerical wave calibration was performed with the CIP-based NWT for all test wave conditions used in simulations with models present. As in the experiments from 2006, both a circular and a rectangular geometry were tested with our NWT. Fourier analysis of the measured and computed force time-series showed that the second harmonic component of the horizontal force is important when the draft is small relative to the beam of the model. Further, when over-topping occur, the horizontal force is almost entirely described by the linear harmonic component, while the second harmonic component becomes pronounced for the vertical force. This was observed for both models tested.

A generalized Morison model (GMM) for computation of wave excitation forces on cylinders in the free surface was proposed. The model was tested using test parameters from the experiments for a rectangular cylinder. Forces obtained with the GMM were compared with results from experiments and simulations with the NWT. The GMM yielded good results for the case when over-topping did not occur. However, when over-topping occur, the GMM is no longer adequate.

The CPU-time for each of the numerical simulations performed with the CIP-based NWT from which results have been presented, were of the order of 30 hours on an Intel® Core$^{\mathrm{TM}}$ Duo 2.4GHz processor.

Chapter 8

A study of a floating circular cylinder in regular waves

In this chapter we investigate the nonlinear wave-induced motions of a moored circular cylinder. Time-series of the body motions in heave and sway obtained with the CIP-based NWT are compared with measured time-series from the model tests. This work has resulted in a journal paper (Kristiansen and Faltinsen 2009).

8.1 Numerical modelling of the 2008-experiments

The experiments from 2008 was characterized by a floating circular cylinder oriented horizontally in the free surface, which was moored and subject to regular waves. Nonlinear wave induced motions of the cylinder were studied. In the following, a numerical model representation of the experiments from 2008 is presented.

8.1.1 The computational domain and grid arrangements

A numerical model of the flume used in the experiments from 2008 was constructed. With the same argumentation as in the previous chapter, the domain length was based on the wave length λ estimated from potential flow theory, corresponding to the wave period tested. The circular model with diameter $D = 0.100$m was for most cases placed at a distance 4.5λ from the wavemaker boundary. The exception was one case where the model was located 9.5λ from the wavemaker boundary in order to run longer simulations. The water depth was $h = 1.00$m as in the experiments. Domain height was chosen to be 1.90m, meaning the distance from the calm water surface to the top boundary was 0.90m. For wave generation, the physical flume is equipped with a flap-type wavemaker. In the NWT, the flap wavemaker was modelled linearly by imposing the horizontal velocity component of the paddle onto the left hand boundary of the domain, which was fixed in space. The flap motion amplitude needed for generation of waves with a given wave height H was estimated from (3.26). A damping zone with length $L_{dz} = 4\lambda$ was applied at the right hand side of the domain. The top boundary was modelled as an open boundary with atmospheric pressure, while at the bottom boundary a no-slip condition was imposed. A no-slip condition was also applied on the floating body. In Fig. 8.1 a qualitative sketch of the computational domain is presented.

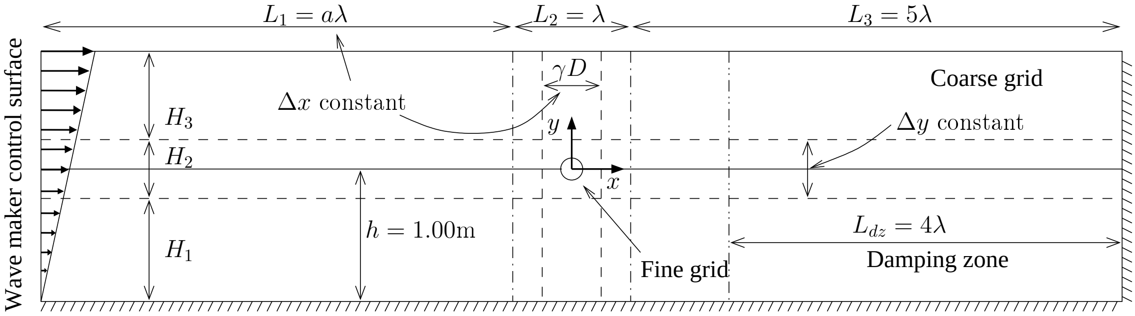

Figure 8.1: Sketch of the domain used in the simulations with the moored floating cylinder. Here λ is wave length, D is model diameter, h is water depth, Δx and Δy are horizontal and vertical grid spacing, respectively. The parameter $\gamma = 2$ for most cases, while $a = 4$ for all tests except when $T = 0.544$s for where $a = 9$ was used.

Table 8.1: Grid parameters used to obtain three grids with different resolution for simulations of the moored floating cylinder in waves. Due the gridding technique will the total number of grid cells vary from case to case.

	N_B	N_λ	N_I
Grid 1	55	40	80
Grid 2	60	45	90
Grid 3	70	45	100

Non-uniform staggered Cartesian grids were used. Grid-stretching was applied in order to increase the grid resolution in regions of the domain where large gradients of the solution occur, while keeping the CPU-time at an acceptable level. The computational domain was divided into sub-regions where different gridding strategies were applied. In the longitudinal direction, the domain was divided in to three sub-regions L_i with $i = 1, 2, 3$ as shown in Fig. 8.1. Constant spacing Δx_i between the vertical grid lines was applied in L_1, where Δx_i was based on the wave length λ. In L_2, Δx_i varied in a squared cosine manner in order to match the relatively coarse grid in L_1 with a fine grid region at the model position. Constant grid line spacing was used in the fine-grid region of width γD inside L_2, where $\gamma = 2$ for most cases. In L_3, the grid increment Δx_i varied as a quadratic function. For the vertical direction, quadratic grid stretching are used in H_1 and H_3, while Δy_j is constant in the interface zone defined by H_2. The height of the interface zone is for the majority of the tests $H_2 = 0.20$m, except for cases with large body motions, where a larger value of H_2 is used to avoid that the model goes out of the fine grid region. Smooth variations of the grid increments between the different grid regions are ensured. For each test condition, three grids with different resolution are constructed such that grid sensitivity of the results could be tested. Grid parameters for the three grids are listed in Tab. 8.1. Due to the gridding method described above, the total number of grid cells in the domain will vary from case to case.

Table 8.2: Computed mean wave height H_{num} from numerical wave calibration tests and measured mean wave height, H_{exp}^{WG2} and H_{exp}^{WG3} corresponding to WG2 and WG3, from the physical wave calibration tests. Linear wavemaker theory is used to calculate the necessary flap amplitude for the input wave height H_{input}.

T [s]	H_{input} [m]	H_{num} [m]	H_{exp}^{WG2} [m]	H_{exp}^{WG3} [m]
0.457	0.023	0.021	0.023	0.023
0.497	0.028	0.024	0.029	0.029
0.544	0.033	0.029	0.035	0.033
0.601	0.040	0.036	0.044	0.042
0.761	0.065	0.060	0.069	0.062
0.878	0.086	0.081	0.085	0.085
1.038	0.120	0.116	0.120	0.119
1.132	0.143	0.139	0.138	0.139

8.1.2 Numerical wave calibration

Numerical wave calibration tests are performed, which are simulation of wave generation with the NWT when the model is not present. Obtained wave heights from the numercial wave calibration tests and measured wave heights from the physical wave calibration tests are presented in Tab. 8.2. The obtained wave heights in the NWT are generally lower than the input wave height used when estimating the necessary flap amplitude of the wavemaker. Computed time-series of the free surface elevation at $x =$m and $x =$m for the two wave periods $T = 1.038$s and $T = 1.132$s are compared with measured free surface elevation from the physical wave calibration tests in Figs. 8.2 and 8.3. Good agreement between the computed and measured free surface elevation is observed for the steady state region of the time-series, while some deviations are observed in the wave fronts. It is in general difficult to reproduce the exact transients of the front of the wave train in the experiments with the NWT. This has different reasons. First of all, when the generated waves are short, it is computationally costly to resolve the waves in a domain with dimensions of the physical flume. Thus, we have used a shorter wave tank in the numerical simulations than the actual physical wave flume. Second, when comparing time-series of the free surface elevation from flumes with different dimensions, there are two important wave characteristics that has to be accounted for. These are the phase velocity and the group velocity. If one travels with the wave front, linearly the wave-front kinematics repeat itself when the wave front has propagated an integral number of wave lengths. Hence, when the computed free surface elevation in the wave front is compared with measurements done in the larger physical flume, the difference of the distance between the wavemaker and wave probe in the physical flume and that in the numerical flume should also be an integral number of wave lengths. However, in the fully nonlinear problem the wave-front kinematics can be different even for two positions located an integral number of wave lengths apart. This means that if the dimensions of the NWT are different from the dimensions of the physical wave tank, the transient behaviour of the wave front will not be captured well.

In the adopted free surface capturing method where the step-like color function $\phi_1(x, y, t)$ is used to define the water phase, the free surface is found from the color function as the

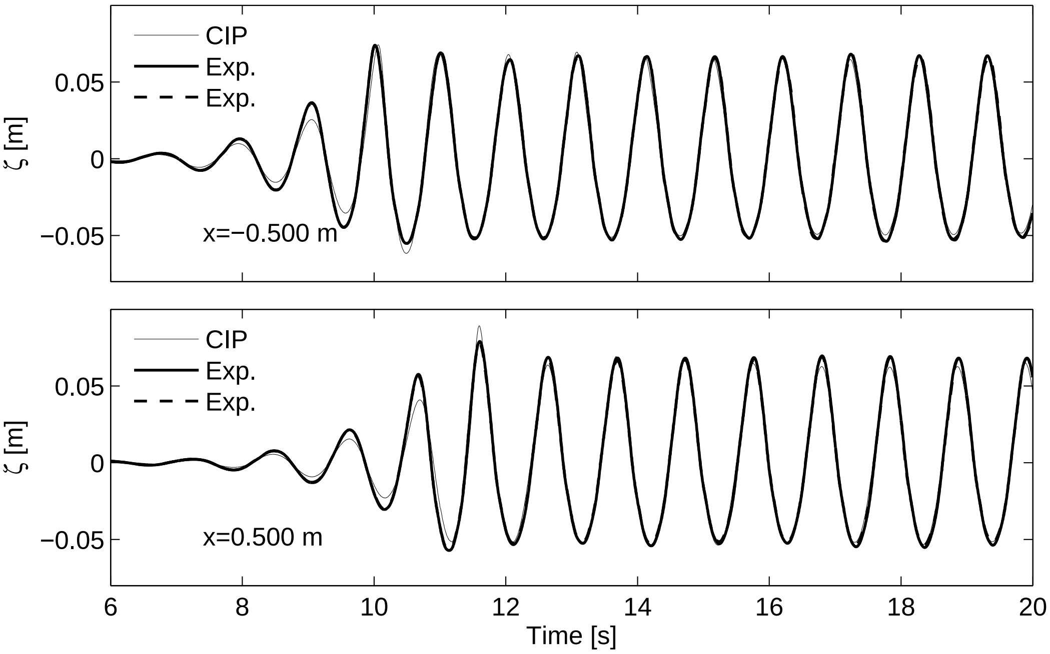

Figure 8.2: Comparison between free surface elevation obtained from numerical and experimental wave calibration tests. Wave period is $T = 1.038$s and input wave height is $H = 0.120$m.

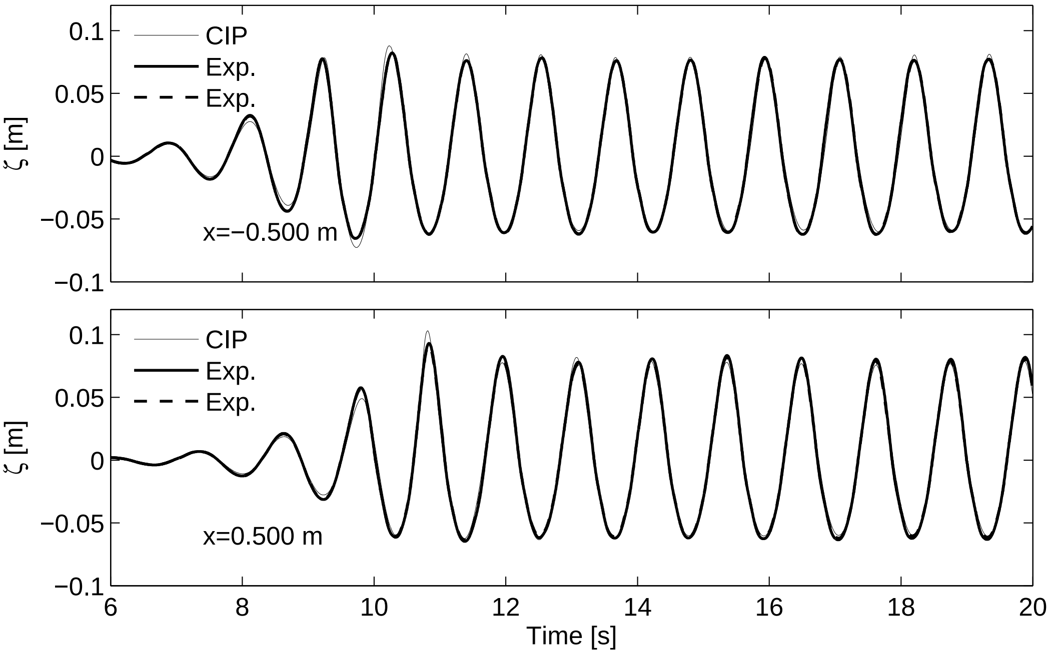

Figure 8.3: Comparison between free surface elevation obtained from numerical and experimental wave calibration tests. Wave period is $T = 1.132$s and input wave height is $H = 0.143$m.

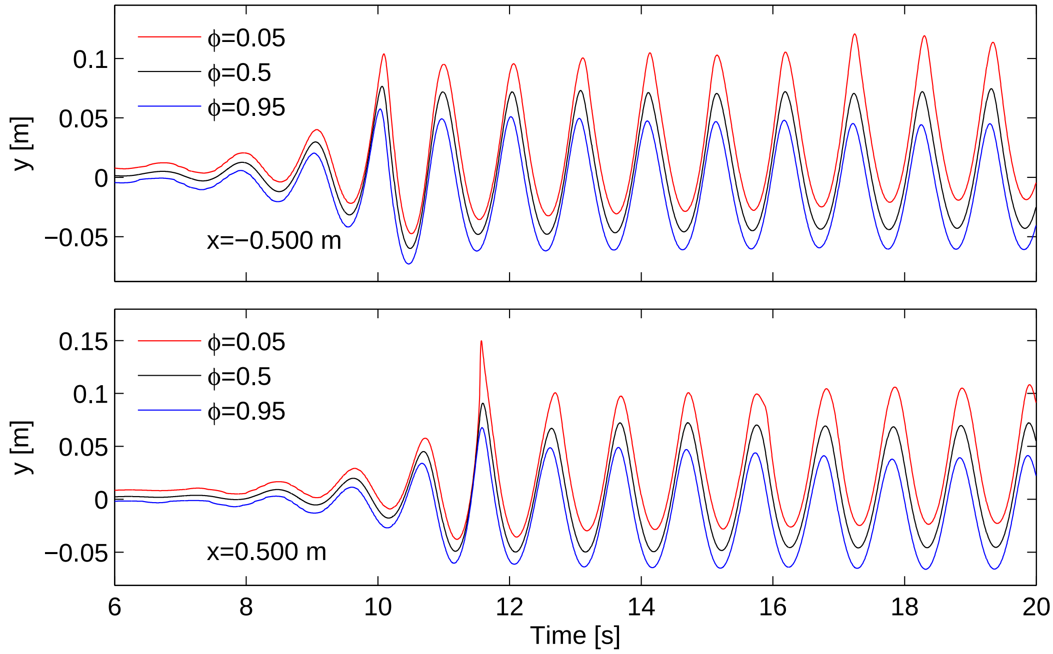

Figure 8.4: Contour levels of the color function ϕ_1 representing water during numerical wave calibration for case with wave period $T = 1.038$s and wave height $H = 0.120$m. The free surface is represented by the contour $\phi_1 = 0.5$.

contour $\phi_1 = 0.5$. Due to numerical diffusion at the steep gradients of the color function, some smearing of the color function is observed during the simulation. This is exemplified in Fig. 8.4, where the vertical position in time of the contours defined by $\phi_1 = 0.05$, $\phi_1 = 0.5$ and $\phi_1 = 0.95$ at the two positions $x =$m and $x =$m are shown. Numerical diffusion is observed as increasing distance between the contour lines in time for the direction given by the steepest gradient.

8.1.3 Modelling of the mooring line arrangement

The mooring system was modelled as straight linearly elastic lines where in the simulations the far end were pin-pointed at the coordinates of the contact point between the mooring line and the pulley from the experimental test setup. The other end of the mooring line was located at the model center, i.e. the cylinder axis, and was thus moving with the body. Two mooring lines were applied and the line geometry was symmetric about the vertical y-axis through the cylinder axis when the model was resting at its equilibrium position. Then, the horizontal and vertical extent of each mooring line was $l_x = 2.43$m and $l_y = 0.136$m, and the mooring lines made an angle $\alpha = 3.2°$ with the calm free surface as in the experiments. The mooring lines had pre-tension $F_{s0} = 38.1\,\mathrm{N}$ and an equivalent spring stiffness $k_e = 151.2\,\mathrm{N/m^2}$ in the 2D model. Mooring line forces were decomposed to yield components in both horizontal direction and vertical direction, depending on the instantaneous position of the model.

8.1.4 Equivalent mass of the circular cylinder with end-plates

In the model tests presented, the model was a circular cylinder equipped with circular end-plates. These end-plates were made of plexi-glass and contributed to 33.7% of the total mass of the model, but their contribution to the total buoyancy were only 13.4%. Since the NWT is a 2D code, it cannot include these end-plates into the calculations. Further, modelling the cylinder with the same cross-sectional dimensions and measured mass divided by the model length, as in the experiments, will give an incongruity between model weight and hydrostatic forces on the model. Hence, an equivalent mass of the model has to be introduced when numerical simulations of the model tests are performed. This effective mass is found by balance of static forces in the vertical direction, deduced from observations and measurements in the model tests. When the model in the experiments was moored and in its equilibrium position, the cylinder axis was observed to have a positive vertical offset $\Delta y = 4$mm from the calm water surface, which means the submerged area A of the circular cross-section can be determined. Then the buoyancy force of the model, excluding the end-plates, is found as $B = \rho g A L_m$, where L_m is the length of the model. The three mooring lines, which all made an angle $\alpha = 3.2°$ with the calm water surface, had a pre-tension measured to be $F_{01} = 10.53$N, $F_{02} = 11.20$N and $F_{03} = 21.67$N. Thus the equivalent mass of the cylinder is found, using Newton's first law, as $M_e = \left(B + \sum_{i=1}^{3} F_{0i} \sin(\alpha)\right) / (g L_m) = 3.940$kg. This equivalent mass is used as input to the NWT.

8.2 Identification of damping in the experiments

Free decay tests of the sway motion of the moored cylinder are conducted, both numerically and experimentally, in order to identify the different sources of damping in the experiments. The numerical free decay tests was performed using the same initial conditions as in the experiments. The initial horizontal offset of the model from equilibrium was $\eta_2(0) = 0.047$m. Numerical and experimental results are compared in the following and deviations are discussed. The relative importance of different physical effects causing decay rates of the motion amplitudes are also presented.

In Fig. 8.5(a), time-series of the sway motion obtained from CIP-simulations are compared with sway motion deduced from the mooring line forces measured in the experiments. Corresponding decay rates of the sway motion amplitudes are shown in Fig. 8.5(b). Both in the experiments and in the simulations, the period of the sway motion was found to be $T \approx 1.09$s, which is the natural period in sway from linear potential flow theory. In Fig. 8.5(b) the theoretical decay rate due to linear wave radiation damping is plotted for comparison. While the decay rate of the sway motion obtained from numerical simulations seems to approach that due to linear wave radiation damping, there is an increase in the decay rate of the sway motion amplitudes obtained from the experiments. This increase in the damping level with decreasing amplitude of oscillation is hard to explain in terms of hydrodynamic effects. If the model oscillates with an amplitude η_{2a} equal to the initial horizontal displacement at its natural frequency, the Reynolds number for oscillatory flow is $Rn = \frac{\omega \eta_{2a}^2}{\nu} \approx 10^4$ which means the boundary layer is laminar in attached flow (Faltinsen 1990). Changes in the damping level are thus not likely to be associated with transitions in the boundary layer flow. In the following, viscous effects are

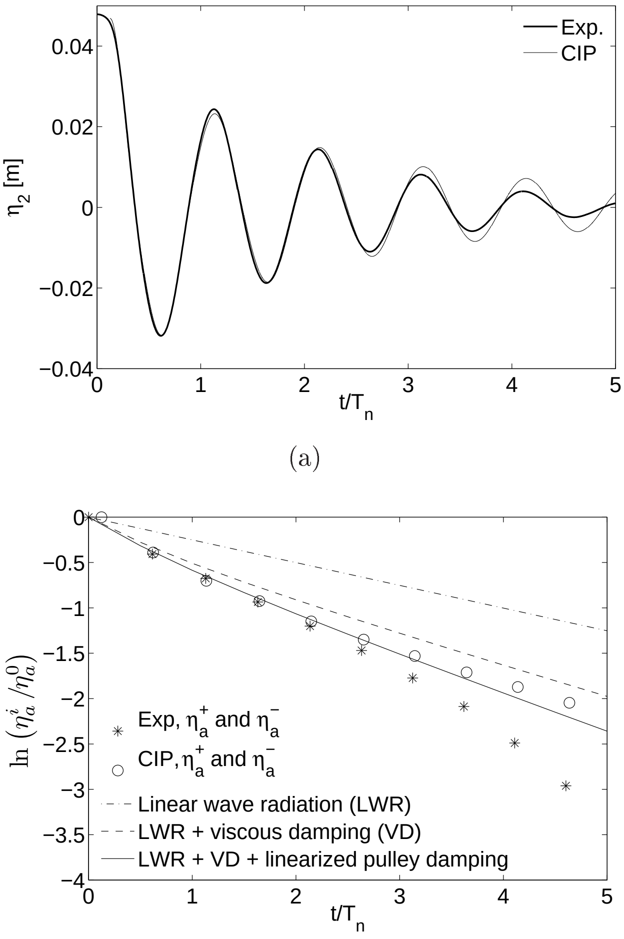

(a)

(b)

Figure 8.5: Free decay of the circular cylinder in the sway mode of motion. The initial horizontal offset from equilibrium is 47mm. Theoretical and empirical damping rates are added in (b) for comparison.

discussed. Investigation of the Keulegan-Carpenter number, defined as $KC = 2\pi\eta_{2a}/D$, shows that $KC > 2$ for the two first periods of oscillation in the free decay test. This means viscous flow separation is likely to occur, which is also seen in the numerical simulations where the flow separates and vortices are shed from the body surface during the two first periods of oscillation. The damping term due to viscous flow separation are alternatively estimated as follows. By assuming that the free surface acts as a wall and that the boundary layer flow is laminar, a linearized viscous damping force $F_D = -b_{22}^v\dot{\eta}_2$ due to flow separation is added to the sway motion equation. Equivalent linearization is applied to obtain $b_{22}^v = \frac{2}{3\pi}\rho C_D D\omega\eta_{2a}L_m$, where $C_D \approx 0.2KC$ (Graham 1980). The boundary layer flow on the model surface will also contribute to the damping of the body motion. If the flow is assumed attached to the body surface an estimate of the damping level in the experiments due to skin friction on the half submerged circular cylinder of length $L_m = 0.58$m with end-plates can be found by linear theory. For harmonic oscillations with constant amplitude $\eta_{2a} = 0.02$m at the natural sway frequency $\omega_{n2} = 5.75\,\text{rad/s}$, the contribution from skin friction, i.e. tangential stresses on the cylindrical part of the model, can be shown to be $|F_v| = \frac{\pi}{2}\mu\omega\eta_{2a}\sqrt{\frac{\omega}{\nu}}DL_m \approx 0.03$N (Batchelor 1967). There is also an effect from normal viscous stresses on the surface, which according to Stokes (Stokes 1851) yields an equal contribution as that from tangential stresses on the surface of the circular cylinder. The skin friction drag on the end-plates used to ensure 2D-conditions are found through Stokes' second problem to contribute $|F_v^{EP}| \approx 0.03$N to the viscous drag force. The influence due to the narrow gap between the end-plates and tank walls on the viscous effects is negligible. Thus, the total damping force due to the boundary layer on the model in the physical free decay test is of order $|F_v^{bl}| \approx 0.09$N. This damping force is shown to decay linearly with η_{2a}. In comparison, the linear wave radiation damping for this case is $|F_w| = 0.27$N. If the flow does not separate, this means that about 25% of the total theoretical hydrodynamic damping force is due to boundary layer effects at the natural period in sway. Theoretical decay rate of the sway motion amplitudes due to viscous damping and linear wave radiation damping is shown in Fig.8.5(b). The obtained damping coefficients shows that initially, damping due to viscous flow separation is of the same order as the linear wave radiation damping. However, the increasing decay rate seen in the later stage of the experiments could not be explained in terms of viscous effects. Damping due to wall contact could be another explanation, but investigation of the jerk parameter for the measured acceleration time-records does not indicate any wall contact events that could have explained the increased damping level. However, friction in the pulleys used in the mooring line arrangement will introduce damping to the system. Free decay tests of the model in air was performed in order to investigate the damping from the mooring line arrangement. Physically, this was done by suspending the model using a long line from the roof and then draining the flume, such that the model appeared as a long pendulum. The sway motion amplitudes from free decay in air also showed the same tendency as seen for free decay of the sway motion for the semi-submerged cylinder, namely an increasing decay rate with decreasing amplitude. This means that the increasing damping level in the last part of the free decay test is not related to hydrodynamic effects, but most probably associated with nonlinear damping due to friction in the pulleys used in the mooring line arrangement. By using the experimentally obtained decay rate for the largest sway motion amplitudes from the free decay test in air, a linear approximation of the damping coefficient due to pulley-friction was estimated. The obtained damping coefficient, b_{22}^p, yielded a corresponding damping ratio in water due to the pulleys as $\xi = b^p_{22}/\left(2\omega_n(m + a_{22})\right) \approx 0.012$. In comparison, the damping ratio due to skin friction on the semi-submerged cylinder in attached flow is $\xi = 0.0091$. The theoretical decay rate of the sway motion amplitudes when all damping terms deduced above are included is presented in Fig. 8.5(b). Since the damping coefficient due to viscous flow separation depends on the motion amplitude, the decay rate is found by iteration. Neither skin friction drag, nor damping due to pulley-friction is included in the numerical simulations with the NWT. However, the forces from normal stresses due to the boundary layer on the cylinder surface are implicitly included in the pressure forces. What the results in Fig. 8.5(b) indicate is that the very good agreement between the experiments and the CIP shown in Fig. 8.5(a) for the initial oscillations is coincidental. Even though the pulley-friction and the skin-friction are not dominant, their effects should appear as a visible difference between the experiments and CIP-simulations.

8.3 Comparisons between model tests and simulations

The wave-induced sway and heave motion of the cylinder are obtained by integration of the measured accelerations. Further are the obtained model motion from numerical simulations band-pass filtered using the same cut-off frequencies as for the measurements. Roll motion of the circular cylinder is not considered in the present study. Comparisons between numerical simulations and experiments are discussed in the following.

8.3.1 A model based on linear potential flow theory

Since we are dealing with nonlinear motions, we define the sway and heave motion amplitudes used for comparison as $\eta_{ka} = 0.5(\eta^+_k + \eta^-_k)$, where $k = 2, 3$ refers to the sway and heave mode, respectively. Here η^+_k is the positive amplitude and η^-_k is the negative amplitude in steady state condition. The motion amplitudes were made dimensionless using the incident wave height H measured in the wave calibration tests. Sway and heave response of the model predicted by linear potential flow theory with additional damping due to viscous and pulley effects, was used for comparison and is derived as follows. The 2D excitation force amplitude F_{ka} has been related to the potential damping coefficient b^w_{kk} as $F_{ka} = 0.5H\sqrt{\rho g^2 b^w_{kk}/\omega}$ (Newman 1962). We assume that roll motion is negligible. Then, it follows from the uncoupled linear equations for sway and heave that

$$\frac{\eta_{ka}}{0.5H} = \frac{F_{ka}/\left(0.5H\right)}{\sqrt{\left(c_{kk} - \omega^2\left(m + a_{kk}\right)\right)^2 + \omega^2 b^2_{kk}}}. \tag{8.1}$$

Here, m is the structural mass of the model per unit length, a_{kk} and b_{kk} are the frequency dependent 2D added mass and damping coefficients, c_{kk} is the 2D restoring coefficient, ω is wave frequency, ρ is mass density of water while g is the acceleration of gravity. For the heave mode, i.e. $k = 3$, only linear wave radiation damping is included and hence $b_{33} = b^w_{33}$ in (8.1). The added mass and potential damping coefficients (a_{kk} and b^w_{kk}) for infinite water depth was provided by Skejic (Skejic 2008). As observed from the free decay tests, viscous damping gives a significant contribution to the total damping at the natural period in sway. Thus, in addition to the linear wave radiation damping, the viscous damping terms due to boundary layer effects and flow separation from the semi-submerged circular cylinder, b^{bl}_{22} and b^v_{22} respectively, are included in b_{22}. The boundary

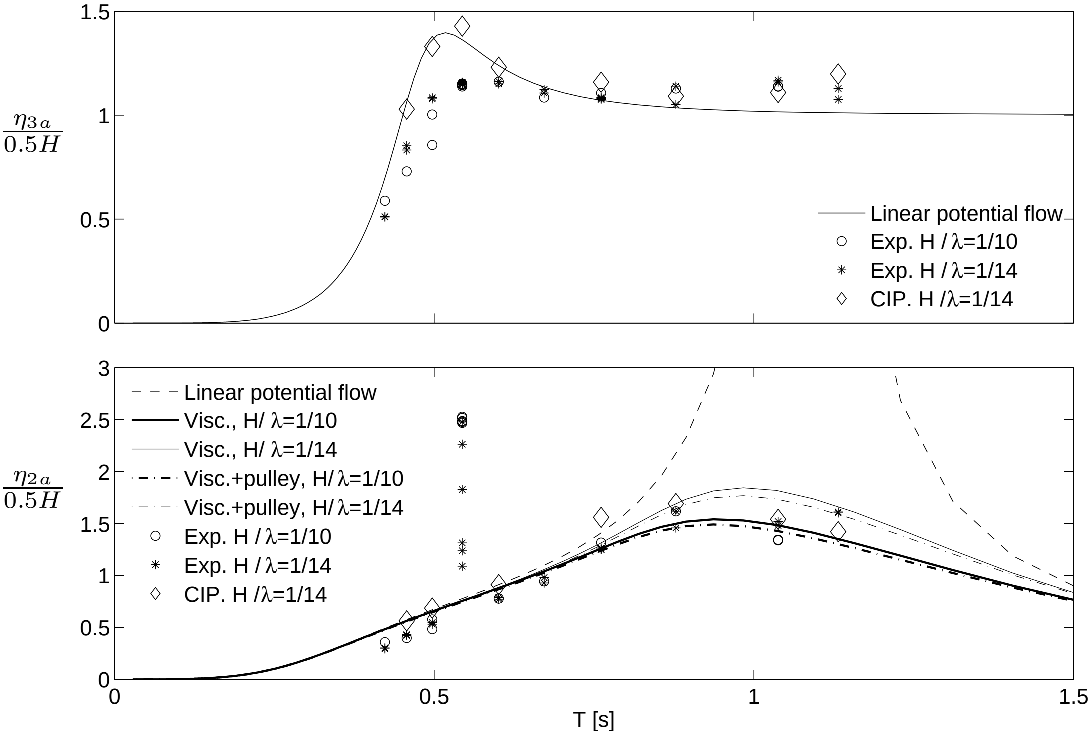

Figure 8.6: Heave and sway response amplitudes, η_{3a} and η_{2a} respectively, obtained from experiments and normalized by incident wave height H from wave calibration tests. Results are compared with linear potential flow theory and theory where viscous damping and pulley friction damping are included. Also results based on the CIP-method are shown.

layer damping is found as $b_{22}^{bl} = \pi\mu D\sqrt{\omega/\nu} + \mu\sqrt{\omega/(2\nu)}S_w/L_m$. Here, the first term is due to skin-friction and normal-stresses on the cylindrical part of the model while the last term is due to skin-friction on the end-plates of the model. Further, S_w is the total wetted area of the end-plates. The hydrodynamic damping coefficient in (8.1) for the sway mode is then $b_{22} = b_{22}^{w} + b_{22}^{v} + b_{22}^{bl}$. Also damping due to friction in the pulleys (b_{22}^{p}) is added for comparison. Since the viscous damping coefficient b_{22}^{v} depends on the amplitude of the sway motion, the sway motion equation including the viscous damping term is solved by iteration to find the sway motion amplitude for a given wave height. In Fig. 8.6, the heave and sway motion amplitudes from the experiments are presented and compared with linear potential flow theory using Eq. (8.1). In addition, the sway motion amplitudes are compared with theory where the linearized viscous damping and linearized pulley damping are included. Two noticeable features are observed. One feature was large amplitude sway motion that occurred when the wave period was half the sway natural period, which also was characterized by a shift in the response frequency. The second feature is the very large discrepancy between measured sway motion and that predicted by linear potential flow theory close to the sway natural period. These two particulars are discussed in the following.

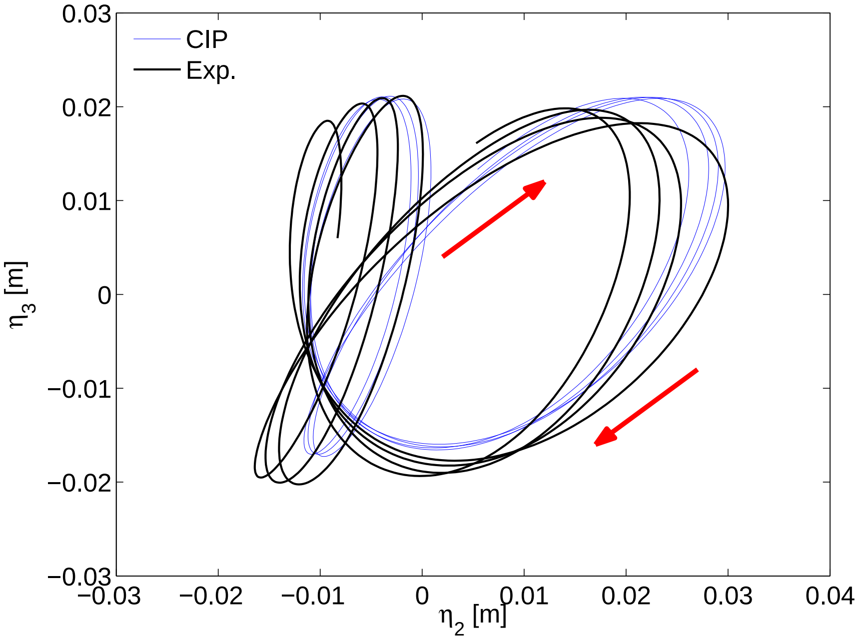

Figure 8.7: An $xy-$plot of the heave and sway motion of the cylinder in the time interval $t \in [22, 25]$s obtained with the NWT compared with measured response in the experiments for the case when $T = 0.544$s and wave steepness is $H/\lambda = 1/14$. The arrows indicates the direction of the motion.

8.3.2 Subharmonic response

Steady-state of the cylinder motion was reached in all the test runs, except for the tests for which the wave period was $T = 0.544$s. For these tests, the response amplitudes of the sway mode of motion were observed to increase until the motion became so large and violent that contact between the model and the side walls of the flume occurred. In Fig. 6.14, time-series of the sway motion from repetition tests with the wave period $T = 0.544$s are compared. The repetition tests shows that this characteristic sway motion was repeatable until wall-contact, but the sway response had different behaviour for the two wave steepnesses tested. Since no steady-state was reached for tests with $T = 0.544$s, the maximum response amplitude before contact occurred is used for comparison here, which explains the scatter of the sway response in Fig. 8.6 for this wave period. The instability phenomenon was also observed to be characterized by a shift in the sway response frequency. In the first stage after the wave train has reached the model, the cylinder started to oscillate in heave and sway with period equal to the wave period, as expected. However, after a build-up through 18 - 20 wave periods, the sway motion frequency had become half the wave frequency, such that the frequency of the sway motion was equal to the natural frequency in sway. In order to get a better impression of the motion, an $xy-$plot of the heave and sway motion is presented in Fig. 8.7. Such subharmonic response cannot be explained in terms of linear potential flow theory. Results shows that the largest sway motion amplitude obtained from experiments for some of the repetition tests was more than 250% of that predicted by linear theory for this wave period. Body motion obtained from numerical simulations for this particular case is compared with experiments in Fig. 8.8 for the smallest wave steepness $H/\lambda = 1/14$.

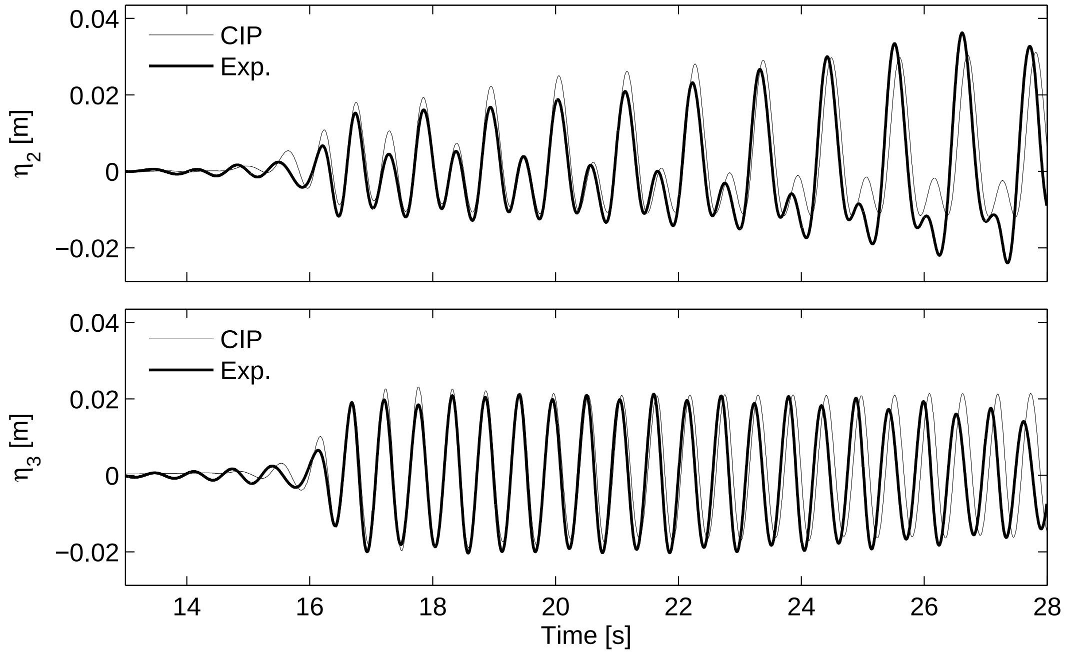

Figure 8.8: Heave and sway motion of the cylinder obtained with the NWT and compared with measured response from experiments when $T = 0.544$s. Input wave steepness was $H/\lambda = 1/14$.

Due to the different length of the NWT relative to the physical flume, there is a phase difference between the measured and simulated time-series. The computed time-series of the body motion is thus tuned such that the wave front reach the model at the same time as in the experiments. The reference time is measured from the startup of the wavemaker in the physical model tests. The heave motion shows good agreement. It is also noted that for the sway motion the numerical simulations also show a subharmonic oscillation with frequency half the forcing frequency. The clearly seen in Fig. 8.9 where the power spectra obtained from computed and measured time-series of the sway motion are compared. Moreover, the calculations are limited in time. The reason is the length of the computational domain in connection with wave reflections. It is after the numerical simulation time that the experimental sway amplitudes shows to increase strongly. In the experiments, the sway response showed to be quite different for the two wave heights tested (see Fig. 6.14). This indicates that the sway response for this wave period is either sensitive to the wave steepness directly, or more likely, sensitive to the transients associated with the wave front. Thus, if the wave front in the experiments is not well reproduced in the simulations, deviations of the resulting sway motion should be expected.

A hypothesis is that the phenomenon is due to instabilities. An analogy is what happens with the Mathieu equation which formally can be expressed as $m\ddot{x} + c(1 + \delta \cos \omega t)x = 0$. Instabilities happen for instance in the vicinity of $\omega_n/\omega = 0.5$, where the natural frequency $\omega_n = \sqrt{c/m}$ (McLachlan 1964). The apparent instability in the present case also happens for $\omega_n/\omega = 0.5$. However, the present coupled equation of motion for the system cannot simply be expressed as the Mathieu equation. One initial speculation was that the mooring system causes a time-dependent restoring coefficient that leads to instabilities. However, numerical simulations with the present NWT using a

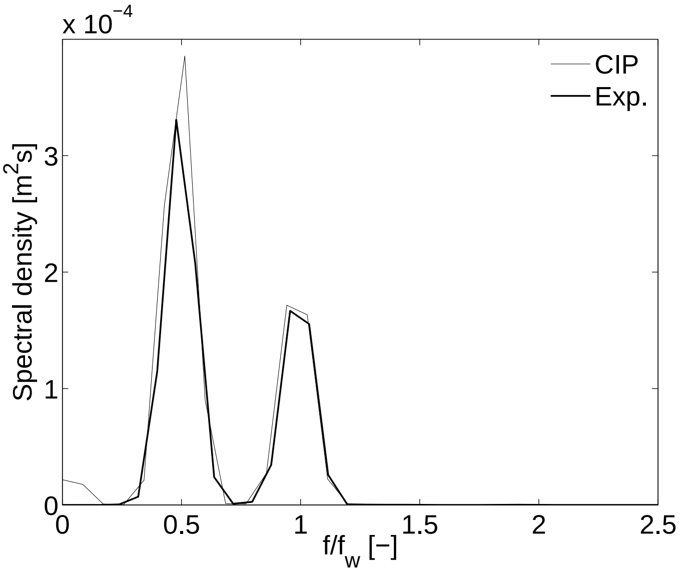

Figure 8.9: Comparison of power spectra from computed and measured sway motion of the cylinder for when subharmonic response occur. Wave period is $T = 0.544$s and input wave steepness is $H/\lambda = 1/14$.

constant restoring coefficient also showed a subharmonic component of the sway motion when $T_{n2}/T = 2$. Sub-harmonic components of the sway response was also observed in the tests with wave period $T = 0.497$s, both in the experiments and in the numerical simulations (see Figs. 8.10 and 8.11). However, the characteristic growth of the sway motion amplitudes as observed for when $T = 0.544$s was not seen here, and a steady state of the model motion was reached.

8.3.3 Sway resonance

The experiments further indicate that linear potential flow theory largely over-predicts the sway motion around resonance. The peak value of $\eta_{2a}/(0.5H)$ from linear potential flow theory is of order 10, while in the experiments $\eta_{2a}/(0.5H) < 2$. This means linear potential flow theory over-predicts the sway motion at resonance by more than 500%. Figure 8.13 shows time-series of the response from numerical simulations by the NWT compared with experiments when the wave period is $T = 1.038$s. This wave period is close to the sway natural period. The wave height obtained from the numerical wave calibration test was $H = 0.116$m, while the wave height from experimental wave calibration tests was $H = 0.114$m. The computed time-series of the body motion agree satisfactorily with measurements. This means the simulations support what is seen from the experimental results, namely that linear potential flow theory highly over-predicts the sway response near resonance. However, the sway motion is still considered large with amplitudes of the order of the diameter of the model. Figure 8.6 shows by using Eq. (8.1) that the discrepancy between predicted sway motion and experiments near sway resonance is mainly explained by viscous effects due to flow separation. It should be noted that in full-scale conditions the boundary layer flow will be turbulent and the viscous drag coefficient due to separation will be lower. Hence, Froude-scaling of the sway motion amplitudes presented

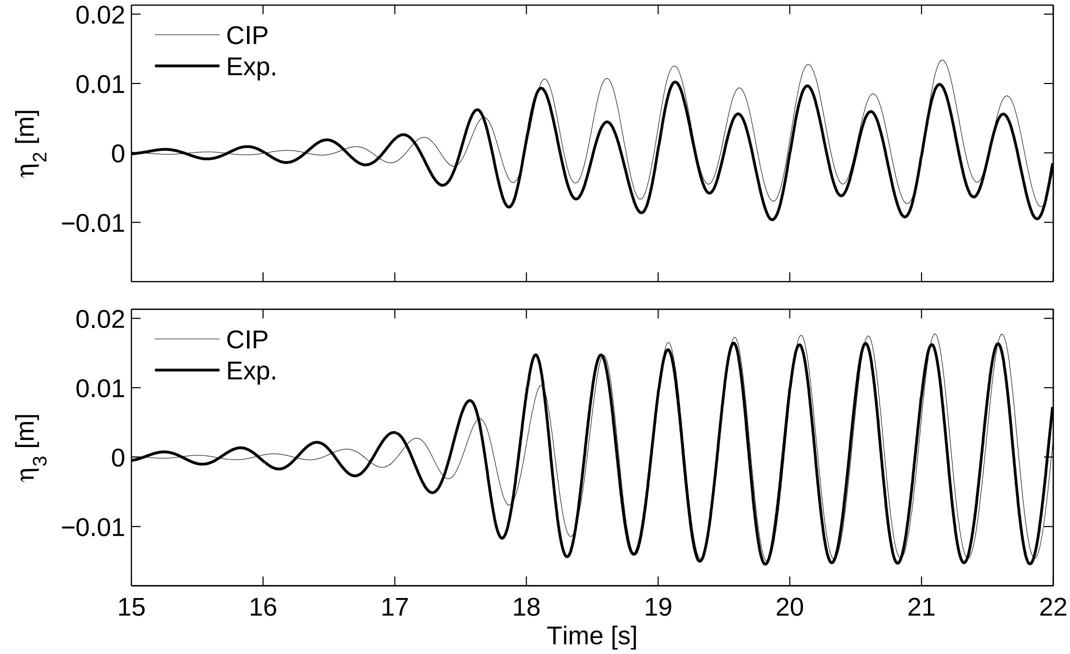

Figure 8.10: Sway and heave motion of cylinder obtained with the NWT compared with measured response from experiments when $T = 0.497$s. Input wave steepness was $H/\lambda = 1/14$. Subharmonic effects of the response in sway is observed.

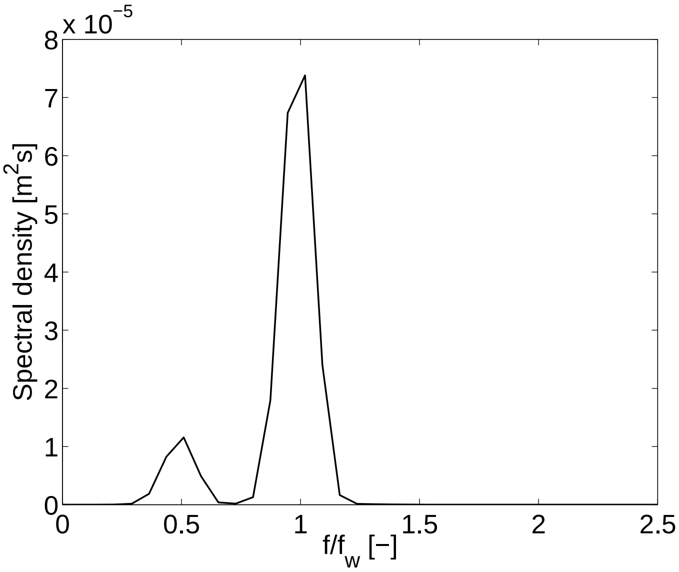

Figure 8.11: Power spectrum of sway motion obtained from model tests. Wave period is $T = 0.497$s and input wave steepness is $H/\lambda = 1/14$. Subharmonic components of the response is seen around half the wave frequency.

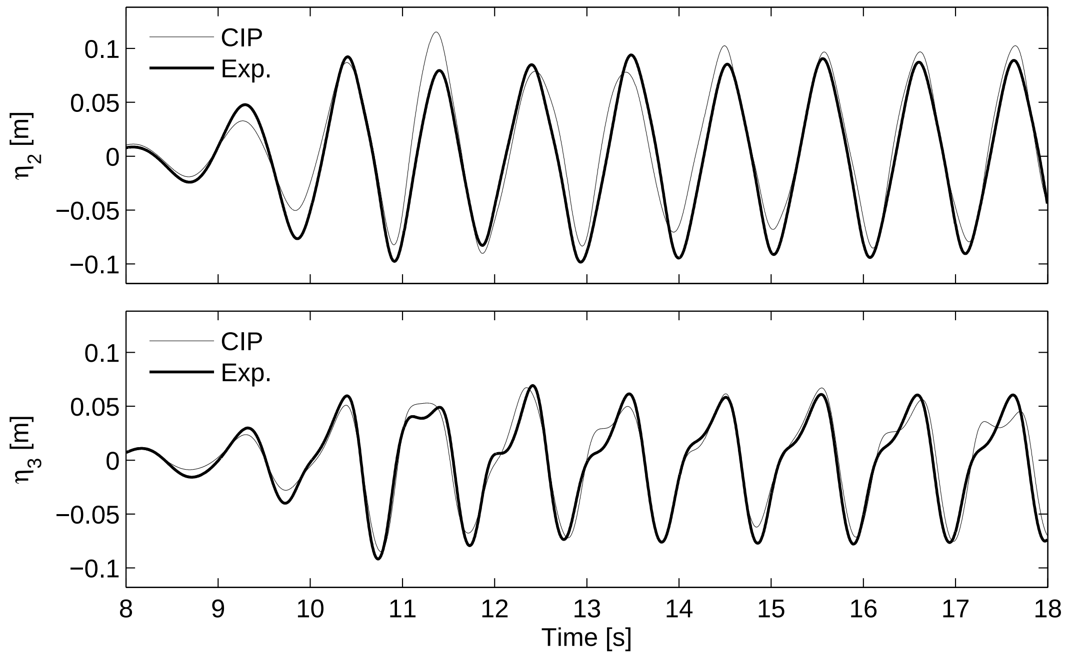

Figure 8.12: Sway and heave motion of cylinder obtained with the NWT compared with measured response from experiments when $T = 1.038$s. Input wave steepness was $H/\lambda = 1/14$.

will be non-conservative for the region around resonance.

8.3.4 Higher order harmonics of wave excitation forces

Accelerations of the cylinder are directly associated with the hydrodynamic forces acting on the body through Newton's second law. Thus, in order to study the frequency content of the hydrodynamic forces acting on the model, the Fourier amplitudes obtained from the acceleration time-series are studied. A comparison of Fourier amplitudes of the body accelerations obtained from simulations with the NWT and from measurements are presented in Figs. 8.14, 8.15 and 8.16. Sub-harmonic components in the Fourier amplitudes of the sway acceleration are seen in the tests with wave period $T = 0.497$s and $T = 0.544$s. The latter test wave period is where the instability phenomenon of the sway motion occurs. Pronounced higher order harmonic components are seen in the model accelerations when the model is excited near the sway natural frequency as shown in Fig. 8.17. Band-pass filtering is applied to isolate the body accelerations in heave and sway associated with the linear-, second- and third-harmonic components. Then by integration, the body motion due to the different components are calculated separately and then compared. Now consider the case where $T = 1.032$s and $H = 0.120$m. Here, the linear- and the third harmonic components of the sway acceleration are the most pronounced. The large third-harmonic component in the measured accelerations, thus also in the forcing, is believed to be caused by viscous drag due to flow separation. It is observed in the free decay tests presented that the effect of flow separation is important for larger motion amplitudes at the sway natural frequency. Further, Fourier analysis of the drag term in Morison's equation shows that the drag term contains most of its energy

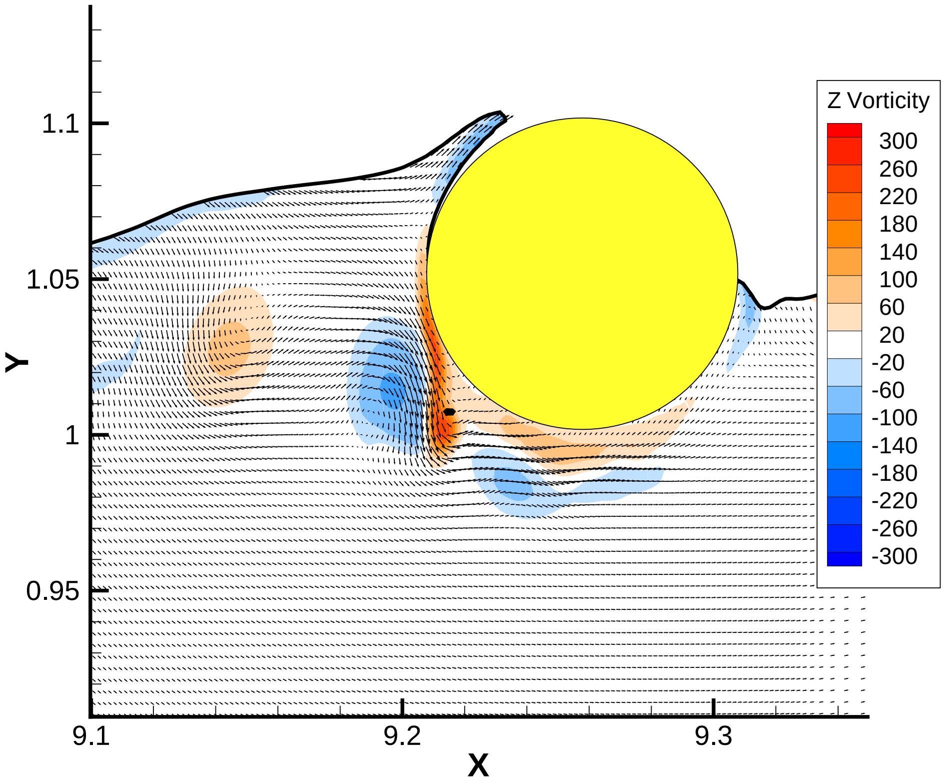

Figure 8.13: Local flow at the model position at sway resonance. Viscous flow separation occur from the body surface. Wave period is $T = 1.038\text{s}$ and wave steepness is $H/\lambda = 1/14$.

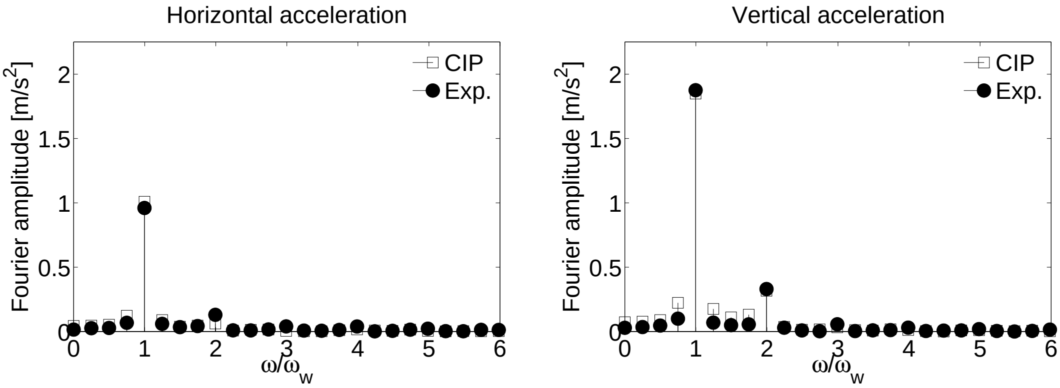

Figure 8.14: Comparison between Fourier amplitudes of sway and heave accelerations of the cylinder, obtained from simulations with the NWT and measurements. Wave period is $T = 0.457\text{s}$ and input wave steepness is $H/\lambda = 1/14$.

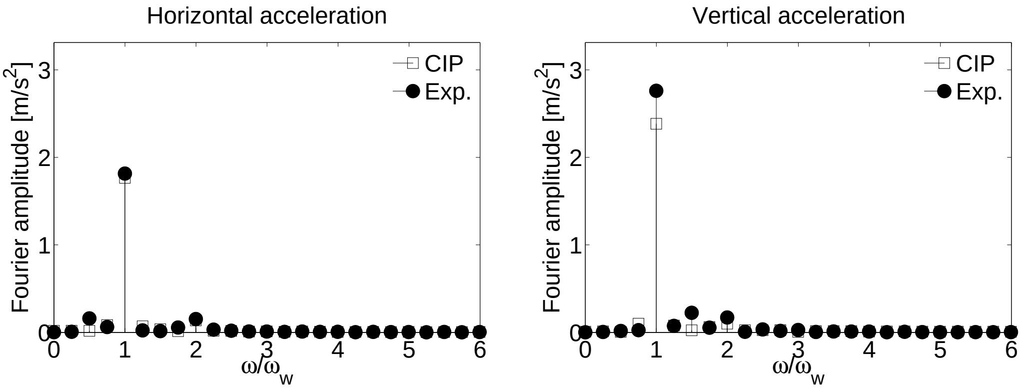

Figure 8.15: Comparison between Fourier amplitudes of sway and heave accelerations of the cylinder, obtained from simulations with the NWT and measurements. Wave period is $T = 0.601$s and input wave steepness is $H/\lambda = 1/14$.

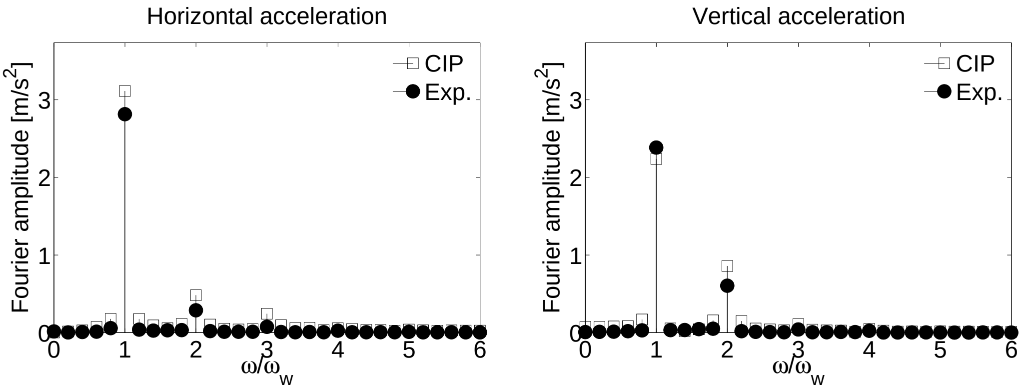

Figure 8.16: Comparison between Fourier amplitudes of sway and heave accelerations of the cylinder, obtained from simulations with the NWT and measurements. Wave period is $T = 0.761$s and input wave steepness is $H/\lambda = 1/14$.

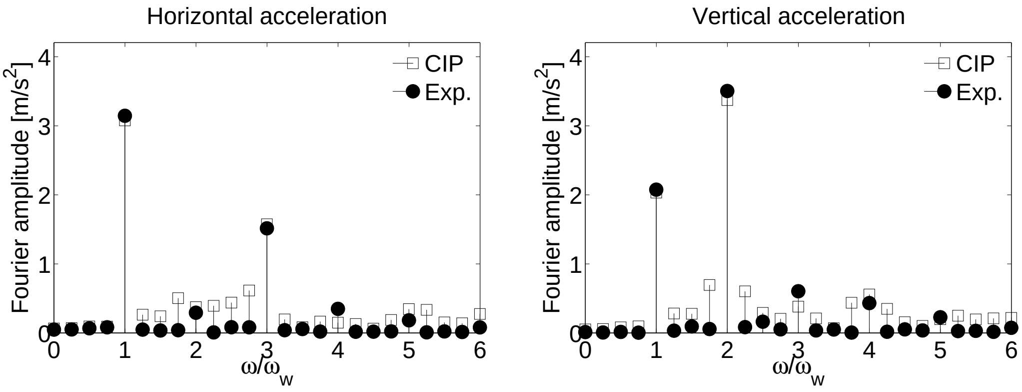

Figure 8.17: Comparison between Fourier amplitudes of sway and heave accelerations of the cylinder, obtained from simulations with the NWT and measurements. Wave period is $T = 1.038$s and input wave steepness is $H/\lambda = 1/14$.

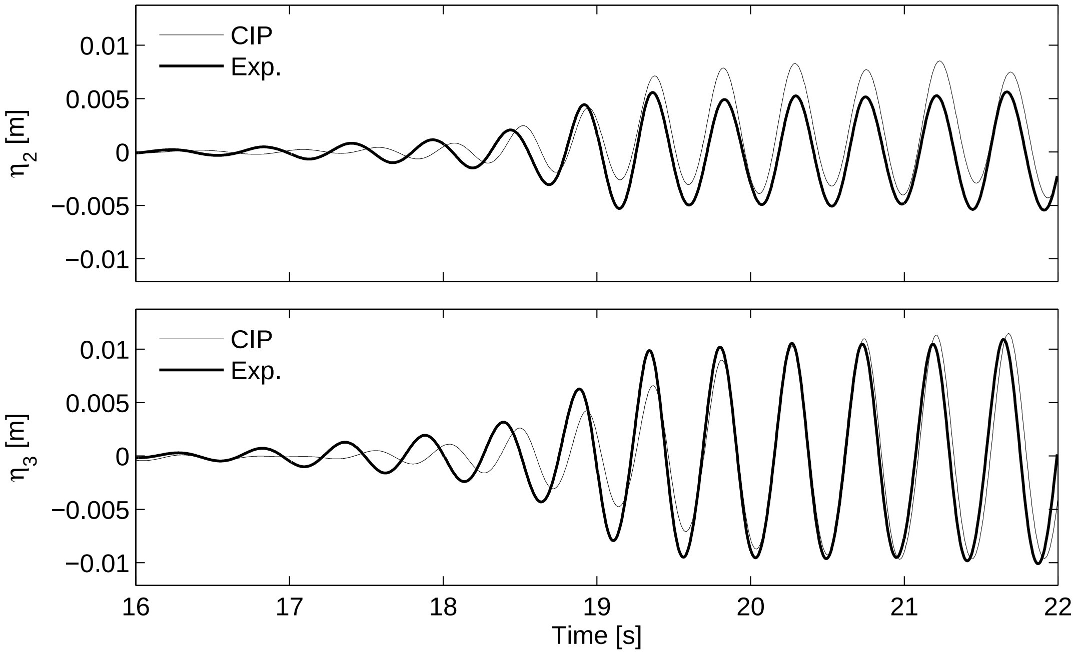

Figure 8.18: Sway and heave motion of cylinder obtained with the NWT compared with measured response from experiments when $T = 0.457$s. Input wave steepness was $H/\lambda = 1/14$.

at the linear- and third-harmonic component. For the case of heave accelerations, the linear- and second harmonic components are dominant, and in fact the second-harmonic component exceeds the linear-harmonic component. Further, the heave motion amplitude due to the second harmonic component is 42% of that due to the linear harmonic component. However, since there is a phase between the motion due to the linear- and second-harmonic component, the motion amplitude due to their sum is 121% (and not 142%) of the motion amplitude due to the linear-harmonic alone. It is noted that the frequency of the second-order harmonic component for this wave frequency is close to the heave natural frequency. Hence, the reason why the second-order harmonic component of the heave acceleration exceeds the linear-harmonic component is associated with that second-order wave forces excites the model at the heave natural frequency. Then, this serves as an example that higher order harmonics of the hydrodynamic forces may excite resonance frequencies of the structure, which are different from the wave frequency.

In the context of open cage fish farms, higher-order harmonics and even sub-harmonic components of the wave loading on the floaters are seen to be significant for moderate design wave conditions. These nonlinear force components may possibly excite elastic modes of the structure and must therefore be considered when fatigue life properties of the fish farm are analyzed.

8.4 Summary of results

Simulations of the moored floating circular cylinder with the same test conditions as in the model tests from 2008 have been performed. Time-series of computed body motions due

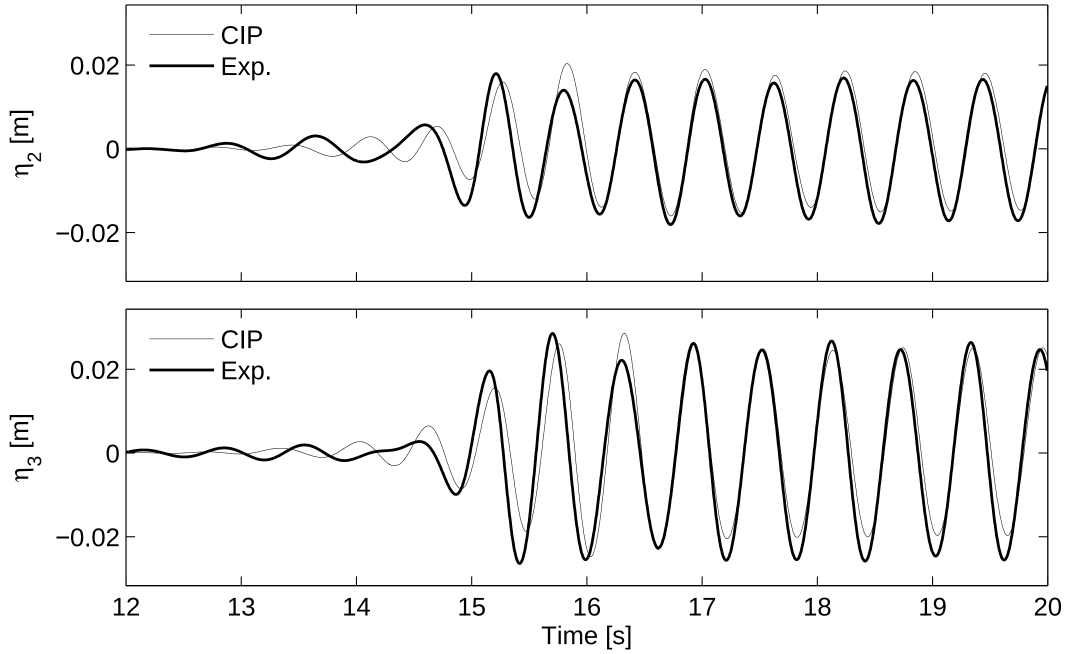

Figure 8.19: Sway and heave motion of cylinder obtained with the NWT compared with measured response from experiments when $T = 0.601$s. Input wave steepness was $H/\lambda = 1/14$.

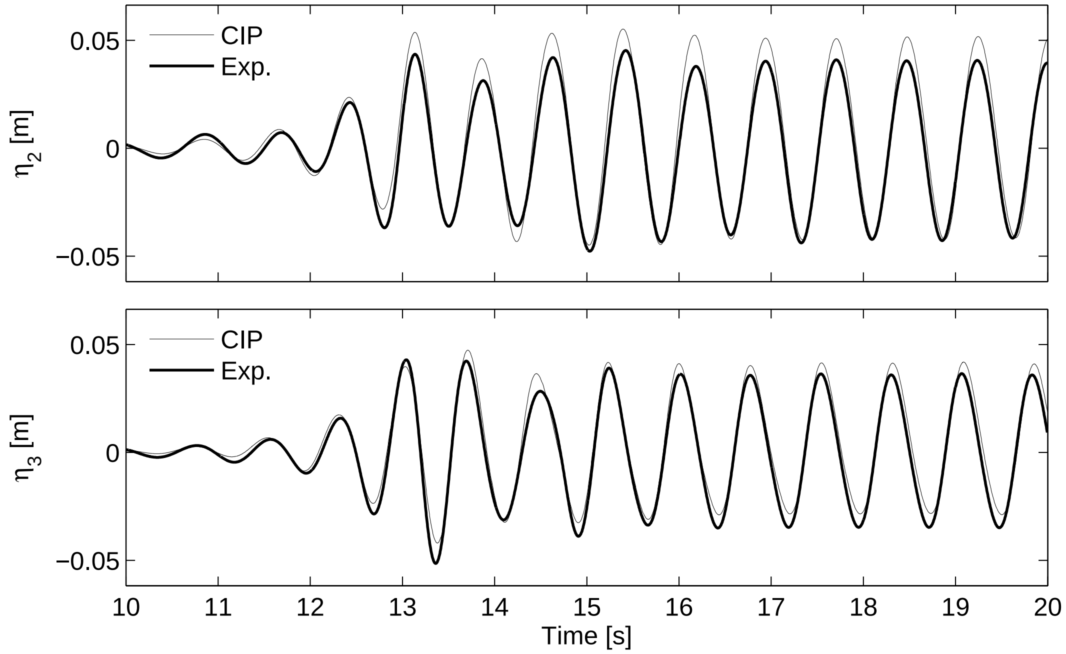

Figure 8.20: Sway and heave motion of cylinder obtained with the NWT compared with measured response from experiments when $T = 0.761$s. Input wave steepness was $H/\lambda = 1/14$.

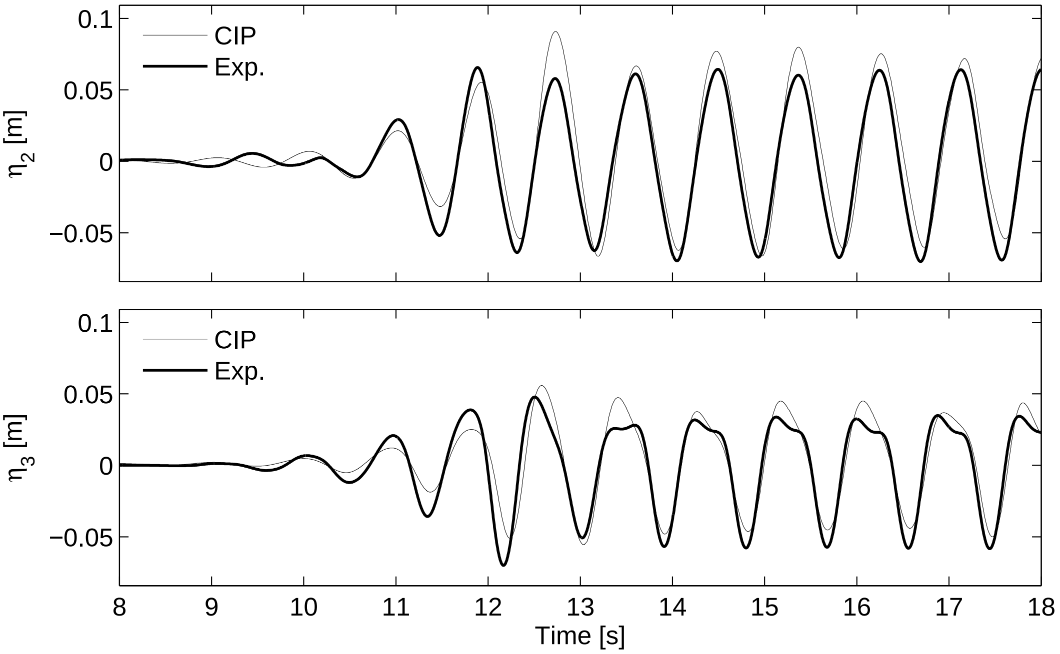

Figure 8.21: Sway and heave motion of cylinder obtained with the NWT compared with measured response from experiments when $T = 0.878\mathrm{s}$. Input wave steepness was $H/\lambda = 1/14$.

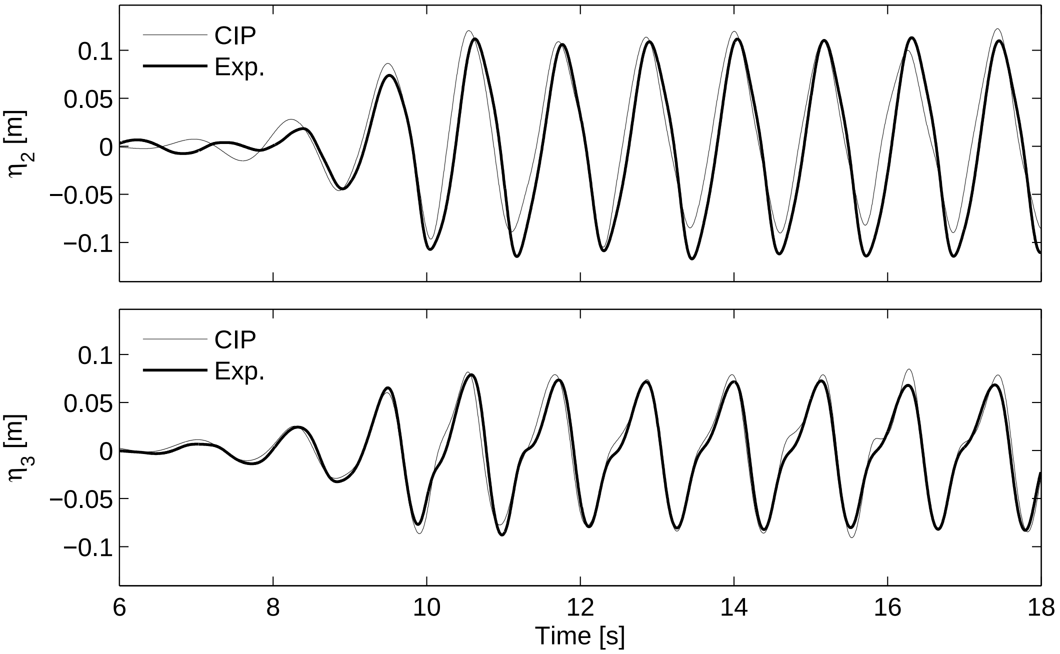

Figure 8.22: Sway and heave motion of cylinder obtained with the NWT compared with measured response from experiments when $T = 1.132\mathrm{s}$. Input wave steepness was $H/\lambda = 1/14$.

to regular beam sea waves was compared with body motions deduced from the measured body accelerations. The different sources of damping in the experiments was studied by means of free decay tests, both physically and numerically with the NWT. It was found that friction from the pulleys in the mooring arrangements introduced nonlinear damping to the system. Further, it was found that nonlinear damping due to viscous flow separation matters at sway resonance for the system considered. This also explains why linear potential flow theory over-predicts the sway response at resonance. The instability-like behaviour of the sway motion as observed in the model tests was also obtained in simulations with the NWT when the wave frequency was two times the sway natural frequency. However, what causes this particular phenomenon could not be concluded. Fourier analysis of the measured and computed body accelerations showed that higher order harmonics of the hydrodynamic forces are important. It was also shown that higher order harmonic components of the wave excitation force can excite natural frequencies of the system that are different from the wave frequency. This is important for fatigue life analyses of fish farms.

Chapter 9

Summary and suggestions for further work

9.1 Summary of the present work

The present work on the wave induced effects on floaters of aquaculture plants was based model tests and numerical simulations.

A CFD numerical wave tank (NWT) for fully nonlinear wave-body interaction problems has been developed. The NWT uses a one-fluid formulation to solve the incompressible Navier-Stokes equations for the air and the water, using CIP-based finite difference method on a Cartesian staggered grid. The NWT can handle floating bodies.

Two sets of model tests have been conducted. In the first set from 2006, fixed horizontal cylinders in the free surface zone were studied. Two cross-section geometries were tested. One circular and one rectangular. The models were subject to regular beam sea waves. Test parameters for the two models were wave period, wave steepness and model draft. Clamping forces on the model were measured in addition to the free surface elevation at eight positions in the flume. Wave over-topping the models were observed for some of the test conditions.

In 2008, model tests with a floating horizontal circular cylinder were performed. The model was tightly moored and subject to regular waves. Test parameters were wave period and wave steepness. The wave period tested covered both the heave resonance period and the sway resonance period. Mooring line tension and model accelerations were measured. Free surface elevation were measured at six positions. A detailed description of how to obtain the rigid body motions by means of integration of measured body accelerations was presented. In order to discover contact between the floating cylinder and the tank walls from the measured signals, the jerk parameter was introduced. The jerk is found as the time derivative of the measured acceleration signals. Wall contact leads to spikes in the jerk time-series. We also discovered an instability phenomenon of the sway motion characterized as subharmonic resonance. This occurred when the wave frequency was twice the sway natural frequency. After some time of building up, the sway motion performed a final phase shift from the wave frequency to the natural frequency in sway.

Two separate studies based on the two model tests are performed. In the first study, the model tests from 2006 are considered. Numerical simulations using the test setup from the experiments are performed with the NWT. Computed time series of the wave excitation forces are compared with the measured clamping forces on the models. Good comparisons are shown. Fourier analysis of the measured and computed forces are performed, which shows that the relative importance of the second harmonic component of the horizontal force increases with decreasing model draft. For the vertical force, the second harmonic component is important when over-topping occurs. A generalized Morison type of model was presented and applied to some of the test conditions from the experiments. We concluded that such a model is not adequate for cases where over-topping occur. However, the method yielded good results when moderate waves were tested.

The moored floating circular cylinder is considered in the second study. Also for this case, numerical simulations using the same test conditions as in the experiments were performed with our NWT. Time-series of the computed body motions were compared with measurements and good agreement were shown. We found that linear potential flow theory over-predicts the sway response at resonance by more than 500% relative to the measured sway response. This discrepancy was explained in terms of viscous flow separation. When adding a linearized viscous damping term as that in Morisons equation to the hydrodynamic forces from potential flow theory, the predicted sway motion at resonance showed good agreement with the measurements. Subharmonic resonance as oberved for the sway motion in the model tests was also obtained in simulations with the NWT. Measured sway amplitude in the model tests was at most 250% of that prediced by linear potential flow theory for the case when subharmonic resonance occured. Fourier analysis of the measured and computed body motions was performed. We found that the third harmonic component is important at sway resonance, which we showed could be related to viscous flow separation. We also found that higher harmonic components of the wave forces can excite natural frequencies of the structure. This was excemplified by that heave resonance was excited for tests where the wave frequency was half the heave natural frequency.

9.2 Suggestions for further work

Further work that could be done relative to the present study is to improve the numerical model by including a model for turbulence such that simulations of the full scale floater with turbulent boundary layers can be performed. Then the effects of the turbulent boundary layer flow on the wave induced loads and the resulting motions of the floater could be investigated. Also an algorithm for computation of the forces due to skin friction and viscous normal stresses on the surface of the floater should be implemented. Improved methods for free surface capturing with less smearing of the free surface should be considered. The numerical code should also be developed to allow for better gridding algorithms, such that the grid can be locally refined near the body and in the free surface zone. A sharp representation of the solid body boundary is also preferable. One problem associated with numerical simulation of a floating body when a no-slip boundary condition is applied on the body surface is how to move the contact point between the free surface and the body boundary. This problem should be investigated. The combined effects of current and waves on the flow around the floater and associated hydrodynamic forces should also be studied.

There are still many hydrodynamic effects related to the floaters of aquaculture plants that cannot be addressed with a 2D numerical model. Examples here are nonlinear 3D effects associated with a horizontal cylinder in the free surface when the incoming waves crests are not parallel to the cylinder axis. Further, hydroelastic effects for a complete floating collar in waves should be investigated.

Bibliography

Aarsnes, J. V., H. Rudi, and G. Løland (1990). Current forces on cage, net deflection. In *Engineering for offshore fish farming*. Thomas Telford, London.

Abramowitz, M. and I. A. Stegun (1970). *Handbook of Mathematical Functions*. Dover Publications, Inc.

Ambardar, A. (1995). *Analog and Digital Signal Processing*. PWS Publishing Company.

Barrett, R., M. Berry, T. F. Chan, J. Demmel, J. M. Donato, J. Dongarra, V. Eijkhout, R. Pozo, C. Romine, and H. V. der Vorst (1994). *Templates for the Solution of Linear Systems: Building Blocks for Iterative Methods*. SIAM.

Batchelor, G. K. (1967). *An Introduction to Fluid Dynamics*. Cambridge University Press.

Bearman, P. W., M. J. Downie, J. M. R. Graham, and E. D. Obasaju (1985). Forces on cylinders in viscous oscillatory flow at low Keulegan-Carpenter numbers. *Journal of Fluid Mechanics 154*, 337–356.

Bearman, P. W., J. M. R. Graham, E. D. Obasaju, and G. H. Drossopoulus (1984). The influence of corner radius on the forces experienced by cylindrical bluff bodies in oscillatory flow. *Applied Ocean Research 6*(2), 83 – 89.

Berthelsen, P. A. and O. M. Faltinsen (2008). A local directional ghost cell approach for incompressible viscous flow problems with irregular boundaries. *Journal of Computational Physics 227*, 4354 – 4397.

Bessonneau, J. S. and D. Marichal (1998). Study of the dynamics of submerged supple nets (application to trawls). *Ocean Engineering 25*, 563 – 583.

Bolton, W. E. and F. Ursell (1973). The wave forces on an infinitely long circular cylinder in an oblique sea. *Journal of Fluid Mechanics 57*, 241 – 256.

Boore, D. M. and J. J. Bommer (2005). Processing of strong-motion accelerograms: needs, options and consequences. *Soil Dynamics and Earthquake Engineering 25*, 93–115.

Brown, D. L., R. Cortez, and M. L. Minion (2001). Accurate projection methods for the incompressible Navier-Stokes equations. *Journal of Computational Physics 168*, 464–499.

Chaplin, J. R. (1984). Nonlinear forces on a horizontal cylinder beneath waves. *Journal of Fluid Mechanics 147*, 449–464.

Chorin, A. J. (1968). Numerical solution of the Navier-Stokes equations. *Mathematics of Computation 22*, 745–762.

Cummins, W. (1962). The impulse response function and ship motions. In *Schiffstechnik*, pp. 101 – 109.

de Tullio, M., A. Cristallo, E. Balaras, G. Pascazio, P. D. Palma, G. Iaccarino, M. Napolitano, and R. Verzicco (2006). Recent Advances in the Immersed Boundary Method. In *European Conference on Computational Fluid Dynamics, ECCOMAS CFD 2006*.

Dean, R. G. and R. A. Dalrymple (1991). *Water Wave Mechanics for Engineers and Scientists*, Volume 2 of *Advanced Series on Ocean Engineering*. World Scientific Publishing Co. Pte. Ltd.

Dixon, A. G., C. A. Greated, and S. H. Salter (1979). Wave forces on partially submerged cylinders. *Journal of the Waterway Port Coastal and Ocean Division 105*(4), 421 – 438.

Engelman, M. S. and M.-A. Jamnia (1990). Transient flow past a circular cylinder: A benchmark solution. *International Journal for Numerical Methods in Fluids 11*, 985–1000.

Ersdal, S. (2004). *An Experimental Study of Hydrodynamic Forces on Cylinders and Cables in Near Axial Flow.* Ph. D. thesis, NTNU, Norwegian University of Science and Technology.

Fadlun, E. A., R. Verzicco, P. Orlandi, and L. Mohd-Yusof (2000). Combined immersed-boundary finite-difference methods for three-dimensional complex flow simulations. *Journal of Computational Physics 161*, 35–60.

Faltinsen, O. M. (1971). *Wave forces on a restrained ship in head-sea waves.* Ph. D. thesis, Naval Architecture Dept., University of Michigan.

Faltinsen, O. M. (1990). *Sea Loads on Ships and Offshore Structures.* Cambridge University Press.

Faltinsen, O. M. (2005). *Hydrodynamics of High-Speed Marine Vehicles.* Cambridge University Press.

Faltinsen, O. M. and A. Timokha (2009). *Sloshing.* Cambridge University Press.

FAO (2006). State of world aquaculture 2006. Technical report, Food and Agriculture Organization of the United Nations, Rome, Italy.

Ferziger, J. H. and M. Peric' (2002). *Computational Methods for Fluid Dynamics.* Springer.

Frank, W. (1967). Oscillation of cylinders in or below the free surface of deep fluids. Report 2375, Washington DC: Naval Ship Research and Development Center.

Fredheim, A. (2005). *Current Forces on Net Structures.* Ph. D. thesis, NTNU, Norwegian University of Science and Technology.

Fredheim, A. (2009). Key numbers in norwegian fish farming. Private communication.

Fredheim, A. and R. Langan (2009). *New Technologies in Aquaculture: Improving production efficiency, quality and environmental management. Part 6 Aquaculture Systems Design*, Chapter Advances in technology for offshore and open ocean fin fish aquaculture. Woodhead Publishing Limited.

Fredriksson, D. W., M. R. Swift, O. Eroshkin, I. Tsukrov, J. D. Irish, and B. Celikkol (2005). Moored fish cage dynamics in waves and currents. *IEEE Journal of Oceanic Engineering 30*.

Fridman, A. L. (1998). *Calculations For Fishing Gear Design*. Farnham, UK: Fishing News Books.

Gansel, L. (2009). *Influence of porosity and fish-induced internal circulation on the flow around fish cages - investigations in the interaction of shear layers, the recirculation zone and vortex streets behind fish cages*. Ph. D. thesis, Norwegian University of Science and Technology (NTNU).

Gentaz, L., B. Alessandrini, and G. Delhommeau (1997). Motion simulation of a two-dimensional body at the surface of a viscous fluid by a fully coupled solver. In *12th International Workshop on Water Waves and Floating Bodies (IWWWFB)*.

Ghia, U., K. Ghia, and C.T.Shin (1982). High-Re Solutions for Incompressible Navier-Stokes Equations and a Multigrid Method. *Journal of Computational Physics 48*, 387–411.

Gingold, R. A. and J. J. Monaghan (1977, Nov.). Smoothed particle hydrodynamics - theory and application to non-spherical stars. *Royal Astronomical Society, Monthly Notices 181*, 375 – 389.

Graham, J. M. R. (1980). The forces on sharp-edged cylinder in oscillatory flow at low Keulegan-Carpenter numbers. *Journal of Fluid Mechanics 97*, 331–346.

Greco, M. (2001). *A Two-Dimensional Study of Green-Water Loading*. Ph. D. thesis, Norwegian University of Science and Technology (NTNU).

Greco, M., G. Colicchio, and O. M. Faltinsen (2007). Shipping of water on a two-dimensional structure. part 2. *Journal of Fluid Mechanics 581*, 371–399.

Greenhow, M. (1988). Water-entry and -exit of a horizontal circular cylinder. *Applied Ocean Research 10*, 191–198.

Greenhow, M. and W.-M. Lin (1983). Non-linear free surface effects: experiments and theory. Technical Report 83-19, Department of Ocean Engineering, Cambridge, Massachusets Institute of Technology (MIT).

Harlow, F. H. and J. E. Welch (1965). Numerical Calculation of Time-Dependent Viscous Incompressible Flow of Fluid with Free Surface. *The Physics of Fluids 8*(12), 2182–2189.

Henderson, R. D. (1995). Details of the drag curve near the onset of vortex shedding. *Physics of Fluids 7*, 2102 – 2104.

Herfjord, K. (1996). *A study of two-dimensional separated flow by a combination of the finite element method and Navier-Stokes equations*. Ph. D. thesis, Norwegian Institute of Technology, Trondheim, Norway.

Hirt, C. W. and B. D. Nichols (1981). Volume of fluid (VOF) method for the dynamics of free boundaries. *Journal of Computational Physics 39*, 201–225.

Hu, C., O. M. Faltinsen, and M. Kashiwagi (2005). 3-D numerical simulation of freely moving floating body by CIP method. In *The Fifteenth International Offshore and Polar Engineering Conference (ISOPE)*, pp. 674 – 679.

Hu, C. and M. Kashiwagi (2004). A CIP-based method for numerical simulations of violent free-surface flows. *Journal of Marine Science and Technology 9*, 143–157.

Hu, C., M. Kashiwagi, and T. Momoki (2003). Numerical simulation of non-linear free surface wave generation by CIP method and its applications. In *The Thirteen International Offshore and Polar Engineering Conference (ISOPE2003)*, pp. 294 – 299.

Hu, F., K. Matuda, and T. Tokai (2001). Effects of drag coefficient of netting for dynamic similarity on model testing of trawl nets. *Fisheries Science 67*, 84 – 89.

Huang, C.-C., H.-J. Tang, and J.-Y. Liu (2006). Dynamic analysis of net cage structures for marine aquaculture: Numerical simulation and model testing. *Aquacultural Engineering 35*, 258 – 270.

Hughes, S. A. (1993). *Physical Models and Laboratory Techniques in Coastal Engineering.* World Scientific.

ITTC (1990). Report of the panel on validation procedures. In *Proceedings of the 19th ITTC*, Madrid, Spain, pp. 577–604.

Kawakami, T. (1959). *Development of mechanical studies of fishing gear. In: Modern Fishing Gear of the World*, pp. 175 – 184. London: Fishing News (Books).

Kawakami, T. (1964). *The theory of designing and testing fishing nets in model. In: Modern Fishing Gear of the World*, pp. 471 – 482. London: Fishing News (Books).

Kim, J. and P. Moin (1985). Application of a Fractional-Step Method to Incompressible Navier-Stokes Equations. *Journal of Computational Physics 59*, 308 – 323.

Kreyszig, E. (1999). *Advanced Engineering Mathematics.* John Wiley & Sons, Inc.

Kristiansen, D. and O. Faltinsen (2009). Non-linear wave-induced motions of cylindrical-shaped floaters of fish farms. *Journal of Engineering for the Maritime Environment 223*(3), 361–375.

Kristiansen, D. and O. M. Faltinsen (2008a). A study of wave loads on fixed horizontal cylinders in the free surface. In *Proceedings of the 8th International Conference on Hydrodynamics (ICHD 2008).*

Kristiansen, D. and O. M. Faltinsen (2008b). Wave loads on floaters of aquaculture plants. In *Proceedings of the 27. Offshore Mechanics and Arctic Engineering Conference (OMAE).*

Kristiansen, T. (2009). *Two-Dimensional Numerical and Experimental Studies of Piston-mode Resonance.* Ph. D. thesis, Norwegian University of Science and Technology.

Lader, P. F., B. Enerhaug, A. Fredheim, and J. Krokstad (2003). Modeling of 3d net structures exposed to waves and current. In *3rd International Conference on Hydroelasticity in Marine Technology*, Oxford, UK.

Landau, L. D. and E. M. Lifshitz (2004). *Fluid Mechanics* (Second ed.), Volume 6 of *Course of Theoretical Physics.* Elsevier.

LeVeque, R. J. (1992). *Numerical Methods for Consevation Laws.* BirkHäuser Verlag.

LeVeque, R. J. (2002). *Finite Volume Methods for Hyperbolic Problems.* Cambridge University Press.

Lien, E. (2009). Private communication.

Løland, G. (1991). *Current forces on and flow through fish farms.* Ph. D. thesis, Norwegian Institute of Technology.

Maskell, S. J. and F. Ursell (1970). The transient motion of a floating body. *Journal of Fluid Mechanics 44*, 303 – 313.

McLachlan, N. W. (1964). *Theory and Application of Mathieu Functions.* Dover Publications, INC.

Mittal, R. and G. Iaccarino (2005). Immersed boundary methods. *Annu. Rev. Fluid Mechanics 37*, 239–261.

Moe, H. (2009). *Strength analysis of net structures.* Ph. D. thesis, Norwegian University of Science and Technology (NTNU).

Mohd-Yusof, J. (1997). Combined immersed-boundary/B-spline methods for simulations of flow in complex geometries. Technical report, Center for Turbulence Research.

Molin, B. (2002). *Hydrodynamique des Structures Offshore (French).* Editions Technip.

Molin, B. (2004). On the frictional damping in roll of ship sections. *International Shipbuilding Progress 51*, 59 – 85.

Monaghan, J. J. (1992). Smoothed particle hydrodynamics. *Annual Review of Astronomy and Astrophysics 30*, 543 – 574.

Monahan, R. L. (1993). *An Overview of Salmon Aquaculture*, Chapter 1, pp. 1 – 9. Fishing News Books.

Morison, J. R., M. P. O'Brien, J. W. Johnson, and S. A. Schaaf (1950). The force exerted by surface waves on piles. *Journal of Petroleum Transactions 189*, 149 – 154.

Newman, J. N. (1962). The Exciting Forces on Fixed Bodies in Waves. *Journal of Ship Research 6*(4), 10 – 17.

Newman, J. N. (1965). The Exciting Forces on a Moving Body in Waves. *Journal of Ship Research 9*, 190 – 199.

Newman, J. N. (1977). *Marine Hydrodynamics.* The MIT Press.

NOAA (2007a). A 10-year plan for marine aquaculture. Technical report, U.S. Department of Commerse. National Oceanic and Atmospheric Administration (NOAA).

NOAA (2007b). The national offshore aquaculture act. Technical report, U. S. Department of Commerse. National Oceanic and Atmospheric Administration (NOAA).

Norwegian Fisheries Directorate (2009a). Rømt oppdrettsfisk av laks pr. 05.10.2009. (Norwegian). Technical report, Norwegian Fisheries Directorate.

Norwegian Fisheries Directorate (2009b). Rømt oppdrettsfisk av regnbueørret pr. 05.10.2009. (Norwegian). Technical report, Norwegian Fisheries Directorate.

Ogilvie, F. (1963). First- and second-order forces on a cylinder submerged under a free surface. *Journal of Fluid Mechanics 16*, 451 – 472.

Ogilvie, T. (1964). Recent progress toward the understanding and prediction of ship motions. In *The Fifth Symposium on Naval Hydrodynamics.*

Ormberg, H. (1991). *Non-linear response analysis of floating fish farm systems.* Ph. D. thesis, Norwegian University of Science and Technology (NTNU).

Osher, S. and R. Fedkiw (2003). *Level Set Methods and Dynamic Implicit Surfaces*, Volume 153 of *Applied Mathematical Sciences.* Springer.

Osher, S. and J. A. Sethian (1988). Fronts propagating with curvature-dependent speed: Algorithms based on Hamilton-Jacobi formulations. *Journal of Computational Physics 79*, 12–49.

Panton, R. (1968). The Transient for Stokes's Oscillating Plate: A Solution in Terms of Tabulated Functions. *Journal of Fluid Mechanics 31*, 819–825.

Patankar, S. V. (1980). *Numerical Heat Transfer and Fluid Flow.* New York: McGraw Hill.

Peskin, C. S. (1972). Flow patterns around heart valves: A numerical method. *Journal of Computational Physics 10*, 252–271.

Press, W. H., S. A. Teukolsky, W. T. Vetterling, and B. P. Flannery (1992). *Numerical Recipes in C.* Cambridge University Press.

Roache, P. J. (1976). *Computational Fluid Dynamics.* Hermosa Publishers.

Schlichting, H. and K. Gersten (2000). *Boundary Layer Theory.* Springer.

Skejic, R. (2008). Added mass and damping coefficients. (Private communication).

Soto, D., F. Jara, and C. Moreno (2001). Escaped salmon in the inner seas, southern Chile: Facing ecological and social conflicts. *Ecological Applications 11*, 1750–1762.

Standard Norway (2005). *Marine fish farms - Requirements for design, dimensioning, production, installation and operation. Norwegian Standard NS 9415.* Standard Norway. (In Norwegian).

Stokes, G. G. (1851). On the effect of the internal friction of fluids on the motion of pendulums. *Transactions of the Cambridge Philosophical Society 9*(II), 8 – 106.

Strikwerda, J. C. (2004). *Finite Difference Schemes and Partial Differential Equations* (Second ed.). SIAM.

Sun, H. (2007). *A Boundary Element Method Applied to Strongly Nonlinear Wave-Body Interaction Problems.* Ph. D. thesis, Norwegian University of Science and Technology.

Takewaki, H., A. Nishiguchi, and T. Yabe (1985). Cubic interpolated pseudo-particle method (CIP) for solving hyperbolic-type equations. *Journal of Computational Physics 61*, 261–268.

Takizawa, K., T. Yabe, Y. Tsugawa, T. E. Tezduyar, and H. Mizoe (2006). Computation of free-surface flows and fluid-object interactions with the CIP method based on adaptive meshless soroban grids. *Computational Mechanics 40*, 167–183.

Tasai, F. (1959). On the damping force and added mass of ships heaving and pitching. In *Rep. of Research Inst. for Applied Mech.*, Volume 7. Kyushu University.

Tasai, F. (1961). Hydrodynamic force and moment produced by swaying and rolling oscillation of cylinders on the free surface. In *Rep. of Research Inst. for Applied Mech.*, Volume 9. Kyushu University.

Tauti, M. (1934). The force acting on the plane net in motion through the water. *Nippon Suisan Gakkaishi 3*, 1 – 4.

Thomassen, P. E. (2008). *Methods for Dynamic Response Analysis and Fatigue Life Estimation of Floating Fish Cages.* Ph. D. thesis, Norwegian University of Science and Technology.

Toro, E. F. (1999). *Riemann Solvers and Numerical Methods for Fluid Dynamics.* Springer.

Tsukrov, I., O. Eroshkin, D. Fredriksson, M. R. Swift, and B. Celikkol (2003). Finite element modeling of net panels using a consistent net element. *Ocean Engineering 30*, 251 – 270.

Ursell, F. (1949). On the heaving motion of a circular cylinder on the surface of a fluid. *The Quarterly Journal of Mechanics and Applied Mathematics 2*, 218 – 231.

Ursell, F. (1950). Surface waves on deep water in the presence of a submerged circular cylinder. *Mathematical Proceedings of the Cambridge Philosophical Society 46*, 141 – 152.

Ursell, F. (1954). Water waves generated by oscillating bodies. *The Quarterly Journal of Mechanics and Applied Mathematics 7*(4), 427 – 437.

Ursell, F. (1964). The decay of the free motion of a floating body. *Journal of Fluid Mechanics 19*, 305 – 319.

Ursell, F. (1968). On head seas travelling along a horizontal cylinder. *Journal of Applied Mathematics 4*(4), 414 – 427.

van der Vorst, H. A. (1992). Bi-CGSTAB: A fast and smoothly converging variant of Bi-CG for the solution of nonsymmetric linear systems. *Journal on Scientific and Statistical Computing 13*, 631–644.

Vestbøstad, T. M., O. M. Faltinsen, and D. Kristiansen (2007). Validation Methods and Benchmark Tests for a 2-D CIP Method Applied to Marine Hydrodynamics. In *The Seventeenth International Offshore and Polar Engineering Conference.*

Vestbøstad, T. M. G. (2009). *A numerical study of wave-in-deck impact using a two-dimensional constrained interpolation profile method.* Ph. D. thesis, Norwegian University of Science and Technology.

Vugts, J. H. (1968). The hydrodynamic coefficients for swaying, heaving and rolling cylinders in a free surface. In *International Shipbuilding Progress*, Volume 15, pp. 251–276.

Whitham, G. B. (1974). *Linear and nonlinear waves.* John Wiley & Sons.

Wood, W. L. (2005). An exact solution for Burgers equation. *Communications in numerical methods in engineering 22*, 797–798.

Wu, G. X. and R. E. Taylor (2003). The coupled finite element and boundary element analysis of nonlinear interactions between waves and bodies. *Ocean Engineering 30*, 387 – 400.

Yabe, T., F. Xiao, and T. Utsumi (2001). The constrained interpolation profile method for multiphase analysis. *Journal of Computational Physics 169*, 556–593.

Yeung, R. W. (1982). The transient heaving motion of floating cylinders. *Journal of Engineering Mathematics 16*, 97 – 119.

Zhu, X. (2006). *Application of the CIP Method to Strongly Nonlinear Wave-Body Interaction Problems*. Ph. D. thesis, NTNU, Norwegian University of Science and Technology.

Appendix A

Details on the numerical wave tank

A.1 Advection calculation using the CIP-method

Some details on the 1D and 2D CIP-method are presented. Also the mathematical foundation for the CIP-method is described.

A.1.1 Advection in 1D - mathematical background

Mathematical background for the 1D CIP-method will now be presented. Consider the 1D advection equation

$$\frac{\partial f}{\partial t} + u\frac{\partial f}{\partial x} = 0. \tag{A.1}$$

This equation describes the transport of a variable $f(t, x)$ with the transport velocity $u(t, x)$ and is classified as a partial differential equation (PDE) of the hyperbolic type, which is in general hard to solve. We assume that both f and u are continuous in time t and space x. We will make use of the material derivative which is defined as

$$\frac{\mathrm{d}f(t, x(t))}{\mathrm{d}t} = \frac{\partial f}{\partial t} + \frac{\partial f}{\partial x}\frac{\mathrm{d}x}{\mathrm{d}t}. \tag{A.2}$$

By taking the material derivative of the variable f along a curve C in the $xt-$plane and say it should be equal to the left hand side of (A.1), we get

$$\begin{aligned}\frac{\mathrm{d}f}{\mathrm{d}t} &= \frac{\partial f}{\partial t} + \frac{\mathrm{d}x}{\mathrm{d}t}\frac{\partial f}{\partial x}\\ &= \frac{\partial f}{\partial t} + u\frac{\partial f}{\partial x} = 0\end{aligned}$$

This means we can reduce the partial differential equation (A.1) to the following set of ordinary differential equations (ODEs) along the curve C.

$$\frac{\mathrm{d}f}{\mathrm{d}t} = 0 \tag{A.3}$$

$$\frac{\mathrm{d}x}{\mathrm{d}t} = u \tag{A.4}$$

The ODE (A.3) implies that f is constant along the curve C defined by (A.4). Two cases will now be discussed.

First, assume that the advection velocity u is constant in time and space. Further, assume that at time $t = 0$, the curve C passes through the point $x(0) = x_0$ for where the advected variable f has the initial value $f_0(x_0)$. The solution to (A.4) is $x = x_0 + ut$. Further, as (A.3) implies that $f(t, x)$ is constant along the curve C, the value of f for pairs of x and t on the curve C can be related to the initial value of f at x_0 as $f(t, x) = f_0(x_0)$. Hence,

$$f(t, x) = f_0(x - ut). \tag{A.5}$$

Next, we consider the case when the advection velocity is linearly varying and described by $u = ax$, where a is a constant. Again, assuming that for the time $t = 0$, the curve C passes through $x(0) = x_0$ for where f has the initial value $f_0(x_0)$. Then, the solution to (A.4) is $x = x_0 \exp(at)$. Further, $f(t, x) = f_0(x_0)$ leads to the solution

$$f(t, x) = f_0(x \exp(-at)). \tag{A.6}$$

We note that for small times $t \ll 1$, using Taylor expansion of the exponential argument, the solution is found approximately as $f(t, x) \approx f(x - ut)$.

Advection with a source term

Consider a modified advection equation, where a source term has been introduced to the right hand side of (A.1). The new PDE is

$$\frac{\partial g}{\partial t} + u\frac{\partial g}{\partial x} = -bg \tag{A.7}$$

Here, g is the transported variable, u is the transport velocity and b is a constant. The material derivative of g along a curve C in the $xt-$plane, initially passing through $x(0) = x_0$, is set equal to the left hand side of (A.7) and we get

$$\begin{aligned}\frac{\mathrm{d}g}{\mathrm{d}t} &= \frac{\partial g}{\partial t} + \frac{\mathrm{d}x}{\mathrm{d}t}\frac{\partial g}{\partial x}\\ &= \frac{\partial g}{\partial t} + u\frac{\partial g}{\partial x} = -bg.\end{aligned}$$

Hence, (A.7) can been reduced to the following pair of ODEs

$$\frac{\mathrm{d}g}{\mathrm{d}t} = -bg \tag{A.8}$$

$$\frac{\mathrm{d}x}{\mathrm{d}t} = u. \tag{A.9}$$

Now, assume that $u = ax$ and $b = u'(x) = a$. Then the solution to (A.9) is $x = x_0 \exp(at)$. The evolution of g along the curve C is described by the ODE (A.8), which has the solution $g(t, x) = g_0(x_0) \exp(-bt)$. Substitution yields

$$g(t, x) = g_0(x \exp(-at)) \exp(-bt). \tag{A.10}$$

For small times $t \ll 1$, we note that $g(t, x) \approx g_0(x - ut)(1 - bt)$.

A.1.2 The 1D CIP-scheme

When solving the 1D advection problem using the traditional CIP-scheme, the advected variable $f(x,t)$ in the upwind cell is approximated by a cubic polynomial $F_i^n(\xi)$, defined as

$$F_i^n(\xi) = C_3\xi^3 + C_2\xi^2 + C_1\xi + C_0, \tag{A.11}$$

where $\xi = x - x_i$ and where C_3, C_2, C_1 and C_0 are unknown coefficients. We also introduce the differentiated profile $G(\xi) = \mathrm{d}F/\mathrm{d}\xi$, which is an approximation to the spatial derivative g of the advected variable f. In order to determine the unknown coefficients, the following constraints are used:

$$F_i^n(0) = f_i^n \qquad F_i^n(x_{iw} - x_i) = f_{iw}^n \tag{A.12}$$

$$G_i^n(0) = g_i^n \qquad G_i^n(x_{iw} - x_i) = g_{iw}^n \tag{A.13}$$

This yields a system of four equations for the four unknown coefficients. To simplify the notation, we introduce the signed node spacing $\Delta\hat{x} = x_{iw} - x_i$. Then, after some algebra we get

$$C_3 = \frac{g_i^n + g_{iw}^n}{\Delta\hat{x}^2} - \frac{2(f_{iw}^n - f_i^n)}{\Delta\hat{x}^3} \tag{A.14}$$

$$C_2 = \frac{3(f_{iw}^n - f_i^n)}{\Delta\hat{x}^2} - \frac{g_{iw}^n + 2g_i^n}{\Delta\hat{x}} \tag{A.15}$$

$$C_1 = g_i^n \tag{A.16}$$

$$C_0 = f_i^n. \tag{A.17}$$

When the approximation function F_i^n is found, the advected variable and the tentative value of the spatial derivative in the node x_i for the next time step can be found as

$$f_i^{n+1} = F_i^n(-u_i^n\Delta t) \tag{A.18}$$

$$g_i^* = G_i^n(-u_i^n\Delta t). \tag{A.19}$$

The spatial derivative at the new time step is obtained by adding the source term due to the tentative value after pure advection of the differentiated profile, as

$$g_i^{n+1} = g_i^* - \Delta t\left(\frac{u_{i+1}^n - u_{i-1}^n}{\Delta x_i + \Delta x_{i+1}}\right) g_i^*. \tag{A.20}$$

A.1.3 The upwind method

The upwind method, which is a first order upwind differencing scheme, was implemented for solving the 1D advection equation and applied to some of the verification test problems. This was to be able to compare the performance of the implemented CIP-scheme with one of the most simple and well-known numerical schemes for advection calculations. The discretized version of the 1D advection equation using the upwind method is

$$\frac{u_i^{n+1} - u_i^n}{\Delta t} + u_i^n\frac{(f_{iw}^n - f_i^n)}{\Delta x} = 0, \tag{A.21}$$

where f is the advected variable, u is the advection velocity, Δt is the time increment and Δx is the spatial increment. Further, the index i refers to the spatial node considered, iw refers to the upwind (upstream) node and n is the time step. The upwind method is described in most of the textbooks on CFD, e.g. (Roache 1976) and (Toro 1999).

A.1.4 2D CIP-coefficients

When using the A-type CIP-method for solving the advection equation, usually a cubic polynomial surface $F^n_{i,j}(\xi,\eta)$ is created to model the advected variable $f^n(x,y)$ in the upwind cell. A complete cubic polynomial surface has ten coefficients that must be determined. For this purpose, the functional values $f^n_{i,j}$ and their spatial derivatives $\frac{\partial f^n}{\partial x}|_{i,j} = g^n_{i,j}$ and $\frac{\partial f^n}{\partial y}|_{i,j} = k^n_{i,j}$ in the four nodes constructing the upwind nodes are utilized. However, the point value of the advected variable plus its two spatial derivatives in four nodes leads to a total of twelve constraints, while we only have ten unknowns. Thus, we neglect the spatial derivatives in the node most far away from the node of computation. This yields the following expressions for the coefficients

$$C_{30} = \frac{is2\big(f_{i,j} - f_{iw,j}\big) + \Delta x\big(g_{i,j} + g_{iw,j}\big)}{\Delta x^3} \tag{A.22}$$

$$C_{21} = \frac{\big(f_{i,j} - f_{iw,j} - f_{i,jw} + f_{iw,jw}\big) + is\Delta x\big(g_{i,j} - g_{i,jw}\big)}{js\Delta x^2\Delta y} \tag{A.23}$$

$$C_{12} = \frac{\big(f_{i,j} - f_{iw,j} - f_{i,jw} + f_{iw,jw}\big) + js\Delta y\big(k_{i,j} - k_{iw,j}\big)}{is\Delta x\Delta y^2} \tag{A.24}$$

$$C_{03} = \frac{js2\big(f_{i,j} - f_{i,jw}\big) + \Delta y\big(k_{i,j} + k_{i,jw}\big)}{\Delta y^3} \tag{A.25}$$

$$C_{20} = \frac{3\big(f_{iw,j} - f_{i,j}\big) - is\Delta x\big(2g_{i,j} + g_{iw,j}\big)}{\Delta x^2} \tag{A.26}$$

$$C_{02} = \frac{3\big(f_{i,jw} - f_{i,j}\big) - js\Delta y\big(2k_{i,j} + k_{i,jw}\big)}{\Delta y^2} \tag{A.27}$$

$$C_{11} = -\frac{f_{i,j} - f_{iw,j} - f_{i,jw} + f_{iw,jw}}{isjs\Delta x\Delta y} + \frac{g_{i,jw} - g_{i,j}}{js\Delta y} + \frac{k_{iw,j} - k_{i,j}}{is\Delta x} \tag{A.28}$$

$$= \frac{f_{i,j} - f_{iw,j} - f_{i,jw} + f_{iw,jw}}{isjs\Delta x\Delta y} - C_{21}is\Delta x - C_{12}js\Delta y \tag{A.29}$$

$$C_{10} = g_{i,j} \tag{A.30}$$

$$C_{01} = k_{i,j} \tag{A.31}$$

$$C_{00} = f_{i,j}. \tag{A.32}$$

Here

$$is = -sign(u_c) \tag{A.33}$$

$$js = -sign(v_c), \tag{A.34}$$

where u_c and v_c being respectively the horizontal and vertical velocity component interpolated to the node of computation. Due to the staggered grid there are three cases which needs different interpolation, namely advection of horizontal momentum, vertical momentum and color function. The advection velocity is interpolated to the node of computation for the three different cases as follows.

Advection of horizontal momentum:

$$u_c = u_{i,j}$$

$$v_c = 0.25\left(v_{i,j} + v_{i+1,j} + v_{i,j-1} + v_{i+1,j-1}\right)$$

Advection of vertical momentum:

$$\begin{aligned} u_c &= 0.25\left(u_{i,j} + u_{i-1,j} + u_{i-1,j+1} + u_{i,j+1}\right) \\ v_c &= v_{i,j} \end{aligned}$$

Advection of color function:

$$\begin{aligned} u_c &= 0.5\left(u_{i,j} + u_{i-1,j}\right) \\ v_c &= 0.5\left(v_{i,j} + v_{i,j-1}\right) \end{aligned}$$

A.2 Details on the diffusion calculation

Some details relative to the discretization of the diffusion calculation will now be presented. First we consider the diffusion calculation for the horizontal velocity component given by equation (4.28). The density at the horizontal velocity node is found by interpolation as $\rho_c = 0.5(\rho_{i,j} + \rho_{i+1,j})$. The dynamic viscosity coefficients are found from

$$\begin{aligned} \mu_E &= \mu_{i+1,j} \\ \mu_W &= \mu_{i,j} \\ \mu_N &= 0.25(\mu_{i,j} + \mu_{i+1,j} + \mu_{i,j+1} + \mu_{i+1,j+1}) \\ \mu_S &= 0.25(\mu_{i,j} + \mu_{i+1,j} + \mu_{i,j-1} + \mu_{i+1,j-1}). \end{aligned}$$

The derivatives of the velocity components are computed as

$$\begin{aligned} \left.\frac{\partial u^*}{\partial x}\right|_E &= \frac{u^*_{i+1,j} - u^*_{i,j}}{\Delta x_{i+1}} & \left.\frac{\partial u^*}{\partial x}\right|_W &= \frac{u^*_{i,j} - u^*_{i-1,j}}{\Delta x_i} \\ \left.\frac{\partial u^*}{\partial y}\right|_N &= \frac{u^*_{i,j+1} - u^*_{i,j}}{\Delta yc_i} & \left.\frac{\partial u^*}{\partial y}\right|_S &= \frac{u^*_{i,j} - u^*_{i,j-1}}{\Delta yc_{i-1}} \\ \left.\frac{\partial v^*}{\partial x}\right|_N &= \frac{v^*_{i+1,j} - v^*_{i,j}}{\Delta xc_i} & \left.\frac{\partial v^*}{\partial x}\right|_S &= \frac{v^*_{i+1,j-1} - v^*_{i,j-1}}{\Delta xc_i}. \end{aligned}$$

Next, we consider the diffusion calculation for the vertical velocity component given by equation (4.29). The mass density is approximated as $\rho_c = 0.5(\rho_{i,j} + \rho_{i,j+1})$, while the dynamic viscosity coefficients are

$$\begin{aligned} \mu_E &= 0.25(\mu_{i,j} + \mu_{i+1,j} + \mu_{i,j+1} + \mu_{i+1,j+1}) \\ \mu_W &= 0.25(\mu_{i,j} + \mu_{i-1,j} + \mu_{i,j+1} + \mu_{i-1,j+1}) \\ \mu_N &= \mu_{i,j+1} \\ \mu_S &= \mu_{i,j}. \end{aligned}$$

Further, central differences yields

$$\begin{aligned} \left.\frac{\partial u^*}{\partial y}\right|_E &= \frac{u^*_{i,j+1} - u^*_{i,j}}{\Delta yc_i} & \left.\frac{\partial u^*}{\partial y}\right|_W &= \frac{u^*_{i-1,j+1} - u^*_{i-1,j}}{\Delta yc_i} \\ \left.\frac{\partial v^*}{\partial x}\right|_E &= \frac{v^*_{i+1,j} - v^*_{i,j}}{\Delta xc_i} & \left.\frac{\partial v^*}{\partial x}\right|_W &= \frac{v^*_{i,j} - v^*_{i-1,j}}{\Delta xc_{i-1}} \\ \left.\frac{\partial v^*}{\partial y}\right|_N &= \frac{v^*_{i,j+1} - v^*_{i,j}}{\Delta y_{j+1}} & \left.\frac{\partial v^*}{\partial y}\right|_S &= \frac{v^*_{i,j} - v^*_{i,j-1}}{\Delta y_i}. \end{aligned}$$

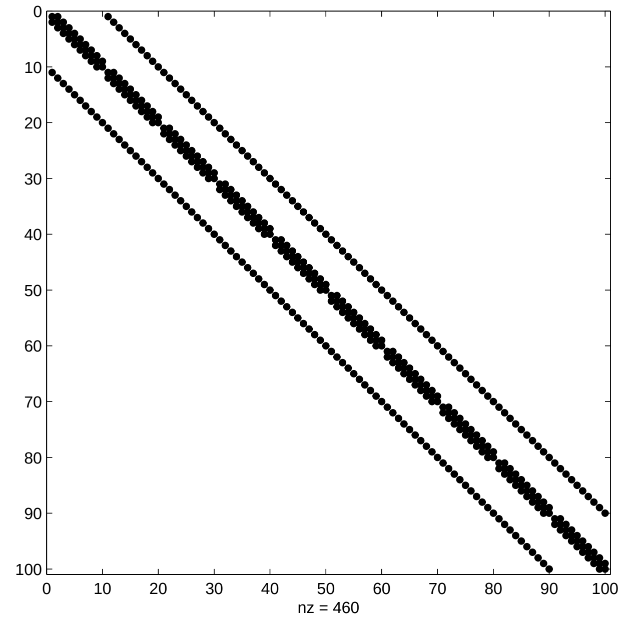

Figure A.1: Non-zero entries of the coefficient matrix A due to a 10×10 grid. All non-zero entries are located in five diagonals.

A.3 Poisson equation for the incremental pressure

The discretized Poisson equation for the incremental pressure defined in (4.38) can be written as

$$A_{i,j}\delta p_{i,j-1} + B_{i,j}\delta p_{i-1,j} + C_{i,j}\delta p_{i,j} + D_{i,j}\delta p_{i+1,j} + E_{i,j}\delta p_{i,j+1} = f_{i,j}, \tag{A.35}$$

where

$$A_{i,j} = \frac{1}{\rho_{i,j-1/2}\Delta y_j \Delta yc_{j-1}} \tag{A.36}$$

$$B_{i,j} = \frac{1}{\rho_{i-1/2,j}\Delta x_i \Delta xc_{i-1}} \tag{A.37}$$

$$D_{i,j} = \frac{1}{\rho_{i+1/2,j}\Delta x_i \Delta xc_i} \tag{A.38}$$

$$E_{i,j} = \frac{1}{\rho_{i,j+1/2}\Delta y_j \Delta yc_j} \tag{A.39}$$

$$C_{i,j} = -\left(A_{i,j} + B_{i,j} + D_{i,j} + E_{i,j}\right). \tag{A.40}$$

These five coefficients represents the five non-zero diagonals of the coefficient matrix **A** as depicted in Fig. A.1. The coefficients $C_{i,j}$ corresponds to the main diagonal. Further, $D_{i,j}$ and $E_{i,j}$ yields the first and second non-zero upper off-diagonals, while $B_{i,j}$ and $A_{i,j}$ yields the first and second non-zero lower off-diagonals, respectively. This yields a symmetric discretization of the Poisson equation (4.34) on a uniform Cartesian grid. However, for the case of a non-uniform grid, the coefficient matrix is not symmetric due to discretization of the divergence operator in eq. (4.34).

Due to the small number of non-zero elements in the coefficient matrix **A** relative to the size of the matrix, **A** is a sparse matrix. From a computational point of view, it is waste of memory to store the total matrix. Hence, instead of solving the total matrix of size $N \times N$, we use the Compressed Diagonal Storage format where only the five diagonals containing the non-zero elements are stored in a $5 \times N$ matrix (Barrett et al. 1994). As the off-diagonals are shorter than the main diagonal of length N, the off-diagonals are padded with zeros to fill the new matrix.

A.3.1 The preconditioned Bi-Conjugate Gradient Stabilized Method

A modified version of the Bi-CGStab algorithm with preconditioning is presented in Barrett et al. (1994). The algorithm is as follows:

```
Compute $r^{(0)} = b - Ax^{(0)}$ for some initial guess $x^{(0)}$
Choose $\tilde{r}$ (for example, $\tilde{r} = r^{(0)}$)
for $i = 1, 2, ...$
    $\rho_{i-1} = \tilde{r}^T r^{(i-1)}$
    if $\rho_{i-1} = 0$ method fails
    if $i = 1$
        $p^{(i)} = r^{(i-1)}$
    else
        $\beta_{i-1} = (\rho_{i-1}/\rho_{i-2})(\alpha_{i-1}/\omega_{i-1})$
        $p^{(i)} = r^{(i-1)} + \beta_{i-1}(p^{(i-1)} - \omega_{i-1}v^{(i-1)})$
    endif
    solve $M\hat{p} = p^{(i)}$
    $v^{(i)} = A\hat{p}$
    $\alpha_i = \rho_{i-1}/\tilde{r}^T v^{(i)}$
    $s = r^{(i-1)} - \alpha_i v^{(i)}$
    check norm of $s$; if small enough: set $x^{(i)} = x^{(i-1)} + \alpha_i \hat{p}$ and stop
    solve $M\hat{s} = s$
    $t = A\hat{s}$
    $\omega_i = t^T s / t^T t$
    $x^{(i)} = x^{(i-1)} + \alpha_i \hat{p} + \omega_i \hat{s}$
    $r^{(i)} = s - \omega_i t$
    check convergence; continue if necessary
    for continuation it is necessary that $\omega_i \neq 0$
end
```

Several preconditioners are presented in Barrett et al. (1994). We have used the simple incomplete LU-factorization preconditioner D-ILU, which is an incomplete factorization preconditioner of level zero. Splitting the coefficient matrix into its diagonal, lower triangular, and upper triangular parts as $A = D_A + L_A + U_A$, respectively, the preconditioner can be written as $M = (D + L_A)D^{-1}(D + U_A)$, where D is the diagonal matrix containing the pivots. Note that it is only the diagonal matrix D that needs to be stored since the upper triangular and lower triangular matrices, U_A and L_A respectively, are left unchanged. The pivots are generated as follows:

```
Let $S$ be the nonzero set $\{(i,j) : a_{ij} \neq 0\}$, where $a_{ij}$ are the elements of the coefficient matrix A
for $i = 1, 2, ...$
    set $d_{ii} \leftarrow a_{ii}$
for $i = 1, 2, ...$
    set $d_{ii} \leftarrow 1/d_{ii}$
    for $j = i + 1, i + 2, ...$
        if $(i,j) \in S$ and $(j,i) \in S$ then
```

```
    set $d_{jj} \leftarrow d_{jj} - a_{ji} d_{ii} a_{ij}$
```

In the preconditioned Bi-CGSTAB algorithm, we need to solve the system $Mx = y$, with $M = (D + L_A)D^{-1}(D + U_A)$ and where y is a known vector. The preconditioner solve is described below.

```
Let $M = (D + L)(I + D^{-1}U)$ and $y$ be given.
for $i = 1, 2, ...$
    $z_i = d_{ii}^{-1}(y_i - \sum_{j<i} l_{ij} z_j)$
for $i = n, n-1, n-2, ...$
    $x_i = z_i - d_{ii}^{-1} \sum_{j>i} u_{ij} x_j$
```

A.4 Time-stepping of the spatial derivatives of the velocity field

As the velocity field after the advection step $\boldsymbol{u}^*$ is updated due to the diffusion step, pressure coupling and due to forces from the floater to obtain the new velocity field $\boldsymbol{u}^{n+1}$, also the spatial derivatives of the velocity field are modified. Hence, the spatial derivatives $\boldsymbol{g} = \partial \boldsymbol{u}/\partial x$ and $\boldsymbol{k} = \partial \boldsymbol{u}/\partial y$ must be updated before a new advection step can be made. We define $\boldsymbol{g} = [g_u, g_v]^T$ and $\boldsymbol{k} = [k_u, k_v]^T$, where $g_u = \frac{\partial u}{\partial x}$, $g_v = \frac{\partial v}{\partial x}$, $k_u = \frac{\partial u}{\partial y}$ and $k_v = \frac{\partial v}{\partial y}$. Time-stepping of the spatial derivatives of the horizontal velocity component are performed as

$$g_{u;(i,j)}^{n+1} = g_{u;(i,j)}^{*} + \frac{u_{i+1,j}^{n+1} - u_{i-1,j}^{n+1} - u_{i+1,j}^{*} + u_{i-1,j}^{*}}{\Delta x_i + \Delta x_{i+1}} \tag{A.41}$$

$$k_{u;(i,j)}^{n+1} = k_{u;(i,j)}^{*} + \frac{u_{i,j+1}^{n+1} - u_{i,j-1}^{n+1} - u_{i,j+1}^{*} + u_{i,j-1}^{*}}{\Delta yc_j + \Delta yc_{j-1}}. \tag{A.42}$$

Similarly, the spatial derivatives of the vertical velocity component are updated by

$$g_{v;(i,j)}^{n+1} = g_{v;(i,j)}^{*} + \frac{v_{i+1,j}^{n+1} - v_{i-1,j}^{n+1} - v_{i+1,j}^{*} + v_{i-1,j}^{*}}{\Delta xc_i + \Delta xc_{i-1}} \tag{A.43}$$

$$k_{v;(i,j)}^{n+1} = k_{v;(i,j)}^{*} + \frac{v_{i,j+1}^{n+1} - v_{i,j-1}^{n+1} - v_{i,j+1}^{*} + v_{i,j-1}^{*}}{\Delta y_j + \Delta y_{j+1}}. \tag{A.44}$$

Appendix B

Details of the verification studies

B.1 Oscillating boundary layers

Here, some mathematical details on the second Stokes problem is considered, and both the steady solution as well as the transient solution when the oscillating wall is abruptly started initially.

B.1.1 Second Stokes Problem, steady-state solution

In the case of the Second Stokes Problem the outer flow is $U_e = 0$, while the wall oscillates harmonically with frequency ω and amplitude U_0. A consequence of $U_e = 0$ is that the linearized Prandtl's boundary layer equations (Schlichting and Gersten 2000) are reduced to the diffusion equation

$$\frac{\partial u}{\partial t} = \nu \frac{\partial^2 u}{\partial y^2}. \tag{B.1}$$

Since the liquid attach to the wall (no-slip condition), viscous shear forces will set the surrounding fluid into motion and a *viscous wave* will propagate from the wall into the fluid domain. The no-slip condition implies that the fluid velocity at the wall is equal to the velocity of the wall. Thus,

$$u(0,t) = U_0 \sin \omega t, \quad \text{for } y = 0. \tag{B.2}$$

The steady state solution of eq.B.1 which can be found in e.g. Schlichting and Gersten (2000) is

$$u(y,t) = U_0 \exp(-\eta) \sin(\omega t - \eta), \tag{B.3}$$

with

$$\eta = y \sqrt{\frac{\omega}{2\nu}}. \tag{B.4}$$

Here $\nu = \mu/\rho$ is the kinematic viscosity coefficient and ω is the frequency of oscillation of the wall.

B.1.2 Second Stokes Problem, transient solution

We are seeking the unsteady solution of (B.1). First we separate the velocity into a steady state term U^s and a transient term U^t:

$$u = U^s + U^t. \tag{B.5}$$

From (B.5) and (B.3) the initial condition $u(y, 0) = 0$ leads to

$$U^t(\eta, 0) = -U_0 \exp(-\eta) \sin(-\eta). \tag{B.6}$$

When $t \to \infty$, the transient term must vanish such that the steady state solution remains. A general solution for the transient term of B.1 in integral form is given in Landau and Lifshitz (2004) as:

$$U^t(y, t) = \frac{1}{2\sqrt{\pi \nu t}} \int_0^\infty f_0(\tilde{y}) \left(\exp\left[\frac{-(y-\tilde{y})^2}{4\nu t}\right] - \exp\left[\frac{-(y+\tilde{y})^2}{4\nu t}\right]\right) \mathrm{d}\tilde{y}, \tag{B.7}$$

where $f_0(\tilde{y})$ is the initial condition for U^t. Substitution of (B.6) into (B.7) does not lead to a tractable integral. Hence, instead of (B.6) a complex continuation of (B.6) is used (Panton 1968):

$$U^t(\eta, 0) = U_0 \Im\big\{ \exp[-(1-i)\eta] \sin(-\eta) \big\}. \tag{B.8}$$

Substitution of (B.9) gives integrals which can be evaluated by standard techniques. This yields:

$$\begin{aligned} U^t(\eta, T) = U_0 \Im \Big\{ &-0.5 \exp\left[C\eta - iT\right] \operatorname{erfc}\left[\sqrt{0.5T}(C + \eta/T)\right] \\ &+ 0.5 \exp[-C\eta - iT] \operatorname{erfc}\left[\sqrt{0.5T}(C - \eta/T)\right]\Big\} \end{aligned} \tag{B.9}$$

Here $T = \omega t$ and the complex constant $C = 1 - i$. This solution includes the complementary error function $\operatorname{erfc}(z) = 1 - \operatorname{erf}(z)$ with complex argument $z = x + \mathrm{i}y$, which must be separated into real and imaginary components to obtain the solution:

$$\operatorname{erfc}(x + iy) = F(x, y) + iG(x, y). \tag{B.10}$$

Unfortunately, an expression for F and G does not exist. Abramowitz and Stegun (1970) gives a series expansion that approximates the complex error function:

$$\begin{aligned} \operatorname{erf}(x + iy) = \operatorname{erf}(x) &+ \frac{\exp(-x^2)}{2\pi x}[(1 - \cos 2xy) + i \sin 2xy] \\ &+ \frac{2}{\pi} \sum_{n=1}^{\infty} \frac{\exp(-\frac{1}{4}n^2)}{n^2 + 4x^2} [f_n(x, y) + i g_n(x, y)] + \epsilon(x, y) \end{aligned} \tag{B.11}$$

where

$$\begin{aligned} f_n(x, y) &= 2x - 2x \cosh ny \cos 2xy + n \sinh ny \sin 2xy \\ g_n(x, y) &= 2x \cosh ny \sin 2xy + n \sinh ny \cos 2xy \\ |\epsilon(x, y)| &\approx 10^{-16} \left|\operatorname{erf}(x + iy)\right| \end{aligned}$$

This is used to evaluate the transient velocity field.

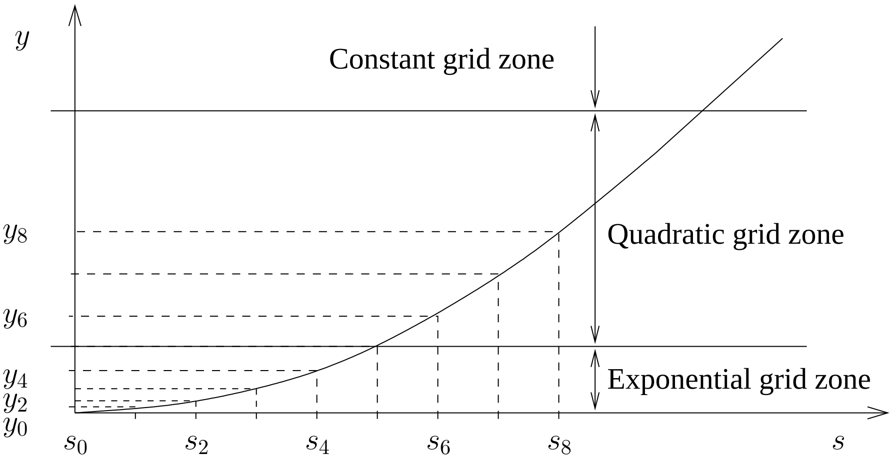

Figure B.1: Schematic view of how the grid arrangement close to the oscillating wall is obtained using the parameter s. An exponential distribution of grid points is applied in the normal direction inside the boundary layer. Constant grid spacing is used far from the wall and a quadratic distribution of grid points is used in a matching zone between the to regions to obtain a smooth transition.

B.1.3 Details on the grid generation

When the second Stokes problem is solved with the present flow solver, grid stretching is applied close to the oscillating wall. The grid is divided into three grid zones, where the grid increment follows an exponential distribution close to the wall. Far away from the wall the grid line spacing is constant, while a quadratic variation is used in a matching zone to merge the exponential grid with the constant grid. The distribution of grid points in the normal direction to the wall is for the exponential zone found as

$$y_i = \beta\big(\exp(\alpha s_i) - 1\big) \tag{B.12}$$

where $s_i \in [0, 1]$ is a equidistant distribution vector with $N_{bl} + 1$ elements and β is a clustering parameter. Further, the coefficient α defined as

$$\alpha = \ln\Big(\frac{\delta_{0.99}}{\beta} + 1\Big). \tag{B.13}$$

The parabolic distribution function describing the position of grid points within the matching zone is

$$y_i = as_i^2 + bs_i + c, \tag{B.14}$$

where the constraints $y_{start} = \delta_{0.99}$, $y_{end} = k\delta_{0.99}$ and $y'(s)|_{end} = 0$ determines the coefficients a, b and c. Here, k is the extension of the matching zone relative to the boundary layer thickness. A schematic view of this mapping is presented in figure B.1. Using the above described procedure, three grids with different resolution of the boundary layer are established. Grid parameters for the three grids are presented in Tab. B.1.3.

Table B.1: Grid parameters used for the second Stokes problem. N_x and N_y are the total number of grid cells in the horizontal and vertical direction, respectively. N_{bl} is the number of cells in the $y-$direction inside the boundary layer, while N_{mz} is the number of grid cells in the $y-$direction in the parabolic matching zone.

Parameters	N_x	N_y	N_{bl}	N_{mz}	k	β/δ
Grid A	200	30	15	12	5	0.08
Grid B	100	20	8	8	5	0.08
Grid C	75	15	6	6	5	0.08

Appendix C

Details of the model tests

C.1 The model tests from 2006

The test matrix from the model tests from 2006, where wave excitation forces on fixed cylinders subject to regular waves were studied, are presented in Tab. C.1. The run index is composed as follows. The first number refers to the model geometry and draft, the second number refers to the wave steepness, while the third number refers to the wave period. The last number is reserved for repetition tests and re-runs.

Two cylindrical model geometries were tested. One with a circular cross-section and one with a rectangular cross-section. Both models were made of steel. A sketch of the models used in the experiments from 2006 are presented in Fig. C.1.

C.1.1 Statistics from the 2006-experiments

Mean values and relative errors of the mean wave height obtained from repetition tests are presented in Fig. C.2 and C.4. Mean values and relative errors of the measured wave excitation forces for the in-line horizontal direction and the vertical direction, obtained from repetition tests are presented in Fig. C.4.

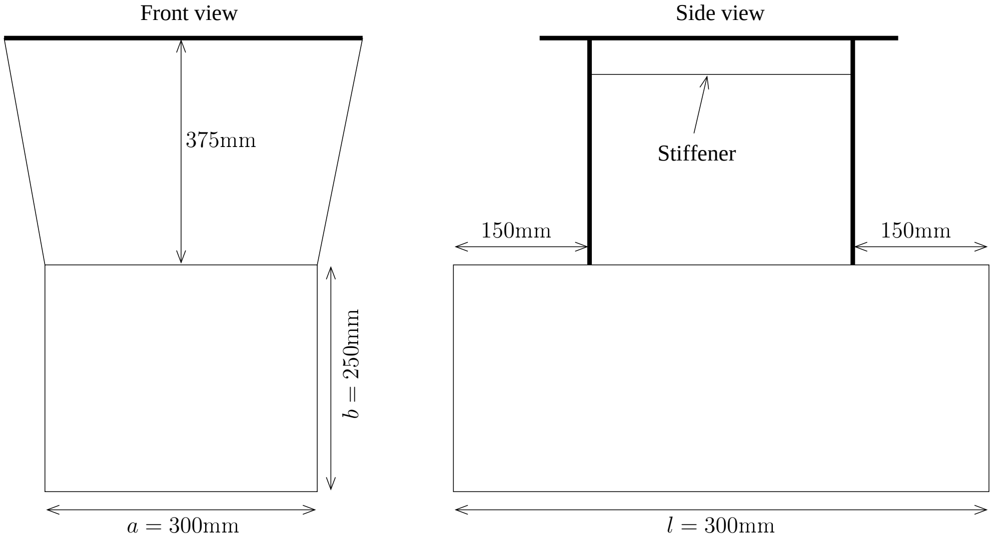

(a) Rectangular cylinder

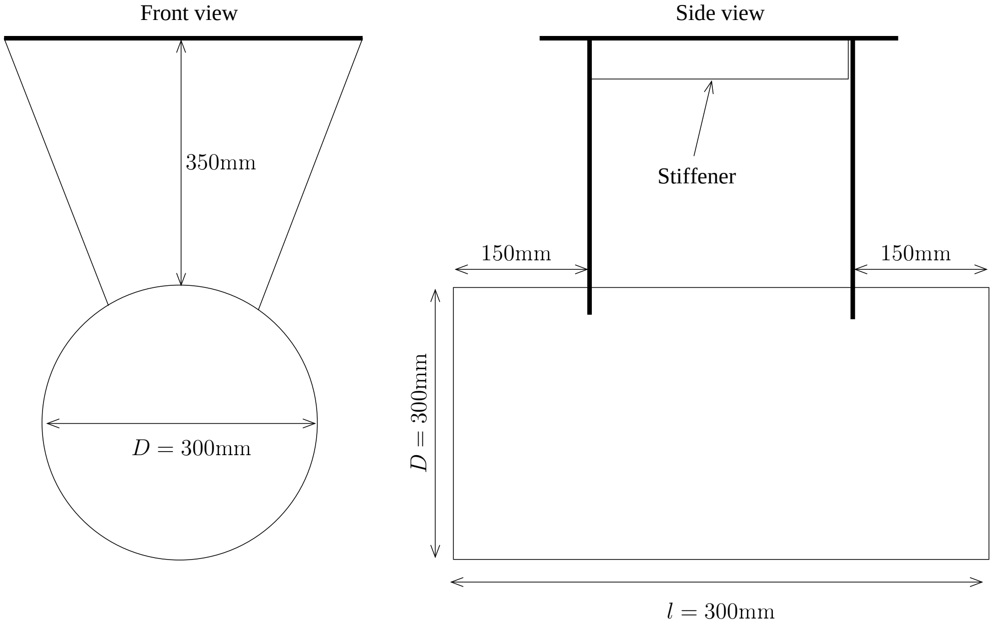

(b) Circular cylinder

Figure C.1: Sketch of models used in the experiments from 2006. The main dimensions are given in the figure.

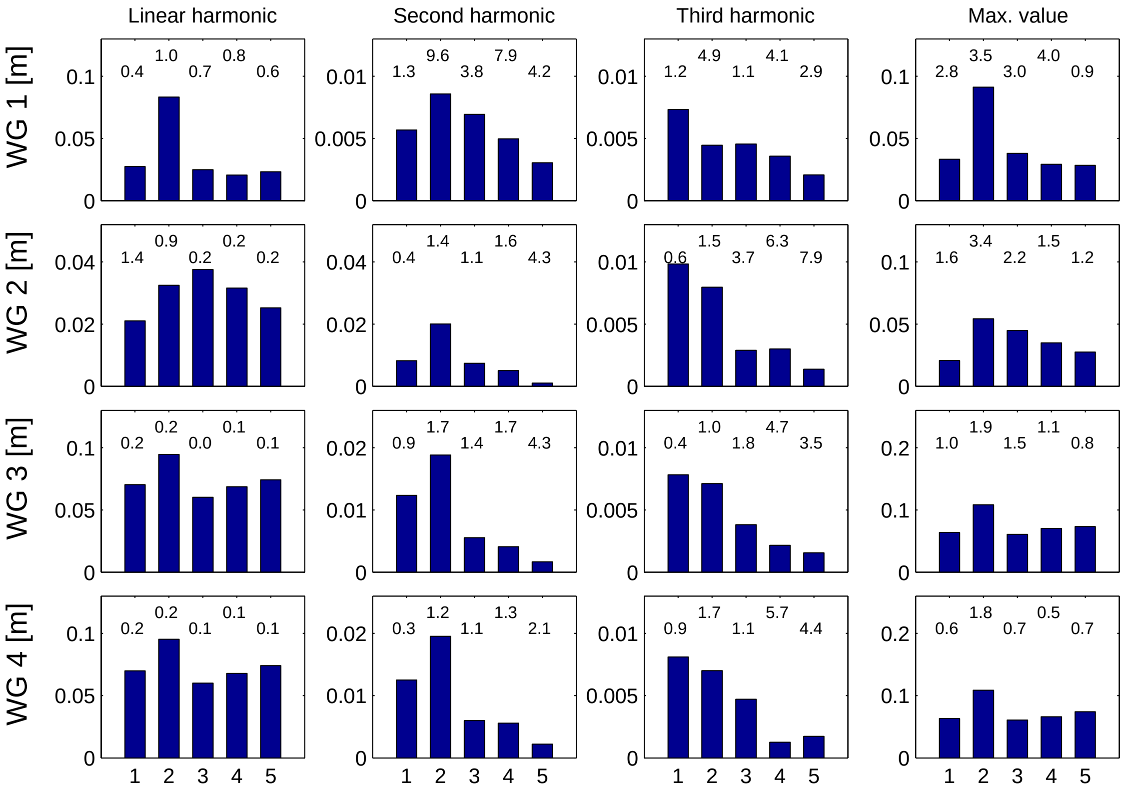

Figure C.2: Mean values of measured free surface elevation obtained from repetition tests for the four wave gauges WG 1 to WG 4. Labels 1 to 5 represents repetition tests for the case numbers 4150, 4250, 5150, 6150 and 7150, respectively. Five repetitions were performed for each case. Corresponding relative errors are given above each bar.

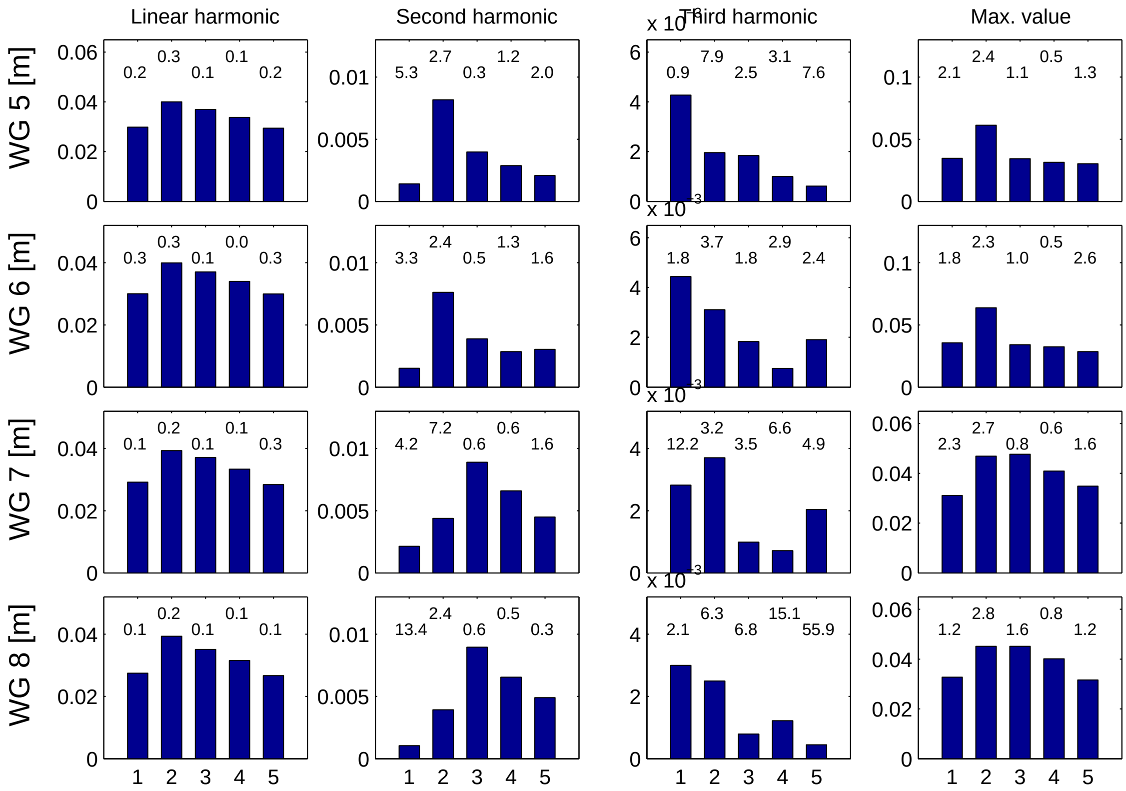

Figure C.3: Mean values of measured free surface elevation obtained from repetition tests for the four wave gauges WG 5 to WG 8. Labels 1 to 5 represents repetition tests for the case numbers 4150, 4250, 5150, 6150 and 7150, respectively. Five repetitions were performed for each case. Corresponding relative errors are given above each bar.

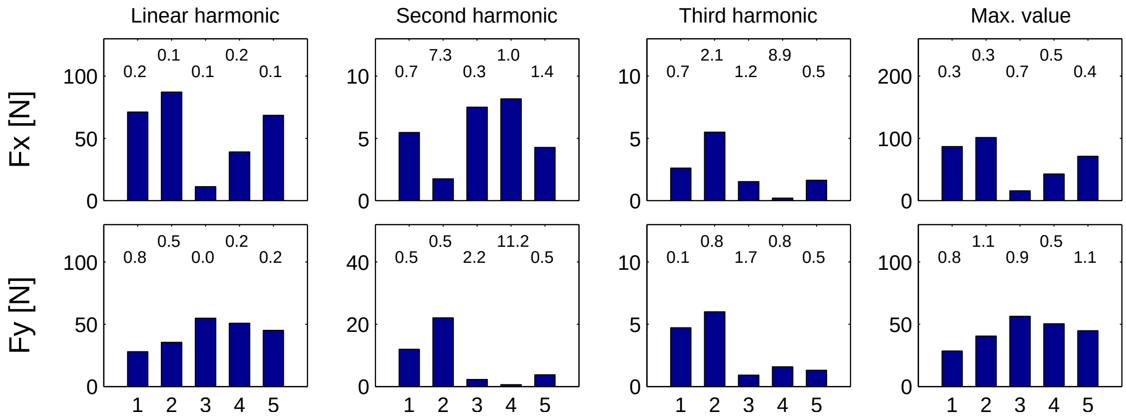

Figure C.4: Mean values of measured clamping forces from repetition tests. Labels 1 to 5 represents repetition tests for the case numbers 4150, 4250, 5150, 6150 and 7150, respectively. Five repetitions were performed for each case. Corresponding relative errors are given above each bar.

		$d/D = 0.2$			$d/D = 0.5$			$d/D = 0.8$		
	T_p	$\varepsilon = 1/50$	$\varepsilon = 1/30$	$\varepsilon = 1/20$	$\varepsilon = 1/50$	$\varepsilon = 1/30$	$\varepsilon = 1/20$	$\varepsilon = 1/50$	$\varepsilon = 1/30$	$\varepsilon = 1/20$
Circular cylinder	0.981	2000	2100	2200	3000	3100	3200	4000	4100	4200
	1.084	2010	2110	2210	3010	3110	3210	4010	4110	4210
	1.179	2021	2121	2220	3020	3120	3220	4020	4120	4220
	1.266	2030	2130	2231	3030	3130	3230	4030	4130	4230
	1.348	2040	2140	2241	3040	3140	3240	4041	4140	4240
	1.348									4241
	1.348									4242
	1.348									4243
	1.348									4244
	1.425	2051	2150	2250	3050	3150	3250	4050	4150	4250
	1.425								4151	
	1.425								4152	
	1.425								4153	
	1.425								4154	
	1.498	2060	2160	2260	3060	3160	3260	4060	4160	4260
	1.568	2070	2170	2270	3070	3170	3270	4070	4170	4270
	1.634	2081	2181	2280	3080	3180	-	4080	4180	-
	1.698	2090	2190	-	3090	3192	-	4090	4190	-
Rectangular cylinder	0.981	5000	5100	5200	6000	6100	6200	7000	7100	7200
	1.084	5010	5110	5210	6010	6110	6210	7010	7110	7210
	1.179	5020	5120	5221	6020	6120	6220	7020	7120	7220
	1.266	5030	5130	5230	6030	6130	6230	7030	7130	7230
	1.348	5040	5140	5240	6040	6140	6240	7040	7140	7240
	1.425	5050	5150	5250	6050	6150	6250	7050	7150	7250
	1.425		5151			6151			7151	
	1.425		5152			6152			7152	
	1.425		5153			6153			7153	
	1.425		5154			6154			7154	
	1.498	5060	5160	5260	6060	6160	6260	7060	7160	7260
	1.568	5070	5170	5270	6070	6170	6270	7070	7170	7270
	1.634	5080	5180	-	6080	6180	-	7080	7180	-
	1.698	5090	5190	-	6090	6190	-	7090	7190	-

Table C.1: Test matrix. Repetition tests have shaded background. The parameter $\varepsilon = H_0/\lambda_0$ is the steepness for the corresponding deep water wave. Tests where over-topping did occur are labeled red. The tests marked with “-” could not be run because of limitations of the wave maker.

C.2 The model tests from 2008

Some details from the experiments in 2008 with the moored circular cylinder are presented.

C.2.1 Acceleration measurements

The total acceleration relative to the Earth-fixed frame of reference in the direction of the body coordinate y' is found as $a'_y = 0.5\,(a_{y'2} + a_{y'1})$, while the angular acceleration is found as $\ddot{\theta} = 0.5\,(a_{y'2}/r_3 - a_{y'1}/r_2)$. The total acceleration of the cylinder in the Earth-fixed coordinate system is thus found by mapping using the Jacobian and correcting for acceleration of gravity, $-g\mathbf{e}_y$, and angular acceleration. Now consider the cylinder at rest. For $\theta = 0$, all accelerometers are calibrated to measure zero acceleration. When θ is increased to 90°, the accelerometers in the y' direction will measure g and the accelerometer in the x'-direction will measure $-g$, when the cylinder is at rest. If we further increase the angle θ to 180°, we get $a_{x'} = 0$, $a_{y'1} = 2g$ and $a_{y'2} = 2g$. This must be accounted for if we want to find the accelerations in an Earth fixed frame of reference. Further, when there is an angular acceleration $\ddot{\theta}$ due to roll motion of the cylinder, we will measure $a_{x'} = -r_1\ddot{\theta}$, $a_{y'1} = -r_2\ddot{\theta}$ and $a_{y'2} = r_3\ddot{\theta}$, where r_1, r_2 and r_3 are defined in Fig.6.10(a). The total accelerations in the Earth-fixed reference frame are thus

$$\begin{bmatrix} a_x \\ a_y \end{bmatrix} = \begin{bmatrix} \cos\theta & -\sin\theta \\ \sin\theta & \cos\theta \end{bmatrix} \begin{bmatrix} a_{x'} \\ a_{y'} \end{bmatrix} + g \begin{bmatrix} \sin\theta \\ \cos\theta - 1 \end{bmatrix} + \ddot{\theta} \begin{bmatrix} r_1 \\ r_2 - r_3 \end{bmatrix} \tag{C.1}$$

For small angles θ, Eq.C.1 can be linearized. Further, applying that $r_1 = r_2 = r_3 = r$, we get

$$\begin{bmatrix} a_x \\ a_y \end{bmatrix} = \begin{bmatrix} 1 & -\theta \\ \theta & 1 \end{bmatrix} \begin{bmatrix} a_{x'} \\ a_{y'} \end{bmatrix} + \begin{bmatrix} g\theta \\ 0 \end{bmatrix} + \begin{bmatrix} r\ddot{\theta} \\ 0 \end{bmatrix} \tag{C.2}$$

These are the linearized expressions, valid for small roll angles θ, giving the accelerations of the model in an Earth-fixed frame of reference.

Linearity test for the springs

The linearity properties of the springs used in the mooring line arrangement are tested. Measured elongation of the three springs from the linearity test is shown in Fig. C.5. The results shows that the springs are linear when loaded below their reported floating limit, which is indicated by the horizontal line in the figure.

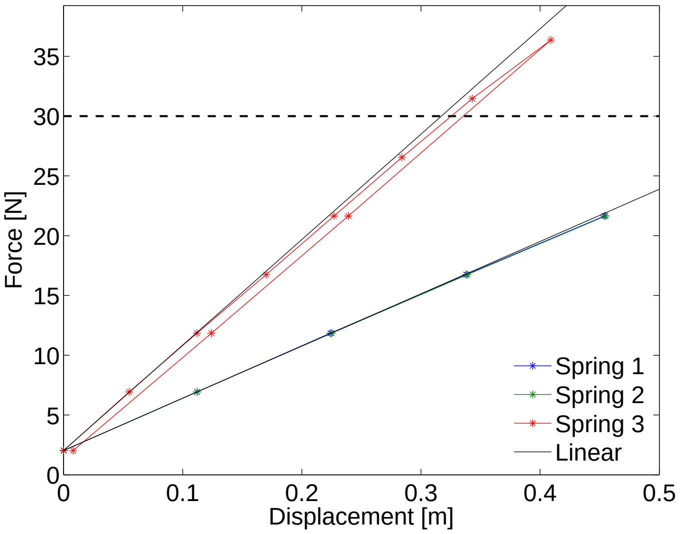

Figure C.5: Test of linearity of the springs used in the model tests. The dashed line shows the given floating limit for the spring. Floating is also verified by noting that spring 3 does not go back to its initial length after unloading.

Appendix D

Time series

D.1 Wave elevation from tests with fixed cylinders

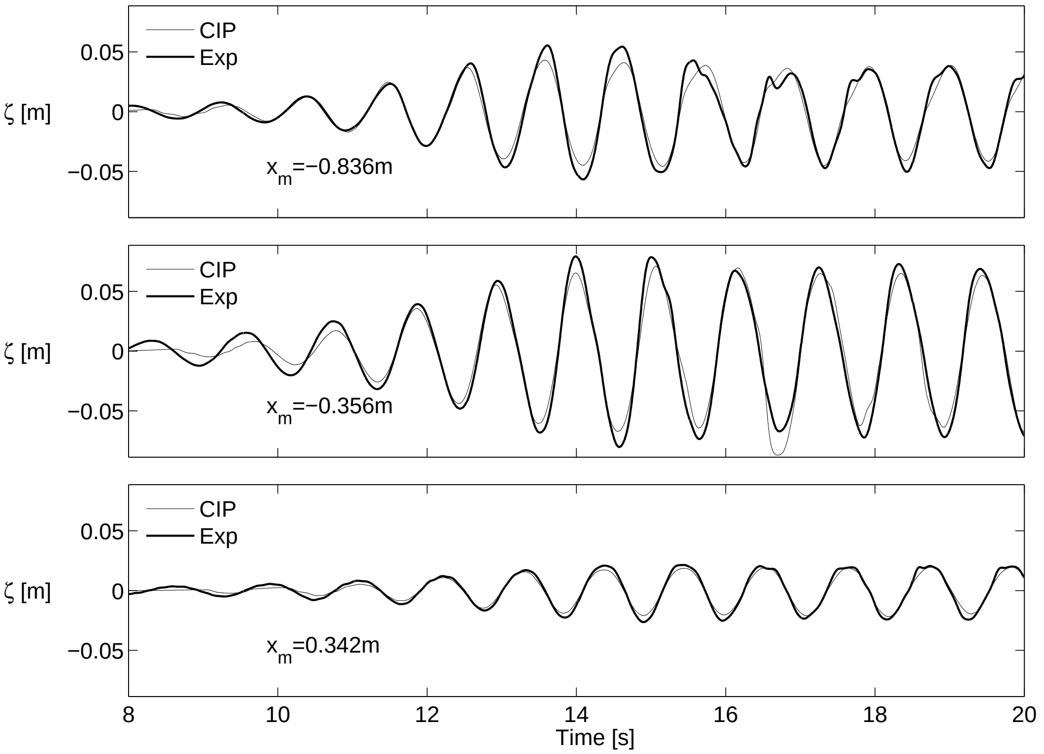

Figure D.1: Computed and measured free surface elevation from tests with fixed rectangular cylinder at WG 2, WG 3 and WG 5. $d/D = 0.5$, $T = 1.084$s, $H_0/\lambda_0 = 1/20$. (Model tests from 2006).

D.2 Wave elevation from tests with moored cylinder

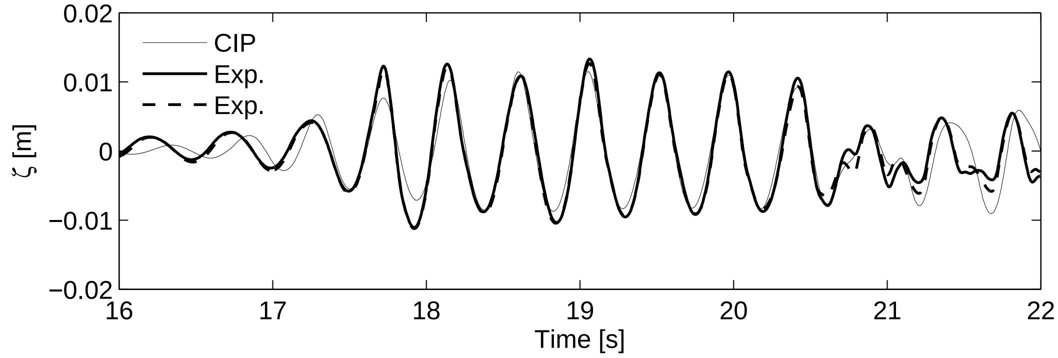

Figure D.2: Computed free surface elevation in front of cylinder is compared with measured free surface elevation from model tests with $T = 0.457$s. Input wave steepness was $H/\lambda = 1/14$. Two parallel wave gauges from the measurements are used for comparison.

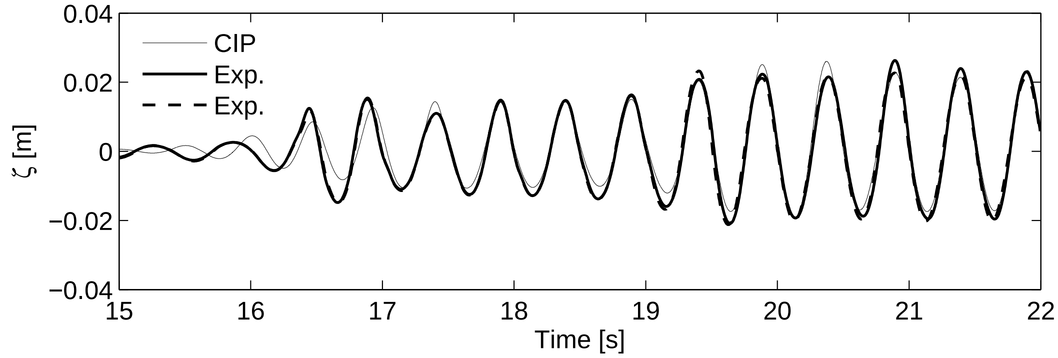

Figure D.3: Computed free surface elevation in front of cylinder is compared with measured free surface elevation from model tests with $T = 0.497$s. Input wave steepness was $H/\lambda = 1/14$. Two parallel wave gauges from the measurements are used for comparison.

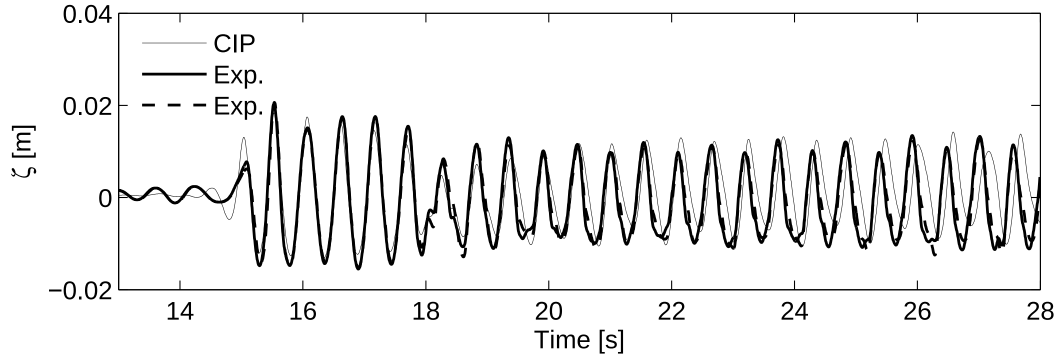

Figure D.4: Computed free surface elevation in front of cylinder is compared with measured free surface elevation from model tests with $T = 0.544$s. Input wave steepness was $H/\lambda = 1/14$. Two parallel wave gauges from the measurements are used for comparison.

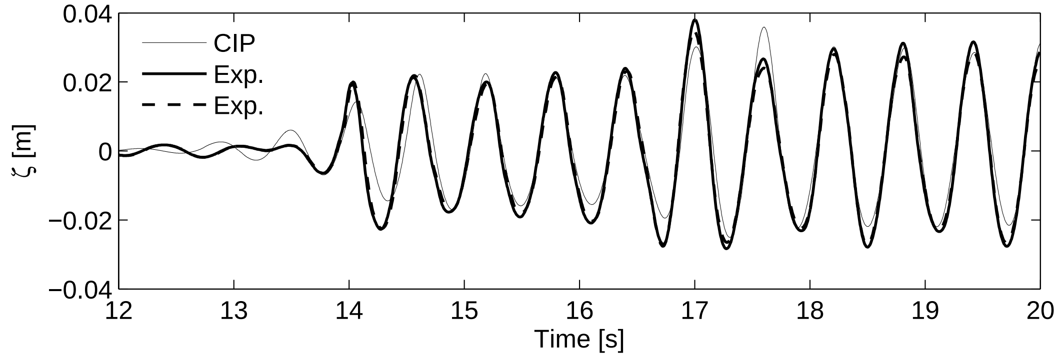

Figure D.5: Computed free surface elevation in front of cylinder is compared with measured free surface elevation from model tests with $T = 0.601$s. Input wave steepness was $H/\lambda = 1/14$. Two parallel wave gauges from the measurements are used for comparison.

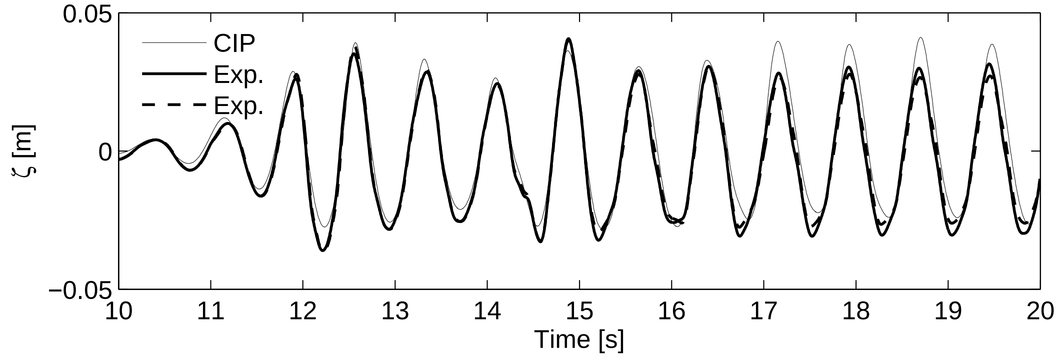

Figure D.6: Computed free surface elevation in front of cylinder is compared with measured free surface elevation from model tests with $T = 0.761$s. Input wave steepness was $H/\lambda = 1/14$. Two parallel wave gauges from the measurements are used for comparison.

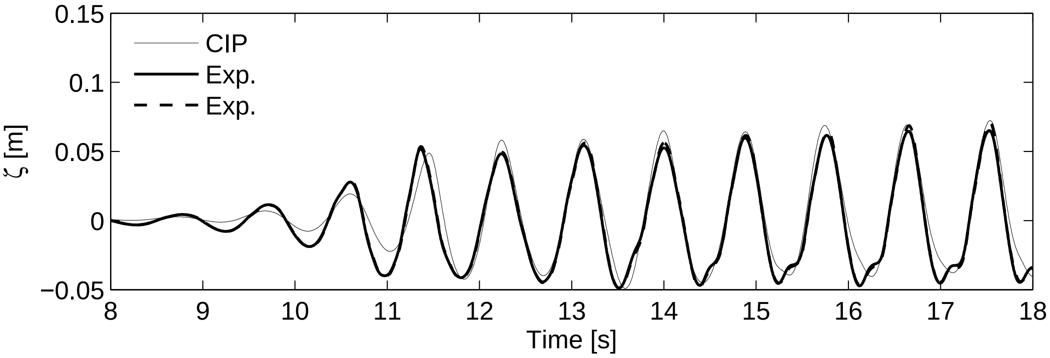

Figure D.7: Computed free surface elevation in front of cylinder is compared with measured free surface elevation from model tests with $T = 0.878$s. Input wave steepness was $H/\lambda = 1/14$. Two parallel wave gauges from the measurements are used for comparison.

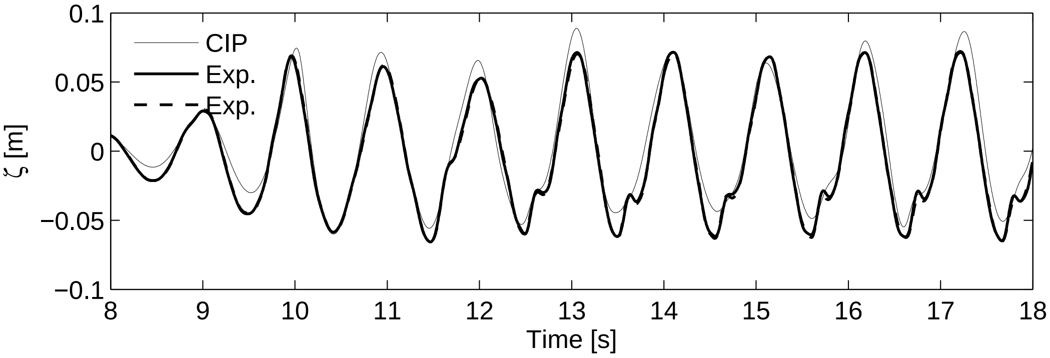

Figure D.8: Computed free surface elevation in front of cylinder is compared with measured free surface elevation from model tests with $T = 1.038$s. Input wave steepness was $H/\lambda = 1/14$. Two parallel wave gauges from the measurements are used for comparison.

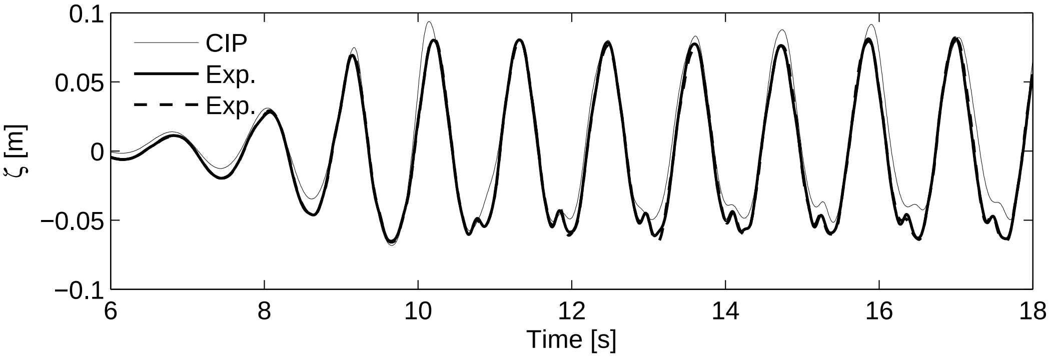

Figure D.9: Computed free surface elevation in front of cylinder is compared with measured free surface elevation from model tests with $T = 1.132$s. Input wave steepness was $H/\lambda = 1/14$. Two parallel wave gauges from the measurements are used for comparison.